2008-07-15

Microkinetic Model of Fischer-Tropsch Synthesis on Iron Catalysts

Uchenna Prince Paul
Brigham Young University - Provo

MICROKINETIC MODEL OF FISCHER-TROPSCH SYNTHESIS ON IRON CATALYSTS

by

Uchenna P. Paul

A dissertation submitted to the faculty of

Brigham Young University

in partial fulfillment of the requirements for the degree of

Doctor of Philosophy

Department of Chemical Engineering

Brigham Young University

August 2008

BRIGHAM YOUNG UNIVERSITY

GRADUATE COMMITTEE APPROVAL

of a dissertation submitted by

Uchenna P. Paul

This dissertation has been read by each member of the following graduate committee and by majority vote has been found to be satisfactory.

_____	_____
Date	Calvin H. Bartholomew, Chair
_____	_____
Date	Richard L. Rowley
_____	_____
Date	William C. Hecker
_____	_____
Date	Hugh B. Hales
_____	_____
Date	Kenneth A. Solen

BRIGHAM YOUNG UNIVERSITY

As chair of the candidate's graduate committee, I have read the dissertation of Uchenna P. Paul in its final form and have found that (1) its format, citations, and bibliographical style are consistent and acceptable and fulfill university and department style requirements; (2) its illustrative materials including figures, tables, and charts are in place; and (3) the final manuscript is satisfactory to the graduate committee and is ready for submission to the university library.

_____ _____

Date

Calvin H. Bartholomew
Chair, Graduate Committee

Accepted for the Department

_____

Larry L. Baxter
Graduate Coordinator

Accepted for the College

_____

Alan R. Parkinson
Dean, Ira A. Fulton College of Engineering and Technology

ABSTRACT

MICROKINETIC MODEL OF FISCHER-TROPSCH SYNTHESIS

ON IRON CATALYSTS

Uchenna P. Paul

Department of Chemical Engineering

Doctor of Philosophy

Fischer-Tropsch synthesis (FTS), developed in the early 1900's, is defined as the catalytic conversion of H_2 and CO to hydrocarbons and oxygenates with the production of H_2O and CO_2. Accurate microkinetic modeling can in principle provide insights into catalyst design and the role of promoters. This work focused on gaining an understanding of the chemistry of the kinetically relevant steps in FTS on Fe catalyst and developing a microkinetic model that describes FTS reaction kinetics.

Stable Al_2O_3-supported/promoted (20% Fe, 1% K, 1% Pt) and unsupported Fe (99% Fe, 1% Al_2O_3) catalysts were prepared and characterized. Transient experiments including temperature programmed desorption (TPD), temperature programmed hydrogenation (TPH), and isothermal hydrogenation (ITH) provided insights into the chemistry and energetics of the early elementary reactions in FTS on Fe catalyst. Microkinetic models of CO TPD, ITH, and FTS were developed for Fe catalyst by combining transition state theory and UBI-QEP formalism. These models support the

conclusion that hydrocarbon formation occurs on Fe via a dual mechanism involving surface carbide and formyl intermediates; nevertheless, hydrocarbon formation is more favorable via the carbide mechanism. Carbon hydrogenation was found to be the rate determining step in the carbide mechanism. CO heat of adsorption on polycrystalline Fe at zero coverage was estimated to be -91.6 kJ/mol and -64.8 kJ/mol from ITH and FTS models respectively, while a mean value of -50.0 kJ/mol was estimated from the TPD model.

Statistically designed steady-state kinetic experiments at conditions similar to industrial operating conditions were used to obtain rate data. The rate data were used to develop a microkinetic model of FTS. FTS and ITH appear to follow similar reaction pathways, although the energetics are slightly different. In both cases, hydrocarbon formation via the carbide mechanism was more favorable than via a formyl intermediate while carbon hydrogenation was the rate determining step.

Promotion of Fe with K does not alter Fischer-Tropsch synthesis reaction pathways but it does alter the energetics for the steps leading to the formation of CO_2. This phenomenon accounts for the CO_2 selectivity of 0.3 observed for K-promoted Fe against 0.17 observed for un-promoted Fe. A Langmuir Hinshelwood rate expression derived from the microkinetic model was put into a fixed bed FTS reactor design code; calculated reactor sizes, throughput, temperature profiles and conversion are similar to those of pilot and demonstration FTS reactors with similar feed rates and compositions.

ACKNOWLEDGEMENTS

I wish to thank Dr. Calvin H. Bartholomew for his mentorship and patience with me during the course of this work, and for helping me realize that "*without catalysis no form of life could exist!"* My gratitude also goes to Dr. William Hecker, Dr. Richard Rowley, Dr. Dennis Tolley for their tutelage especially in subject areas that helped me in this work. To my other graduate committee members, I say *I mee la (thank you)!*

Special thanks to Dr. Hu Zou for his assistance with catalyst preparation and experimental setup. I will remain indebted to the members of Brigham Young University, Provo catalysis lab whom I got to work with and learn from during the course of this work for their support throughout every aspect of this work. I will not forget to thank Brian Critchfield for the assistances he gave me while he was pursuing his graduate work here at BYU.

Most importantly, I will like to thank my lovely wife Jennifer for her patience, and the many times she came to the lab with me both in the evenings and on weekends. Your encouragement and assistance helped me finish this work. *I love you Babe!*

Finally, I wish to express my gratitude to Heavenly Father for making this a dream come true

TABLE OF CONTENTS

LIST OF TABLES

LIST OF FIGURES

NOMENCLATURE

θ_i	fractional surface coverage of species *i*
α	chain propagation probability
ΔH	net reaction enthalpy (J/mol)
θ	estimated parameter
$\alpha_i, \beta_i, \mu_i, \gamma_i$	Lorentzian constants
ΔH_{ads}	adsorbate heat of adsorption (J/mol)
τ	residence time (s)
ρ_b	catalyst bed density (kg/m^3)
ε_b	bed void fraction
β	temperature ramp rate (K/s)
θ_A^0	initial fractional coverage of species *A*
$\Psi(\phi)$	objective function
ΔH_B	apparent heat of adsorption (J/mol)
C_A^0	initial concentration of species *A*
$f(T_i, \phi)$	predicted normalized mole fractions
r_A'''	reaction rate with respect to species *A* (mol/m^3 s)
w_{ε_i}	weighted error in observed response
$Y_{A_{\max}}$	maximum observed mole fraction of species *A*
A	rate constant
A_i	apparent pre-exponential factor
B	rate constant
C_A	concentration of specie *A* (mol/m^3)
D	optimality criteria
D	fractional dispersion of active catalytic material
D_{AB}	gas phase bonding energy for species *AB* (J/mol)
D_{isp}	fractional dispersion of active catalytic material

DODR	double precision orthogonal distance regression
DVODE	double precision variable coefficient ordinary differential equation solver
Ea_A	apparent activation energy (J/mol)
E_f	activation energy for forward reaction step (J/mol)
E_r	activation energy for reverse reaction step (J/mol)
$f(x)$	Lorentzian function
$F(X, \theta)$	Jacobian matrix containing partial derivatives of reaction rate expression with respect to the parameter to be estimated, evaluated at run condition *i*.
F_o	inlet molar flow rate of limiting reactant (mol/s)
$F^T(X, \theta)$	transpose of the Jacobian matrix
FTS	Fischer-Tropsch synthesis
ITH	isothermal hydrogenation
k_i	rate constant
K_i	equilibrium constant
L	catalyst bed length (m)
LH	Langmuir Hinshelwood
LM	Levenberg Marquardt
M_L	fractional loading of active catalyst material
$M_{loading}$	fractional active catalytic metal loading
m_n	mole fraction of species n
M_W	molecular weight of active catalyst metal (kg/mol)
N	carbon number
N	coordination number
p_A	partial pressure of species A
P_{CO}	partial pressure of CO (atm)
P_{H2}	partial pressure of H_2 (atm)
P_{tot}	total reactor pressure (Pa)
Q_{0A}	atomic heat of adsorption for adsorbate A (J/mol)
Q_A	Binding energy of adsorbate A (J/mol)
Q_{AB}	heat of adsorption for adsorbate AB (J/mol)
R	gas constant
R^2	correlation coefficient
r_A	reaction rate (1/s)
r_{CO}	rate of CO disappearance (mol/kg s)

r_{CO2}	rate of CO_2 formation (mol/kg s)
R_G	reaction rate (1/s)
R_g	gas constant (J/mol K)
R_I	reaction rate (1/s)
r_p	rate of chain propagation
r_t	rate of chain termination
T	time (s)
T	temperature (K)
T^0	initial reactor temperature (K)
T_p	peak disorption temperature (K)
TPD	temperature programmed desorption
TPH	temperature programmed hydrogenation
TPR	temperature programmed reduction
TPSR	temperature programmed surface reaction
$u(t)$	superficial velocity (m/s)
UBI-QEP	unity bond index quadratic exponential potential
W	weight of catalyst (kg)
$W_{½}$	full-width-at-half-maximum
w_n	weight fraction for species n
X	fractional conversion
y_A	mole fraction of species A
Y_A	normalized mole fraction of species A
Z	axial reactor distance (m)

1. Chapter 1: Introduction

1.1 Background

Global demand for energy derived from petroleum liquids is on the increase. The United States Energy Information Administration (EIA) projects an increase in world liquid fuel demand from 80 million barrels per day in 2004 to 118 million barrels per day in 2030, while demand of natural gas is projected to increase from 100 trillion cubic feet in 2004 to 163 trillion cubic feet in 2030 [1]. However, proven petroleum reserves are not expected to increase at the same rate as demand. Moreover, most of the world's oil reserves are in remote places and regions that are probably unstable politically. Although natural gas is used widely in urban areas, a large amount is flared daily in remote oil fields due to lack of access to markets. Probable shortages of petroleum feedstock and global awareness towards climate change have stimulated a quest for environmentally friendly fuel alternatives from sources other than crude oil. Conversion of natural gas, coal and biomass to high quality liquid fuels via Fischer-Tropsch synthesis is an economically and technically viable option, since the world's proven reserves of natural gas, coal and biomass exceed those of crude oil and this technology is cost effective at present and projected prices of oil.

Concentrated, large-scale reserves of stranded natural gas can be economically liquefied (LNG) [2] and transported to available markets; however, LNG is not readily

adaptable for use as a transportation fuel. Moreover, production of LNG from medium and small reserves of stranded and flared gas is not economical. Although natural gas can also be converted to liquid fuel via oxidative coupling of methane (OCM) [3], it is however, neither technically or economically viable. On the other hand, smaller or dispersed reserves of natural gas, coal, biomass, or domestic waste can be converted to synthesis gas (a mixture of CO and H_2) through gasification [4] followed by conversion to liquid fuels via Fischer-Tropsch Synthesis (FTS). Liquid products from FTS can be refined using existing refining methods to produce premium grade, sulfur-free liquid fuels and chemicals [5] that can be transported and used within the existing infrastructure. This is the basis of gas-to-liquid (GTL), coal-to-liquid (CTL), and biomass-to-liquid (BTL) technologies.

FTS, developed in the 1920's by German scientists Fischer and Tropsch, is a combination of hydrogenation and polymerization of CO to form hydrocarbons and oxygenates (including H_2O and CO_2) in the presence of Co, Fe or Ru catalysts [6]. The Germans used this method to produce diesel and aircraft fuels during World War II while South Africa used CTL to meet its fuel and chemical needs from 1955 to present. South Africa's energy giant Sasol, and Shell, Malaysia, are presently operating commercial scale FTS processes; in addition, Shell, Qatar, ENI/Agip, and ConocoPhillips are either building or planning to build GTL processes [7, 8]. Also, some power plants are planning to incorporate an FTS process in their power generation cycle with the hope of making FTS liquids during off-peak periods from natural gas, coal or biomass. Table 1-1, adapted from [9] is a summary of operating and announced FTS plants.

Table 1-1: Currently operating and planned FTS plants worldwide[9].

Country	Company	Reactor technology	Prod. level (bpd)	Start-up year
South Africa	PetroSA	Sasol's slurry phase technology	20000	1992
Malaysia	Shell	Shell middle distillate synthesis (SMDS); fixed-bed technology	15000	1993
Qatar	Sasol & Qatar Petroleum in alliance with Chevron	Sasol's slurry phase technology	34000	2005
Nigeria	Chevron Nigeria (Sasol-Chevron alliance) and Nigerian National Petroleum Company	Slurry phase technology	34000	Unknown
Qatar	Shell and Qatar Petroleum	Shell middle distillate synthesis (SMDS); fixed-bed technology	140000	2009

Although substantial research into the mechanism and kinetics of FTS has been conducted over the past 70 years and is on-going, much of the detail chemistry at the molecular level is not well understood. To date, simple power-law or Langmuir-Hinshelwood type rate expressions are used in the design of industrial FTS reactors [7, 10]. Such expressions are only accurate over a narrow range of temperatures. Indeed improvements in catalyst, reactor, and process design and economics are needed for large-scale GTL, and especially for smaller-scale BTL, CTL, and GTL processes. Such improvements will require robust mechanistic and process models and will depend on the development of an accurate microkinetic model.

1.2 Microkinetic Analysis: A Background

In *The Microkinetics of Heterogeneous Catalysis*, Dumesic et al. [11] define microkinetic analysis as "the examination of catalytic reactions in terms of elementary chemical reactions that occur on the catalytic surface and their relation with each other during a catalytic cycle." They further define catalytic reaction synthesis as the combination of information obtained from various experimental and theoretical studies to create a coherent description on how the catalyst, reactions, and reaction conditions could be formulated to achieve high yields of a particular product.

Development of microkinetic models for FTS is in an early stage and has focused on models for cobalt catalysts [12-14], while microkinetic modeling of FTS on iron catalyst has not been addressed. Microkinetic modeling can in principle provide (1) insights into catalyst design, and the role of promoters and support, (although this potential has not yet been tapped); (2) modeling of activity and selectivity over a wide range of process parameters; and (3) more reliable predictions of reactor and process designs and costs.

1.3 Objectives and Approach

The objectives of this work were to (1) gain a basic understanding of the chemistry of the kinetically relevant steps in FTS on iron catalyst, and (2) develop a microkinetic model that describes the reaction kinetics at the molecular level over a wide range of experimental conditions, such as temperature, pressure and gas phase concentrations in the absence of influences of heat and mass transfer. These latter processes should be modeled separately.

To accomplish these objectives, a research methodology involving both experiment and theory was used. It involved (1) preparation and characterization of stable supported Fe and unsupported Fe catalysts with and without K, and Pt promoters, (2) kinetic modeling of unsteady-state experiments such as temperature-programmed desorption, temperature-programmed hydrogenation, and isothermal hydrogenation of carbon species to obtain kinetic parameters for the early elementary reaction steps in FTS, (3) use of transition-state theory and unity bond index quadratic exponential potential to calculate pre-exponential factors and activation energies for steps where it was not possible to measure these quantities, (4) derivation of a Langmuir-Hinshelwood type rate expressions consistent with the proposed mechanisms, and (5) performing statistically designed steady-state kinetic experiments in a Berty reactor to obtain data used to validate the model.

The microkinetic model presented in this work was limited to the formation of hydrocarbons with carbon number not greater than two. It also included the formation of CO_2 and H_2O. Similarly, the macrokinetic model presented in this work will be in the form of the overall rate expression for the disappearance of CO, in which case the rates of all other species can be obtained by multiplying the CO disappearance rate by the appropriate selectivity.

1.4 Dissertation Organization

This work has been organized into seven chapters. Chapter 1 provides background information on FTS and microkinetic modeling while chapter 2 reviews pertinent FTS literature with emphasis on that dealing with FTS mechanisms. Chapter 3 describes the preparation and characterization of the catalysts used in this study as well as

various experimental techniques. In chapters 4 and 5, results of the various experiments including theories used in developing the model are discussed. Chapter 4 presents the results of transient experiments such as temperature-programmed desorption experiments, hydrogenation of stable surface species – isothermal hydrogenation, and temperature-programmed hydrogenation. Chapter 5 presents the results from the statistically designed steady-state kinetic experiments. In chapter 6, the results are discussed in detail while chapter 7 presents the summary, conclusion, and recommendations. The appendix includes detailed catalyst preparation procedures, a sequential design algorithm, and summary of calculations, derivations and a sample computer codes used.

2. Chapter 2: Fischer-Tropsch Synthesis Mechanism and Kinetics: A Literature Review

2.1 Introduction and Reaction Chemistry

2.1.1 Introduction

Since the discovery of FTS in the late 1920s by two German scientists named F. Fischer and H. Tropsch, numerous review papers, books and reports have addressed FTS mechanisms and kinetics [6, 7, 9, 15]. Despite these numerous studies, researchers are divided on the precise details of the mechanism. To date, there is no accurate microkinetic model of FTS on Fe.

Microkinetic analysis is defined as the examination of catalytic reactions in terms of elementary chemical reactions that occur on the catalytic surface and their relation to each other during a catalytic cycle. It provides precise kinetic parameters, such as pre-exponential factors and activation energies for each elementary reaction step in the reaction mechanism. Such an understanding can facilitate the design of better active and selective catalysts and more compact reactors. It also eliminates the serious limitations inherent in the rate-determining-step approximation. Therefore, by solving the steady-state balance for each surface intermediate in the sequence of elementary steps and the reactor design equations simultaneously, the surface coverages and gas phase

compositions can be determined more accurately. For a steady-state isothermal plug-flow reactor, the necessary equations are shown in Equations 2.1 and 2.2 below.

$$\frac{d\theta}{dt} = R_I = 0 \tag{2.1}$$

$$\frac{dX}{d(W/F_o)} = \frac{D_{isp} \cdot M_L \cdot R_G}{M_W} \tag{2.2}$$

where θ is an n x n matrix of surface coverages (where n is equal to the number of surface intermediates + vacant sites), X is an m-dimensional vector of fractional conversion (where m is equal to the number of gas phase species in the model). D_{isp} is the fractional dispersion of active catalytic metal; M_L is the fractional loading of the active catalytic metal; and M_w is the molecular weight of the active catalyst metal. W is the amount of catalyst, and F_o is the flow rate of the limiting reactant. R_I and R_G are matrices for the reaction rates of intermediates and terminal gas species (reactants and products) in turnover frequency units [16].

The steps in the development of a microkinetic model include (1) formulation of detailed reaction mechanism, (2) determination of the activation energies and pre-exponential factors for the reactions in the network, (3) optimization of the reaction network to remove kinetically irrelevant reactions, and (4) validation of the model [11, 17]. Fishtik et al. suggested the use of a reaction network analysis analogous to electrical networks to formulate microkinetic models [18].

The literature review presented in this chapter will focus on the mechanistic aspects of FTS and the various theoretical and experimental methods for determining reaction energetics.

2.1.2 Chemistry and mechanistic aspects of FTS

The principle stoichiometric reactions occurring in FTS can be described as follows [10, 19, 20]:

$$CO + 3H_2 \rightarrow CH_4 + H_2O \tag{2.3}$$

$$nCO + 2nH_2 \rightarrow C_nH_{2n} + nH_2O \tag{2.4}$$

$$nCO + (2n+1)H_2 \rightarrow C_nH_{2n+2} + nH_2O \tag{2.5}$$

$$CO + H_2O \rightarrow CO_2 + H_2 \tag{2.6}$$

$$2CO \rightarrow C + CO_2 \tag{2.7}$$

Reaction 2.3 represents the formation of methane. Reactions 2.4 and 2.5 represent the formation of olefins and alkanes, respectively, while Reaction 2.6 is the water-gas-shift reaction. Reaction 2.7 is the Boudouard reaction involving formation of carbon. The formation of oxygenates is not accounted for in the above reactions. Side reactions such as isomerization, cracking and hydrogenolysis, secondary hydrogenation and chain initiation have been observed or proposed as the case may be [7] but are not included above.

Catalysts for FTS (Reactions 2.4 and 2.5) include cobalt, iron, and ruthenium. Iron is also known to catalyze Reaction 2.6 involving hydrogen production from the water-gas-shift reaction, thereby making it a better catalyst for FTS with low H_2/CO feed ratios [21] typical of *syngas* derived from coal or biomass. Cobalt and ruthenium are the most active catalysts. Ru is less selective towards methane, however, it is very expensive; thereby limiting its use as FTS catalyst to merely an academic exercise.

However, Ru has been used extensively as a promoter in some Co [7] catalysts and has been found to increase the activity and reducibility of Co catalysts [22-25]. Similar increases in both activity and reducibility of Fe FTS catalysts promoted with K and Cu have been reported [26-29]. Detailed understanding of the effects of promoters and supports is a current subject of study at various laboratories [7] including the Brigham Young University catalysis laboratory.

While Ru catalyst is the most active metal for FTS, Co on the other hand is three times more active than Fe catalyst; however, it is also several times more expensive than Fe [9]. Also, Fe catalyst is more resistant to poisons and has a flexible product slate [30, 31] than Co or Ru catalyzed FTS process. Despite these merits, Co catalyst is preferred over Fe catalyst especially for syngas derived from natural gas because the cost savings in the construction of smaller reactors outweighs the other former benefits. Fe tends to form bulk metal carbides during FTS. The active catalytic phase on cobalt catalyst is believed to be the pure metal while on iron catalysts, the active phase is assumed to be the Haag carbide (Fe_5C_2) [7, 26, 32].

2.1.3 FTS as a polymerization process

FTS is a polymerization process involving the coupling of carbon-carbon bonds to form higher hydrocarbons and oxygenates [6, 7, 15, 33-36]. The product distribution of FTS follows a monomer addition mechanism initially postulated by Flory and others [37] and is referred to as the Anderson-Schulz-Flory (ASF) distribution as shown in Equations 2.8 and 2.9.

$$w_n = n(1-\alpha)^2 \alpha^{n-1} \tag{2.8}$$

$$\alpha = \frac{m_{n+1}}{m_n} = \frac{r_p}{(r_p + r_t)} \tag{2.9}$$

where n is the number of carbon atoms, w_n and m_n are the weight and mole fractions of products containing n carbon atoms, α is the chain growth probability, r_p and r_t are the rates of chain propagation and termination. Values of n are typically observed to range from 1 to 150. Equation 2.8 predicts that w_n goes through a maximum with increasing n while Equation 2.9 predicts that the mole fraction m_n decreases with increasing n. Thus the FTS process is not selective to a single reaction product or to a narrow range of carbon numbers, (methane is the only exception). It is observed that the selectivity range in FTS is influenced by reaction conditions such as temperature, pressure and feed composition. High pressures (25 – 40 bar), low temperatures (493 – 523 K) and low H_2/CO ratios favor the formation of waxes, while low pressures and higher temperatures favor the formation of methane and low molecular weight hydrocarbons.

Although the ASF model predicts hydrocarbon selectivity in FTS fairly well, deviations from ASF distributions of products from FTS are observed [38-44]. Such deviations include higher than expected C_1 selectivity, lower than expected C_2 selectivity, and chain-length-dependent chain growth probability, leading to higher than expected probabilities for heavier hydrocarbons.

Various theories and models have been proposed to explain these deviations from ASF. They include: a two-active-site model [45], diffusion-enhanced olefin re-adsorption [46-48], solvent-enhanced olefin re-adsorption [49] due to the greater

solubility of larger olefins[50] and/or greater physisorption strength of higher olefins [51], and vapor-liquid equilibrium phenomena [52]. Buchang and Davis concluded from their analysis of accumulated products in FTS that previously reported α values might be in error, thereby explaining reported deviations from ASF [41].

2.1.4 Selectivity models

Several mathematical models have been proposed by various researchers to predict FTS product selectivity [37, 49, 53, 54]. Most of the chemical models are enhancements of Anderson-Flory probability model with readsorption of olefins.

Iglesia and coworkers propose mass transfer effects as important factors in determining FTS selectivity. Mims and coworkers observe that selectivity depends on the amount of carbon on the catalytic surface [38-40, 42]. A review of previous selectivity models can be found in Bartholomew and Farrauto [7]. Water enhancement of CO conversion during FTS has been reported [55]. Nevertheless, this concept has remained controversial and requires further study to fully understand the effect of water.

2.2 Mechanisms of FTS

2.2.1 Mechanistic aspects of FTS

Hundreds of elementary steps have been proposed to occur during FTS with the steps either in series or in series/parallel with each other resulting in the formation of the various reaction products. As illustrated below, these elementary reactions can be divided into three steps; namely: adsorption steps, surface reactions or Langmuir-

Hinshelwood reactions, and desorption steps. In some cases, Eley-Rideal type reactions have been proposed as well.

Adsorption:

$$CO_{(g)} + * \rightarrow CO* \tag{2.10}$$

$$H_{2_{(g)}} + 2* \rightarrow 2H* \tag{2.11}$$

CO dissociation:

$$CO* + * \rightarrow C* + O* \tag{2.12}$$

$$CO* + H* \rightarrow C* + OH* \tag{2.13}$$

Hydrogenation:

$$CO* + H* \rightarrow CHO* + * \tag{2.14}$$

$$C* + H* \rightarrow CH* + * \tag{2.15}$$

C – C coupling:

$$CH_2^* + CH_2^* \rightarrow {}^*H_2C = CH_2^* \tag{2.16}$$

$$CH_3^* + CH_2^* \rightarrow H_3C - CH_2^* \tag{2.17}$$

$$CH^* + CH_2^* \rightarrow H_2C = CH^* \tag{2.18}$$

H transfer:

$$H_2C = CH^* \rightarrow H_3C - C^* \tag{2.19}$$

$${}^*H_2C = CH_2^* \rightarrow H_3C - CH^* + * \tag{2.20}$$

Desorption:

$$R - CH_3^* \rightarrow R - CH_3 + * \tag{2.21}$$

$$R - CH = CH_2^* \rightarrow R - CH = CH_2 + * \tag{2.22}$$

2.2.1.1 Hydrogen Adsorption

Hydrogen gas is believed to first physisorb and then dissociate on transition metal surfaces at low temperatures [6, 56-58]. However, at FTS reaction temperatures, the rate of hydrogen physisorption is so fast that it is difficult to separate the physisorption step from the dissociation step. Hence hydrogen temperature programmed desorption experiments and theoretical calculations show H_2 gas adsorbing dissociatively on transition metal surfaces [59-61] as shown in Equation 2.23. Density functional theory (DFT) calculation on Fe(110) by Mavrikakis et.al [62] indicate that H adsorbs on-top sites.

$$H_{2(g)} + 2* \leftrightarrow 2H* \tag{2.23}$$

2.2.1.2 Carbon Monoxide Adsorption and Dissociation

CO adsorption and dissociation on Fe have been studied using density functional theory (DFT), spectroscopic, and temperature programmed adsorption and desorption techniques [63-69]. Studies by various researchers such as Mehandru, Stibor, Jiang, and Erley on an Fe(110) surface, indicate that CO adsorbs on four high-symmetry sites, namely: long-bridge, quasi threefold, short-bridge, and on-top sites [68, 70, 71]. Their studies also show that the site of preference is dependent on CO coverage. Similarly, at

temperatures similar to those of FTS, CO adsorbs on transition metal surfaces both molecularly and dissociatively [61, 69, 72, 73] as shown in Equations 2.24 and 2.25 respectively. The ease of CO dissociation is facilitated by the availability of vacant sites for the dumping of the dissociation products [68]. Joyner also reported that CO dissociation was facilitated with increasing heat of CO adsorption[74, 75]. The presence of other adsorbates such as carbon, oxygen, and hydrogen lowers the CO heat of adsorption. Boden et al. in their study of CO adsorption and dissociation on potassium-promoted Fe(110) using UPS, XPS, AES and flash desorption techniques observed that CO adsorbs molecularly at room temperature with a heat of adsorption greater than that of unpromoted Fe(110). They also report increased ease of CO dissociation with increased potassium promotion of Fe(110) [76].

$$CO_{(g)} + * \leftrightarrow CO* \tag{2.24}$$

$$CO_{(g)} + 2* \leftrightarrow C* + O* \tag{2.25}$$

In fact, the subject of CO adsorption and dissociation has been studied extensively especially on well defined single crystal surfaces. It however remains a subject of controversy on whether CO dissociation, especially on Fe catalyst, is facile or whether CO dissociation is assisted by hydrogen as has been suggested by some researchers[77-81]. This subject will be discussed in detail in Chapter 4 of this work.

2.2.1.3 Reactions of Undissociated CO

Molecularly adsorbed CO has been proposed to undergo hydrogenation by adsorbed H to form formyl and alcoholic intermediates[6, 82-84] as shown in Equations 2.26 and 2.27 below.

$$CO* + H* \leftrightarrow CHO* \quad (2.26)$$

$$CO* + H* \leftrightarrow COH* \quad (2.27)$$

Both CHO and COH species could dissociate to form adsorbed C and OH species, or they could be further hydrogenated as shown in Equations 2.28, 2.29 and 2.30 below.

$$COH* + H* \leftrightarrow CHOH* \quad (2.28)$$

$$CHO* + H* \leftrightarrow CHOH* \quad (2.29)$$

$$CHOH* + H* \leftrightarrow CH_2OH* \quad (2.30)$$

Adsorbed CO species could also react with adsorbed OH species to form adsorbed CO_2 and H according to Equation 2.31 below and may well be the source of CO_2 formation on Fe catalyst during FTS.

$$CO* + OH* \leftrightarrow CO_2* + H* \quad (2.31)$$

2.2.1.4 Reactions of Adsorbed C, O, and OH with Adsorbed H

Adsorbed C species can react with adsorbed H species to form a CH intermediate which is subsequently hydrogenated to CH_2 and CH_3 species according to Equations 2.32, 2.33 and 2.34

$$C* + H* \leftrightarrow CH* + * \quad (2.32)$$

$$CH* + H* \leftrightarrow CH_2* + * \quad (2.33)$$

$$CH_2* + H* \leftrightarrow CH_3* + * \quad (2.34)$$

McCarty et al. propose that about four forms of C species exist on the surface of Ni catalyst during methanation reactions [85]. Some of these C species could be hydrogenated at FTS reaction temperatures while others are difficult to hydrogenate except at elevated temperatures. Bartholomew et al. propose that carbon hydrogenation is a slow step and could be one of the rate determining steps in FTS [7].

Adsorbed O species could react with adsorbed H species to form adsorbed hydroxyl species. Although this reaction could be one of the rate determining steps for Fe and Co catalysts, Iglesia argues that this reaction is not kinetically favorable, especially on Co [86]. Hydrogenation of adsorbed OH species by adsorbed H to form H_2O is believed to be the reaction leading to the formation of water.

2.2.1.5 C-C Coupling Reactions

Coupling of carbon species is proposed to be the building block for chain growth. However, the form of the monomeric carbon species (C, CH, CH_2, and CH_3) has remained a source of controversy. Storsaeter et al. [84] suggest that C_{2+} species are formed by the coupling of CH_2/CH_2 species or CH_2/CH_3 species with CH_2 species as the monomeric species. Lo et al. [87] on the other hand suggest that coupling is between C and CH_2/CH_3 species followed by migratory insertion of H at the α carbon. Nevertheless, it is obvious that the formation of C_{2+} species will require a form of coupling of carbon species.

2.2.1.6 Classification of Mechanisms

FTS mechanisms found in the literature can be classified into three major mechanisms and variations or combinations of these three mechanisms. These three

mechanisms are commonly referred to as the carbide or carbine mechanism, the hydroxycarbene or enol mechanism, and the CO-insertion mechanism.

2.2.1.7 Carbide Mechanism

The carbide or *carbene mechanism* was proposed by Fischer and Tropsch in 1926[88]. In this mechanism, adsorbed CO is dissociated to C and O, the carbide is then hydrogenated to CH_x (the monomer). The methylene monomer polymerizes to surface alkyl species that terminate to products. This mechanism is illustrated in Figure 2-1 below. It is widely supported despite the fact that it does not account for the formation of oxygenates.

CO temperature-programmed desorption on both Co and Fe catalysts yield significant amounts of CO_2 [61]. This CO_2 is believed to be formed by the reaction of adsorbed CO with adsorbed O derived from already dissociated CO. Although activation energy calculations show that this reaction is very facile, CO_2 formation is rarely observed during FTS on Co catalyst even though the carbide mechanism suggests that CO dissociation into C and O is an important elementary step during FTS. Similarly, the binding energy of O is about 5.35eV on Co [84] and 6.05eV on Fe [89]. This higher O binding energy on Fe would mean that CO dissociation is more facilitated on Fe than on Co, and would lead to increased FTS rates on Fe than on Co. However, the FTS rate is much faster on Co than on Fe. The issues stated above suggest that perhaps the carbide mechanism, although widely supported, may not necessarily be the primary mechanism of FTS.

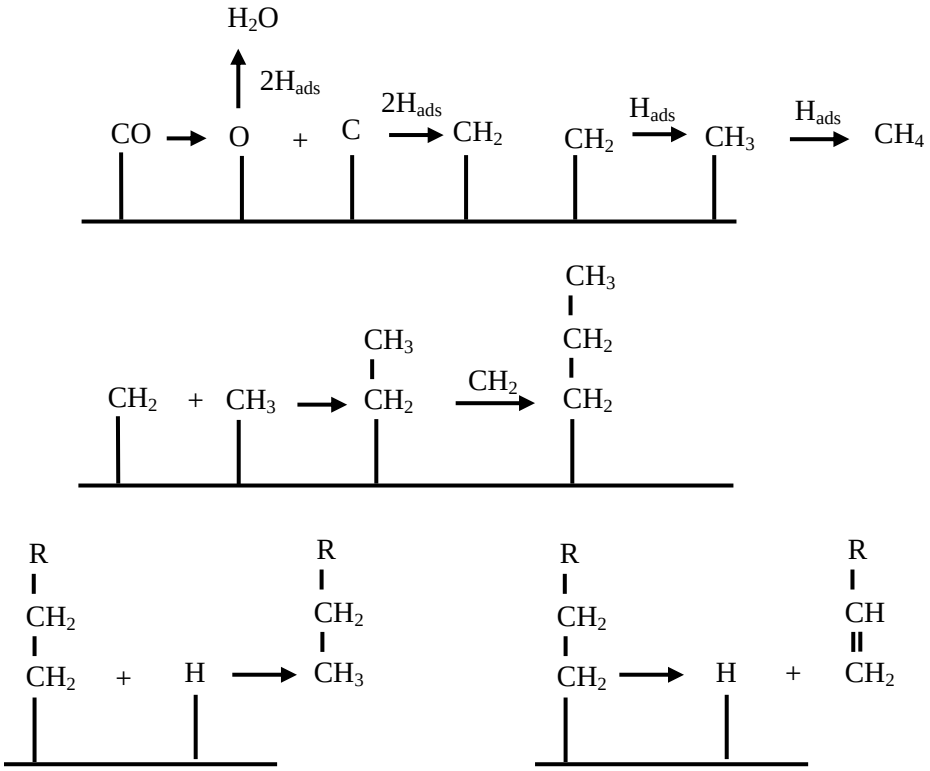

Figure 2-1: Carbene or carbide mechanism

2.2.1.8 Hydroxycarbene or Enol Mechanism

The *hydoxycarbene or enol mechanism* was proposed by Storch et al. in the 1950s [90]. In this mechanism, chain growth is initiated through the condensation of two hydroxycarbene species $CHOH_{ads}$ with the elimination of water. This is illustrated in Figure 2-2. Although this mechanism explains the formation of oxygenates and was strongly supported by Emmett et al. who used ^{14}C-alcohols or alkenes as a co-feed and observed that these alcohols participated in the chain growth [91], nevertheless, the details of the chemistry of this mechanism are unclear.

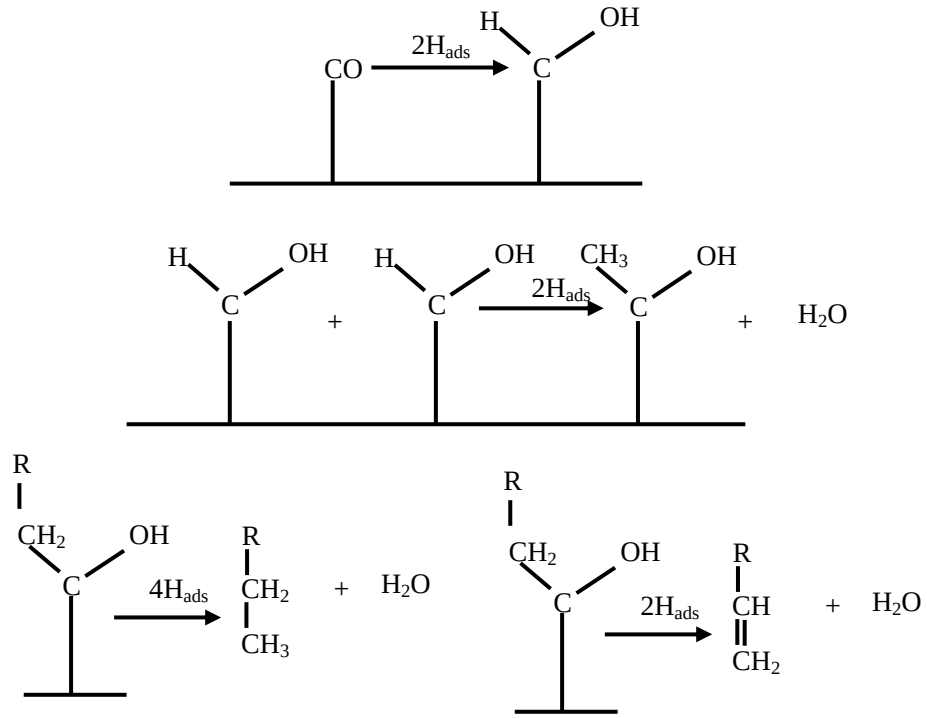

Figure 2-2: Hydroxycarbene or enol mechanism

2.2.1.9 CO-insertion Mechanism

The *CO insertion mechanism* (Figure 2-3) was proposed by Pichler and Schulz in the 1970s [92]. This mechanism involves the insertion of adsorbed CO into the methyl-alkyl bond. The oxygenated carbon is subsequently hydrogenated to remove the oxygen. CO insertion is a well known reaction in complex chemistry [93]; however, there is still no conclusive experimental evidence that this reaction occurs on surfaces. Brown and Davis, however, suggest that this may be the primary mechanism in iron FTS [94].

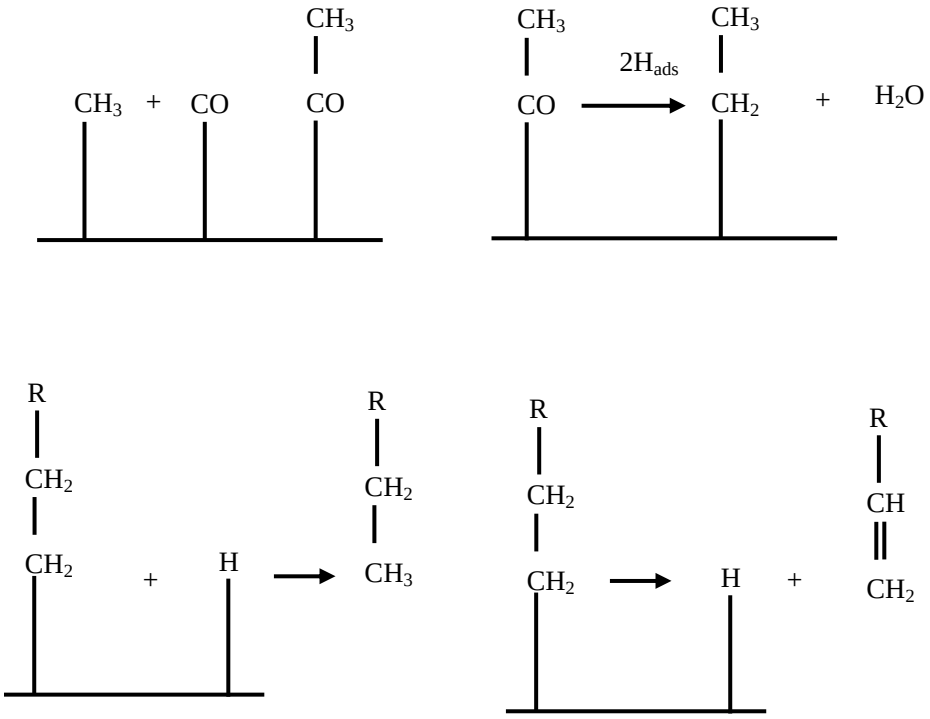

Figure 2-3: CO insertion mechanism

2.3 Microkinetic Models and Variations on the Three Major Mechanisms

Variations or combinations for each of these mechanisms have since emerged. In his thesis work, van Dijk published a mechanism for cobalt catalyst similar to the carbene mechanism with the incorporation of ethylene re-adsorption [12]. This mechanism is illustrated in Figure 2-4 below. Van Dijk proposed that chain growth occurs by insertion of a methylene species (CH_2) into an adsorbed alkylidene species. More than a half-dozen varients of this carbide mechanism have been proposed, including CH_2 insertion into alkyl, alkylidene, and alkenyl chains and CH or C insertion into alkylidene or alkenyl chains[7].

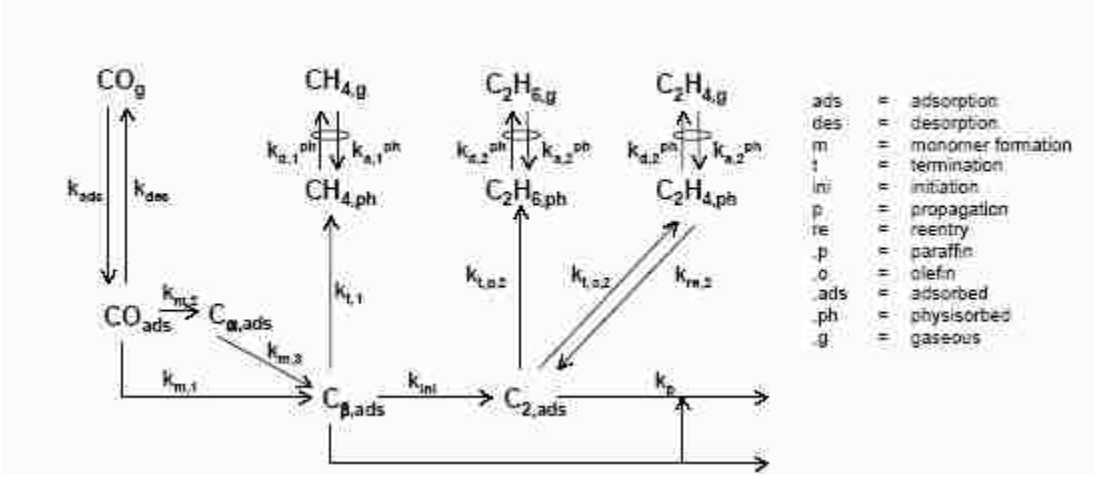

Figure 2-4: Microkinetic model of van Dijk (figure reproduced from reference [36])

Although van Dijk was able to predict rate constants and intermediate concentrations that seem reasonable, he was however unable to predict activation energies and pre-exponential factors because he did his studies at one *temperature and at 1 atm pressure*. The study was based on one catalyst and neglected the effect of promoters on the reaction mechanism/energetics. Also, in his mechanism discrimination studies, van Dijk only considered forms included in the carbide mechanism and neglected others. Similarly, C^{13} tracer studies alone are unable to differentiate the carbide mechanism from mechanisms involving the formation of CHO species since C tracer studies will yield similar results for such mechanisms. Lastly, he neglected the formation of carbon dioxide via the water-gas-shift reaction, perhaps due to low CO_2 formation in cobalt catalyzed FTS. However, in iron catalyzed FTS, CO_2 formation is significant and must be considered in the development of a microkinetic model for FTS catalyzed by iron.

Most recently, Storeaster et al. published a microkinetic model for cobalt catalyst that is a combination of the carbene, formyl, and hydrogen-assisted CO dissociation mechanisms [16]. They used transition state theory and unity-bond index-quadratic exponential potential (UBI-QEP) to calculate the pre-exponential factors and activation energies respectively for the elementary steps in each of the three major mechanisms above. They next eliminated some steps based on the energetics of the reactions. Their proposed mechanism which they claim predicts accurately CO conversion at three inlet conditions at one temperature is illustrated in Figure 2-5. The numbers in the diagram represent the activation energies in kJ/mol.

Although the microkinetic model by Storeaster et al. may accurately model FTS on Co catalyst, it may not work for Fe-catalyzed FTS since Fe is known to catalyze the water-gas-shift reaction. Similarly, the model was not validated with FTS data at industrial process conditions. Lastly, the study was done on one catalyst and did not explore the effect promoters will have on the mechanism and energetics of the reaction. The addition of support and/or promoters to FTS catalysts has been found to affect the overall reactivity or selectivity of the catalyst by increasing the number of active sites, either through an increase in the dispersion or in the reducibility of the catalyst. Perhaps the enegetics of FTS may also be altered by the addition of support and/or promoters as it has been reported to influence the turnover frequency of catalytic sites [95-97].

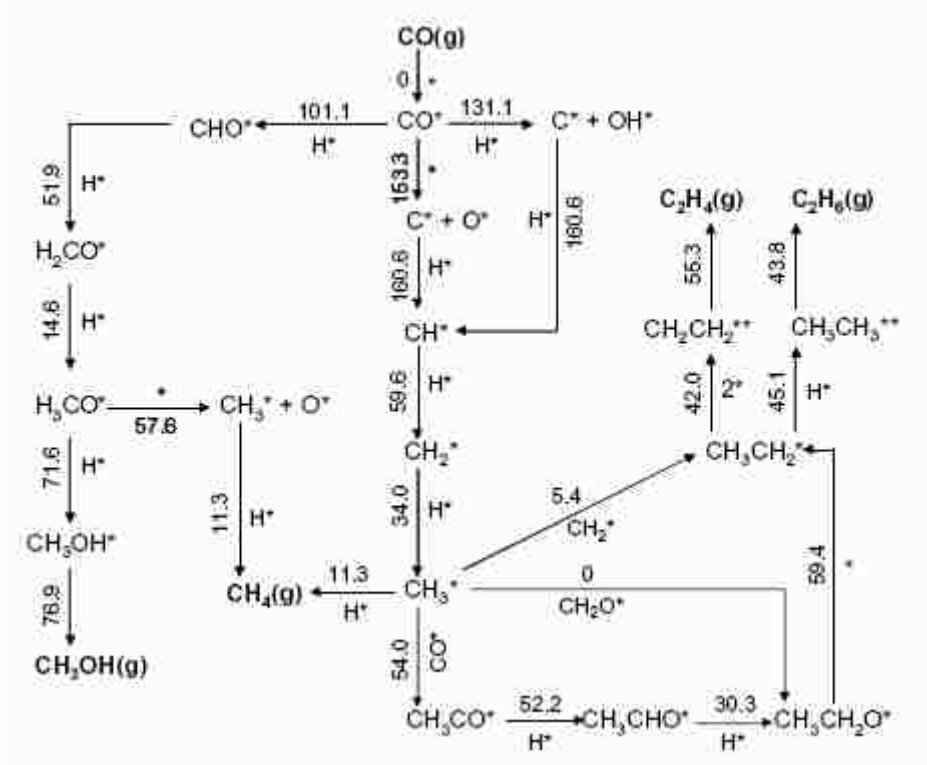

Figure 2-5: Microkinetic model of FTS on cobalt proposed by Storeaster et al. The numbers on the arrows represents the activation energies (kJ/mol) for the reaction step (figure reproduced from reference [16]).

2.3.1 Variations on the mechanism of water-gas-shift reaction

The water-gas-shift (WGS) reaction (Equation 2.6)is generally believed to be the source of CO_2 formation in FTS [98-104]. Although Co and Fe based FTS catalysts are capable of catalyzing WGS reaction, Fe is more active than Co towards the WGS reaction. This property makes Fe catalyst attractive as a catalyst for FTS with low H_2/CO feed ratios characteristic of syngas derived from coal or biomass.

Copper and iron oxide catalysts are mostly used as industrial WGS catalysts. While copper is used for low temperature WGS (210ºC to 240ºC), iron oxide(s) is used for high temperature WGS (310ºC to 450ºC) [105-108].

The mechanism of WGS reaction especially during FTS is still not well understood. CO_2 can be formed during FTS by direct reaction of adsorbed CO and adsorbed O, or by direct reaction of adsorbed CO and adsorbed OH, or by direct reaction of adsorbed CO and adsorbed water, or by a combination of all these. The correct route for CO_2 formation will depend on the prevailing FTS mechanism.

Activation energies for the above reactions calculated using the UBI-QEP method indicate that all of these reactions have favorable energetics for both Co and Fe catalysts. However, very little CO_2 formation is observed during FTS on Co catalyst. In fact, Davis et al. suggest that FTS and WGS may occur on different catalytic sites [109, 110] and that WGS may not be part of FTS mechanism. If the suggestion by Davis et al. is correct, it then means that water that is produced during FTS re-adsorbs or hop's over to the site where WGS takes place.

Shustorovich and coworkers [79, 111-113] calculated activation energies of FTS on Fe/W, Ni, Cu, and Pt single crystals respectively using UBI-QEP and concluded that (1) direct CO dissociation to form carbidic carbon was more favorable on Fe/W and on Ni than on Pt or Cu, and (2) coupling reactions to form higher hydrocarbons were more feasible on Cu than on Fe/W. Hence they suggested that an Fe/Cu catalyst will be a better FTS catalyst for making higher hydrocarbons. They however, did the calculations only for the carbide mechanism and did not consider other mechanisms. They did not

give the pre-exponential factors for the elementary steps they considered, nor did they consider the water-gas-shift reaction.

2.4 Methods of Mechanistic Study

Mechanistic and microkinetic studies are usually studied by (1) experimental techniques that include transient [114], steady-state, calorimetric, and spectroscopic experiments; (2) theoretical simulations and calculations such as first principles calculations, Monte Carlo and molecular dynamics simulations [11]. Transient experimental techniques such as temperature-programmed desorption (TPD), temperature-programmed surface reaction (TPSR), and isotopic tracing can provide information on the kinetics of surface reactions [115] as well as on the nature of the catalytic surface [7, 30, 116]. Theoretical calculations especially ab initio, density functional theory (DFT) [117], and semi-empirical methods (unity bond index quadratic exponential potential) have been used to calculate the activation energies of surface reactions. The review presented in this section will mostly focus on methods that were pertinent to this work.

2.4.1 Transient studies: TPD, TPSR

2.4.1.1 TPD

TPD or flash desorption involves (1) adsorption of a gas unto a surface, and (2) heating the sample according to a temperature program while monitoring the composition of desorbing gaseous products with a mass spectrometer. It was first described by Redhead [118], but was first applied to the study of catalytic reactions by Amenomiya et al. [119]. It is usually carried out either in ultra high vacuum (UVH) or at atmospheric

pressure. Desorption kinetics are more readily deduced from the TPD thermogram carried out in ultra high vacuum conditions. Due to multiple rate processes occurring during TPD conducted under atmospheric pressure conditions, some have discouraged the extraction of kinetic information from the thermogram resulting from such experiments [120]. However, from the results of TPD simulation, Kanervo et al.[121], concluded that intrinsic kinetic information can be extracted from the analysis of atmospheric pressure TPD thermogram as long as the experimental conditions satisfied certain criteria in order to avoid interference from mass transfer limitations.

Methods for deducing adsorbate heat of adsorption from TPD thermograms, and in some cases simulated TPD thermograms, have been described or applied in several studies [118, 120-128]. These methods presume that only one type of adsorbate species is on the catalyst surface. However, in some instances (especially when CO was the only initially adsorbed gas), the evolution of more than one gaseous species during desorption has been reported [61, 129]. In this case more than one adsorbate species will probably be on the catalyst surface and the heat of adsorption deduced from the analysis of its TPD thermogram using the classical methods of analysis may only be an approximation.

2.4.1.2 TPSR

TPSR is similar to TPD except that in the case of TPSR, the inert carrier gas is replaced with a reactive gas during the desorption process [7, 130]. When the reactive gas is hydrogen, the process is called temperature-programmed hydrogenation (TPH).

TPH has been mostly used to qualitatively analyze the nature of the catalytic surface and reactive intermediates, as well as the deduction of apparent kinetic parameters using methods similar to those of TPD analysis referred to in the previous

section [30, 124, 131]. Isothermal hydrogenation (ITH) is similar to TPH but without temperature ramping. Just as with TPH, it is used to study the nature of reactive intermediates and to extract apparent kinetic information [114, 132]. By combining TPH and ITH with mathematical modeling, it is possible to extract more detailed kinetic information for a given reaction system. This approach is explored in this study.

2.4.2 Theoretical studies

Extension of transition state theory (TST) to include the estimation of pre-exponential factors for elementary surface reactions can be found in the work of Dumesic et al. [11]. This method was used by Storaester et al. [84] to calculate the pre-exponential factors of the plausible FTS elementary reactions assuming an immobile transition state and binding on a three-fold-site at 483 K. Where applicable, the values calculated in reference [84] were used in this work. Although TST provides only an approximation of the pre-exponential factor, it offers a molecular perspective of the reaction rate determination. Its application is sometimes complicated by difficulty in knowing the nature of the transition state *a priori* [133]. Nevertheless, it provides good order-of-magnitude estimates of the pre-exponential factor.

Most theoretical approaches for calculating the energetics and mechanisms of surface reactions are based on quantum mechanics. Activation energies of elementary surface reactions can (in principle) be determined from first-principle calculations including density functional theory (DFT). A recent review article by Norskov et al. [134] on DFT in surface science and heterogeneous catalysis sufficiently describes the application of DFT in mechanistic studies. In recent times, increased use of DFT

calculations in several mechanistic studies and catalyst design including FTS mechanism on Co catalyst [135, 136] has been made possible by recent improvements in computer technology. This is because DFT calculations for surface reactions require sophisticated computer codes and lots of computing time even on the most sophisticated super computers. Another drawback in the use of DFT calculations for surface reactions is that they can only be performed on well defined-surfaces whereas real catalysts are polycrystalline, possessing poorly defined surface structure [137].

On the other hand, a semi-empirical approach for calculating activation energies of elementary surface reactions using a more pragmatic approach with an estimated error of about 5% was developed by Shustorovich et al. [137, 138]. This approach will be discussed in detail since it was pertinent to this work.

2.4.2.1 Unity Bond index Quadratic Exponential Potential (UBI-QEP)

The UBI-QEP method formerly known as BOC-MP (Bond-order-conservation Morse-potential) is a semi-empirical approach used to calculate adsorbate heats of adsorption and reaction activation energies [113, 138]. Unlike first-principle calculations, it requires minimal or no computer cost. It uses gas phase bond energies of the species (D_{AB}) in the reaction sequence and the atomic binding energies (Q_A) of the precursor atoms that combine to form the intermediate species and products (in the case of FTS on Fe, this will be the respective binding energies of C, O, and H on Fe) to calculate the heats of adsorption for the adsorbate species (Q_{AB}) and the respective forward and reverse activation energies (E_f *and* E_r) for the reaction steps. For each adsorbed species, assumptions about the coordination, number of metal atoms involved, and the binding strength must be made. The above information is used to calculate the

species heat of adsorption which is subsequently used to calculate the reaction activation energy based on a thermodynamic cycle analysis. Hence the UBI-QEP formalism is inherently thermodynamically consistent.

Adsorbed species are classified as weakly, moderately, or strongly bound to the metal surface. Closed-shell molecules or radicals with strong delocalized unpaired electrons are weakly bound to the metal surface. Monovalent radicals and tetravalent carbon are classified as intermediate bound on the metal surface, while strong bound species have unpaired electrons. Table 2-1 and Table 2-2 adapted from [84, 113, 138] provide formulas for calculating heats of adsorption for the various binding strengths and the activation energies for the various kinds of reactions in catalysis. Similarly, gas-phase bond energies (adapted from [84]) for some likely FTS reaction intermediates are tabulated on Table 2-3. A sample calculation of activation energy using the equations in Table 2-1 to Table 2-3 is illustrated in Appendix A.4

Strength of the UBI-QEP method lies in its simplicity when compared to other theoretical methods for calculating activation energies. Nevertheless, the heats of adsorption calculated with the UBI-QEP method are at zero coverage limit. Accuracy of the method depends on the accuracy of the binding energies of the primary atoms, and the correctness of the assumptions regarding adsorbate binding strength and coordination. UBI-QEP formalism has been used in the development of microkinetic models for reactions such as CO oxidation on Pt [139], the water-gas-shift reaction on Cu(111) [18], etc.

Table 2-1: Equations for calculating adsorbate heat of adsorption based on the UBI-QEP formalism [84, 113, 138]

Description	Equation for calculation species heat of adsorption	
Metal – atom heat of adsorption	$$Q_{0A} = \frac{Q_A}{2 - \frac{1}{n}}$$	(2.35)
Heat of adsorption for weakly-bound molecule AB	$$Q_{AB} = \frac{Q_{0A}^2}{Q_{0A} + D_{AB}}$$	(2.36)
Heat of adsorption for moderately-bound adsorbate AB with A end down	$$Q_{AB} = \frac{1}{2}\left[\frac{Q_{0A}^2}{\frac{Q_{0A}}{n} + D_{AB}} + \frac{Q_A^2}{Q_A + D_{AB}}\right]$$	(2.37)
Heat of adsorption for moderately-bound adsorbate AB where AB is coordinated via A and B respectively	$$Q_{AB} = \frac{ab(a+b) + D_{AB}(a-b)^2}{ab + D_{AB}(a+b)}$$	(2.38)
	$$a = \frac{Q_{0A}^2(Q_{0A} - 2Q_{0B})}{(Q_{0A} + Q_{0B})^2}$$	(2.39)
	$$b = \frac{Q_{0B}^2(Q_{0B} - 2Q_{0A})}{(Q_{0A} + Q_{0B})^2}$$	(2.40)
Heat of adsorption for strongly-bound adsorbate	$$Q_{AB} = \frac{Q_A^2}{Q_A + D_{AB}}$$	(2.41)
Heat of adsorption for diatomic molecules weakly bound to the the surface via two atoms (A and B) e.g. $H_2C{=}CH_2$ (where A = B = CH_2 and m = m' = 2	$$Q_{AB} = \frac{ab(a+b) + D_{AB}(a-b)^2}{ab + D_{AB}(a+b)}$$	(2.42)
	$$a = Q_{0A}\left(1 - \left(\frac{mQ_{0X}}{mQ_{0A} + Q_{0X}}\right)^2\right)$$	(2.43)

Table 2-1 – *Continued*

Description	**Equation for calculation species heat of adsorption**	
	$b = Q_{0B}\left(1-\left(\frac{m'Q_{0Y}}{m'Q_{0B}+Q_{0Y}}\right)^2\right)$	(2.44)
For symmetric species e.g. CO_2 and H_2.	$a = \frac{\frac{9}{2}Q_{0A}^2}{3Q_{0A}+8D_{AB}}$	(2.45)

Table 2-2: Equations for calculating activation energies for surface reactions based on the UBI-QEP formalism [84, 113, 138]

Description	**Equation**	
For dissociation of adsorbed species, e. g. $AB^* \leftrightarrow A^* + B^*$:	$\Delta H = D_{AB} + Q_{AB} - Q_A - Q_B$	(2.46)
Forward activation energy	$E_f = 0.5\left(\Delta H + \frac{Q_A Q_B}{Q_A + Q_B}\right)$	(2.47)
Reverse activation energy	$E_r = E_f - \Delta H$	(2.48)
For the reaction $X^* + Y^* \leftrightarrow Z^* + F^*$	$D_{XY} = D_X + D_Y - D_Z - D_F$	(2.49)
	$Q_{XY} = Q_X + Q_Y$	(2.50)
	$\Delta H = D_{XY} + Q_{XY} - Q_Z - Q_F$	(2.51)

Table 2-2 – *Continued*

Description	**Equation**	
Forward activation energy	$E_f = 0.5\left(\Delta H + \frac{Q_Z Q_F}{Q_Z + Q_F}\right)$	(2.52)
Reverse activation energy	$E_r = E_f - \Delta H$	(2.53)
For the reaction $AB_{(g)} \leftrightarrow A^* + B^*$	$E_f = 0.5\left[\left(D_{AB} + \frac{Q_A Q_B}{Q_A + Q_B}\right) - Q_{AB} - Q_A - Q_B\right]$	(2.54)
	$E_r = Q_A Q_B - D_{AB} + E_f$	(2.55)

Table 2-3: Total bond energies (D_{AB}) for calculating heat of adsorption using UBI-QEP formalism [84]

Species	**Gas-phase bond energy, D [kcal/mol]**	**D_{AB} [kcal/mol] for calculating Q_{AB}**
C	0	-
H	0	-
O	0	-
CO	257	257
H_2	104	104
OH	102	102
CH	81	81
CH_2	183	183

Table 2-3 – *Continued*

Species	Gas-phase bond energy, D [kcal/mol]	D_{AB} [kcal/mol] for calculating Q_{AB}
CH_3	293	293
CH_4	397	397
CH_3CH_3	674	674
CH_2CH_2	538	538
CH_3CH_2	576	283
CH_3CH	466	173
CH_2CH	421	157
CHCH	392	392
CCH_3	376	114
CCH	259	161
CCH_2	348	155
H_2O	220	220
CO_2	385	385
CHO	274	274
CH_2O	361	361
CH_3O	383	90

2.5 State of FTS Mechanistic and Microkinetic Model Knowledge and Why Further Study Is Needed

From the literature review presented above, it is obvious that there are numerous elementary reactions that occur during FTS on both Co and Fe catalysts. However, not all the reactions are kinetically relevant especially at commercial reaction conditions. Although substantial efforts have focused on identifying the kinetically relevant reactions on Co and Fe catalysts, mechanistic understanding is incomplete. Additionally, accurate values of the kinetic parameters for the kinetically relevant steps over a wide range of reaction conditions are still wanting, especially in the case of Fe. Because most of the available mechanism/microkinetic models were derived at conditions far from industrial conditions as well as from data for only one catalyst, they perform poorly when extended to other catalysts or conditions. Additionally, most of the mechanistic work has been focused on cobalt catalysts and does not include the formation of CO_2, a major product in iron-catalyzed FTS. A robust FTS microkinetic model especially on Fe catalyst will provide better understanding of FTS chemistry which will lead to the design of more active, selective and stable Fe catalysts and therefore more efficient FTS processes.

Therefore the objectives of this work were to incorporate theory and experiment at industrially relevant conditions to (1) gain a basic understanding of the chemistry of the kinetically relevant steps in FTS on iron catalyst, and (2) develop a microkinetic model that describes the reaction kinetics at the molecular level over a wide range of experimental conditions, such as temperature, pressure and gas phase concentrations. Hopefully, this knowledge will contribute to the advancement of FTS technologies as viable alternatives for producing transportation fuels.

3. Chapter 3: Catalyst Preparation, Characterization and Experimental Setup

This chapter describes the preparation and characterization methods of the catalysts used in this study. The catalysts described here are of two general types: supported and unsupported. Supported and unsupported catalysts are further classified as powder/pellet type and immobilized-monolith type respectively. Also included in this chapter is a description of the experimental setup and procedures used in this work.

3.1 Unsupported 99%Fe, 1%Al_2O_3 Catalyst (Powder) 99Fe1ALa-307

Various methods for preparing Fe Fischer-Tropsch catalysts based on precipitation have been described in the literature. Such methods include the precipitation of active metallic Fe from aqueous solution of ferric nitrate precursor using a base such as NH_4OH as described in Bartholomew and Farrauto [7]. Iglesia et al. [26, 27] proposed the addition of an alcohol during the precipitation process to enhance the surface area of the precipitated catalyst. Goodwin et al. [140-143] proposed spray drying to reduce attrition especially when the catalyst is to be used in a slurry or fluidized-bed reactor. Various other methods for preparing precipitated Fe Fisher-Tropsch catalyst can be found in previous literature [103, 144-149]. Wu et al. reported an increase in FTS activity with a ferrous sulfate precursor instead of the traditionally used ferric nitrate precursor [148].

In this study, 99Fe1ALa-307 was prepared by aqueous co-precipitation of $Fe(OH)_3$ and $Al(OH)_3$ from their respective nitrate salts using NH_4OH. The precipitated hydroxides were calcined in air to form oxides. Detailed description of the preparation procedure is given in the section below. The addition of 1% Al_2O_3 was to provide textural promotion of the catalyst.

3.1.1 Preparation of 99%Fe, 1%Al_2O_3 (powder/pellet, 99Fe1ALa-307)

357.0 g of $Fe(NO_3)_3.9H_2O$ (Spectrum) and 7.0 g of $Al(NO_3)_3.9H_2O$ were dissolved together in 823 mL of HPLC grade H_2O (Sigma Aldrich) in a 2.5 L beaker. 200 mL of concentrated NH_4OH (Merck) solution was added to 750 mL of HPLC grade H_2O in a 1 L Erlenmeyer flask. The beaker containing the solution of ferric and aluminum nitrates was transferred to a hot water bath maintained at 70ºC. The NH_4OH solution was transferred to a 2 L separation funnel (serving as a burette). The nitrate solution was slowly titrated with the NH_4OH solution for about 2 h while stirring with a magnetic stirrer and controlling the pH within the range of 8 – 9. The brown precipitate was filtered using a vacuum filtration apparatus. The filtrate (the catalyst) was washed with HPLC grade H_2O and filtered again. This procedure was repeated three times.

The wet catalyst paste was dried overnight in an oven at 60ºC and then at 110ºC for 12 h. The catalyst was next calcined in air to decompose the metal hydroxides to oxides by heating it from room temperature to 300°C at 0.5°C/min, and maintaining it at 300oC for 8 h. The calcination profile was formulated from a temperature programmed oxidation thermogram using about 20 mg of the catalyst sample.

3.1.2 Preparation of 99%Fe, 1%Al_2O_3 (on a monolith -99Fe1ALa-mon-907)

Five 2 inch diameter by 1 inch long ceramic monoliths were washed with dilute nitric acid, rinsed with HPLC grade H_2O, and subsequently dried in an oven at 60ºC for 24 h. 146.90 g of $Fe(NO_3)_3.9H_2O$ and 1.53 g of $Al(NO_3)_3.9H_2O$ were melted in a water bath at 70ºC. The monoliths were dipped one by one in the melt for about 5 min until there were no more visible air bubbles. The wet monolith channels were blown clear with He, and dried for about 4 h first at room temperature and later, overnight at 60ºC in an oven. The resulting catalyst was calcined in air at 300ºC for 8 hr. The coating and calcination process was repeated to get a final catalyst weight (monolith free basis) of about 5 g. Catalyst weights after calcination are summarized in Table 3-1.

Table 3-1: Summary of results of catalyst weight for each 99Fe1ALa-mon-907 monolith

Monolith #	Weight of monolith (g)	Weight of monolith after coating and calcination at 300ºC (g) (1)	(2)	Weight of catalyst (monolith free basis) (g)
1	20.55	23.31	25.61	5.06
2	19.71	22.07	23.91	4.20
3	20.98	23.68	25.59	4.61
4	18.77	22.07	22.99	4.23

Also used in this study was a 99%Fe, 1% Al_2O_3 coated on four 400-mesh ceramic monoliths dubbed 99Fe1ALa-mon-506. This catalyst was prepared by Hu Zou. The weight composition of each of the monoliths is summarized in Table 3-2.

Table 3-2: Summary of catalyst weight for each 99Fe1ALa-mon-506 monolith

Monolith #	**Weight of monolith (g)**	**Weight of monolith after coating and calcination at 300°C (g)**		**Weight of catalyst (monolith free basis) (g)**
		(1)	**(2)**	
1	19.08	21.41	23.40	4.31
2	18.07	20.34	22.21	4.14
3	12.90	14.38	15.70	2.80
4	11.03	12.22	13.45	2.42

3.2 Preparation of 20%Fe, 1%K, 1%Pt, La-Al_2O_3

Two supported catalysts containing 20% Fe, 1% K, and 1% Pt on La modified Al_2O_3 were prepared, one in granular form, the other coated on a monolith. Preparation of both forms are described in this section. The granular catalyst with the above composition will hereafter be referred to as 20Fe1K1Pt-ALa-705 while its equivalent coated on a monolith is referred to as 20Fe1K1Pt-ALa-mon-507

3.2.1 Preparation of 20Fe1K1Pt-ALa-705 granular catalyst

Alumina supported Fe catalysts can sinter at high water vapor pressures due to the formation of inactive metal-support compounds such as iron-aluminates, or by the collapse of the catalyst pores, or by a combination of both mechanisms. Oxides of La, Ba, Ce, and Ca can be incorporated into the alumina to form a stable spinel. Spinels are resistant to reaction with Fe phases and hydrothermal sintering [7]. In order to minimize catalyst deactivation during FTS due to loss of active surface area in steam (hydrothermal sintering), the alumina support in this study was stabilized with La oxide using the method described by Tijburg et al. [150]. This catalyst was prepared by Hu Zou.

3.2.1.1 Support Modification Procedure

About 20 g of alumina (Catapal A, Sasol) was added to 750 mL of HPLC grade H_2O in a 1.5 L beaker. The suspension was stirred and the pH adjusted to about 5.0 with concentrated HNO_3. 5.2 g of $La(NO_3)_3.6H_2O$ was dissolved in 18 mL of HPLC grade H_2O in a 100 mL beaker. 3.5 g of EDTA (equimolar amount, Spectra) was dissolved in 90 mL H_2O in a 250 mL beaker. The pH of the resulting solution was adjusted to about 5.0 by adding drops of concentrated NH_4OH.

The lanthanum nitrate solution was slowly added to the EDTA solution while maintaining the pH at about 5.0. The resulting EDTA-lanthanum nitrate solution was added to the alumina suspension while stirring vigorously and maintaining the pH at 5.0. After about 2 h, the suspension was vacuum filtered, washed in H_2O, and filtered again.

The filtrate was analyzed for La to determine how much of the La adsorbed on the Al_2O_3 support, while the filtrand was transferred to a cover glass and dried in the oven at

60ºC for 24 h, then at 80ºC for 12 h, and finally at 120ºC for 12 h. The modified support was calcined in air by heating to 700ºC at 5ºC/min and then maintaining at 700ºC for 8 h.

3.2.1.2 Impregnation Method

Two-step aqueous impregnation to incipient wetness was used. This was done by dissolving the exact weights of $Fe(NO_3)_3.9H_2O$, KNO_3, and chloroplatinic acid in H_2O such that the total volume of the solution was equal to the pore volume of the support and give a composition of 10 wt% of Fe, 0.5 wt% of K and 0.5 wt% of Pt after calcination. The catalyst was calcined for 8 h at 300ºC in air to decompose the nitrates and chlorides.

3.2.2 Preparation of 20Fe1K1Pt-ALa-mon-507

This catalyst was prepared using similar procedures described by Critchfield, Nijhuis et al. and Retalick [19, 151, 152] as follows:

3.2.2.1 Support Modification

γ-Al_2O_3 (Pural NG, Sasol) was modified with lanthana according to the procedure previously described in Section 3.2.1.1. The La – modified Al_2O_3 support was wash-coated onto five 2-inch diameter by 1-inch long 300 mesh ceramic monoliths using Dispal 18N4-80 alumina (boehmite, Sasol) as binder. After wash-coating (see Appendix A.6) and calcination in air at 700ºC for 8 h as in Section 3.2.1.1, the weight of support ranged approximately from 3.8 g to 5.5 g respectively. Table 3-3 summarizes the results of support wash-coating on each of the five monoliths.

Table 3-3: Weight of support for each monolith after wash-coating and calcination at 700ºC

Monolith #	Weight of monolith (g)	Weight of monolith after washing coating and calcination at 700ºC (g) (1)	(2)	Weight of support (monolith free basis) (g)
1	24.61	26.55	29.10	4.50
2	22.93	24.77	27.47	4.54
3	25.40	27.24	30.13	4.73
4	23.21	25.05	27.10	3.88
5	25.51	27.35	31.02	5.50

3.2.2.2 Catalyst Impregnation

Four-step aqueous impregnation was used to obtain approximately a metal loading of 18-21 wt% Fe, 1 wt% K, and 1 wt% Pt (on a monolith free basis) after calcination in air at 300ºC for 8 hr. Summary of approximate metal loading and catalyst weight for each monolith is shown on Table 3-4.

3.3 Catalyst Characterization Methods and Results

The catalysts prepared above were characterized by (1) temperature-programmed reduction; (2) N_2 adsorption to measure BET surface area and pore size distribution; (3) CO chemisorption uptake; (4) extent of reduction; and (5) transmission electron microscopy (TEM).

Table 3-4: Catalyst weight and approximate metal loading
for 20Fe1K1Pt-ALa-mon-507 monoliths

Monolith #	wt. monolith + support	Wt. (g) after impregnation and calcination at 300ºC (1)	(2)	(3)	(4)	Wt. catalyst (monolith free basis) (g)	%wt K, and %wt Pt[a] (assumed)	%wt Fe[a]
1	29.10	29.48	29.90	30.40	30.95	6.36	1.0	18.8
2	27.47	27.82	28.18	28.69	29.23	6.30	1.0	17.8
3	30.13	30.56	30.97	31.54	32.16	6.76	1.0	19.3
4	27.10	27.57	27.95	28.45	29.06	5.84	1.0	21.8
5	31.02	31.61	32.06	32.71	33.40	7.89	1.0	19.4

[a]wt.% relative to catalyst wash-coat layer

3.3.1 Temperature programmed reduction

Temperature-programmed reduction (TPR) of all the catalysts was performed on a Perkin Elmer TGA7 thermogravimetric analyzer by flowing a stream of 10% H_2/90% He gas (20 mL/min H_2 and 180 mL/min) through about 30 mg of the catalyst sample while ramping the sample temperature from 20ºC to 700ºC at 5ºC/min. The sample weight as a function of time and temperature was recorded by the analyzer. The procedure was repeated with a reducing gas composition of 20 mL/min CO/Ar and 180 mL/min He. The resulting theromograms and derivative curves for 99Fe1ALa-307 are shown in Figure 3-1 and Figure 3-2 respectively.

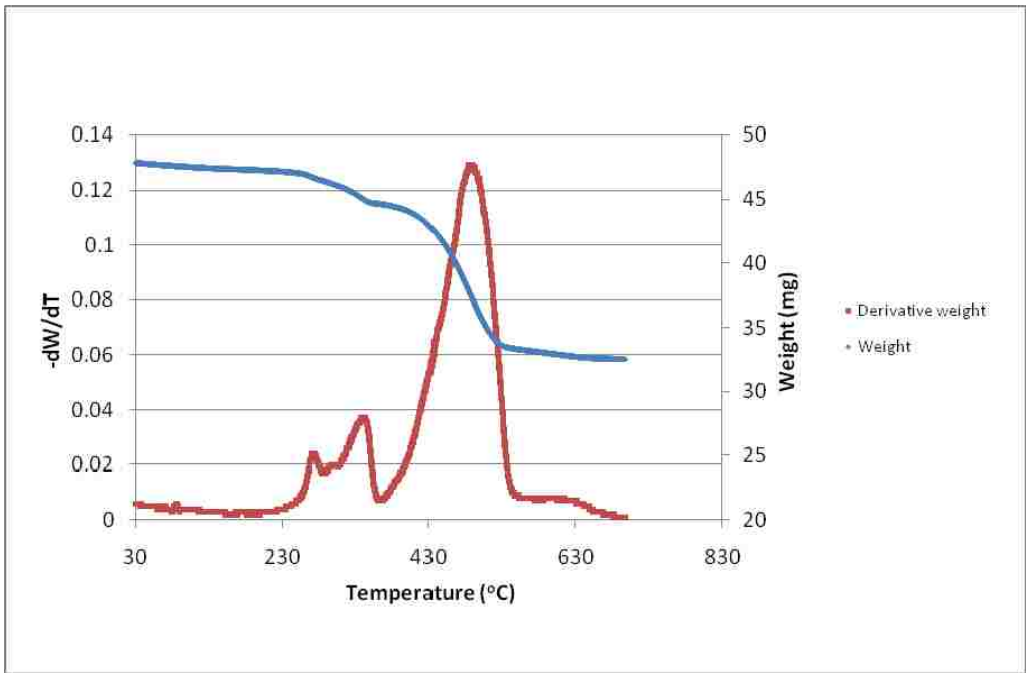

Figure 3-1: Temperature-programmed reduction thermogram (reduction in H_2) for 99Fe1ALa-307

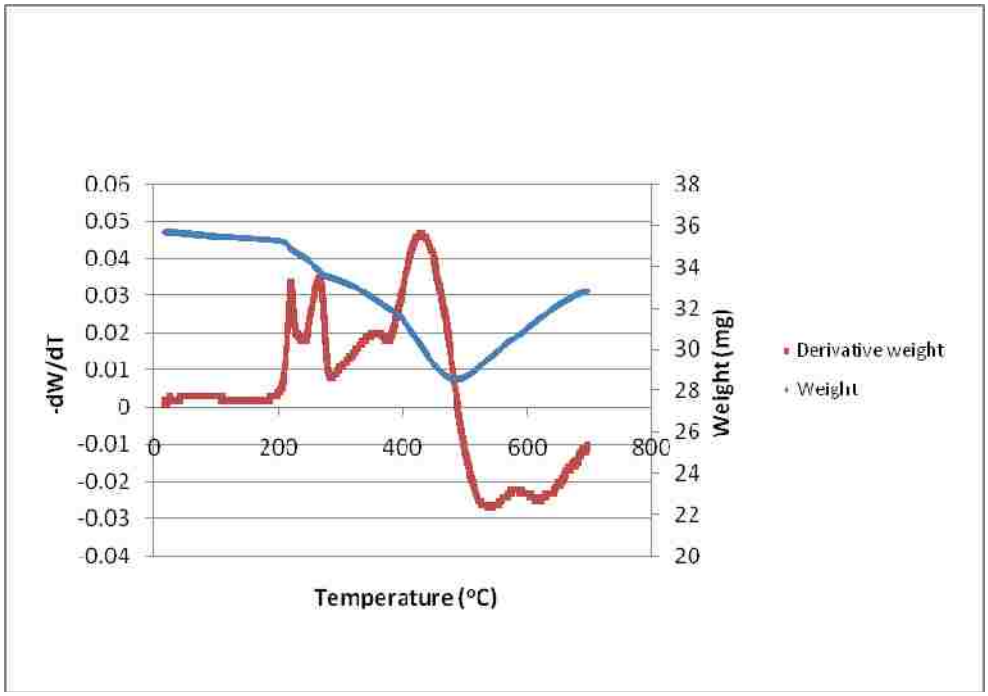

Figure 3-2: Temperature-programmed reduction thermogram (reduction in CO) for 99Fe1ALa-307

The weight losses observed in the thermograms shown in Figure 3-1 and Figure 3-2 in the regions between 30ºC and 500ºC are attributed to the sequential loss of oxygen in the form of H_2O or CO_2 respectively, decomposition of residual nitrates, and reduction to metallic iron of mostly ferric oxide predominantly present in the catalyst after calcination in air. The increase in weight observed in the thermogram in Figure 3-2 (reduction in CO) in the region 490ºC to 700ºC is attributed to carbide formation and deposition of C.

The stoichiometric equations for the reduction of Fe_2O_3 in H_2 are shown in Equations 3.1 to 3.3.

$$3Fe_2O_3 + H_2 \rightarrow 2Fe_3O_4 + H_2O \quad (3.1)$$

$$Fe_3O_4 + H_2 \rightarrow 3FeO + H_2O \quad (3.2)$$

$$FeO + H_2 \rightarrow Fe + H_2O \quad (3.3)$$

$$3Fe_2O_3 + CO \rightarrow 2Fe_3O_4 + CO_2 \quad (3.4)$$

$$Fe_3O_4 + CO \rightarrow 3FeO + CO_2 \quad (3.5)$$

$$FeO + CO \rightarrow Fe + CO_2 \quad (3.6)$$

$$15Fe + 12CO \rightarrow 3Fe_5C_2 + 6CO_2 \quad (3.7)$$

The assignment of Fe_2O_3 as the predominant form of iron oxide in the calcined catalyst is justified by the observation that the weight loss during TPR based with hydrogen as the reducing gas (see Figure 3-1), was about 33%, of which less than 3% was attributed to loss of water. This implies that the remaining 30% loss was due to weight loss associated to the reduction of Fe_2O_3 to Fe metal. A simple calculation of the

percent weight loss for the reduction of the three forms of iron oxides is illustrated in Appendix A.2. The percent weight loss due to the reduction of Fe_3O_4 to Fe is 27.642% while that due to the reduction of Fe_2O_3 and FeO are 30.058% and 22.27% respectively.

The thermogram for reduction with CO was different from that with H_2. The stoichiometric equations for reduction in CO are shown in Equations 3.4 to 3.7 showing both reduction to metallic Fe and carburization. The formation of FeC_x provide sites for CO adsorption and dissociation [26], thereby resulting in the increase in weight observed in the region above 490°C in Figure 3-2.

Figure 3-3, Figure 3-4, and Figure 3-5 show TPR (in H_2) thermograms for 99Fe1ALa-mon-907, 20Fe1K1Pt-ALa-mon-507, and 20Fe1K1Pt-ALa-705, respectively.

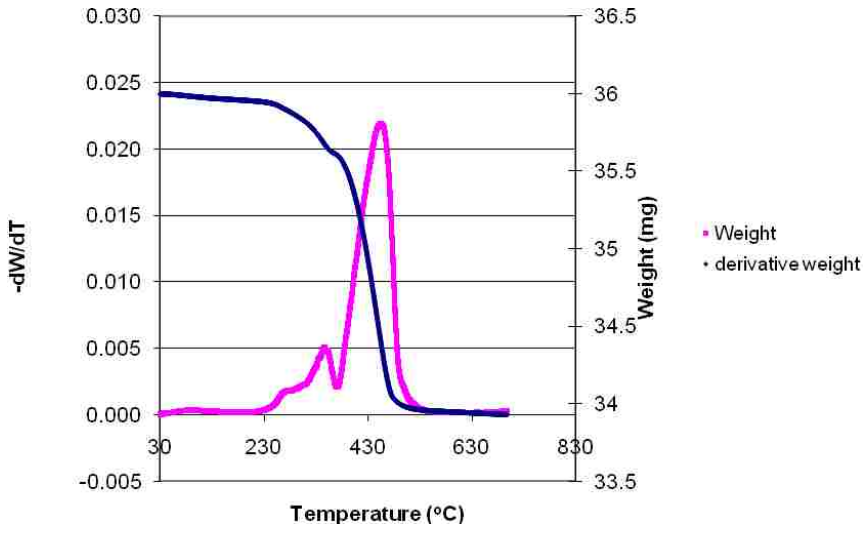

Figure 3-3: Temperature-programmed reduction in H_2 thermogram for 99Fe1ALa-mon-907

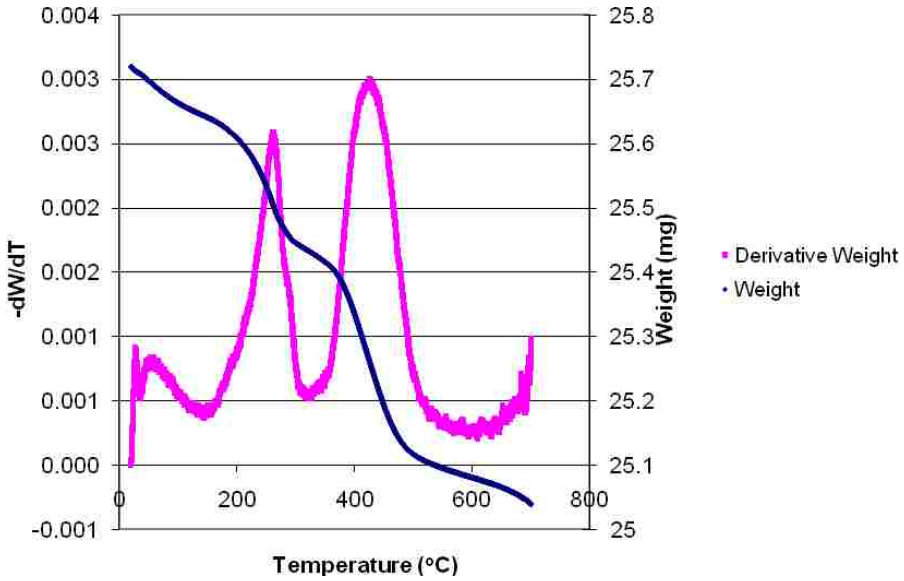

Figure 3-4: Temperature-programmed reduction in H_2 thermogram for 20Fe1K1Pt-ALa-mon-507

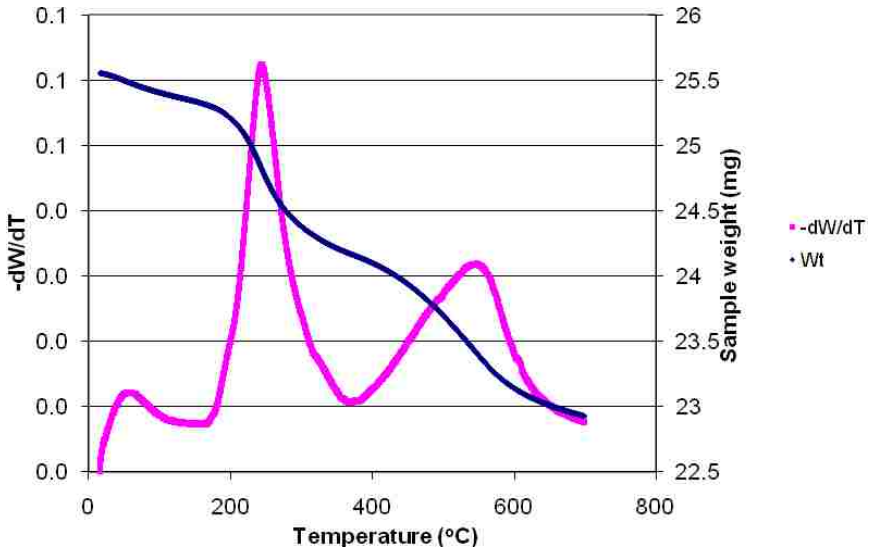

Figure 3-5: Temperature-programmed reduction in H_2 thermogram for 20Fe1K1Pt-ALa-705

The thermogram for 99Fe1ALa-mon-907 is similar to that for 99Fe1ALa-307. This suggests that the monolith was inert with little or no modification to the chemical structure of the catalyst. On the other hand, the thermogram for 20Fe1K1Pt-ALa-mon-507 is different from that of 99Fe1ALa-mon-907, as can be seen by comparing the relative peak heights in the regions between 180°C to 320°C and 320°C to 500°C. This may be due to the effects of support and the addition of K and Pt promoters. The subject of the effect of promoters on the reduction profile and reducibility of FTS catalysts have been discussed by Iglesia [27]and Davis [24].

TPR experiments were repeated at least three times for each catalyst. The variability in the transition temperatures was below 0.5%.

3.3.2 BET surface area analysis

Surface areas of the catalysts were determined using full range N_2 sorption isotherms obtained at 96 K with a Micromeritics Tri-Star 3000 BET surface area and pore size analyzer after pretreatment at 120°C for 12 h. The results are summarized in Table 3-5. The pore size distributions and the corresponding average mesopore diameters were calculated from the BET data by the method proposed by Gregg and Sing as illustrated in Bartholomew and Farrauto [7]. BET surface area analysis was repeated at least three times for each catalyst. The variability in the BET surface area was about 5% for each catalyst. Because the average pore diameter was calculated through a rigorous method, the error was not estimated.

Table 3-5: Summary of BET surface area, pore volume and pore diameter measurements for 99Fe1ALa-307, 99Fe1ALa-mon-907, 20Fe1K1Pt-ALa-705, and 20Fe1K1Pt-ALa-mon-507

Catalyst	**BET surface Area (m^2/g)**	**Average mesopore diameter (nm)**
99Fe1ALa-307	86.85	12.0
99Fe1ALa-mon-907	67.2	9.8
20Fe1K1Pt-ALa-705	83.1	11.3
20Fe1K1Pt-ALa-mon-507	65.5	15.7

3.3.3 CO chemisorption uptake and O_2 titration

CO chemisorption uptake at room temperature and O_2 titration at 400ºC were performed in sequence on a Perkin Elmer TGA7 thermogravimetric analyzer to determine approximate values of the catalyst extent of reduction (EOR) and dispersion. The sample was prepared for CO chemisorption by (1) reducing in situ in 20 mL/min H_2 and 180 mL/min He with a temperature profile chosen from careful analysis of the TPR profile for the individual catalyst (Table 3-6 for 99Fe1Al-307), (2) purging in 200 mL/min He for 1hr at 470ºC, (3) cooling to room temperature in 200 mL/min He. After the sample temperature had stabilized at room temperature, the sample weight was recorded as a function of time for about 5 min to establish a base line; subsequently a flow of 20 mL/min of CO/Ar was introduced to the sample while the He flow was reduced to 180 mL/min to maintain a constant total gas flow of 200 mL/min.

After the sample weight has reached a plateau (see Figure 3-6), gas phase CO was removed by purging in the cell with He for 1 hr. The sample was reduced again in 20 mL/min H_2 and 180 mL/min He by ramping the temperature to 500ºC at a 1ºC/min ramp rate and holding the temperature at 500ºC for 24 hr. The CO uptake procedure was repeated twice. Following the third CO uptake and subsequent reduction at 500ºC and purging at 470ºC, the sample was cooled to 400ºC. After the temperature had been allowed to stabilize for about an hour, sample weight was recorded as a function of time while maintaining a He flow of 200 mL/min again to establish a stable baseline. After about 5 min, 20 mL/min O_2 was introduced while the He flow was reduced to 180 mL/min. Sample weight was measured until it had reached a plateau (see Figure 3-7).

Table 3-6: Reduction profile based on TPR of 99Fe1ALa-307

Step	Procedure
1	Heat from 20ºC to 100ºC at 0.5ºC/min
2	Hold 60 min at 100ºC
3	Heat from 100ºC to 280ºC at 0.5ºC/min
4	Hold for 720 min at 280ºC
5	Heat from 280ºC to 500ºC at 0.5ºC/min
6	Hold for 2160 min at 500ºC
7	Cool from 500ºC to 470ºC at 0.5ºC/min

Figure 3-6 is the CO uptake profile at 20ºC for 20Fe1K1Pt-La-mon-507 while Figure 3-7 is the profile of the O_2 uptake at 400ºC for the same catalyst. Table 3-7 summarizes the approximate percent active metal dispersion and extent of reduction (EOR) for the respective catalysts. The EOR calculation is based on the assumption that all metallic Fe present after reduction is converted to Fe_2O_3 in 10% O_2 at 400°C.

A Mathcad worksheet showing the calculation EOR, CO uptake and dispersion are shown in Appendix A.3. Approximate percent dispersion was calculated on the assumption that CO adsorption stoichiometry was 1:1. This assumption is not completely valid and is discussed in more details in Section 6.1.

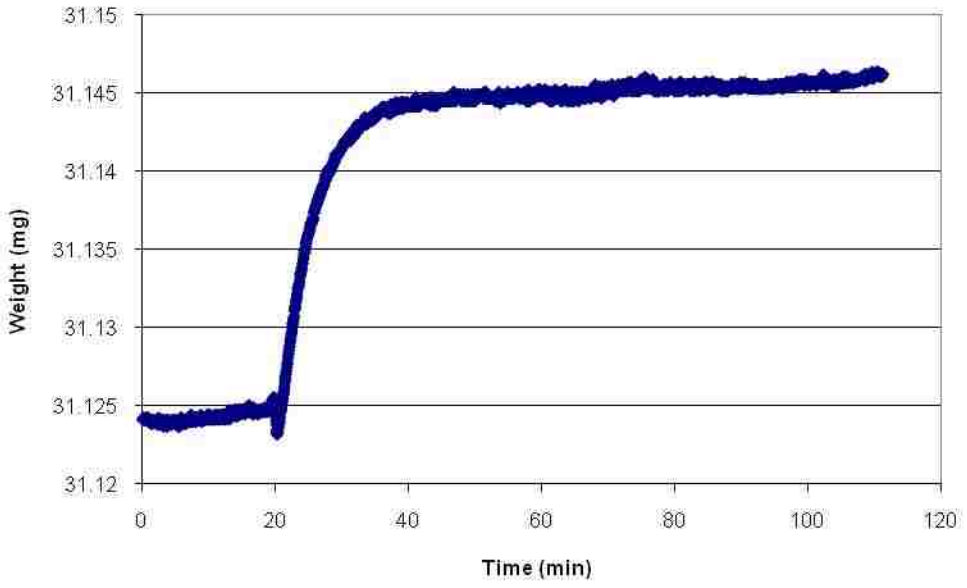

Figure 3-6: CO uptake at 20°C for 20Fe1K1Pt-ALa-mon-507 recorded with Perkin Elmer thermogravimetric analyzer (TGA 7)

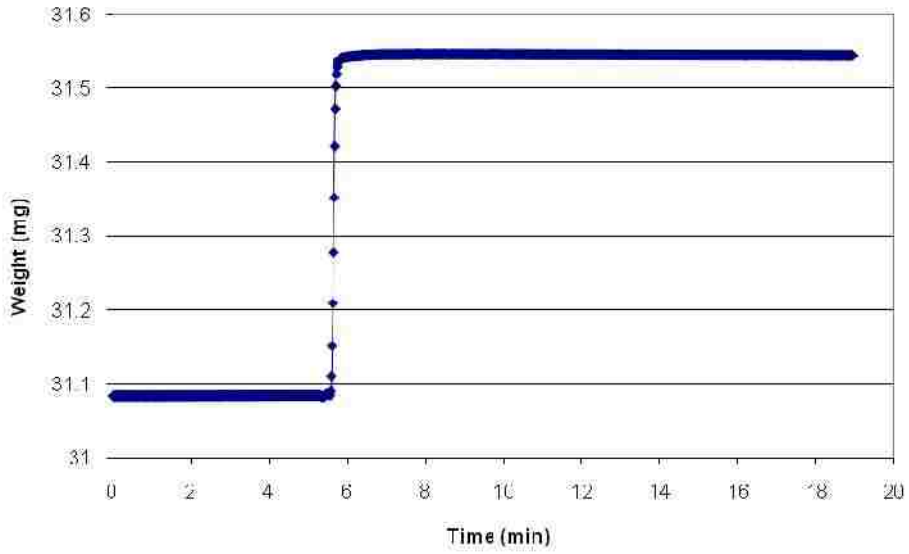

Figure 3-7: O_2 uptake at 400^{o}C for 20Fe1K1Pt-ALa-mon-507 recorded with Perkin Elmer thermogravimetric analyzer (TGA 7)

Table 3-7: Summary of %EOR and %Dispersion based on O_2 titration and CO chemisorptions uptake at room temperature

Catalyst	**% EOR**	**CO uptake (μmol/g)**	**[a]Approximate %Dispersion**
99Fe1ALa-307	37.9	109.6	3.2
99Fe1ALa-mon-907	80.3	508.1	7.1
20Fe1K1Pt-ALa-705	67.7	358.0	29.6
20Fe1K1Pt-ALa-mon-507	91.2	196.9	13.5

[a]Based on a metal - CO stoichiometry of 1:1

3.3.4 Transmission electron microscopy (TEM)

TEM was used to qualitatively study the dispersion of the calcined catalysts to obtain an idea of the uniformity of the crystallite size and distribution for each catalyst. The images are shown in Figure 3-8 to Figure 3-10 for 99Fe1ALa-307, 20Fe1K1Pt-ALa-705, and 20Fe1K1Pt-ALa-mon-507, respectively. Since the images are for the calcined catalysts, it cannot be used to estimate the crystallite diameter of the working catalyst. However, from the images, it can be concluded that the oxide phases were distributed fairly uniformly on the surface.

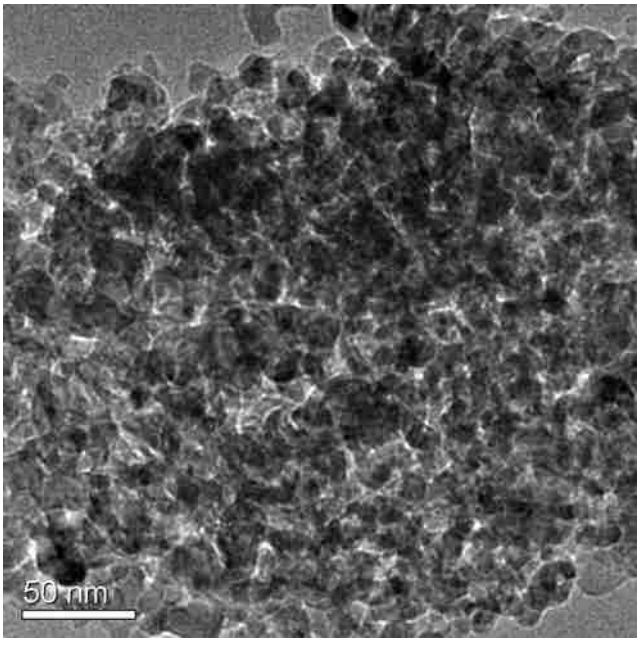

Figure 3-8: TEM image for 99Fe1ALa-307 before reduction

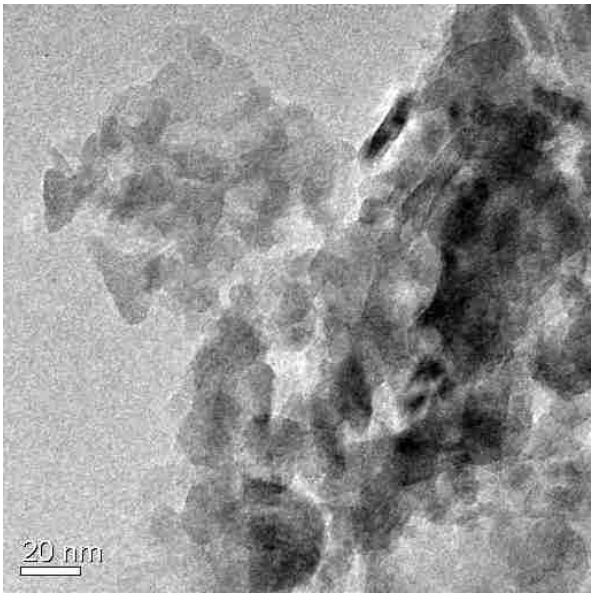

Figure 3-9: TEM image for 20Fe1K1Pt-ALa-705 before reduction

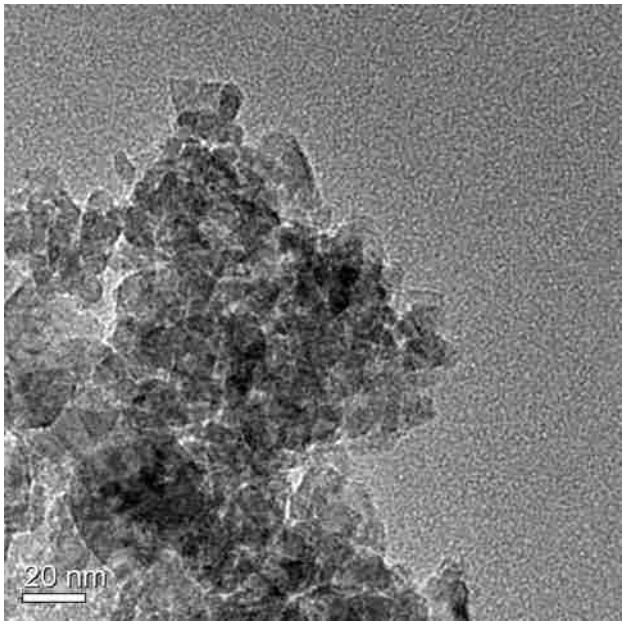

Figure 3-10: TEM image for 20Fe1K1Pt-ALa-mon-507 before reduction

3.4 Apparatus for Transient Experiments

Transient experiments such as TPD, ITH, and TPH were performed on a computer-automated fixed-bed reactor system shown schematically in

Figure **3-11**. Although the reactor system was used for TPD, ITH, and TPH experiments, it can be easily adapted to other transient experiments such as steady-state isotopic transient kinetic analysis (SSITKA). All gases were purified before connecting to the reactor system. Description of the purification system is found in Critchfield's Thesis [19]. 11.8% Ar was pre-mixed with the CO for use as an internal standard.

The reactor was made of quartz tube with an internal diameter of 5 mm. The middle of the tube was bulb-shaped to minimize pressure drop and temperature gradients through the catalyst bed. A quartz frit was used to support the powdered catalyst in the reactor. Its pressure was controlled either by a needle valve or by a back-pressure regulator (Alicat) connected to a National instruments FieldPoint analog input and output module. Gas flow to the reactor was controlled by a set of mass flow controllers (Brooks). The mass flow controllers were interfaced with the computer via National Instruments FieldPoint analog input and output modules (-10 to +10 V) while interfacing of the thermocouple (used to measure reactor temperature) with the computer was accomplished with a thermocouple FieldPoint module. A program written in National Instruments LabView 8.0 environment was used to control, collect, and record online temperature and process flow data.

Also, the reactor system was equipped with an electronically-actuated six-port injection valve having a 128.48 μL sample loop. The timing on the valve was also provided electronically.

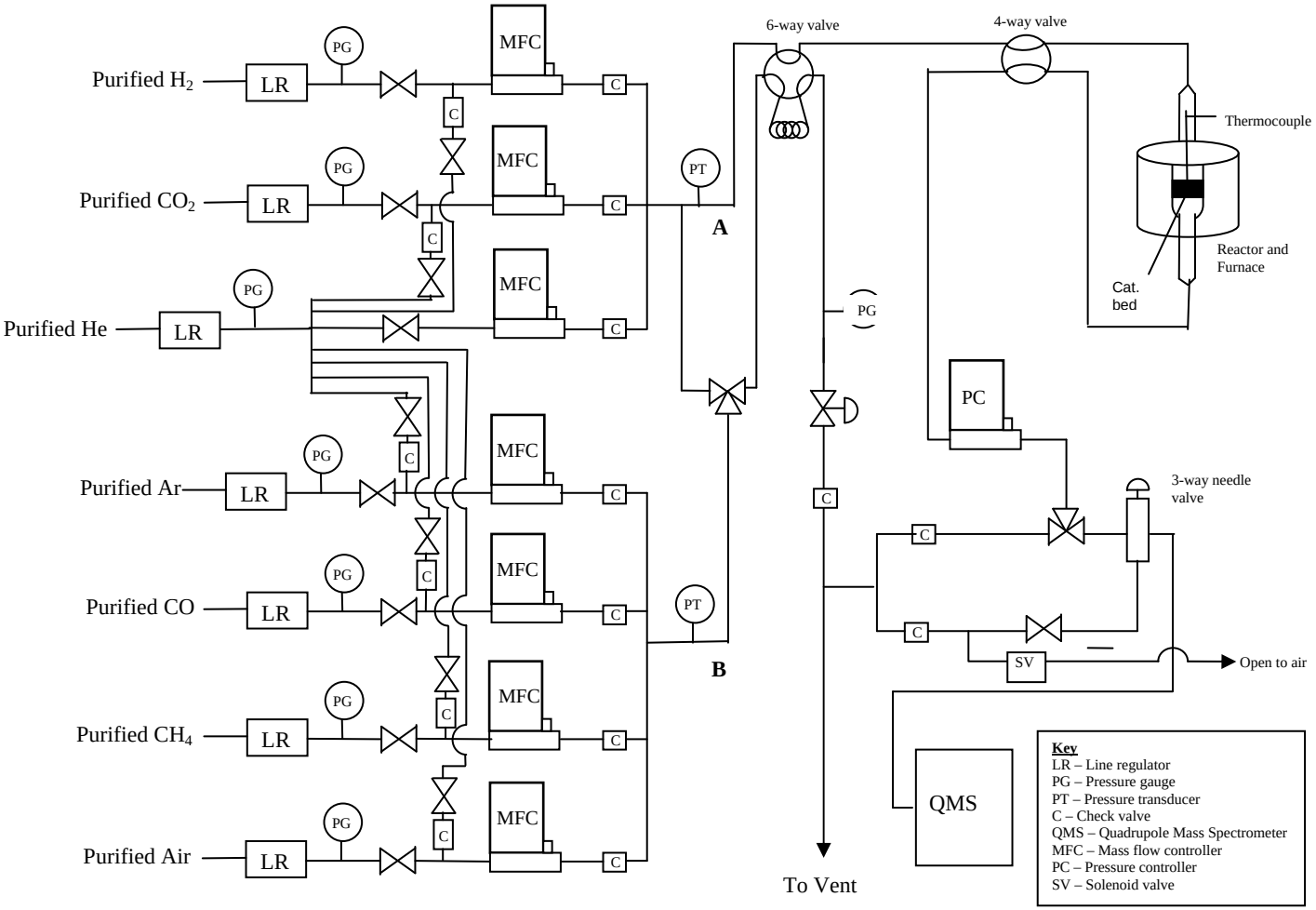

Figure 3-11: Fixed bed reactor system for transient experiments

The furnace was made by winding about 50 turns of Ni-Cr wire (NI80/CR20, Omega Engineering) on a 1 inch diameter by 5 inch long quartz tube (open at both ends). Insulation was provided by casting cement (electrotemp cement No. 8, Sauereisen) (about 4 inch thick) around the tube and windings. The furnace was able to attain temperatures up to 1000ºC at ramp rates up to 60ºC/min but had a slow cooling rate. Temperature control was accomplished with an Omega CN3000 temperature controller.

Concentrations of gaseous species exiting the reactor were monitored online with a UTI 100C quadrupole mass analyzer. The mass analyzer was connected to the computer for control and data acquisition via an RS 232 interface and controlled with computer program written in National Instruments LabView 8.0 environment. The mass spectrometer system was equipped with two vacuum stages. The first vacuum stage was maintained at about 5 mTorr (with no sample feed) using a mechanical pump. The second vacuum stage was maintained at about 7.5×10^{-8} Torr with a combination of roughing and turbo pumps. A control-leak-valve was used as an interface to the second vacuum stage.

The mass analyzer was equipped with a relatively soft ion source. Hence the molecular ion peaks for CO, CO_2, and CH_4 were usually higher than those of their respective fragments.

3.4.1 Flow characteristics of the fixed-bed reactor system

The transient response recorded by a mass spectrometer is generally a convolution of the reactor system flow characteristics and the reaction kinetics. Therefore accurate

modeling of reaction kinetics obtained with a particular reactor system requires understanding of the reactor flow characteristics.

To determine the flow characteristics of the fixed-bed reactor system, exit concentrations as a function of time of argon (inert tracer) was monitored with the mass spectrometer after the tracer was injected through the sample loop by (1) bypassing the reactor and (2) through the reactor. Argon exit concentration profiles for these two cases are shown in Figure 3-12.

Davis and Davis [133] showed that for a CSTR and PFR with an impulse input, the exit concentration profile will look exactly like the input for an ideal PFR but the output from a CSTR will exhibit a sharp rise followed by an exponential decay. However, for a non-ideal PFR, the exit concentration profile will exhibit significant spread in the width of the exit concentration profile when compared to that of the input pulse. Thus by examining the profile in Figure 3-12, one can infer that the fixed bed reactor system used in this study was neither an ideal PFR nor an ideal CSTR, but reasonably close to a PFR in performance. Unfortunately, it was not possible to quantitatively model actual reactor performance from the data in Figure 3-12. Accordingly, it was necessary to assume ideal PFR behavior in analyzing the transient data in this study.

3.5 Apparatus for Steady-State Kinetic Experiments

Steady-state kinetic experiments were performed in the same Berty Reactor system described by Critchfield [19]. However, the reactor control and data analysis programs were modified. Online analysis of reactor effluents was performed using an HP

5890 gas chromatograph equipped with both TCD and FID detectors. The GC was connected to a computer via a RS232 interface. Control and data acquisition was performed using Chrom Perfect Spirit software (Justice Innovations).

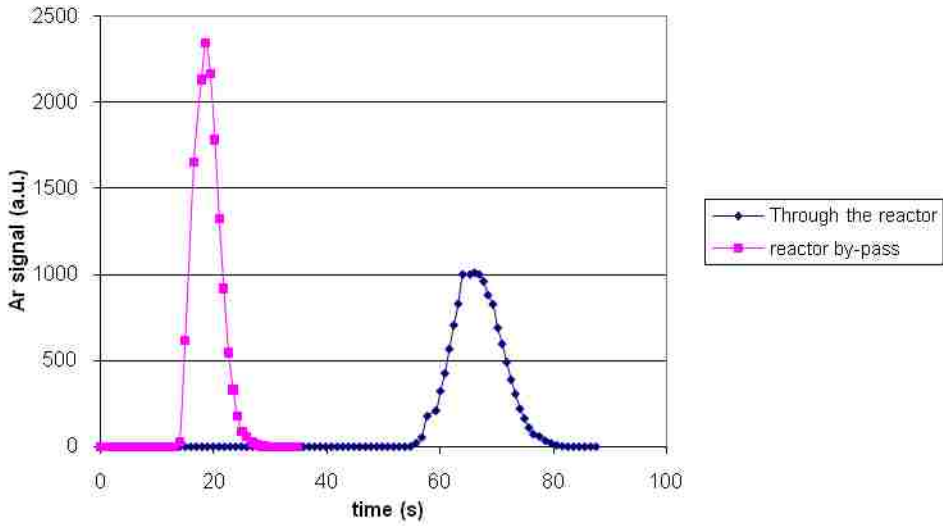

Figure 3-12: Concentration of Ar tracer following injection into the fixed-bed reactor system (a) reactor by-pass, (b) through the reactor.

3.6 Transient Experimental Procedure

TPD, ITH, and TPH were performed respectively on 99Fe1ALa-307 and 20Fe1K1Pt-ALa-705. This section describes the experimental procedures used for each of these transient experiments.

3.6.1 TPD experimental procedure

The TPD experimental procedure involved (1) in situ reduction of the sample; (2) CO adsorption at a specified temperature; and (3) desorption of adsorbed species. Details of the three steps are provided in the paragraph below.

3.6.1.1 In-Situ Reduction and CO Adsorption to Saturation

About 200 mg of calcined catalyst was loaded into the reactor. The sample was reduced in situ by flowing 20 mL/min H_2 and 80 mL/min He using the temperature profile in Table 3-6. Following reduction, the sample was cooled to 470ºC and purged with He for about 1 hr. After purging, the sample was cooled to room temperature while maintaining the He flow. After the temperature had stabilized, the He flow through the sample was reduced to 10 mL/min. The gas exiting the reactor was directed to the mass spectrometer while the needle valve or pressure controller was adjusted to maintain a pressure of about 1 atm in the reactor. At this carrier flow rate and reactor pressure, the first vacuum stage pressure was usually about 150 μm Hg. The control-leak-valve was gradually adjusted so that the second stage vacuum was about 8.0×10^{-6} Torr. After the reactor and mass spectrometer pressures had been stabilized, a mixture of 3 mL/min CO/Ar and 47 mL/min He was introduced into the sample loop in the 6-port injection valve with the valve switched in the OFF position to ensure that the gas mixture in the sample loop was vented rather than going through the reactor.

The mass spectrometer data acquisition program was started and the signals for AMU 28 (CO^+), 40 (Ar^+), and 44 (CO_2^+) were recorded simultaneously as a function of time. After obtaining a stable baseline (usually about 10 min), the injection valve was

switched ON, injecting pulses of CO/Ar into the reactor while the mass spectrometer data acquisition was continuously recording signals for AMU's 28, 40, and 44 simultaneously. CO/Ar injection into the reactor was stopped after the peak height for AMU's 28 and 40 had reached a plateau. The reactor was subsequently purged for about 1 hr.

To obtain the heat of CO adsorption as a function of coverage, CO adsorption to saturation at temperatures other than room temperature were conducted. The reason for this approach was to circumvent the limitations on CO detection by the UTI 100 mass analyzer system coupled with the relatively low surface area of the catalysts used in this study. Zowtiak also employed this technique in his H_2 TPD study on Co catalysts [61]. After adsorption and purging for about 30 min at the adsorption temperature (40ºC, 125ºC, 175ºC, and 195ºC respectively), the reactor was cooled to room temperature while still purging for another 30 min at room temperature.

3.6.1.2 Desorption Procedure

With the reactor and mass spectrometer flow and pressures at the same levels during the adsorption experiment, desorption was performed by recording the mass spectrometer signals corresponding to AMU 28, AMU 40, and AMU 44, respectively, as a function of time and temperature while the temperature of the reactor was increased at a linear rate from room temperature to 600ºC or 800ºC. The observed signals were subsequently converted to concentrations and mole fractions of CO, Ar CO_2 and. Usually, no Ar signal was detected during the desorption experiment.

3.6.2 ITH experimental procedure

ITH experiments involved (1) in situ reduction of about 200 mg of the catalyst sample in H_2 using the temperature profile shown in Table 3-6; (2) FTS reaction for 5 min at 125ºC, 165ºC, and 175ºC, respectively, and 1 atm pressure; and (3) hydrogenation of adsorbed species at a constant temperature (same as the FTS temperature). The in situ reduction procedure was similar to that described in Section 3.6.1.1 above.

Following the reduction and purging with He, the reactor was cooled to the desired temperature. While maintaining the reactor at atmospheric pressure and at the desired temperature, FTS was carried out by flowing 5 mL/min CO/Ar, 5 mL/min He, and 20 mL/min H_2 for 5 min. Low temperature and pressure operation was chosen to favor methane formation and avoid the formation of carbon species that are difficult to hydrogenate. The reactor was purged with He for 30 min. After the purge, the mini-cold-trap connected between the reactor and the needle valve was immersed in an ice bath to trap out water formed during hydrogenation and prevent it from entering into the mass spectrometer, thereby minimizing the oxygen interference from water fragmentation in the mass spectrometer with methane signal at AMU 16.

The hydrogenation step was initiated by adjusting the He flow rate to 10 mL/min and directing the reactor exit gas to the mass spectrometer. The reactor pressure was adjusted to about 1 atm using the needle valve while the mass spectrometer's first stage and second stage vacuum pressures were about 150 mTorr and 8.0×10^{-6} Torr, respectively. After the reactor pressure had stabilized, 1 mL/min H_2 was introduced into the reactor while the He flow was reduced to 9 mL/min to maintain a constant total flow of 10 mL/min. The mass spectrometer's data acquisition program was turned ON and

signals corresponding to AMU 15 (CH_3^+), AMU 16 (CH_4^+), and AMU 28 (CO^+) were recorded as a function of time. The experiment was stopped after the AMU 15 signal had gone through a maximum. The remaining carbon species left on the catalyst at this point were removed by heating the reactor to 600ºC and holding at 600ºC for 24 hr while flowing 20 mL/min H_2 and 80 mL/min He. The reactor was subsequently cooled to 470ºC and purged with He. It was further cooled to the previous temperature where FTS was again performed and the entire process repeated. The same sample was used to perform ITH at the other temperatures using the same procedure though the inital reduction procedure was not repeated.

3.6.3 TPH experimental procedure

TPH experiments involved the hydrogenation of stable carbon and oxygenated species formed on the catalyst surface after 5 minutes of FTS. The same sample that was used for the ITH experiment was used for this experiment. After completing the ITH experiment, the sample was again reduced at 600ºC for 24 hrs to ensure the removal of left over surface carbon. Thereafter, the sample was cooled to 300ºC. The H_2 flow was replaced with He to purge the reactor for 1 hr. After the purge was completed, the reactor was further cooled to 125ºC, 165ºC, 175ºC, 200ºC, 220ºC, and 250ºC, respectively. FTS was carried for 5 min at these temperatures by flowing 20 mL/min H_2, 5 mL/min CO/Ar and 5 mL/min He. The reactor was purged again for 15 min by replacing the H_2 and CO/Ar flows with He. While flowing He through the reactor, the reactor was cooled to 125ºC to ensure a uniform temperature ramp rate. The reactor pressure was adjusted to about 1 atm using the needle valve while the mass spectrometer's first and second stage

vacuum pressures were about 150 μmHg and 8.0 x 10^{-6} Torr, respectively. After the reactor pressure had stabilized, 1 mL/min H_2 was introduced into the reactor while the He flow was reduced to 9 mL/min to maintain a constant total flow of 10 mL/min. Temperature was next increased from 125ºC to 600ºC at 22.6ºC/min. The mass spectrometer's data acquisition program was turned ON and signals corresponding to AMU 15 (CH_3^+), AMU 16 (CH_4^+), and AMU 28 (CO^+) were recorded as a function of time and temperature simultaneously.

The remaining carbon species left on the catalyst at this point were removed by holding at 600ºC for 24 hr while flowing 20 mL/min H_2 and 80 mL/min He. The reactor was subsequently cooled to 470ºC and purged with He. It was further cooled to the previous temperature where FTS was performed and the entire process repeated again.

3.7 Steady-State Kinetic Experiments

Steady-state kinetic studies were designed to provide estimates of kinetic parameters, i.e. pre-exponential factors, heats of adsorption, and activation energies. These parameters are usually obtained by measuring reaction rate as a function of temperature and reactant partial pressures or concentrations followed by fitting the observed rate of reaction to an empirical rate equation or Langmuir-Hinshelwood (LH) type rate expression. Linear or non-linear least squares regression (single or multi-variable) is usually used to fit the experimental data to the model. Since the rate model is non-linear, the error in the parameter estimates is usually large, especially when the number of experiments is too small and/or when the experimental parameters do not cover the entire sample space or surface [153].

To minimize variability in estimated parameters in linear models, a factorial design is often adequate [154]; however, for nonlinear response models (usually the case with rates of catalytic reactions), a sequential design involving an optimality criteria, coupled with a robust nonlinear least squares regression algorithm, is recommended [19, 155, 156]. Usually the Levenberg-Marquardt algorithm [157] is very efficient for non-linear regression. In this study, both a Levenberg-Marquardt algorithm and an orthogonal distance regression method were used in estimating kinetic parameters. Optimization criteria used in a sequential experimental design include: D-optimal, A-optimal, V-optimal, E-optimal and G-optimal. The D-optimal method was most pertinent to this study since it enabled the selection of experimental conditions that minimize the overall variances in the estimated kinetic parameters while reducing parameter correlation. The D-optimal criterion is given by Equation 3.8:

$$D = \left| F^T(X,\theta) F(X,\theta) \right|^{-1/2} \tag{3.8}$$

where X is a set of design parameter inputs, θ is a set of parameters to be estimated, F is a Jacobian matrix while F^T is the transpose of F. The Jacobian is defined in Equation 3.9 as:

$$F(X,\theta) = \begin{pmatrix} \left(\frac{\partial R(X,\theta)}{\partial \theta_1}\right)_1 & \left(\frac{\partial R(X,\theta)}{\partial \theta_2}\right)_1 & \left(\frac{\partial R(X,\theta)}{\partial \theta_3}\right)_1 & \cdots & \left(\frac{\partial R(X,\theta)}{\partial \theta_m}\right)_1 \\ \left(\frac{\partial R(X,\theta)}{\partial \theta_1}\right)_2 & \left(\frac{\partial R(X,\theta)}{\partial \theta_2}\right)_2 & \left(\frac{\partial R(X,\theta)}{\partial \theta_3}\right)_2 & \cdots & \left(\frac{\partial R(X,\theta)}{\partial \theta_m}\right)_2 \\ \vdots & \vdots & \vdots & \vdots & \vdots \\ \left(\frac{\partial R(X,\theta)}{\partial \theta_1}\right)_{n-1} & \left(\frac{\partial R(X,\theta)}{\partial \theta_2}\right)_{n-1} & \left(\frac{\partial R(X,\theta)}{\partial \theta_3}\right)_{n-1} & \cdots & \left(\frac{\partial R(X,\theta)}{\partial \theta_m}\right)_{n-1} \\ \left(\frac{\partial R(X,\theta)}{\partial \theta_1}\right)_n & \left(\frac{\partial R(X,\theta)}{\partial \theta_1}\right)_n & \left(\frac{\partial R(X,\theta)}{\partial \theta_1}\right)_n & \cdots & \left(\frac{\partial R(X,\theta)}{\partial \theta_1}\right)_n \end{pmatrix} \tag{3.9}$$

$R(X,\theta)$ is the reaction rate expression and $\left(\frac{\partial R(X,\theta)}{\partial \theta}\right)_1$ is the partial derivative of the reaction rate with respect to the parameter to be estimated, evaluated at experimental run Condition *1*. Condition *n* is the new run condition to be determined. Sequential design of experiments was accomplished by: (a) using factorial design to define an initial set of experimental conditions; (b) performing experiments at these conditions; (c) using nonlinear least squares regression to estimate the values of the parameters; (d) evaluating the matrix *F* as a function of the new unknown run conditions, and (e) determining the values of X that maximize Equation 3.8. Experiments were performed at these new conditions, following which the parameters were re-estimated and confidence intervals re-calculated. The procedure was repeated until the values of the re-estimated parameters become constant as detailed in Section 3.7.1.

3.7.1 Steady-state kinetic experimental procedure

Steady-state kinetic experiments were performed in the Berty reactor system using sequential design of experiment based on D-optimal criteria. For this design, reactor temperatures of 220ºC, 240ºC, 250ºC, and 260ºC, respectively, and a total reactor pressure of 20 atm were chosen to minimize catalyst deactivation and ensure significant formation of long-chain hydrocarbons. These conditions are similar to industrial FTS operating conditions.

The catalysts used in the experiments were 99Fe1Ala-mon-506 (monolith # 1), 20Fe1K1Pt-ALa-mon-507 (monolith # 3), and 99Fe1ALa-mon-907 (monolith # 1) respectively. In each case, the catalyst was reduced in situ in the Berty reactor with the

temperature program shown in Table 3-6 while flowing 20 mL/min H_2 and 180 mL/min He. The reactor was subsequently purged with He and cooled to 220ºC. After the temperature had stabilized, the reactor was pressurized to 20 atm with He.

Scoping runs were done at 220ºC starting with a 2^n fractional factorial experimental design with center point based on two input parameters – outlet partial pressures of CO (P_{CO}) and H_2 (P_{H2}) – while blocking the temperature. For the 20Fe1K1Pt-ALa-mon-507, the low and high values of P_{CO} were chosen to be 1.3 atm and 5 atm, respectively, while those for P_{H2} were 3.7 atm and 11.5 atm respectively. These translated to the inlet volumetric flow rates shown on Table 3-8 (conditions for the other catalysts are presented in the results section). These 5 points provided the starting data for the sequential design of experiment using the LH type rate expression in Equation 3.10 similar to that used by Critchfield [19], where A and B are kinetic constants.

$$-r_{CO} = \frac{AP_{CO}^{2/3}P_{H_2}^{5/6}}{\left(1+BP_{CO}^{2/3}P_{H_2}^{1/3}\right)^2} \tag{3.10}$$

Run 1 was chosen as a standard condition to check periodically for catalyst deactivation. Also, the Weisz modulus was calculated at each run condition, and the Weisz criterion was applied to ensure that the pore diffusion resistance was negligible.

Each run began with a 24 h time-on-stream (break-in period) to ensure steady-state. At the end of the factorial experiment, the kinetic constants were estimated using the observed rate data at the above conditions using a nonlinear regression technique. The estimated kinetic constants, and the rate data were used in the sequential design algorithm (developed as a Mathcad 14 worksheet – see appendix) to determine the new set of outlet partial pressures of CO and H_2 that maximizes the D-optimal criteria as well

as meets the practical constraints imposed by the physical limitations of the Berty reactor system. By choosing an outlet conversion, and with the partial pressures of CO and H_2 determined from the sequential design algorithm, new inlet flow rates of CO, H_2 and He were calculated and the reactor conditions were adjusted accordingly.

Table 3-8: Experimental design used for the catalyst scoping experiment

Run	**Inlet He Flow (mL/min) @ s.t.p.**	**Inlet CO/Ar Flow (mL/min) @ s.t.p.**	**Inlet H_2 Flow (mL/min) @ s.t.p.**
1	44	74	130
2	11	32	60
3	32	41	91
4	183	20	52
5	116	44	90

The experiment at 220ºC continued until the estimated values of the kinetic constants approached asymptotic values. Thereafter, the reactor temperature was increased to 240ºC. At 240ºC, the experiment was conducted at inlet conditions similar to those used at 220ºC. After setting the reactor temperature at 240ºC, the kinetic constants A and B were expanded into Arrhenius forms requiring the estimation of four kinetic parameters – pre-exponential factor for the numerator, apparent activation energy

for the numerator, pre-exponential factor for the denominator, and apparent heat of adsorption for the denominator, respectively. The values of the estimated kinetic parameters were used in the sequential design algorithm to determine a new set of experimental conditions that optimize the values of the estimated kinetic parameters. After the values of the estimated kinetic parameters approached an asymptotic value, the reactor temperature was increased to 260ºC while continuing with the sequential design. The experiment was stopped after the values of the kinetic constants approached asymptotic values at this temperature.

The data obtained from the above experiment were fitted to various forms of LH-type rate expressions derived from different sets of elementary steps with different assumed rate determining steps (r.d.s.) using multi-response nonlinear regression. The rates of CO disappearance and CO_2 formation were the response variables. The various sequences of elementary steps and the derivation of the resulting LH-type rate expressions are shown in Appendix A.5. Order of magnitude estimates of the pre-exponential factors were obtained using transition state theory. The estimated values from transition state theory were used as constraints during the data fitting process to obtain macrokinetic models.

To obtain microkinetic models from the data obtained above, activation energies of each elementary reaction step in the set of sequences of elementary steps used in deriving the macrokinetic model were calculated using the UBI-QEP method. The values of C, H, and O binding energies were regressed using nonlinear regression to correct for surface heterogeneity and the effect of surface coverage on the heats of adsorption of these atoms and other species involved in the reaction sequence.

4. Chapter 4: Results: Transient Experiments

In this chapter, the results of TPD, ITH, and TPH experiments on both supported and unsupported Fe catalysts are presented. Also presented in this chapter is the development of the mathematical model that formed the basis of microkinetic modeling of the above experiments.

4.1 Results of CO TPD on 20Fe1K1Pt-ALa-705

CO TPD was carried out on 20Fe1K1Pt-La-705 after adsorption at 313 K, 423 K, and 448 K as described in Section 3.6.1. Figure 4-1 and Figure 4-2 show CO and CO_2 TPD spectra obtained after CO adsorption at 313 K, while Figure 4-3 to Figure 4-4 show the TPD spectra obtained after CO adsorption to saturation at 423 K and 443 K respectively. The observed TPD spectrum is broad and represents overlapping desorption phenomena probably due to surface site heterogeneity. In order to identify the various desorption processes, each TPD spectrum was fitted to Gaussian and Lorentzian type functions. Brown et al. and others reported the use of a similar approach in interpreting overlapping spectra [158-160].

$$f(x) = \sum_{i=1}^{6} \frac{\alpha_i^{\gamma_i}}{(x-\mu_i)^2 + \beta_i^2} \tag{4.1}$$

The Lorentzian type function shown in Equation 4.1 provided a better fit of the observed respective CO TPD spectra. The peak positions are shown in Table 4-1.

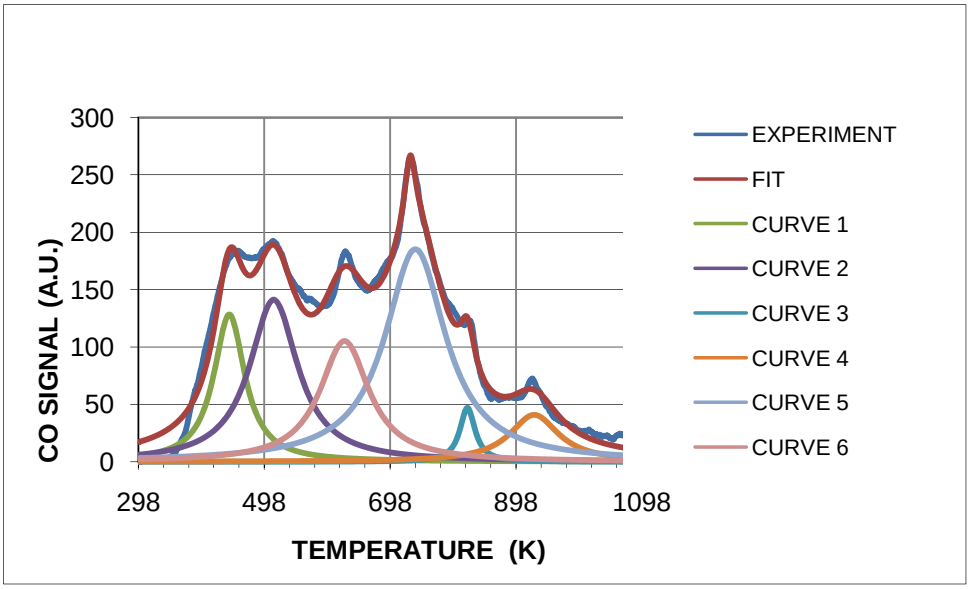

Figure 4-1: CO TPD after CO adsorption to saturation at 313 K for 20Fe1K1Pt-ALa-705. The observed TPD profile was fitted with 6 Lorentzian type peaks

The first two Lorentzian peaks (Curves 1 and 2) in Figure 4-1, Figure 4-3 and Figure 4-4 are assigned to molecularly adsorbed CO on Fe and on Fe surrounded by Pt and K promoters respectively, while the other peaks are due to recombination of dissociated C and O on various surface sites (Fe, Fe-Pt, and Fe-K).

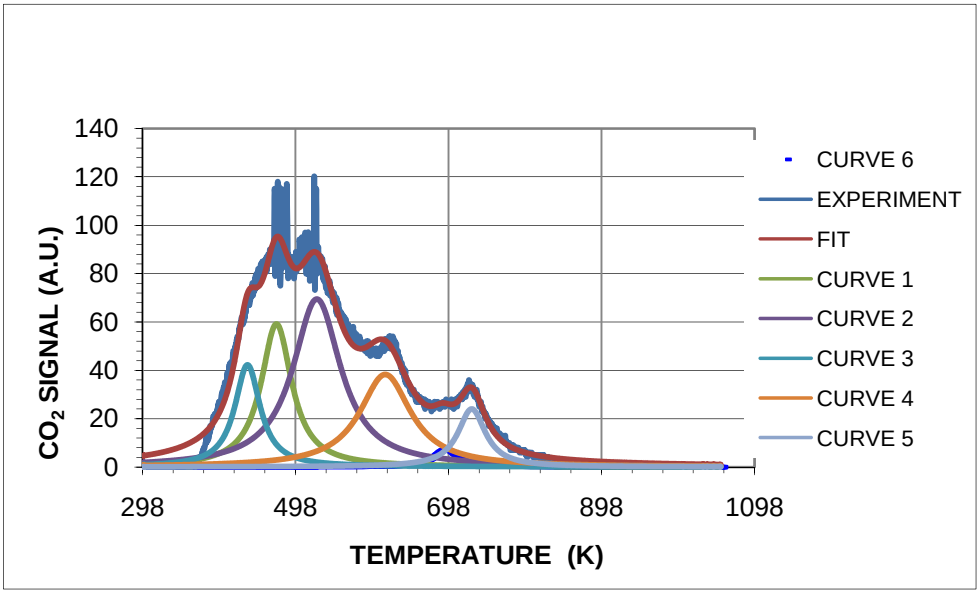

Figure 4-2: CO_2 TPD after CO adsorption to saturation at 313 K for 20Fe1K1Pt-ALa-705. The observed TPD profile was fitted with 6 Lorentzian type peaks

Table 4-1: Peak centers for the Lorentzians used to fit CO TPD after CO adsorption to saturation at 313 K, 423 K, and 448 K respectively for 20Fe1K1Pt-ALa-705

$T_{CO\ ad}$ (K)	**Peak position (K)**					
	(1)	**(2)**	**(3)**	**(4)**	**(5)**	**(6)**
313	443	513	626	738	821	927
423	524	657	634	731	812	924
448	539	577	632	721	821	933

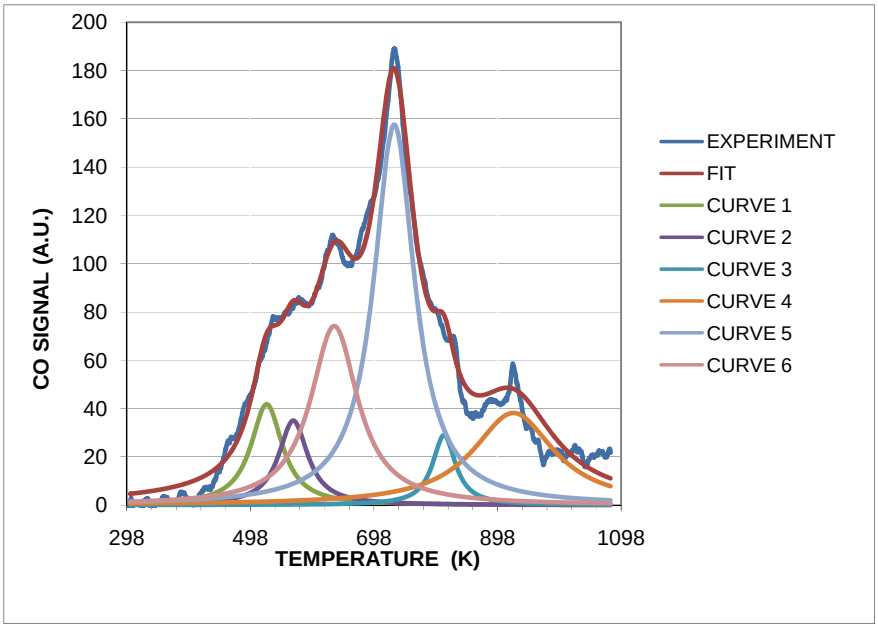

Figure 4-3: CO TPD after CO adsorption to saturation at 423 K for 20Fe1K1Pt-ALa-705. The observed TPD profile was fitted with 6 Lorentzian type peaks

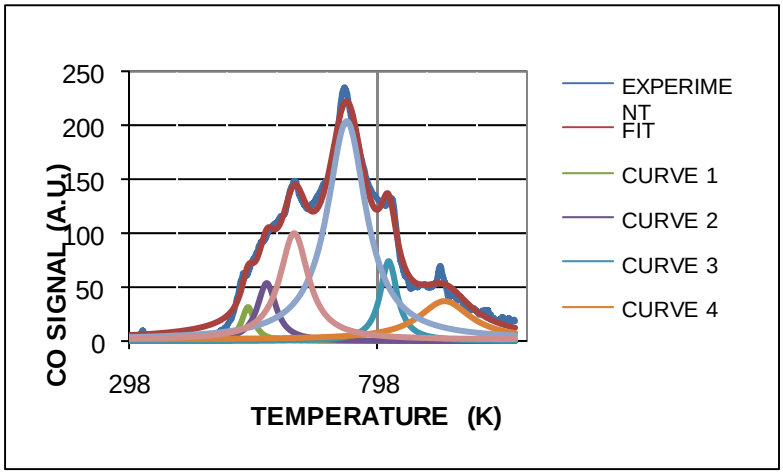

Figure 4-4: CO TPD after CO adsorption to saturation at 448 K for 20Fe1K1Pt-ALa-705. The observed TPD profile was fitted with 6 Lorentzian type peaks

Inspection of the TPD spectra shown above indicates that (1) a larger amount of CO adsorbed molecularly on the catalyst at 313 K than at the higher temperatures; (2) CO dissociation was more significant as adsorption temperature increased; (3) shifts in the temperature at peak maxima indicate that the overall desorption process may not be first order especially considering that some adsorbed CO dissociated as well as reacted with adsorbed O to form CO_2.

4.1.1 Determination of CO heat of adsorption for 20Fe1K1Pt-ALa-705

Two classical methods of calculating heats of adsorption from TPD spectra (free re-adsorption method and peak width analysis) as published by Falconer and Schwartz [124] were used to calculate CO heats of adsorption from the CO TPD spectra shown above. In order to apply the classical methods of calculating heats of adsorption to the CO TPD spectra above, the first Lorentzian peaks assigned to the desorption of molecularly adsorbed CO obtained at the respective adsorption temperatures were used (see Figure 4-5). For the free re-adsorption method, Figure 4-6 shows plots of 1/T vs ln(rate) at CO surface coverages of 0.7, 0.8, and 0.9 respectively. The slope of each of the lines multiplied by the gas constant gives the CO heat of adsorption at that coverage. The slopes and corresponding CO heats of adsorption for the three coverages are tabulated in Table 4-2. Based on the above method, CO heats of adsorption were found to range from -88.1 kJ/mol to -54.1 kJ/mol for fractional coverages 0.9 to 0.7. Using the temperature at a peak maximum (T_p) of 443 K and a full-width-at-half-maximum ($W_{1/2}$) of 60.2 K (both corresponding to the first Lorentzian peak for CO adsorption at 313 K) the CO heat of adsorption (ΔH_{ads}) was calculated based on peak width analysis method

for second order in Equation 4.2 was found to be -88.6 kJ/mol. This value is in close agreement with that calculated from the free-re-adsorption method at 0.9 fractional coverage. However, the calculated trend of increasing CO heat of adsorption with increasing CO surface coverage based on the free-re-adsorption method is the reverse of what is expected based on theory, and it is probably not correct. The likely reason for this reversal in trend will be addressed in Chapter 6.

$$\Delta H_{ads} = R_g \cdot T_p \cdot 2 \cdot \left[-1 + \left(1 + \frac{3.117 \cdot T_P^2}{W_{1/2}} \right)^{1/2} \right] \tag{4.2}$$

Table 4-2: CO heat of adsorption at three surface coverages (0.7, 0.8, and 0.9 respectively) for 20Fe1K1Pt-ALa-705 calculated using the method of free re-adsorption.

Coverage	**Slope**	**ΔH(kJ/mol)**
0.7	-6503.5	-54.1
0.8	-8137.3	-67.7
0.9	-10595.4	-88.1

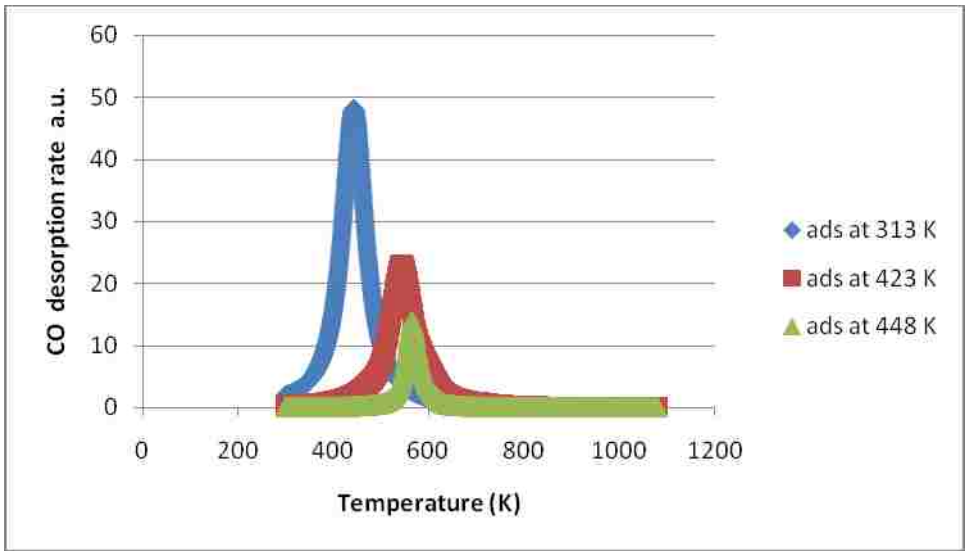

Figure 4-5: Overlay of CO desorption rate spectra of the first Lorentzian peak corresponding to desorption of molecularly adsorbed CO after adsorption at 313 K, 423 K and 448 K respectively for 20Fe1K1Pt-ALa-705.

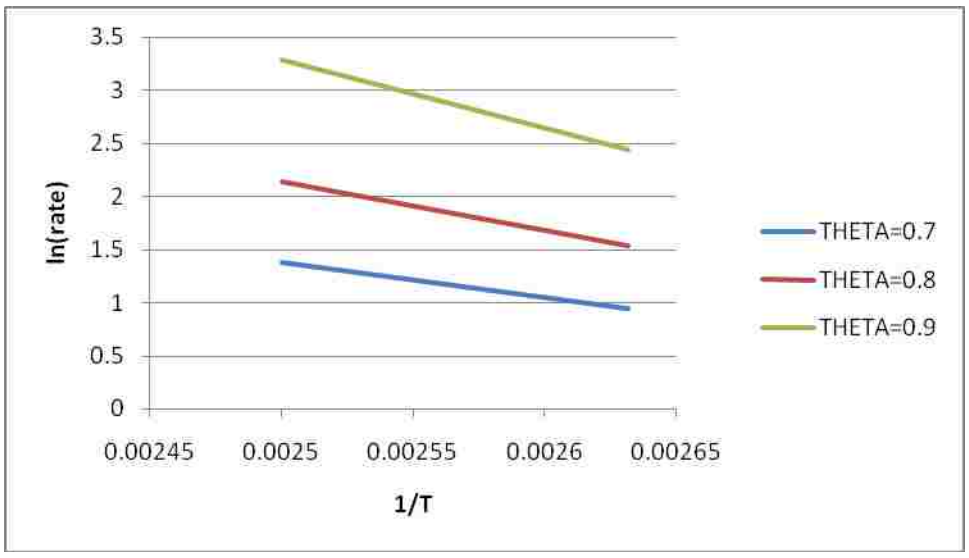

Figure 4-6: Plot of 1/T vs ln(rate) at 0.7, 0.8, and 0.9 fractional coverages used to calculate CO heat of adsorption as a function of coverage for 20Fe1K1Pt-ALa-705. CO heat of adsorption at the respective surface coverage is obtained by multiplying the slope of the line corresponding to that coverage by the gas constant.

4.2 Microkinetic Model of CO TPD

A microkinetic model of CO TPD was developed from TPD data obtained after CO was adsorbed on 99Fe1ALa-307 at room temperature based on the analysis of the measure CO and CO_2 TPD profiles.

4.2.1 Model development

At room temperature and atmospheric pressure, CO adsorbs molecularly on Fe. Previous studies [61, 129] teach that during TPD of CO from porous Fe catalysts: (1) adsorbed CO is in equilibrium with gas phase CO and hence at relatively low temperatures (300-400 K) a significant fraction of adsorbed molecular CO desorbs as gas phase CO; (2) above a temperature of about 400-450 K a fraction of the adsorbed CO dissociates to C and O atoms; (3) at significantly higher temperatures (500-600 K) a fraction of the dissociated O combines with adsorbed CO to form CO_2 and (4) at even higher temperatures (700-900 K) C and O atoms recombine to molecular CO which desorbs as gaseous CO. A possible sequence of elementary steps describing the above process is shown in Equations 4.3 to 4.6 below:

$$CO^* \leftrightarrow CO_{(g)} + * \tag{4.3}$$

$$CO^* + * \leftrightarrow C^* + O^* \tag{4.4}$$

$$CO^* + O^* \leftrightarrow CO_2^{**} \tag{4.5}$$

$$CO_2^{**} \leftrightarrow CO_{2(g)} + 2^* \tag{4.6}$$

Since the observed profiles of CO and CO_2 at the reactor outlet is a convolution of the reactor flow characteristics and the reaction kinetics, it is important to incorporate the

characteristics of the reactor in the model development. In the sections below, generalized models for two ideal reactor types – CSTR and PFR – will be presented following which it will be specifically applied to CO TPD.

4.2.1.1 CSTR Model

For an isothermal CSTS with constant volume, the unsteady- state mass balance for a gas phase species is given by:

accumulation = input – output + generation (4.7)

$$\frac{dC_A}{dt} = \frac{C_A^0 - C_A}{\tau} + r_A''' \tag{4.8}$$

where C_A (mol/m^3) is the concentration of species *A* in the reactor, C_A^0 (mol/m^3) is inlet concentration of species *A*, t (s) is time, τ (s) is reactor residence time and r_A''' is the observed rate of formation of species *A* (mol/m^{3}s). If film and pore diffusion resistances are negligible, then, r_A''' can be approximated to be the intrinsic reaction rate. During a TPD experiment the feed is an inert carrier gas containing no *A*. This implies that C_A^0 is equal to zero. As such, Equation 4.8 becomes:

$$\frac{dC_A}{dt} = \frac{-C_A}{\tau} + r_A''' \tag{4.9}$$

If the rates of the elementary reactions are expressed in turn-over-frequency units (s^{-1}), then Equation 4.9 can be written as:

$$\frac{dC_A}{dt} = \frac{-C_A}{\tau} + \frac{M_{loading} \cdot D \cdot \rho_b \cdot r_A}{\varepsilon_b \cdot M_W} \tag{4.10}$$

where $M_{loading}$ is the fraction of active metal loading in the catalyst, D is the dispersion of the catalyst, ρ_b (kg/m^3) is the reactor bed density, r_A is the reaction rate of A (s^{-1}), ε_b is the reactor bed void fraction, and M_W is the atomic weight of the active catalyst material.

By writing C_A in terms of the partial pressure of A, Equation 4.10 can be written as:

$$\frac{d}{dt}\left(\frac{p_A}{RT}\right) = \frac{-1}{\tau}\left(\frac{p_A}{RT}\right) + \frac{M_{loading} \cdot D \cdot \rho_b \cdot r_A^{'}}{\varepsilon_b \cdot M_W} \tag{4.11}$$

Here, p_A is the partial pressure of A (Pa), R (J/mol K), and T (K) is the reactor temperature. Expanding the derivative on the left-hand-side of Equation 4.11 results in:

$$\frac{1}{RT}\frac{dp_A}{dt} - \frac{p_A}{RT^2}\frac{dT}{dt} = \frac{-1}{\tau}\left(\frac{p_A}{RT}\right) + \frac{M_{loading} \cdot D \cdot \rho_b \cdot r_A^{'}}{\varepsilon_b \cdot M_W} \tag{4.12}$$

During TPD, the temperature is ramped at a constant rate β (K/s). If T^0 (K) is the initial reactor temperature, then the temperature at anytime is given by:

$$T = T^0 + \beta t \tag{4.13}$$

and

$$\frac{dT}{dt} = \beta \tag{4.14}$$

The differential variable in Equation 4.12 can be transformed from t to T by recognizing that:

$$\frac{dp_A}{dt} = \frac{dp_A}{dT} \cdot \frac{dT}{dt} \Rightarrow \frac{dp_A}{dt} = \beta \frac{dp_A}{dT} \tag{4.15}$$

Substituting Equation 4.15 into Equation 4.12 and simplifying, the expression in Equation 4.16 is obtained.

$$\frac{dp_A}{dT} = p_A\left(\frac{1}{T} - \frac{1}{\beta \cdot \tau}\right) + \frac{R \cdot T \cdot M_{loading} \cdot D \cdot \rho_b \cdot r_A}{\varepsilon_b \cdot M_W \cdot \beta} \tag{4.16}$$

Equation 4.16 describes the desorption rate of *A* in terms of its partial pressure as a function of temperature during TPD. This equation can be written in terms of the gas phase mole fraction of species A and total pressure (see Equation 4.17) and in terms of the normalized gas phase mole fraction for the same species (see Equation 4.18).

$$\frac{dy_A}{dT} = y_A\left(\frac{1}{T} - \frac{1}{\beta \cdot \tau}\right) + \frac{R \cdot T \cdot M_{loading} \cdot D \cdot \rho_b \cdot r_A}{\varepsilon_b \cdot M_W \cdot \beta \cdot P_{tot}} \tag{4.17}$$

$$\frac{dY_A}{dT} = Y_A\left(\frac{1}{T} - \frac{1}{\beta \cdot \tau}\right) + \frac{R \cdot T \cdot M_{loading} \cdot D \cdot \rho_b \cdot r_A}{\varepsilon_b \cdot M_W \cdot \beta \cdot P_{tot} \cdot Y_{A_{\max}}} \tag{4.18}$$

$$y_A = Y_A \cdot Y_{A_{\max}} \tag{4.19}$$

Here Y_A is the normalized mole fraction of species A while $Y_{A_{\max}}$ is the maximum observed mole fraction of A. P_{tot} (Pa) is the total reactor pressure.

From a material balance for an adsorbed species *A* on the catalyst surface,

$$\frac{d\theta_A}{dt} = r_A \tag{4.20}$$

θ_A is the fractional coverage of *A*. By applying the transformation used in Equation 4.12, Equation 4.20 becomes:

$$\frac{d\theta_A}{dT} = \frac{r_A}{\beta} \tag{4.21}$$

If the kinetic parameters are known, then Equations 4.18, 4.21, and the site balance can be integrated simultaneously with the initial conditions shown in Equation 4.22 to obtain the TPD profile for species A.

$$\begin{aligned} y_A\left(T^0\right) &= 0 \\ \theta_A\left(T^0\right) &= \theta_A^0 \end{aligned} \tag{4.22}$$

Here θ_A^0 is the initial surface coverage of A at the beginning of the TPD experiment. Alternatively, kinetic parameters can be estimated from experimental TPD data by a curve fitting algorithm that calculates values of the dependent variable (y_A) from Equations 4.18 and 4.21 (in conjunction with an appropriate site balance) by initially guessing and then optimizing the values of the kinetic parameters.

4.2.1.2 PFR Model

The isothermal unsteady state mass balance for a PFR can be written as:

$$\frac{\partial C_A}{\partial t} = \frac{-u(t)}{L}\frac{\partial C_A}{\partial z} + \frac{M_{loading} \cdot D \cdot \rho_b \cdot r_A}{\varepsilon_b \cdot M_W} \tag{4.23}$$

$$\frac{\partial C_A}{\partial t} = \frac{-1}{\tau}\frac{\partial C_A}{\partial z} + \frac{M_{loading} \cdot D \cdot \rho_b \cdot r_A}{\varepsilon_b \cdot M_W} \tag{4.24}$$

Here $u(t)$ is the gas velocity (m/s), L (m) is the catalyst bed length, z (m) is the reactor axial dimensionless distance, and $\tau = u(t)/L$.

Applying similar transformations and simplifications described in Section 4.2.1.1, Equation 4.24 reduces to:

$$\frac{\partial y_A}{\partial T} = -\frac{1}{\beta \cdot \tau}\frac{\partial y_A}{\partial z} + \frac{y_A}{T} + \frac{R \cdot T \cdot M_{loading} \cdot D \cdot \rho_b \cdot r_A}{\varepsilon_b \cdot M_W \cdot \beta \cdot P_{tot} \cdot Y_{A_{\max}}} \tag{4.25}$$

As in the case of CSTR model, if the kinetic parameters are known, then Equations 4.21, 4.25 and the site balance can be integrated simultaneously with the initial and boundary conditions in Equation 4.26 to obtain the TPD profile for species *A*.

$$\begin{aligned} y_A\left(T^0, z\right) &= 0 \\ \theta_A\left(T^0\right) &= \theta_A^0 \end{aligned} \tag{4.26}$$

4.2.1.3 Application to CO TPD

After CO adsorption to saturation at room temperature and 1 atm pressure on 99Fe1ALa-307, CO TPD was carried out as explained in Section 3.6.1. The observed thermograms of CO and CO_2 were recorded simultaneously. The analysis of the thermograms to obtain a microkinetic model for CO TPD is presented in this section. Model characteristics and assumptions include (1) the reactor operates in plug flow, (2) external mass transfer and pore diffusion resistances are negligible, (3) all reaction steps are reversible, (4) temperature gradients within the catalyst bed can be neglected, (5) the catalyst surface consists of more than one uniform energetic site perhaps due to varying proportions of edge and corner sites or interactions between Al_2O_3 with Fe, and (6) adsorption energies were non-activated. In addition, quasi-equilibrium was not assumed while coverage and temperature effects on heats of adsorption and pre-exponential factors were not considered.

For the elementary steps given in Equations 4.3 to 4.6, assuming sites of uniform energy, the net reaction rates in Arrhenius form are as follows:

$$r_1 = A_{1f} \cdot \exp\left(-\frac{E_{1f}}{R \cdot T}\right) \cdot \theta_{CO} - A_{1r} \cdot \exp\left(-\frac{E_{1r}}{R \cdot T}\right) \cdot P_{tot} \cdot y_{CO} \cdot Y_{CO_{\max}} \cdot \theta_V \tag{4.27}$$

$$r_2 = A_{2f} \cdot \exp\left(-\frac{E_{2f}}{R \cdot T}\right) \cdot \theta_{CO} \cdot \theta_V - A_{2r} \cdot \exp\left(-\frac{E_{2r}}{R \cdot T}\right) \cdot \theta_C \cdot \theta_O \tag{4.28}$$

$$r_3 = A_{3f} \cdot \exp\left(-\frac{E_{3f}}{R \cdot T}\right) \cdot \theta_{CO} \cdot \theta_O - A_{3r} \cdot \exp\left(-\frac{E_{3r}}{R \cdot T}\right) \cdot \theta_{CO_2} \tag{4.29}$$

$$r_4 = A_{4f} \cdot \exp\left(-\frac{E_{4f}}{R \cdot T}\right) \cdot \theta_{CO_2} - A_{4r} \cdot \exp\left(-\frac{E_{4r}}{R \cdot T}\right) \cdot P_{tot} \cdot y_{CO_2} \cdot Y_{CO_{2\max}} \cdot \theta_V^2 \tag{4.30}$$

For the gas phase species CO and CO_2, the following mass balance equations are obtained:

$$\frac{\partial y_{CO}}{\partial T} = -\frac{1}{\beta \cdot \tau}\frac{\partial y_{CO}}{\partial z} + \frac{y_{CO}}{T} + \frac{R \cdot T \cdot M_{loading} \cdot D \cdot \rho_b \cdot r_1}{\varepsilon_b \cdot M_W \cdot \beta \cdot P_{tot} \cdot Y_{CO_{\max}}} \tag{4.31}$$

$$\frac{\partial y_{CO_2}}{\partial T} = -\frac{1}{\beta \cdot \tau}\frac{\partial y_{CO_2}}{\partial z} + \frac{y_{CO_2}}{T} + \frac{R \cdot T \cdot M_{loading} \cdot D \cdot \rho_b \cdot r_4}{\varepsilon_b \cdot M_W \cdot \beta \cdot P_{tot} \cdot Y_{CO_{2\max}}} \tag{4.32}$$

For chemisorbed surface species, the following set of mass balance equations is obtained:

$$\frac{d\theta_{CO}}{dT} = \frac{\left(-r_1 - r_2 - r_3\right)}{\beta} \tag{4.33}$$

$$\frac{d\theta_C}{dT} = \frac{r_2}{\beta} \tag{4.34}$$

$$\frac{d\theta_O}{dT} = \frac{\left(-r_2 - r_3\right)}{\beta} \tag{4.35}$$

$$\frac{d\theta_{CO_2}}{dT} = \frac{\left(-r_3 - r_4\right)}{\beta} \tag{4.36}$$

And,

$$\tau = \tau^0 \cdot \left(\frac{T^0}{T}\right) \tag{4.37}$$

A_{1f}, A_{1r},…, A_{4r} are the pre-exponential factors for Reactions 1 through 4 with units of (1/s) for surface reactions and (1/(Pa s) for gas phase reactions. E_{1f}, E_{1r}, …, E_{4r} are the activation energies for Reactions 1 through 4 with units of (J/mol). τ^0 is the space time at $T = T^0$ while θ_V is the fraction of vacant sites.

To estimate kinetic parameters for CO, TPD on 99Fe1ALa-307, two sites of uniform energy (designated α_1 and α_2) were assumed implying that additional equations similar to Equations 4.27 to 4.30 and Equations 4.33 to 4.36 are needed to account for the rates and species coverages on the α_2 sites. A numerical method of lines was used to solve the resulting sets of partial differential equations, ordinary differential equations, and algebraic equations by discretizing the space variable into a uniform grid size using backward-difference approximations, and subsequently integrating the resulting system of first order differential equations with a robust stiff ODE solver – DVODE (developed by Livermore National Labs [161]) – while the kinetic parameters were estimated by multi-response regression using an orthogonal distance regression routine (DODRPACK [162]) by minimizing the objective function $\Psi(\phi)$ in Equation 4.38.

$$\Psi(\phi) = \sum_{i=1}^{n} w_{\varepsilon_i} \left(y_i - f(T_i, \phi) \right)^2 \tag{4.38}$$

Where y_i is the set of observed or experimentally measured normalized mole fractions of CO and CO_2 respectively at each temperature point, $f(T_i, \phi)$ is the set of predicted normalized mole fractions of CO and CO_2 at the same temperature point as y_i, ϕ is a vector of activation energies and pre-exponential factors to be estimated, and w_{ε_i} is the set of weighted errors in the observed response variables (y_{CO} and y_{CO2}).

The data analysis procedure can be summarized as follows:

1. Make initial guesses of the kinetic parameters i.e. activation energies and pre-exponential factors for all the reaction steps.
2. With the guessed parameters, use DVODE to integrate the discretized forms of Equations 4.27 through 4.37.
3. Check whether $\Psi(\phi)$ in Equation 4.38 is minimized. If yes, then the values of the guessed parameters have been successfully estimated. If not, use DODR to refine the guesses and repeat Steps 2 and 3 until $\Psi(\phi)$ is minimized.

A Fortran routine that implements this process is listed in the Appendix A.7.

Figure 4-7 and Figure 4-8 show the observed normalized mole fractions of CO and CO_2 in comparison with that predicted by the model; Figure 4-9 shows the calculated surface coverages of CO, C, O, and CO_2. Table 4-3 lists the estimated pre-exponential factors, activation energies, and their respective 95% confidence intervals for the

elementary steps for α_1 and α_2 sites respectively. The results indicated an average ΔH_{ads} values of CO on α_1 and α_2 sites of -50 and -36.1 kJ/mol respectively, while the surface coverage of C rose from 0 at the beginning of desorption to a maximum value of 0.9 at about 550 K and thereafter plateau to 0.19 at about 1000 K. Similarly, O coverage rose from 0 initial coverage to a max value of 0.3 at about 600 K, but fell back to 0 after about 1000 K. The reason C coverage approached an asymptotic value after 1000 K was because there was no more O on the surface to combine with to form CO.

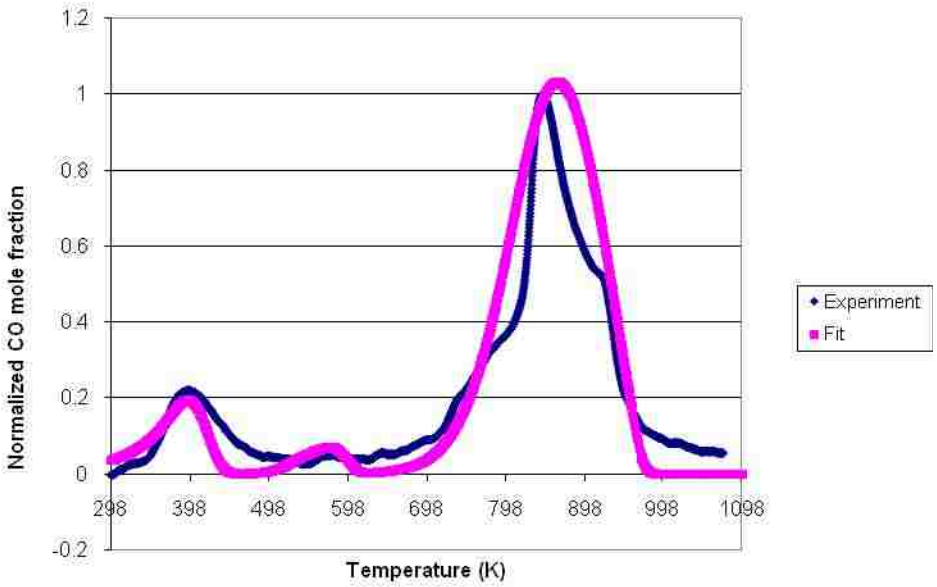

Figure 4-7: Observed normalized CO mole fraction during TPD after CO adsorption to saturation at 297K for 99Fe1ALa-307 in comparison to model prediction. This was used to develop CO TPD microkinetic model

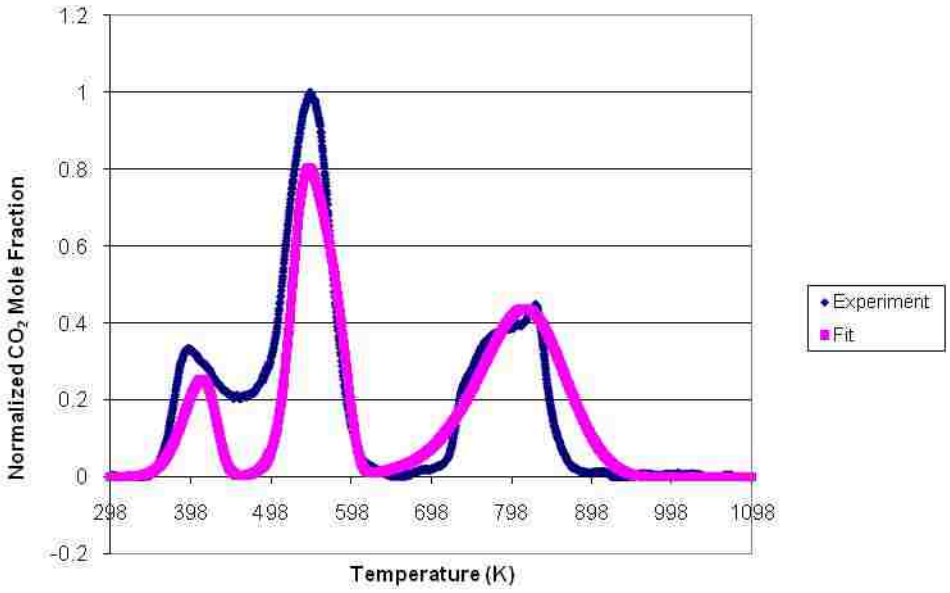

Figure 4-8: Observed normalized CO_2 mole fraction during TPD after CO adsorption to saturation at 297K for 99Fe1ALa-307 in comparison to model prediction. This was used to develop CO TPD microkinetic model

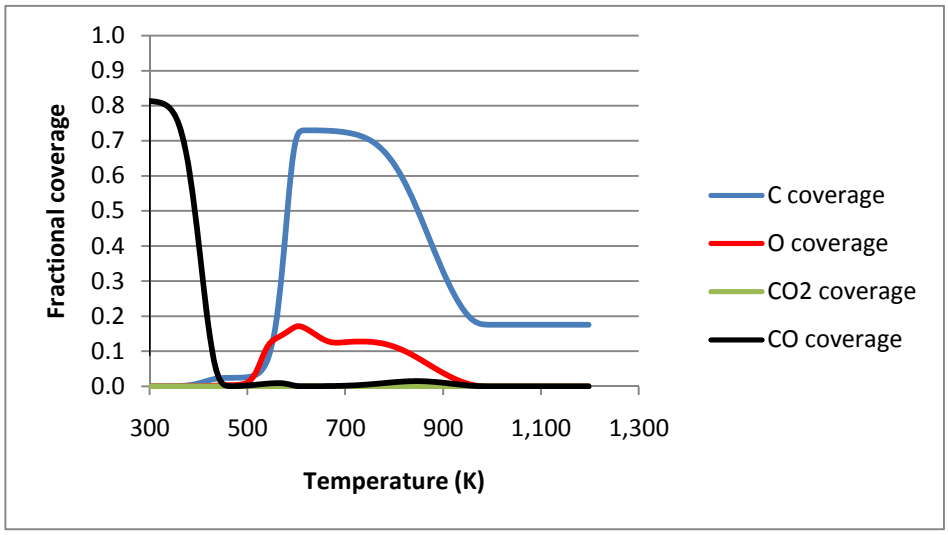

Figure 4-9: Calculated surface coverages as a function of temperature for CO (site 2), C, O, and CO_2 during CO TPD on 99Fe1ALa-307 after adsorption to saturation at 297 K.

Table 4-3: Estimated kinetic parameters and their 95% confidence intervals for each elementary step. CO adsorption was at room temperature and pressure. TPD was at atmospheric pressure. The confidence intervals are given in parenthesis. Initial CO coverage for α_1 and α_2 sites was estimated to be 0.09 and 0.81 respectively

Reaction	A_f[a]	A_r[a]	E_f (J/mol)	E_r (J/mol)	Remarks
$CO^* \leftrightarrow CO_{(g)} + *$	1.53E+12 (1.52E+12 TO 1.54E+12)	8.20E-01 (8.13E-01 TO 8.26E-01)	5.00E+04 (4.96E+04 TO 5.04E+04)	0.00E+00	
$CO^* + * \leftrightarrow C^* + O^*$	1.84E+13 (1.83E+13 TO 1.85E+13)	5.81E+13 (5.72E+13 TO 5.89E+13)	8.94E+04 (8.90E+04 TO 8.99E+04)	1.90E+05 (1.89E+05 TO 1.91E+05)	ΔH_{ads} = -50 kJ/mol α_1 site
$CO^* + O^* \leftrightarrow CO_2^{**}$	2.75E+09 (2.73E+09 TO 2.76E+09)	1.04E+13 (1.04E+13 TO 1.05E+13)	3.82E+04 (3.79E+04 TO 3.85E+04)	3.17E+04 (3.15E+04 TO 3.19E+04)	
$CO_2^{**} \leftrightarrow CO_{2_{(g)}} + 2^*$	1.03E+13 (1.03E+13 TO 1.04E+13)	1.73E-01 (1.72E-01 TO 1.74E-01)	9.02E+03 (8.96E+03 TO 9.08E+03)	0.00E+00	
$CO^* \leftrightarrow CO_{(g)} + *$	1.19E+06 (1.18E+06 TO 1.20E+06)	5.20E-01 (5.16E-01 TO 5.24E-01)	3.61E+04 (3.58E+04 TO 3.63E+04)	0.00E+00	
$CO^* + * \leftrightarrow C^* + O^*$	1.26E+06 (1.25E+06 TO 1.26E+06)	6.57E+13 (6.49E+13 TO 6.65E+13)	5.46E+04 (5.43E+04 TO 5.49E+04)	1.60E+05 (1.59E+05 TO 1.61E+05)	ΔH_{ads} = -36.1 kJ/mol α_2 site
$CO^* + O^* \leftrightarrow CO_2^{**}$	2.50E+12 (2.47E+12 TO2.52E+12)	1.38E+13 (1.37E+13 TO 1.39E+13)	1.23E+05 (1.23E+05 TO 1.24E+05)	1.19E+05 (1.19E+05 TO 1.20E+05)	
$CO_2^{**} \leftrightarrow CO_{2_{(g)}} + 2^*$	2.85E+04 (2.83E+04 TO 2.87E+04)	3.59E-01 (3.57E-01 TO 3.62E-01)	3.53E+03 (3.49E+03 TO 3.56E+03)	0.00E+00	

[a] Units = [1/s] for surface reaction and [$(Pa\ s)^{-1}$] for gas phase reaction

4.2.1.4 Test of Robustness of CO TPD Microkinetic Model

To check the robustness of the CO TPD microkinetic model developed above, CO TPD after adsorption to saturation at 313 K and at 1 atm was carried out on 99Fe1ALa-307. A comparison of the ratio of the magnitude of the first CO desorption peak after CO adsorption at room temperature to that obtained after CO adsorption at 313 K suggests a significant reduction in the initial CO coverage at 313 K. Hence to apply the model to this particular experiment, estimates of initial CO, C, and O coverages were made based on the analysis of the relative magnitudes of the first CO peak. Figure 4-10 and Figure 4-11 show the observed normalized mole fractions of CO and CO_2 in comparison with those predicted by the model. Examination of these profiles indicates that the model was fairly able to predict both CO and CO_2 TPD mole fraction profiles.

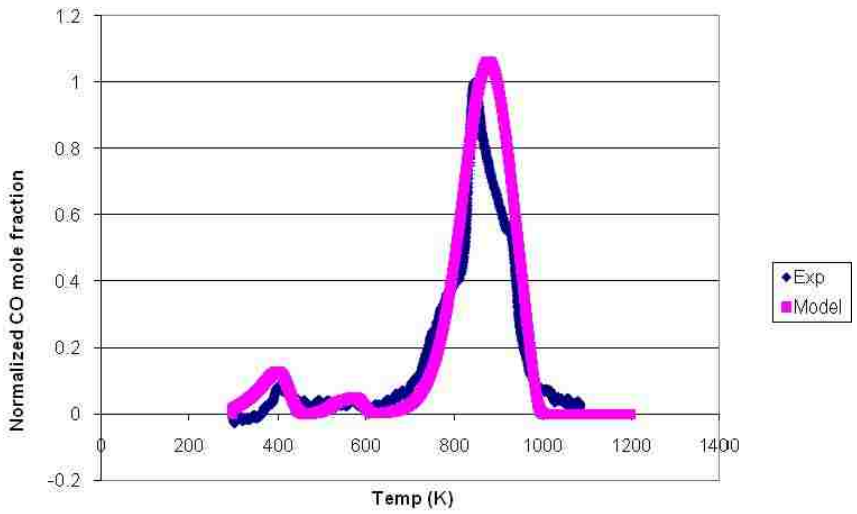

Figure 4-10: Observed and model predicted (based on the microkinetic model developed in Section 4.2.1.3) CO TPD profiles after adsorption to saturation at 313K for 99Fe1ALa-307

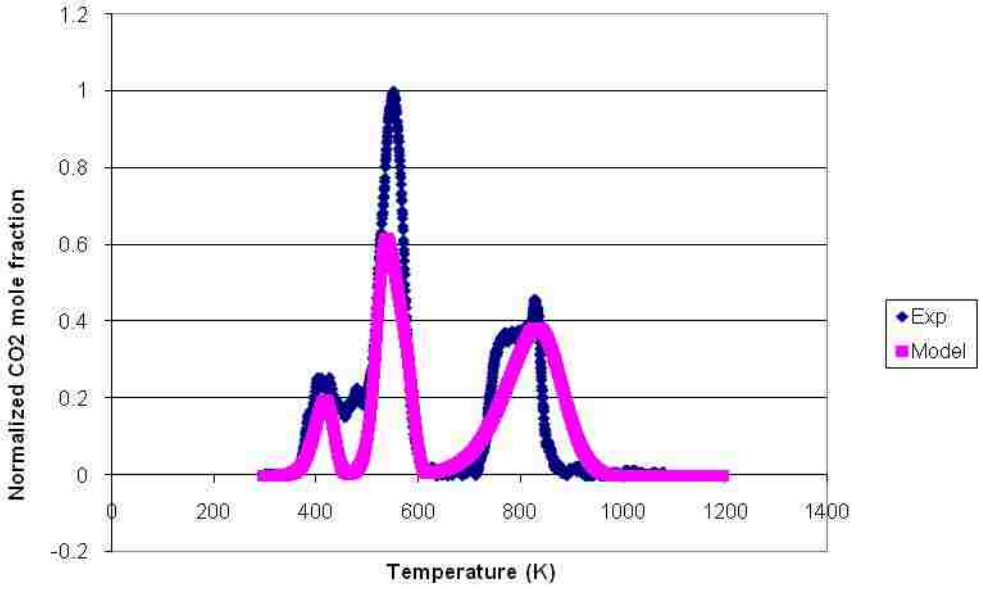

Figure 4-11: Observed and model predicted (based on the microkinetic model developed in Section 4.2.1.3) CO_2 TPD profiles after adsorption to saturation at 313K for 99Fe1ALa-307

4.3 Results of TPH for 99Fe1ALa-307

Temperature-programmed hydrogenation of stable surface species after Fischer-Tropsch synthesis at 1 atm on 99Fe1ALa-307 was carried out as described in Section 3.6.3. Observed reactor products included CH_4, H_2O, CO, and un-reacted H_2. However, within the limits of detection of the UTI 100 mass analyzer used in this study, CO_2 production was insignificant. Most of the water produced was trapped out before the reactor effluent was sent to the mass analyzer to avoid damaging the ionizer filaments. Methane mole fraction is shown as a function of temperature following FTS at 448 K, 473 K, and 493 K, respectively, in Figure 4-12 while the observed CO signal as a function of temperature is shown in Figure 4-13.

Inspection of CH_4 mole fraction profiles in Figure 4-12 indicates (1) a right-shift in methane peak maxima and an increase in peak intensity with increasing initial FTS reaction temperatures from 448 K to 493 K (meaning that the overall reaction order is not unity); (2) broad and overlapping spectra with two visible peak maxima at 710 K and 790 K for the spectrum corresponding to an initial FTS temperature of 448 K; and (3) formation of multiple carbon species or forms that are more difficult to hydrogenate increases with increasing FTS temperature.

Similarly, inspection of CO profile in Figure 4-13 reveals overlapping peaks with maxima at 494 K and 690 K for the three initial FTS reaction temperatures, and thereafter, a right-shift in the peak maxima in the region from 750 K to 940 K. The observed first CO peak (with maxima at 494 K) for each of the CO profiles following FTS is assigned to desorption of molecularly adsorbed CO by comparison to the CO TPD shown in Figure 4-7 (the difference in the peak location from 398 K in Figure 4-7 to 494 K in Figure 4-13 was due to difference in the desorption/reaction temperature ramp rate, and the initial CO coverage. The CO peak with a maximum beginning at 690 K is due to the recombination of C and O.

4.4 Result of TPH on 20Fe1K1Pt-ALa-705

Temperature-programmed hydrogenation of stable surface species after Fischer-Tropsch synthesis at 1 atm at 398 K, 438 K and 448 K, respectively, on 20Fe1K1Pt-ALa-705 was carried out as described in Section 3.6.3. Figure 4-14 shows the observed methane profiles as a function of initial FTS temperatures while Figure 4-15 shows the corresponding CO profiles. CO desorption peaks maxima are observed at 475 K, 488 K and 490 K after FTS at 398 K, 438 K and 448 K respectively. These peaks are due to

desorption of molecularly adsorbed CO since these values correlate to the ones observed for Peak 1 during CO TPD on the same catalyst as shown on Table 4-1. The differences in the values observed during CO TPD and during TPH are due to different initial CO coverages and temperature ramp rates. Examination of the CH_4 and CO profiles for this catalyst reveals observations similar to that on 99Fe1ALa-307 listed in Section 4.3 such as a right-shift in methane peak maxima and increase in peak intensity with increasing initial FTS reaction temperature, broad and overlapping spectra, and the formation of multiple carbon species or forms that are more difficult to hydrogenate increases with increasing FTS temperature.

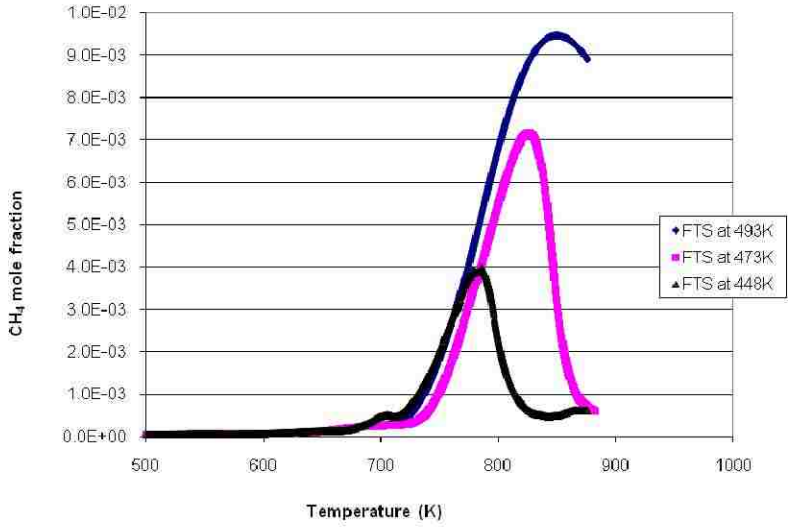

Figure 4-12: Methane mole fraction as a function of temperature obtained during temperature-programmed hydrogenation of stable surface species after FTS for 5 min at 448 K, 473 K, and 493 K, respectively, at 1 atm pressure at 22.6°C/min temperature ramp rate for 99Fe1ALa-307.

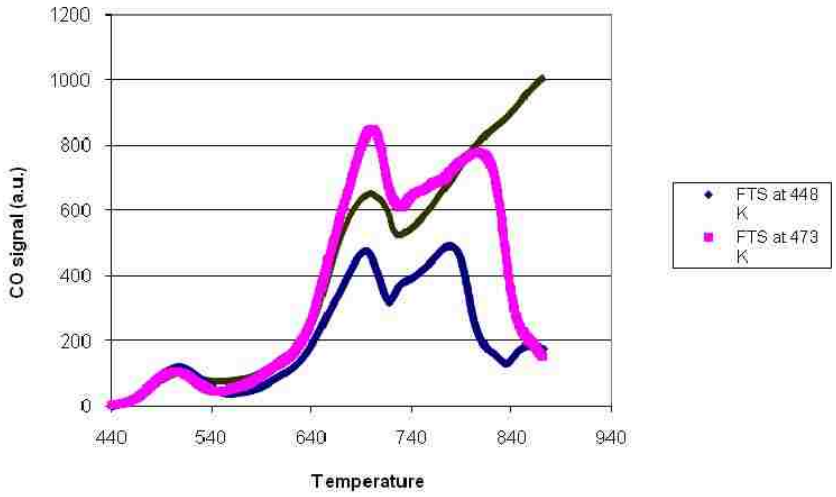

Figure 4-13: CO signal as a function of temperature obtained during temperature-programmed hydrogenation of stable surface species after FTS for 5 min at 448 K, 473 K, and 493 K, respectively, at 1 atm pressure at 22.6°C/min temperature ramp rate for 99Fe1ALa-307.

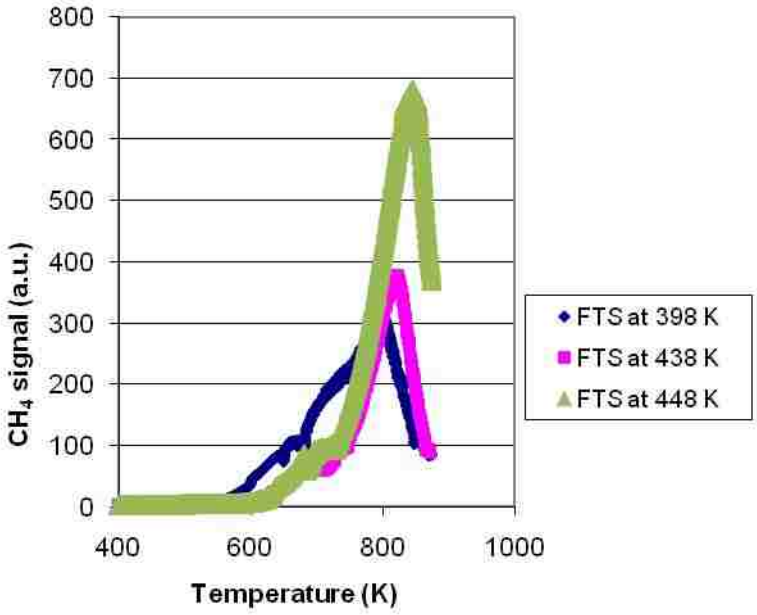

Figure 4-14: Methane signal as a function of temperature obtained during temperature-programmed hydrogenation of stable surface species after FTS for 5 min at 398 K, 438 K, and 448 K respectively at 1 atm pressure at 22.6°C/min temperature ramp rate for 20Fe1K1Pt-ALa-705.

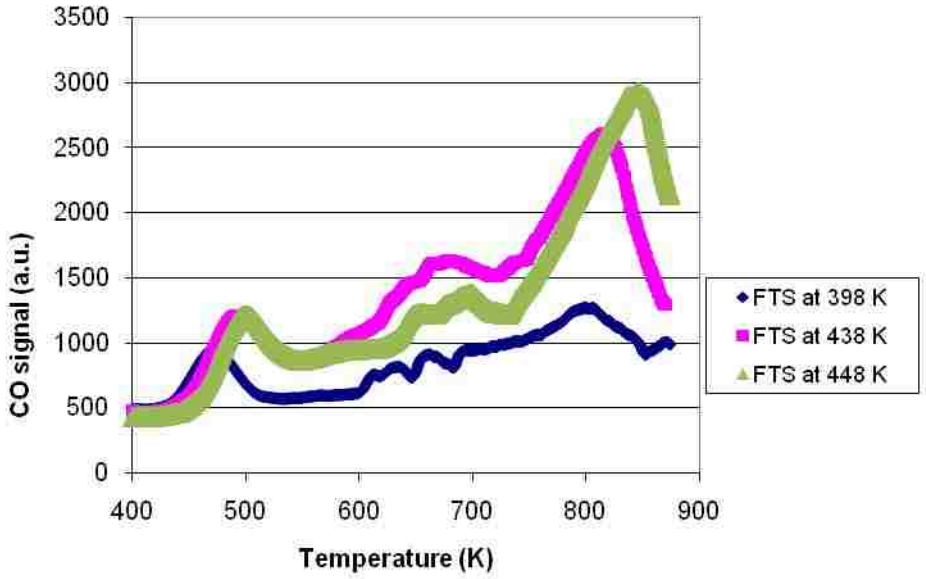

Figure 4-15: CO signal as a function of temperature obtained during temperature-programmed hydrogenation of stable surface species after FTS for 5 min at 398 K, 438 K, and 448 K respectively at 1 atm pressure at 22.6°C/min temperature ramp rate for 20Fe1K1Pt-ALa-705.

4.5 Results of ITH on 99Fe1ALa-307

Isothermal hydrogenation following FTS on 99Fe1ALa-307 for 5 min at 1 atm pressure and 448 K and 458 K, respectively, was performed as described in Section 3.6.2. The observed CH_4 mole fraction profile was used to develop a microkinetic model for hydrogenation of stable surface species on polycrystalline Fe.

4.5.1 Microkinetic model of ITH on polycrystalline Fe

As described previously, CH_4, CO, H_2O and H_2 were observed as gas phase species leaving the reactor during ITH. However, no CO_2 was observed during the ITH experiments in this study. After FTS reaction for 5 min and a reactor purge with He to

evacuate gas phase species, it was assumed that the significant stable surface species remaining on the catalyst surface included C, CO, and O respectively. The initial coverage of H_2O after the purge was assumed to be negligible because of its relatively low heat of adsorption. Similarly, initial H coverage was assumed negligible because the initial FTS reaction was not allowed to reach steady-state; as such the unstable species that were on the surface just after the FTS reaction was stopped, would react with the H on the surface to form gas phase products that were subsequently evacuated from the reactor during the He purge.

If a PFR reactor model is assumed, then the concentration profile for gas phase species *A* at any time at constant temperature and volume is given by Equation 4.24. In terms of mole fraction, Equation 4.24 becomes:

$$\frac{\partial y_A}{\partial t} = -\frac{1}{\tau}\frac{\partial y_A}{\partial z} + \frac{R \cdot T \cdot M_{loading} \cdot D \cdot \rho_b \cdot r_A}{\varepsilon_b \cdot M_W \cdot P_{tot}} \tag{4.39}$$

The symbols in Equation 4.39 are as defined previously in Equations 4.8 to 4.25. Similarly, the change in the fractional coverage for an adsorbed species *i* as a function of time is given by:

$$\frac{d\theta_i}{dt} = r_i \tag{4.40}$$

where θ_i is the fractional coverage of species *i*, and r_i [s^{-1}] is the net rate of formation or disappearance of *i*. Assuming that the sequence of elementary steps shown in Table 4-4 adequately describes the elementary reactions leading to the formation of the gas phase species observed from the hydrogenation of the surface species C, CO, and O, then Equation 4.39 can be written for each gas phase species H_2, CH_4, H_2O, CO, and CO_2

respectively. Similarly, Equation 4.40 is written for the fractional coverages of the surface species C, O, CO, H, CH, CH_2, CH_3, CHO, CH_2O, CH_3O, OH, H_2O, and CO_2 respectively. The resulting equations are shown below:

Net reaction rates (s^{-1}):

$$R_1 = A_{1f} \cdot \exp\left(-\frac{E_{1f}}{R \cdot T}\right) \cdot y_{H_2} \cdot P_{Tot} \cdot \theta_V^2 - A_{1r} \cdot \exp\left(-\frac{E_{1r}}{R \cdot T}\right) \cdot \theta_H^2 \tag{4.41}$$

$$R_2 = A_{2f} \cdot \exp\left(-\frac{E_{2f}}{R \cdot T}\right) \cdot \theta_C \cdot \theta_H - A_{2r} \cdot \exp\left(-\frac{E_{2r}}{R \cdot T}\right) \cdot \theta_{CH} \cdot \theta_V \tag{4.42}$$

$$R_3 = A_{3f} \cdot \exp\left(-\frac{E_{3f}}{R \cdot T}\right) \cdot \theta_{CH} \cdot \theta_H - A_{3r} \cdot \exp\left(-\frac{E_{3r}}{R \cdot T}\right) \cdot \theta_{CH_2} \cdot \theta_V \tag{4.43}$$

$$R_4 = A_{4f} \cdot \exp\left(-\frac{E_{4f}}{R \cdot T}\right) \cdot \theta_{CH_2} \cdot \theta_H - A_{4r} \cdot \exp\left(-\frac{E_{4r}}{R \cdot T}\right) \cdot \theta_{CH_3} \cdot \theta_V \tag{4.44}$$

$$R_5 = A_{5f} \cdot \exp\left(-\frac{E_{5f}}{R \cdot T}\right) \cdot \theta_{CH_3} \cdot \theta_H - A_{5r} \cdot \exp\left(-\frac{E_{5r}}{R \cdot T}\right) \cdot y_{CH_4} \cdot \cdot P_{Tot} \cdot \theta_V^2 \tag{4.45}$$

$$R_6 = A_{6f} \cdot \exp\left(-\frac{E_{6f}}{R \cdot T}\right) \cdot \theta_{CO} \cdot \theta_H - A_{6r} \cdot \exp\left(-\frac{E_{6r}}{R \cdot T}\right) \cdot \theta_{CHO} \cdot \theta_V \tag{4.46}$$

$$R_7 = A_{7f} \cdot \exp\left(-\frac{E_{7f}}{R \cdot T}\right) \cdot \theta_{CHO} \cdot \theta_H - A_{7r} \cdot \exp\left(-\frac{E_{7r}}{R \cdot T}\right) \cdot \theta_{CH_2O} \cdot \theta_V \tag{4.47}$$

$$R_8 = A_{8f} \cdot \exp\left(-\frac{E_{8f}}{R \cdot T}\right) \cdot \theta_{CH_2O} \cdot \theta_H - A_{8r} \cdot \exp\left(-\frac{E_{8r}}{R \cdot T}\right) \cdot \theta_{CH_3O} \cdot \theta_V \tag{4.48}$$

$$R_9 = A_{9f} \cdot \exp\left(-\frac{E_{9f}}{R \cdot T}\right) \cdot \theta_{CH_3O} \cdot \theta_H - A_{9r} \cdot \exp\left(-\frac{E_{9r}}{R \cdot T}\right) \cdot \theta_{CH_3} \cdot \theta_{OH} \tag{4.49}$$

$$R_{10} = A_{10f} \cdot \exp\left(-\frac{E_{10f}}{R \cdot T}\right) \cdot \theta_{CO} \cdot \theta_{O} - A_{10r} \cdot \exp\left(-\frac{E_{10r}}{R \cdot T}\right) \cdot \theta_{CO_2} \cdot \theta_{V} \quad (4.50)$$

$$R_{11} = A_{11f} \cdot \exp\left(-\frac{E_{11f}}{R \cdot T}\right) \cdot \theta_{O} \cdot \theta_{H} - A_{11r} \cdot \exp\left(-\frac{E_{11r}}{R \cdot T}\right) \cdot \theta_{OH} \cdot \theta_{V} \quad (4.51)$$

$$R_{12} = A_{12f} \cdot \exp\left(-\frac{E_{12f}}{R \cdot T}\right) \cdot \theta_{OH} \cdot \theta_{H} - A_{12r} \cdot \exp\left(-\frac{E_{12r}}{R \cdot T}\right) \cdot \theta_{H_2O} \cdot \theta_{V} \quad (4.52)$$

$$R_{13} = A_{13f} \cdot \exp\left(-\frac{E_{13f}}{R \cdot T}\right) \cdot \theta_{H_2O} - A_{13r} \cdot \exp\left(-\frac{E_{13r}}{R \cdot T}\right) \cdot y_{H_2O} \cdot P_{Tot} \cdot \theta_{V} \quad (4.53)$$

$$R_{14} = A_{14f} \cdot \exp\left(-\frac{E_{14f}}{R \cdot T}\right) \cdot \theta_{CO_2} - A_{14r} \cdot \exp\left(-\frac{E_{14r}}{R \cdot T}\right) \cdot y_{CO_2} \cdot P_{Tot} \cdot \theta_{V} \quad (4.54)$$

$$R_{15} = A_{15f} \cdot \exp\left(-\frac{E_{15f}}{R \cdot T}\right) \cdot \theta_{CO} \cdot \theta_{V} - A_{15r} \cdot \exp\left(-\frac{E_{15r}}{R \cdot T}\right) \cdot \theta_{C} \cdot \theta_{O} \quad (4.55)$$

$$R_{16} = A_{16f} \cdot \exp\left(-\frac{E_{16f}}{R \cdot T}\right) \cdot \theta_{CO} \cdot \theta_{H} - A_{16r} \cdot \exp\left(-\frac{E_{16r}}{R \cdot T}\right) \cdot \theta_{C} \cdot \theta_{OH} \quad (4.56)$$

$$R_{17} = A_{17f} \cdot \exp\left(-\frac{E_{17f}}{R \cdot T}\right) \cdot \theta_{CH_3O} \cdot \theta_{V} - A_{17r} \cdot \exp\left(-\frac{E_{17r}}{R \cdot T}\right) \cdot \theta_{CH_3} \cdot \theta_{O} \quad (4.57)$$

$$R_{18} = A_{18f} \cdot \exp\left(-\frac{E_{18f}}{R \cdot T}\right) \cdot \theta_{CO} - A_{18r} \cdot \exp\left(-\frac{E_{18r}}{R \cdot T}\right) \cdot y_{CO} \cdot P_{Tot} \cdot \theta_{V} \quad (4.58)$$

$$R_{19} = A_{19f} \cdot \exp\left(-\frac{E_{19f}}{R \cdot T}\right) \cdot \theta_{CH_2O} \cdot \theta_{H} - A_{19r} \cdot \exp\left(-\frac{E_{19r}}{R \cdot T}\right) \cdot \theta_{CH_2} \cdot \theta_{OH} \quad (4.59)$$

Partial differential equations for gas phase species obtained from mass balance:

$$\frac{\partial y_{H_2}}{\partial t} = -\frac{1}{\tau}\frac{\partial y_{H_2}}{\partial z} - \frac{R \cdot T \cdot M_{loading} \cdot D \cdot \rho_b \cdot R_1}{\varepsilon_b \cdot M_W \cdot P_{tot}} \tag{4.60}$$

$$\frac{\partial y_{CH_4}}{\partial t} = -\frac{1}{\tau}\frac{\partial y_{CH_4}}{\partial z} + \frac{R \cdot T \cdot M_{loading} \cdot D \cdot \rho_b \cdot R_5}{\varepsilon_b \cdot M_W \cdot P_{tot}} \tag{4.61}$$

$$\frac{\partial y_{CO}}{\partial t} = -\frac{1}{\tau}\frac{\partial y_{CO}}{\partial z} + \frac{R \cdot T \cdot M_{loading} \cdot D \cdot \rho_b \cdot R_{18}}{\varepsilon_b \cdot M_W \cdot P_{tot}} \tag{4.62}$$

$$\frac{\partial y_{CO_2}}{\partial t} = -\frac{1}{\tau}\frac{\partial y_{CO_2}}{\partial z} + \frac{R \cdot T \cdot M_{loading} \cdot D \cdot \rho_b \cdot R_{14}}{\varepsilon_b \cdot M_W \cdot P_{tot}} \tag{4.63}$$

$$\frac{\partial y_{H_2O}}{\partial t} = -\frac{1}{\tau}\frac{\partial y_{H_2O}}{\partial z} + \frac{R \cdot T \cdot M_{loading} \cdot D \cdot \rho_b \cdot R_{13}}{\varepsilon_b \cdot M_W \cdot P_{tot}} \tag{4.64}$$

Ordinary differential equations for surface species obtained from mass balance:

$$\frac{d\theta_H}{dt} = 2 \cdot R_1 - R_2 - R_3 - R_4 - R_5 - R_6 - R_7 - R_8 - R_9 - R_{11} - R_{12} - R_{16} \tag{4.65}$$

$$\frac{d\theta_C}{dt} = -R_2 + R_{15} + R_{16} \tag{4.66}$$

$$\frac{d\theta_{CH}}{dt} = R_2 - R_3 \tag{4.67}$$

$$\frac{d\theta_{CH_2}}{dt} = R_3 - R_4 \tag{4.68}$$

$$\frac{d\theta_{CH_3}}{dt} = R_4 - R_5 + R_9 + R_{17} \tag{4.69}$$

$$\frac{d\theta_{CO}}{dt} = -R_6 - R_{15} - R_{16} - R_{18} \tag{4.70}$$

$$\frac{d\theta_{O}}{dt} = -R_{10} - R_{11} + R_{15} + R_{17} \tag{4.71}$$

$$\frac{d\theta_{CHO}}{dt} = R_6 - R_7 \tag{4.72}$$

$$\frac{d\theta_{CH_2O}}{dt} = R_7 - R_8 \tag{4.73}$$

$$\frac{d\theta_{CH_3O}}{dt} = R_8 - R_9 - R_{17} \tag{4.74}$$

$$\frac{d\theta_{OH}}{dt} = R_9 + R_{11} - R_{12} + R_{16} \tag{4.75}$$

$$\frac{d\theta_{CO_2}}{dt} = R_{10} - R_{14} \tag{4.76}$$

$$\frac{d\theta_{H_2O}}{dt} = R_{12} - R_{13} \tag{4.77}$$

Site balance:

$$\theta_V = 1 - \left(\theta_H + \theta_{CO} + \theta_C + \theta_O + \theta_{CH} + \theta_{CH_2} + \theta_{CH_3} + \theta_{CHO} + ... + \theta_{H_2O}\right) \tag{4.78}$$

Mole fraction and surface coverage profiles for these species are found by solving the set of partial differential equations resulting from the mass balance of the gas phase species and the set of ordinary differential equations resulting from the mass balances of the surface species and the appropriate site balance simultaneously with the initial and

boundary conditions shown in Equation 4.79. The solutions are dependent upon the activation energies and pre-exponential factors of the elementary reactions.

$$\begin{aligned} y_A(0,z) &= y_A^0 \\ \theta_A(0) &= \theta_A^0 \end{aligned} \tag{4.79}$$

The UBI-QEP method can be used to estimate the activation energies for the elementary steps but requires knowledge of C, O, and H binding energies. Transition state theory can be used to estimate the pre-exponential factors for the elementary steps.

Binding energies of C, O, and H on Fe as a function of coverage are available in the literature. For example from first principles calculation, Jiang et al. [163] reported a C binding energy of 765 kJ/mol to 552 kJ/mol for coverages ranging from 0.11 ML to 1.0 ML on Fe(110). They also reported C binding energies on Fe(100) from 804 kJ/mol to 738 kJ/mol for coverages ranging from 0.11 ML to 1.0 ML. Similarly, Blonski et al. [164] reported O binding energies on Fe(110) ranging from 628 kJ/mol to 290 kJ/mol for coverages ranging from clean to 0.75 ML and for similar coverages on Fe(100), they reported values of O binding energy ranging from 666 kJ/mol to 579 kJ/mol from DFT calculations. Since the exact surface morphology of the polycrystalline Fe catalyst used in this study was not known, the strategy adopted here was to fit the observed CH_4 mole fraction to the calculated CH_4 mole fraction using binding energies of C, O, and H as adjustable parameters. Initial coverages of C, CO, and O were also optimized. R_1 was multiplied by its stoichiometric number and because no CO_2 was observed during the ITH experiment, the pre-exponential factors leading to the formation of CO_2 species were set to zero. The numerical method of lines was used to solve Equations 4.41 to 4.78, while the data analysis procedure was similar to that described in Section 4.2.1.3. The

Fortran driver code used in the data analysis is provided in the Appendix A.8. Adsorption of gas-phase species was assumed to be non-activated except for H_2(g) and CH_4(g) that were assumed to undergo dissociative adsorption on Fe.

Figure 4-16 shows experimentally observed and predicted CH_4 profiles for ITH at 448 K on 99Fe1ALa-307 catalyst. The estimated binding energies of C, O, and H were 605 kJ/mol, 450 kJ/mol, and 250 kJ/mol respectively, while the initial fractional coverages of C, CO, and O were estimated to be 0.3, 0.65, and 0.01 respectively. The activation energies, pre-exponential factors, and rate constants for the elementary steps are tabulated on Table 4-4. During the data fitting process, the forward pre-exponential factor for the carbon hydrogenation step (Reaction # 2) was adjusted, i.e. multiplied by 1000 to compensate for the uncertainty in the configuration of the transition state [133].

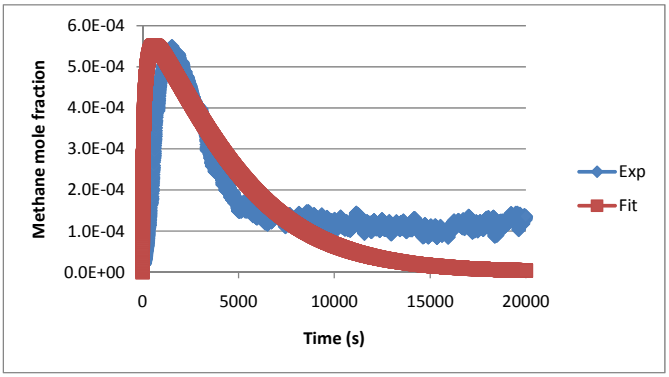

Figure 4-16: Experimentally observed and model predicted CH_4 mole fraction profiles during isothermal hydrogenation of stable surface species after FTS at 448 K and 1 atm for 99Fe1ALa-307. Fitted binding energy values of C, O, and H used to calculate the activation energies for the elementary steps were 605 kJ/mol, 450 kJ/mol, and 250 kJ/mol respectively. This fit is the basis for the microkinetic model shown in Table 4-4. The initial fractional coverages of C, CO, and O were estimated to be 0.3, 0.65, and 0.01 respectively.

Table 4-4: Microkinetic model of hydrogenation of stable surface species after FTS for 5 min at 448 K for 99Fe1ALa-307 based on estimated binding energies of C, O, and H of 6.05 x 10^5 J/mol, 4.5 x 10^5 J/mol, and 2.5 x 10^5 J/mol respectively. The pre-exponential factors were calculated from transition state theory. The calculated forward pre-exponential factor for reaction number 2 was multiplied by 1000 to adjust for the uncertainty in the structure of the transition state. The "=" sign implies that a reaction is reversible.

Rxn #	Reaction	Forward activation energy (J/mol)	Reverse activation energy (J/mol)	[a]Forward pre-exponential factor (Pa^{-n} s^{-1})	[a]Reverse pre-exponential factor (Pa^{-n} s^{-1})	[b]Forward rate constant (Pa^{-n} s^{-1})	[b]Reverse rate constant (Pa^{-n} s^{-1})
1	$H_2(g) + 2* = 2H*$	1.71E+04	8.21E+04	2.20E+01	1.90E+13	2.22E-01	5.06E+03
2	$C* + H* = CH*$	1.53E+05	2.43E+04	1.40E+17	1.00E+13	2.28E-01	1.45E+10
3	$CH* + H* = CH_2*$	4.78E+04	1.04E+05	2.60E+13	1.00E+13	6.90E+07	7.15E+00
4	$CH_2* + H* = CH_3*$	1.82E+04	1.11E+05	2.60E+13	4.70E+13	1.95E+11	5.56E+00
5	$CH_3* + H* = CH_4(g) + 2*$	0.00E+00	3.22E+04	1.60E+12	9.80E-01	1.60E+12	1.72E-04
6	$CO* + H* = CHO* +*$	1.14E+05	0.00E+00	1.70E+14	1.00E+13	8.33E+00	1.00E+13
7	$CHO* + H* = CH_2O* + *$	3.42E+04	6.21E+04	2.70E+12	1.00E+13	2.81E+08	5.81E+05
8	$CH_2O* + H* = CH_3O* + *$	1.86E+04	3.62E+04	2.10E+13	1.00E+13	1.41E+11	5.94E+08
9	$CH_3O* + H* = CH_3* + OH*$	7.78E+04	1.27E+04	2.60E+13	6.80E+12	2.19E+04	2.28E+11
10	$CO* + O* = CO_2* + *$	2.89E+04	4.72E+04	7.70E+12	1.00E+13	3.32E+09	3.12E+07
11	$O* + H* = OH* + *$	1.01E+05	5.93E+04	1.10E+14	1.00E+13	1.67E+02	1.20E+06
12	$OH* + H* = H_2O* + *$	2.79E+04	9.22E+04	1.10E+13	1.00E+13	6.19E+09	1.80E+02
13	$H_2O* = H_2O(g) + *$	5.12E+04	0.00E+00	1.10E+13	8.20E-01	1.19E+07	8.20E-01
14	$CO_2* = CO_2(g) + *$	2.39E+04	0.00E+00	1.00E+13	2.20E-01	1.62E+10	2.20E-01
15	$CO* + * = C* + O*$	1.85E+05	7.27E+04	1.00E+13	6.10E+13	2.47E-09	2.01E+05
16	$CO* + H* = C* + OH*$	1.61E+05	6.25E+03	1.70E+14	9.60E+13	2.99E-05	1.79E+13
17	$CH_3O* + * = CH_3* + O*$	6.75E+04	4.43E+04	1.00E+13	2.80E+13	1.36E+05	1.90E+08
18	$CO* = CO(g) + *$	9.16E+04	0.00E+00	1.00E+13	4.20E-01	2.10E+02	4.20E-01
19	$CH_2O* + H* = CH_2* + OH*$	1.32E+05	0.00E+00	2.00E+13	1.40E+12	8.12E-03	1.40E+12

[a] for surface reaction, n = 0, while n = 1 for gas-phase reaction; [b]at 448 K and 1 atm.

4.5.1.1 Result of Microkinetic Model of ITH Using Binding Energies Derived from Modeling Steady-State Kinetic Data from the Berty Reactor

As will be described in Chapter 5, steady-state data from a kinetic study of FTS 99Fe1ALa-mon-907 in the Berty reactor were obtained using a statistical design of experiments and used to estimate values of C, O, and H binding energies. The estimated binding energies were 497 kJ/mol, 767 kJ/mol, and 270.01 kJ/mol for C, O, and H, respectively. By using the same system of elementary steps as in Table 4-4 and these new binding energies, the sets of partial and ordinary differential equations were too stiff for DVODE solver. However, by reducing the O binding energy from 767 kJ/mol to 667 kJ and by multiplying the forward rate constants of the carbon hydrogenation and CO desorption steps by 2.5 and 0.1 respectively, reasonable agreement was obtained between calculated and experimentally observed CH_4 profiles for ITH at 448 K on 99Fe1ALa-307 as shown in Figure 4-17. The resulting activation energies and rate constants are tabulated in Table 4-5.

The predicted coverage profiles of H, CO, C, and O as a function of time are graphed in Figure 4-18. CO coverage dropped rapidly from an initial value of 0.85 to almost zero within the first 100 s, while H coverage rose quickly from an initial value of zero to about 1.0 after 10000 s. Similarly, C and O coverages rose quickly to 0.1 and 0.06 before decreasing to almost zero after about 10000 s.

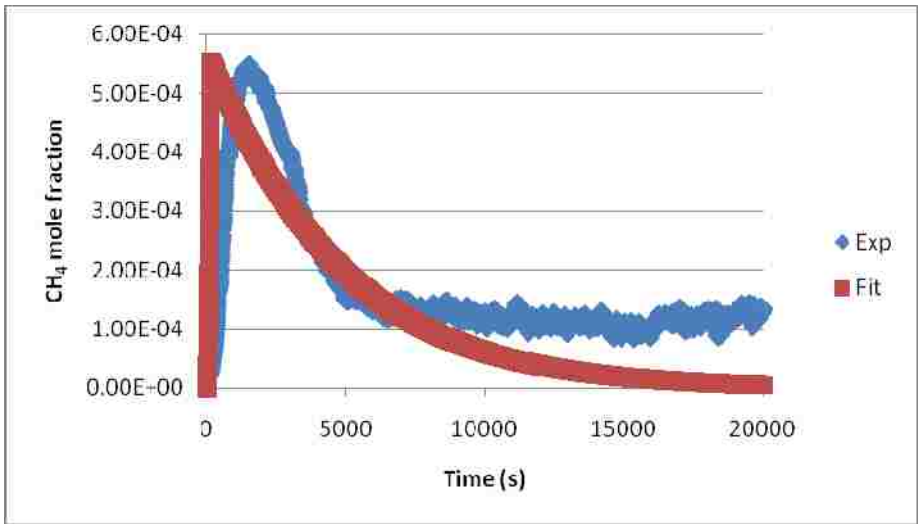

Figure 4-17: Experimentally-observed and model-predicted CH_4 mole fraction profiles during isothermal hydrogenation of stable surface species after FTS at 448 K and 1 atm for 99Fe1ALa-307. Fitted binding energy values of C, O, and H used to calculate the activation energies for the elementary steps were 497 kJ/mol, 666 kJ/mol, and 270 kJ/mol respectively.

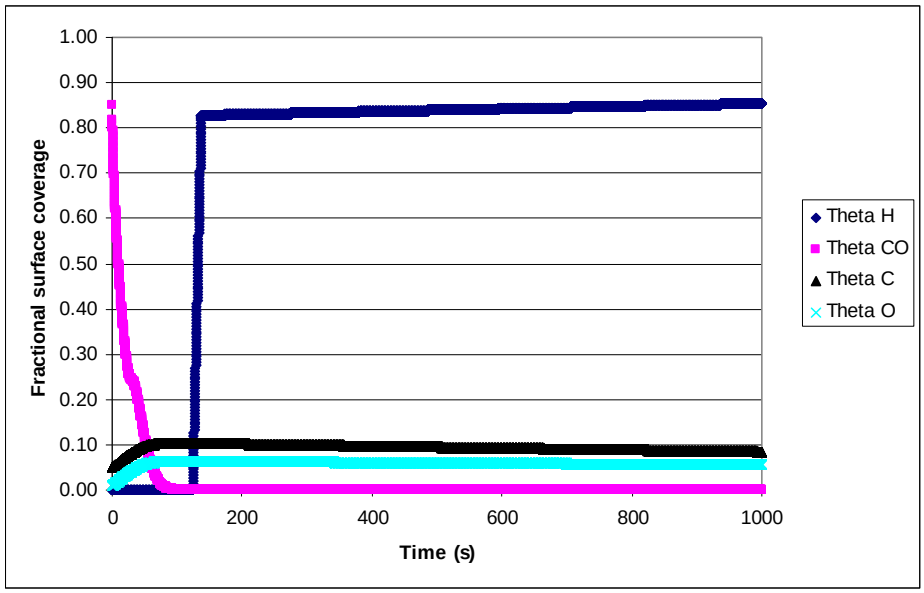

Figure 4-18: Predicted H, CO, C, and O surface coverages during ITH at 448 K after FTS for 5 min at 1 atm using 99Fe1ALa-307 catalyst.

Table 4-5: Microkinetic model of hydrogenation of stable surface species after FTS for 5 min at 448 K for 99Fe1ALa-307. Fitted binding energy values of C, O, and H used to calculate the activation energies for the elementary steps were 497 kJ/mol, 667 kJ/mol, and 270 kJ/mol respectively The "=" sign implies that a reaction is reversible.

Rxn #	Reaction	Forward activation energy (J/mol)	Reverse activation energy (J/mol)	[a]Forward pre-exponential factor (Pa^{-n} s^{-1})	[a]Reverse pre-exponential factor (Pa^{-n} s^{-1})	[b]Forward rate constant (Pa^{-n} s^{-1})	[b]Reverse rate constant (Pa^{-n} s^{-1})
1	$H_2(g) + 2* = 2H*$	1.01E+02	1.05E+05	2.20E+01	1.90E+13	2.14E+01	1.05E+01
2	$C* + H* = CH*$	1.54E+05	2.12E+04	3.50E+14	1.00E+13	4.10E-04	3.35E+10
3	$CH* + H* = CH_2*$	4.20E+04	9.91E+04	2.60E+13	1.00E+13	3.28E+08	2.76E+01
4	$CH_2* + H* = CH_3*$	6.60E+03	1.07E+05	2.60E+13	4.70E+13	4.42E+12	1.61E+01
5	$CH_3* + H* = CH_4(g) + 2*$	0.00E+00	4.50E+04	1.60E+12	9.80E-01	1.60E+12	5.55E-06
6	$CO* + H* = CHO* +*$	1.53E+05	0.00E+00	1.70E+14	1.00E+13	2.56E-04	1.00E+13
7	$CHO* + H* = CH_2O* + *$	2.32E+04	5.54E+04	2.70E+12	1.00E+13	5.33E+09	3.43E+06
8	$CH_2O* + H* = CH_3O* + *$	0.00E+00	1.21E+05	2.10E+13	1.00E+13	2.10E+13	8.27E-02
9	$CH_3O* + H* = CH_3* + OH*$	1.09E+05	0.00E+00	2.60E+13	6.80E+12	5.19E+00	6.80E+12
10	$CO* + O* = CO_2* + *$	1.45E+05	0.00E+00	7.70E+12	1.00E+13	1.06E-04	1.00E+13
11	$O* + H* = OH* + *$	1.48E+05	4.45E+04	1.10E+14	1.00E+13	6.54E-04	6.54E+07
12	$OH* + H* = H_2O* + *$	6.81E+04	9.42E+04	1.10E+13	1.00E+13	1.28E+05	1.04E+02
13	$H_2O* = H_2O(g) + *$	2.09E+05	0.00E+00	1.10E+13	8.20E-01	5.05E-12	8.20E-01
14	$CO_2* = CO_2(g) + *$	5.11E+04	0.00E+00	1.00E+13	2.20E-01	1.10E+07	2.20E-01
15	$CO* + * = C* + O*$	1.31E+05	1.54E+05	1.00E+13	6.10E+13	5.78E-03	6.34E-05
16	$CO* + H* = C* + OH*$	1.52E+05	7.20E+04	1.70E+14	9.60E+13	3.46E-04	3.87E+05
17	$CH_3O* + * = CH_3* + O*$	6.09E+04	3.00E+04	1.00E+13	2.80E+13	7.86E+05	8.85E+09
18	$CO* = CO(g) + *$	6.48E+04	0.00E+00	1.00E+12	4.20E-01	2.78E+04	4.20E-01
19	$CH_2O* + H* = CH_2* + OH*$	8.34E+04	4.88E+04	2.00E+13	1.40E+12	3.81E+03	2.86E+06

[a] for surface reaction, n = 0, while n = 1 for gas-phase reaction; [b]at 448 K and 1 atm.

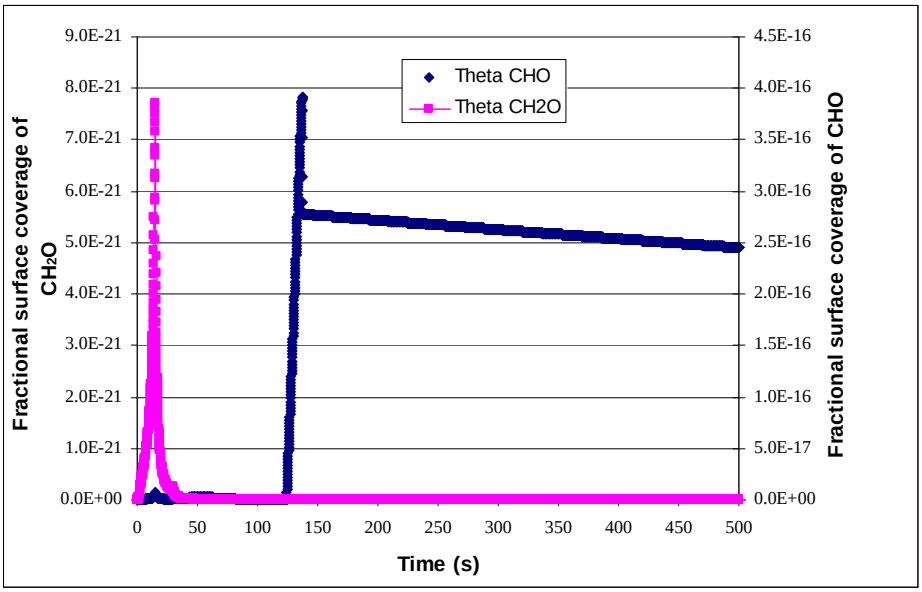

Figure 4-19: Predicted CHO and CH_2O surface coverages during ITH at 448 K after FTS for 5 min at 1 atm using 99Fe1ALa-307 catalyst.

The predicted surface coverages of CHO and CH_2O are shown in Figure 4-19. The fractional coverage of CHO rises to about 4 x 10^{-16} and slowly decays to zero, while that for CH_2O coverage rises quickly to about 8 x 10^{-21} and decays to zero in less than 100 s indicating that it is a very reactive intermediate. The net turnover frequencies for the steps involving the reaction steps $C^* + H^* \leftrightarrow CH^* + *$ and $CO^* + H^* \leftrightarrow CHO^* + *$ are shown in Figure 4-20. The rate for the carbon hydrogenation step rose initially to about five orders of magnitude higher than that for the formyl formation step. Similarly, the net turnover frequencies for the steps $CO^* + * \leftrightarrow C^* + O^*$ and $CO^* + H^* \leftrightarrow C^* + OH^*$ are shown in Figure 4-21. The predicted net rate of direct CO dissociation was several orders of magnitude higher than that of hydrogen assisted CO dissociation, meaning that direct CO dissociation was facile when compared to hydrogen assisted CO dissociation.

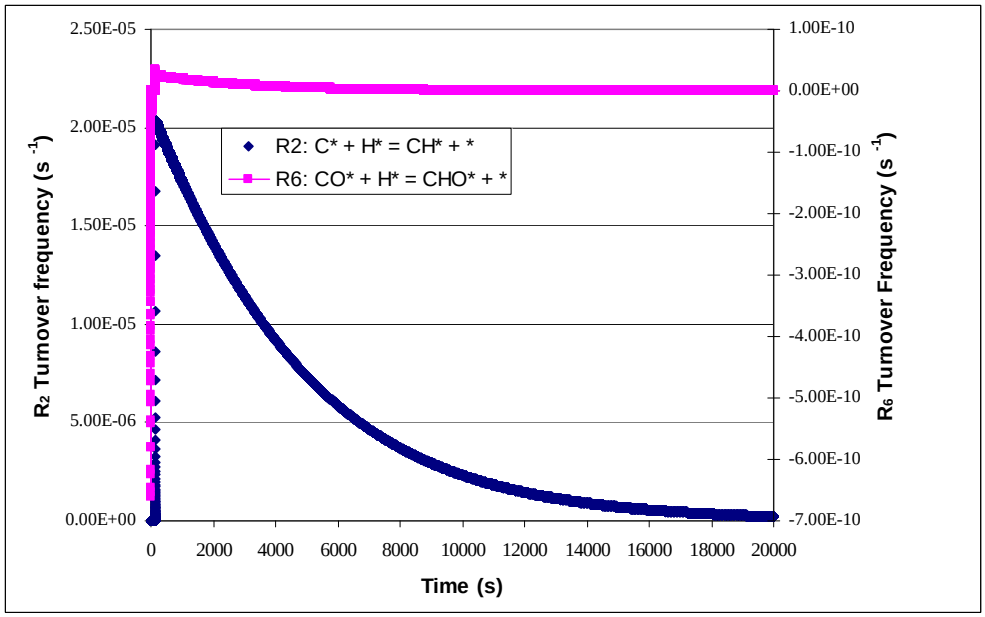

Figure 4-20: Predicted rates of elementary steps involving (1) direct hydrogenation of carbon to CH, and (2) direct hydrogenation of CO to CHO during ITH at 448 K after FTS for 5 min at 1 atm using 99Fe1ALa-307 catalyst.

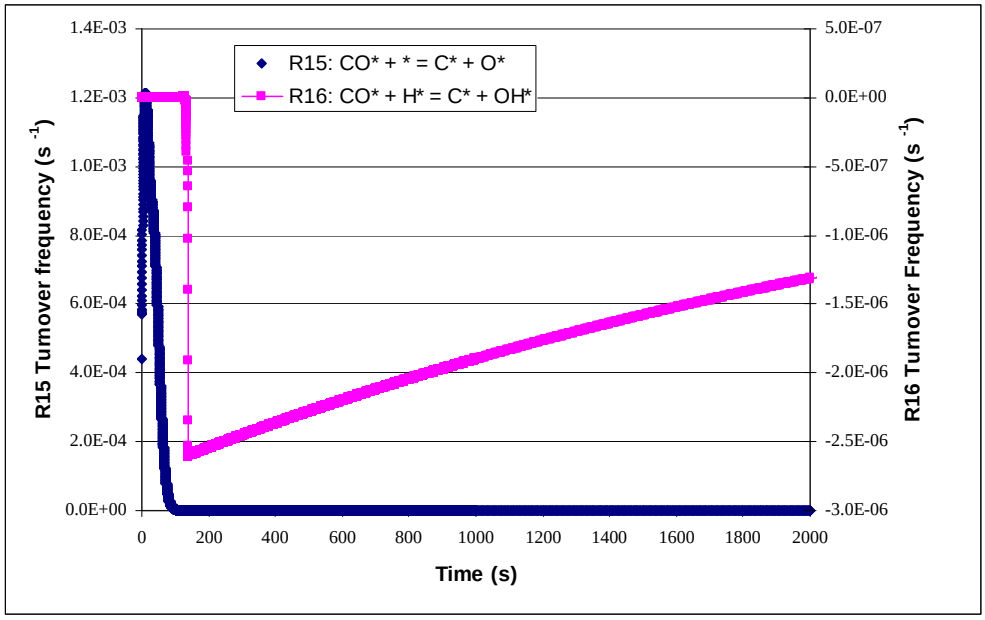

Figure 4-21: Predicted rates of elementary steps involving (1) direct hydrogenation of carbon to CH, and (2) direct hydrogenation of CO to CHO during ITH at 448 K after FTS for 5 min at 1 atm using 99Fe1ALa-307 catalyst.

4.5.2 Test of robustness of ITH microkinetic model for 99Fe1ALa-307

The robustness of the ITH microkinetic model presented above was tested with ITH data after FTS for 5 min at 458 K at 1 atm. Figure 4-22 shows good agreement between the model-predicted and experimental CH_4 profiles at the above conditions with the activation energies and pre-exponential factors for the elementary steps shown in Table 4-5.

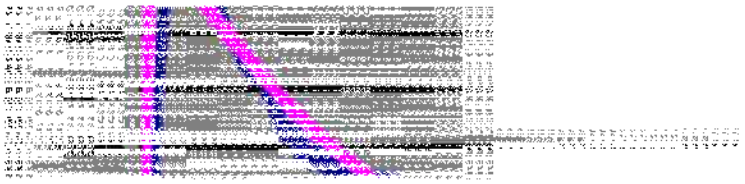

Figure 4-22: Experimentally-observed and model-predicted CH_4 mole fraction profiles as a function of time for isothermal hydrogenation of stable surface species on 99Fe1ALa-307 after FTS at 458 K and 1 atm.

4.6 Result of ITH Using 20Fe1K1Pt-ALa-705

ITH after FTS on 20Fe1K1Pt-ALa-705for 5 min at 1 atm was performed as described in Section 3.6.2 at two temperatures 398 K and 438 K respectively. Using the

methodology described previously in section 4.5.1, a microkinetic model was developed for this catalyst from ITH data at 438 K.

Binding energies of C, O, and H were estimated to be 399 kJ/mol, 734 kJ/mol and 265 kJ/mol respectively. For ITH at 438 K, initial surface coverages of C, CO, and O were estimated to be equal to 0.5, 0.03, and 0.4 respectively. As in the previous section, activation energies for elementary steps used in the model were calculated using the UBI-QEP method while pre-exponential factors were calculated from transition state theory. As in the previous section, the forward pre-exponential factor for the carbon hydrogenation step was adjusted by multiplying by 0.013 while that for the CO desorption step was multiplied by 0.99. ITH microkinetic model parameters resulting from these calculations are tabulated on Table 4-6 while model-predicted and experimentally-observed CH_4 mole fraction profiles are shown on Figure 4-23.

As previously described in the Chapter 3, the H_2 inlet mole fraction during ITH was maintained at 0.1. The model prediction of H_2 mole fraction serves as a check on the accuracy of the model and calculations. Figure 4-24 shows the predicted H_2 mole fraction profile at the reactor outlet. The H_2 mole fraction at the reactor outlet rose from zero to 0.1 in about 2000 seconds and thereafter remained constant.

Model-predicted profiles of C, CH, and CHO intermediates are shown in Figure 4-25 and Figure 4-26. Figure 4-27 and Figure 4-28 show net reaction rates for the elementary steps involving direct carbon hydrogenation to CH and hydrogenation of adsorbed CO to CHO species as a function of time respectively. The rate of C hydrogenation appears to be much faster than the rate of adsorbed CO hydrogenation to CHO species, having a shape almost similar to that of the CH_4 mole fraction profile.

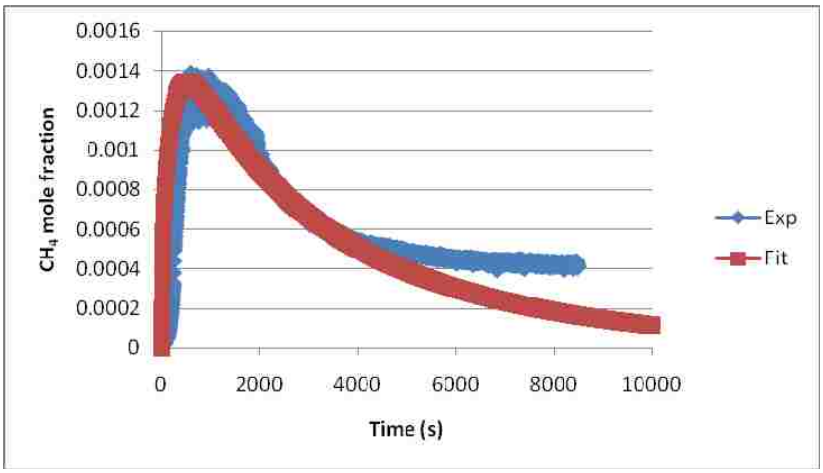

Figure 4-23: Experimentally-observed and model-predicted CH_4 profiles for ITH following FTS for 5 min on 20Fe1K1Pt-ALa-705 at 1 atm pressure and 438 K. The estimated initial fractional coverages of C, CO, and O were 0.5, 0.03, and 0.4 respectively.

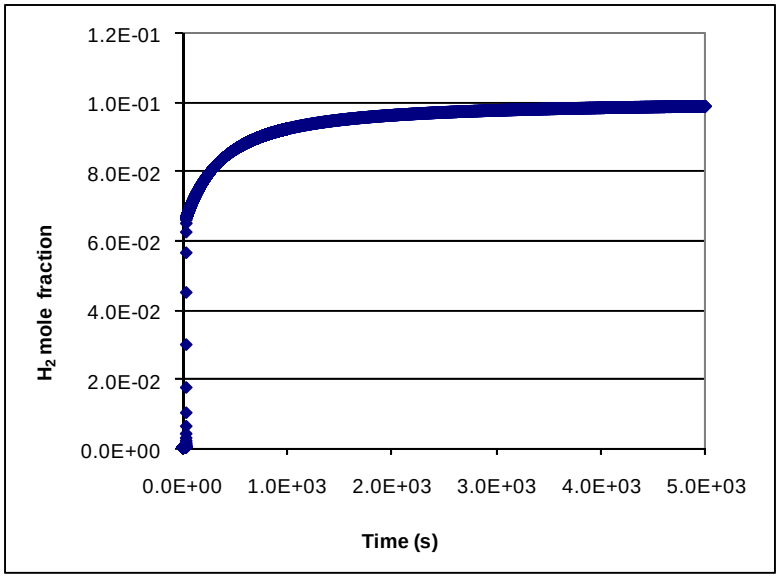

Figure 4-24: Predicted H_2 mole fraction during ITH at 438 K on 20Fe1K1Pt-ALa-705. Inlet H_2 mole fraction was experimentally maintained at 0.1.

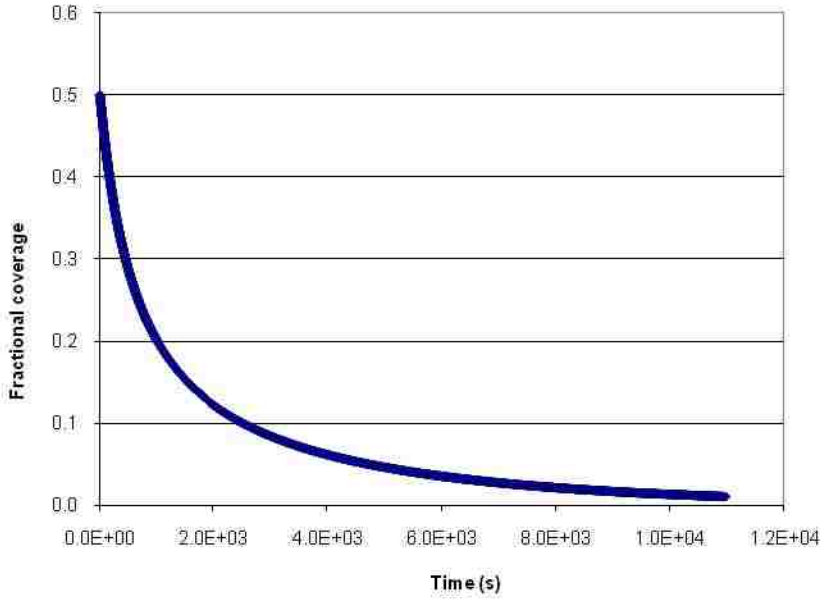

Figure 4-25: Predicted fractional C coverage profile during ITH at 438 K on 20Fe1K1Pt-ALa-705.

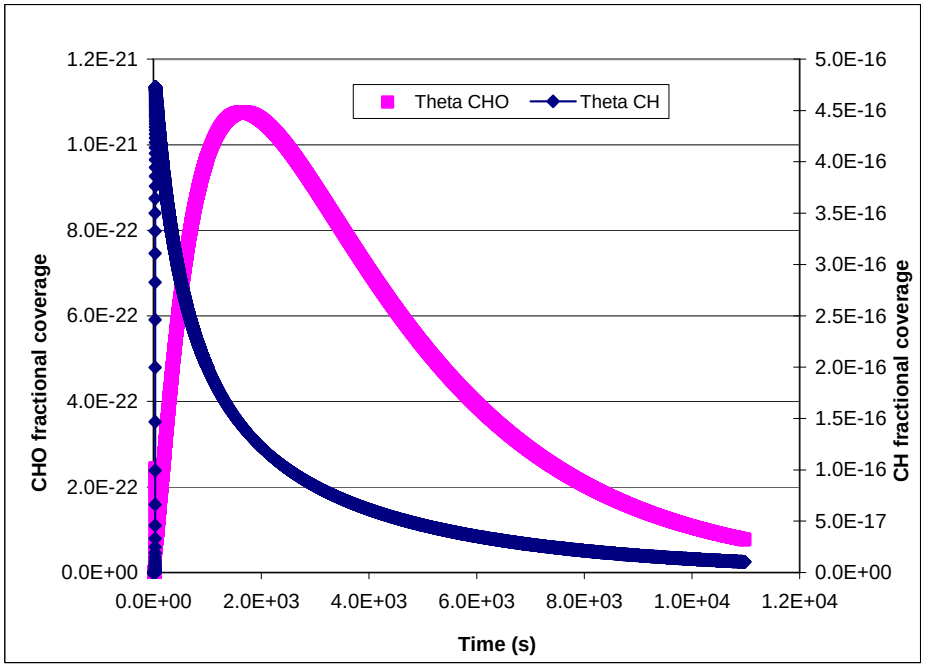

Figure 4-26: Predicted CH and CHO fractional coverages profile during ITH at 438 K on 20Fe1K1Pt-ALa-705.

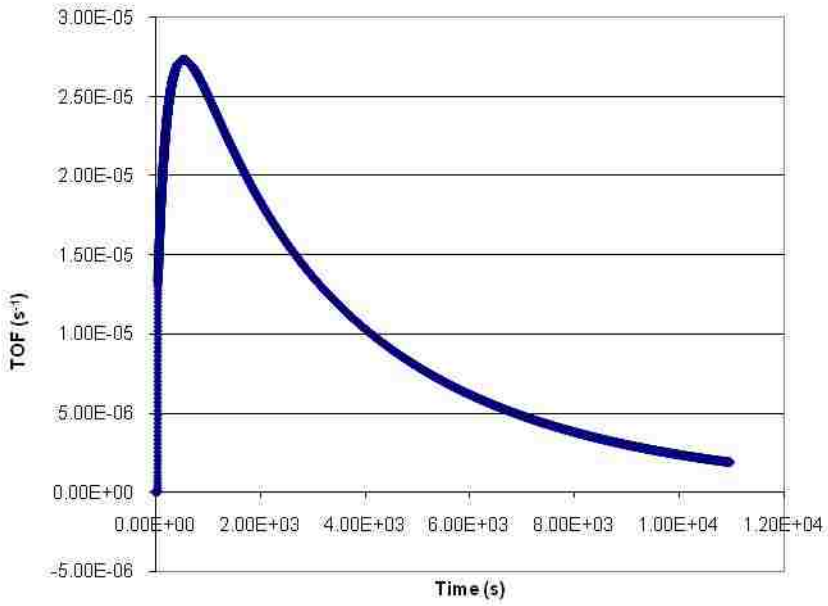

Figure 4-27: Predicted net reaction rate for the elementary step $C^* + H^* \leftrightarrow CH^* + *$ as a function of time during ITH at 438 K on 20Fe1K1Pt-ALa-705.

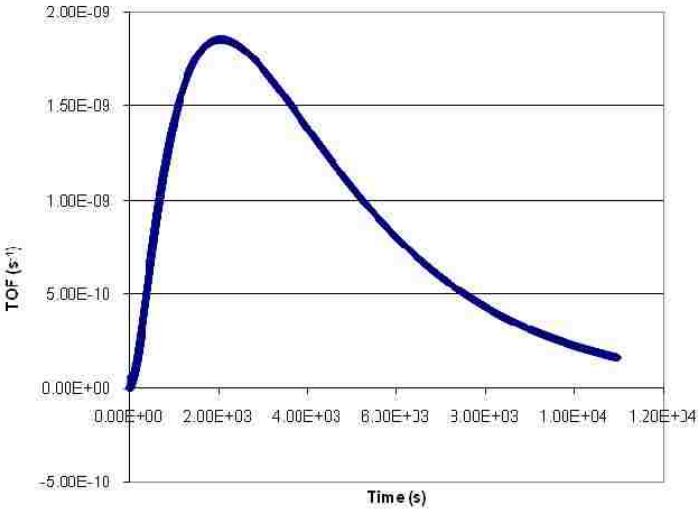

Figure 4-28: Predicted net reaction rate for the elementary step $CO^* + H^* \leftrightarrow CHO^* + *$ as a function of time during ITH at 438 K on 20Fe1K1Pt-ALa-705.

4.6.1 Test of robustness of ITH microkinetic model on 20Fe1K1Pt-ALa-705

The robustness of the ITH microkinetic model presented above for 20Fe1K1Pt-ALa-705 was tested with ITH data after FTS for 5 min at 398 K at 1 atm. Figure 4-29 shows the model and experimentally predicted CH_4 profiles at the above conditions with the activation energies and pre-exponential factors for the elementary steps shown in Table 4-6. Initial fractional coverages of C, CO, and O were estimated to be 0.005, 0.95, and 0.004 respectively. The pre-exponential factor calculated from transition state theory for the elementary step involving hydrogenation of surface carbon to a CH intermediate was adjusted by multiplying by a factor of 2.2.

The predicted fractional C coverage profile is shown on Figure 4-30. C coverage rose initially from 0.005 to a maximum of about 0.025 in about 200 s. The net turnover frequency profiles for the elementary steps involving direct dissociation of adsorbed CO, and H assisted CO dissociation are shown in Figure 4-31 below. The model predicts that the net turnover frequency for direct dissociation of adsorbed CO is much faster than the corresponding H assisted CO dissociation within the few seconds of the experiment, implying that the increase in C coverage predicted within a similar time period was dominated by direct CO dissociation to C and O species.

Table 4-6: Microkinetic model for ITH on 20Fe1K1Pt-ALa-705 based on the analysis of ITH experiment at 1 atm pressure and 438 K. The activation energies were calculated using UBI-QEP with C, O, and H binding energies of 399 kJ/mol, 734 kJ/mol, and 265 kJ/mol respectively while the pre-exponential factors were calculated from transition state theory.

Rxn #	Reaction	Forward activation energy (J/mol)	Reverse activation energy (J/mol)	Forward pre-exponential factor (Pa^{-n} s^{-1})	Reverse pre-exponential factor (Pa^{-n} s^{-1})	Forward rate constant (Pa^{-n} s^{-1})	Reverse rate constant (Pa^{-n} s^{-1})
1	$H_2(g) + 2* = 2H*$	4.37E+03	9.94E+04	2.20E+01	1.90E+13	6.62E+00	2.67E+01
2	$C* + H* = CH*$	1.34E+05	2.50E+04	1.92E+12	1.00E+13	1.89E-04	1.04E+10
3	$CH* + H* = CH_2*$	1.79E+04	1.01E+05	2.60E+13	1.00E+13	1.89E+11	9.07E+00
4	$CH_2* + H* = CH_3*$	0.00E+00	1.10E+05	2.60E+13	4.70E+13	2.60E+13	3.48E+00
5	$CH_3* + H* = CH_4(g) + 2*$	0.00E+00	6.24E+04	1.60E+12	9.80E-01	1.60E+12	3.49E-08
6	$CO* + H* = CHO* +*$	1.63E+05	0.00E+00	1.70E+14	1.00E+13	6.66E-06	1.00E+13
7	$CHO* + H* = CH_2O* + *$	7.33E+02	5.76E+04	2.70E+12	1.00E+13	2.21E+12	1.34E+06
8	$CH_2O* + H* = CH_3O* + *$	0.00E+00	1.55E+05	2.10E+13	1.00E+13	2.10E+13	3.54E-06
9	$CH_3O* + H* = CH_3* + OH*$	1.13E+05	0.00E+00	2.60E+13	6.80E+12	8.08E-01	6.80E+12
10	$CO* + O* = CO_2* + *$	1.80E+05	0.00E+00	7.70E+12	1.00E+13	2.50E-09	1.00E+13
11	$O* + H* = OH* + *$	1.51E+05	4.34E+04	1.10E+14	1.00E+13	9.93E-05	6.66E+07
12	$OH* + H* = H_2O* + *$	6.37E+04	1.05E+05	1.10E+13	1.00E+13	2.76E+05	3.06E+00
13	$H_2O* = H_2O(g) + *$	2.76E+05	0.00E+00	1.10E+13	8.20E-01	1.26E-20	8.20E-01
14	$CO_2* = CO_2(g) + *$	6.14E+04	0.00E+00	1.00E+13	2.20E-01	4.77E+05	2.20E-01
15	$CO* + * = C* + O*$	1.23E+05	1.36E+05	1.00E+13	6.10E+13	2.44E-02	3.72E-03
16	$CO* + H* = C* + OH*$	1.54E+05	6.00E+04	1.70E+14	9.60E+13	6.38E-05	6.65E+06
17	$CH_3O* + * = CH_3* + O*$	6.09E+04	3.75E+03	1.00E+13	2.80E+13	5.48E+05	9.99E+12
18	$CO* = CO(g) + *$	4.36E+04	0.00E+00	9.90E+12	4.20E-01	6.30E+07	4.20E-01
19	$CH_2O* + H* = CH_2* + OH*$	6.02E+04	4.54E+04	2.00E+13	1.40E+12	1.33E+06	5.43E+06

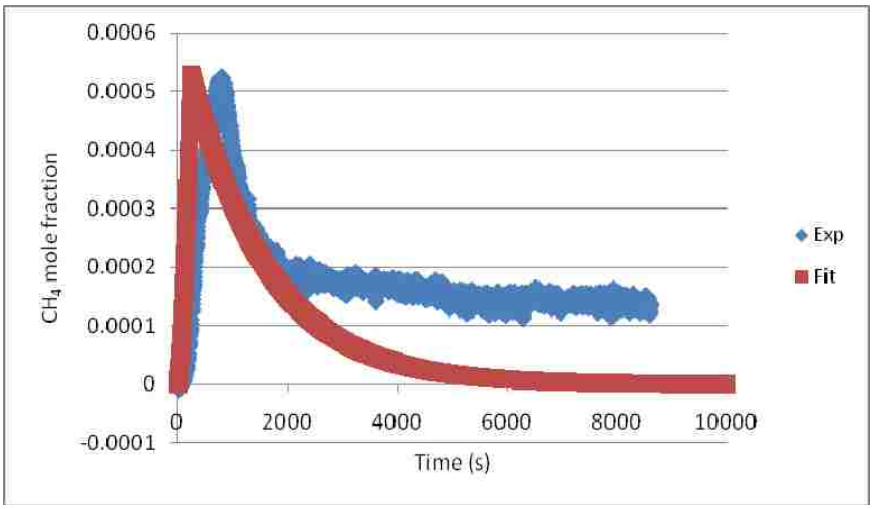

Figure 4-29: Experimentally-observed and predicted CH_4 mole fraction profile as a function of time during ITH at 1 atm pressure and 398 K on 20Fe1K1Pt-ALa-705. Estimated initial fractional coverages of C, CO, and O were 0.005, 0.95, and 0.004 respectively.

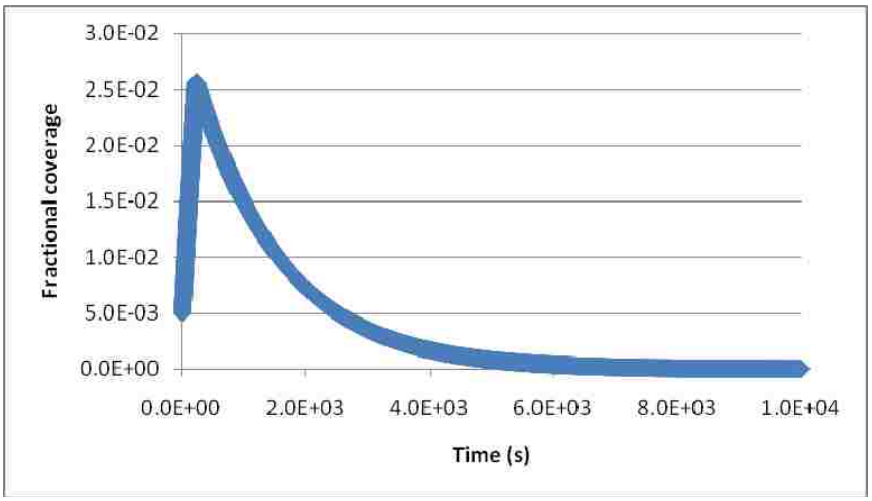

Figure 4-30: Model-predicted C coverage profile during ITH at 398 K and 1 atm pressure for 20Fe1K1Pt-ALa-705 catalyst.

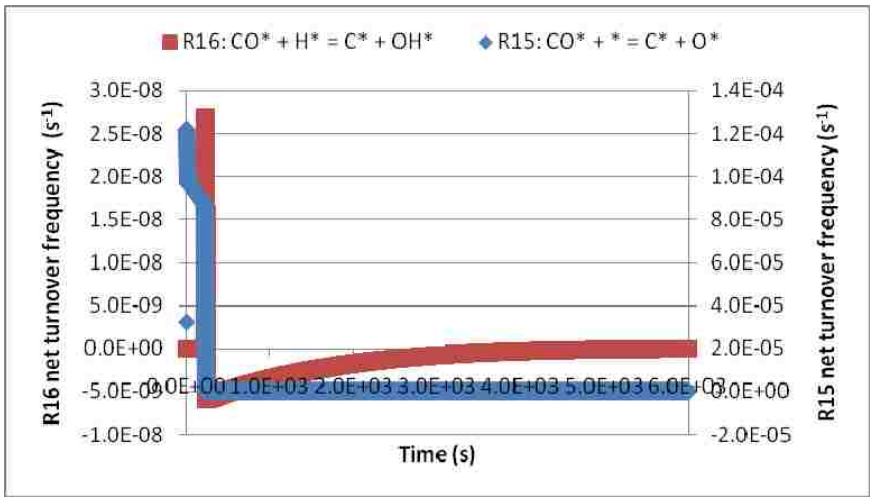

Figure 4-31: Net turnover frequency profiles for the reactions involving direct dissociation of adsorbed CO to C and O, and H assisted dissociation of CO to C and OH, respectively, during ITH at 398 K and 1 atm pressure for 20Fe1K1Pt-ALa-705 catalyst.

5. Chapter 5: Results: Steady-State Kinetic Experiments

5.1 Steady-State Experimental Result for 20Fe1K1Pt-ALa-mon-507

Steady-state gas phase concentrations (partial pressures) of CO, H_2, CO_2, and CH_4 were measured during FTS on monolithic supported Fe-K-Pt/La-Al_2O_3 (Monolith # 3) over a range of inlet H_2, CO, and He concentrations and temperatures (493 – 533 K) during a set of statistically designed kinetic experiments at a total pressure of about 21 atm (absolute). Partial pressures, rate and selectivity data from these experiments are summarized in Table 5-1. Pressures reported here are absolute. Before switching from one run condition to another, the reaction was allowed to reach steady state as indicated by a constant rate of CO disappearance as a function of time on stream. For example, CO rate data for Run 12 in Figure 5-1 reached a constant value after about 10 h. The slight oscillation observed in Figure 5-1 in the region between 17 to 25 h is attributed to reactor temperature fluctuations. Runs 31 to 37 were replicated twice.

Stability of the catalyst at each temperature was monitored by frequently returning the reactor to the inlet conditions chosen as standard (44 mL/min He, 74 mL/min CO/Ar, and 130 mL/min H_2). Runs 1, 6, and 10 at 493 K ; Runs 11, 16, and 21 at 513 K; Runs 22, 26, and 29 at 523 K; Runs 30, 33, and 35 at 533 K were conducted at the standard flow conditions. The standard deviation in the rate of reaction of CO at standard flow conditions at 493 K, 513 K, 523 K, and 533 K were within the limits of

experimental error indicating no significant loss of catalyst activity during the experiment. This is illustrated by data from these runs in Table 5-2.

5.1.1 Effects of pore diffusion on rate measurement

The effects of pore diffusional resistance on observed rates of CO conversion were tested using the Weisz criteria. The calculated Weisz Modulus for the run conditions ranged from 0.007 to 0.1 (for most of the runs except for Run 31 and 32) as shown in Table 5-3. From these data, it is evident that pore diffusional resistance was negligible at the reaction conditions in this study since they were below the critical value of 0.15 for significant pore diffusional resistance although those for runs 31 and 32 were slightly higher than 0.15.

5.1.2 Sequential design of experiments

Steady-state kinetic experiments were carried out in the Berty reactor on 20Fe1K1Pt-ALa-mon-507 using a sequential-design-of-experiments methodology based on the D-optimal criteria as explained in Chapter 3 using Equation 3.10 with the rate constants written in their respective Arrhenius forms. Progressive changes in the estimated values of the four kinetic parameters as a function of run number (beginning with Run 22) are tabulated in Table 5-4 and graphed in Figure 5-2 to Figure 5-5 for the respective kinetic parameters. From the data in these figures and in Table 5-4, it is evident that the kinetic parameters initially changed significantly as the next set of experimental conditions was added to the sequential design, but they approached asymptotic values at about 31 runs.

Table 5-1: Kinetic data obtained during statistically-designed, steady-state kinetic experiment for 20Fe1K1Pt-ALa-mon-507

Run	Temp (K)	$V_{CO}o$ (mL/min) @s.t.p.	$V_{H2}o$ (mL/min) @s.t.p.	V_{Inert} (mL/min) @s.t.p.	P_{TOT} (atm)	P_{CO} (atm)	P_{H2} (atm)	P_{CO2} (atm)	P_{CH4} (atm)	P_{H2O} (atm)	$-r_{CO}$ (mol/kg-s)	r_{C2+} (mol/kg-s)	r_{CO2} (mol/kg-s)	X_{CO} (%)	X_{H2} (%)	Sel_{CH4} (%)	Sel_{CO2} (%)
1	493	65.3	130	52.7	21.1	5.1	10.7	0.1	0.0	0.3	7.05E-04	5.35E-04	1.10E-04	8.24	3.82	8.47	15.58
2	493	28.3	60	14.7	21.0	4.7	11.5	0.2	0.1	0.6	7.02E-04	4.93E-04	1.52E-04	18.95	6.37	8.11	21.65
3	493	36.2	91	36.8	21.1	4.1	11.1	0.1	0.1	0.4	6.32E-04	4.45E-04	1.22E-04	13.31	6.69	10.2	19.3
4	493	17.7	52	185.3	21.3	1.3	3.8	0.1	0.0	0.1	2.70E-04	1.35E-04	9.31E-05	11.69	16.37	15.48	34.48
5	493	38.9	90	121.1	21.2	3.2	7.1	0.1	0.0	0.1	3.82E-04	2.23E-04	1.05E-04	7.5	10.66	14.08	27.61
6	493	65.3	130	52.7	20.8	5.1	10.6	0.1	0.0	0.3	7.20E-04	5.44E-04	1.12E-04	8.41	3.93	8.93	15.56
7	493	31.8	72	21.2	21.1	4.4	11.5	0.2	0.1	0.6	7.58E-04	5.46E-04	1.49E-04	18.22	5.92	8.36	19.67
8	493	30.0	68	34.0	21.3	4.2	10.3	0.2	0.1	0.4	5.73E-04	3.91E-04	1.27E-04	14.57	7.72	9.67	22.21
9	493	31.8	65	41.2	20.9	4.3	9.2	0.1	0.1	0.4	5.58E-04	3.86E-04	1.22E-04	13.4	9.17	8.89	21.91
10	493	65.3	130	52.7	21.0	5.1	10.6	0.1	0.0	0.3	7.12E-04	5.40E-04	1.09E-04	8.31	4	8.8	15.32
11	513	65.3	130	52.7	21.1	4.6	10.2	0.3	0.1	0.6	1.68E-03	1.11E-03	4.18E-04	19.64	11.14	9.31	24.82
12	513	28.3	60	14.7	20.9	3.4	10.6	0.8	0.2	1.0	1.65E-03	9.83E-04	5.13E-04	44.48	18.59	9.14	31.15
13	513	36.2	91	36.8	21.2	3.3	10.5	0.5	0.2	0.7	1.59E-03	9.62E-04	4.54E-04	33.42	15.59	10.7	28.62
14	513	26.5	60	43.5	21.4	2.9	8.5	0.6	0.2	0.6	1.31E-03	7.52E-04	4.26E-04	37.79	19.73	10.19	32.48
15	513	38.9	90	121.1	21.2	2.7	6.6	0.3	0.1	0.3	1.12E-03	6.17E-04	3.69E-04	21.97	17.22	11.82	32.97
16	513	65.3	130	52.7	21.2	4.6	10.2	0.3	0.1	0.6	1.69E-03	1.10E-03	4.27E-04	19.71	11.14	9.72	25.33
17	513	32.7	65	221.3	21.4	1.9	3.5	0.2	0.0	0.1	7.56E-04	3.70E-04	2.98E-04	17.68	22.22	11.76	39.38
18	513	61.8	124	18.2	21.2	5.0	11.9	0.4	0.1	0.8	1.93E-03	1.27E-03	4.82E-04	23.81	9.89	9.3	24.99
19	513	29.1	59	101.9	21.3	2.5	5.5	0.3	0.1	0.3	1.02E-03	5.42E-04	3.70E-04	26.74	20.57	10.58	36.3
20	513	45.9	93	133.1	21.1	3.0	6.3	0.2	0.1	0.3	1.15E-03	6.65E-04	3.65E-04	19.19	17.36	10.61	31.71
21	513	65.3	130	52.7	21.2	4.6	10.2	0.3	0.1	0.6	1.72E-03	1.11E-03	4.39E-04	20.05	11.13	9.6	25.6
22	523	65.3	130	52.7	21.3	4.1	9.9	0.6	0.2	0.7	2.63E-03	1.56E-03	8.11E-04	30.78	16.4	10.04	30.81
23	523	33.6	68	32.4	21.2	2.9	8.8	1.1	0.3	0.9	2.24E-03	1.22E-03	7.93E-04	50.98	25.46	10.1	35.4
24	523	37.1	74	19.9	21.2	3.0	10.0	1.2	0.4	1.1	2.63E-03	1.46E-03	9.08E-04	54.14	24.16	10.04	34.51
25	523	25.6	138	51.4	21.3	0.9	12.6	0.5	0.4	0.7	2.26E-03	1.11E-03	6.73E-04	67.26	12.12	20.76	29.86
26	523	65.3	130	52.7	21.1	4.0	9.7	0.6	0.2	0.8	2.76E-03	1.66E-03	8.28E-04	32.2	17.72	9.98	30
27	523	83.0	167	28.0	21.3	4.6	11.5	0.6	0.2	0.9	3.31E-03	2.05E-03	9.26E-04	30.48	14.41	10.09	27.94
28	523	83.9	170	21.1	21.3	4.8	11.9	0.6	0.2	0.9	3.33E-03	2.02E-03	9.59E-04	30.3	13.93	10.46	28.82
29	523	65.3	130	52.7	21.3	4.0	9.9	0.6	0.2	0.7	2.76E-03	1.56E-03	9.03E-04	32.19	16.65	10.73	32.76
30	533	65.3	130	52.7	21.3	3.2	9.4	1.1	0.3	0.8	4.09E-03	2.14E-03	1.49E-03	47.82	23.51	11.12	36.5
31	533	36.2	153	61.8	21.3	0.9	11.3	0.8	0.5	0.9	3.47E-03	1.66E-03	1.13E-03	73.16	20.16	19.39	32.68
32	533	46.8	148	23.2	21.5	1.5	12.6	1.2	0.6	1.3	4.39E-03	2.27E-03	1.44E-03	71.58	22.17	15.61	32.72
33	533	55.6	130	31.4	21.4	2.4	10.7	1.3	0.5	1.1	4.38E-03	2.33E-03	1.52E-03	60.1	24.99	12.27	34.61
34	533	46.8	140	32.2	21.3	1.6	11.6	1.2	0.5	1.2	4.18E-03	2.17E-03	1.40E-03	68.23	23.98	14.84	33.35
35	533	65.3	130	52.7	21.5	3.1	9.3	1.1	0.3	0.9	4.29E-03	2.32E-03	1.51E-03	50.1	25.21	10.84	35.09
36	533	65.3	153	25.7	21.5	2.6	11.4	1.3	0.5	1.2	5.11E-03	2.74E-03	1.74E-03	59.67	22.9	12.4	33.97
37	533	83.9	170	21.1	21.7	3.7	11.5	1.2	0.4	1.2	5.36E-03	2.95E-03	1.82E-03	48.82	22.4	11.1	33.84

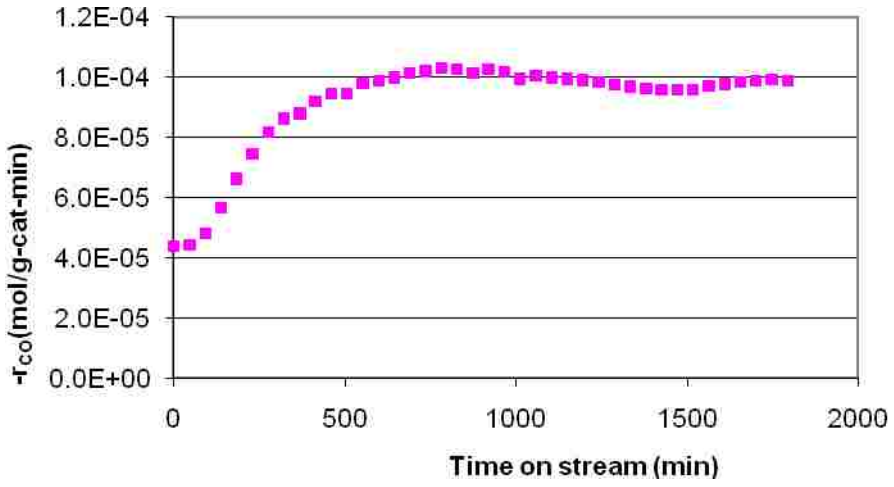

Figure 5-1: Carbon monoxide reaction rate as a function of time on stream for 20Fe1K1Pt-ALa-mon-507 obtained for Run 12 at 513 K and 21.1 atm absolute pressure with inlet flow rates at s.t.p. of 28.3 mL/min CO, 60.0 mL/min H_2 and 14.7 mL/min inert gas (He + Ar).

Table 5-2: Average values of rate and corresponding standard deviations for runs at standard flow conditions (74 mL/min CO/Ar, 130 mL/min H_2, and 44 mL/min He) at 493, 513, 523, and 533 K used to check catalyst stability during FTS on 20Fe1K1Pt-ALa-mon-507.

Temperature (K)	**Average of $-r_{CO}$ (mol/kg-cat-s)**	**Standard deviation of $-r_{CO}$ (mol/kg-cat-s)**
493	7.12×10^{-4}	7.51×10^{-6}
513	1.70×10^{-3}	1.74×10^{-5}
523	2.72×10^{-3}	7.13×10^{-5}
533	4.25×10^{-3}	1.46×10^{-4}

Table 5-3: Weisz Modulus for the kinetic runs for 20Fe1K1Pt-La-Ala507. Based on the Weisz criteria, the influence of pore diffusion on the observed reaction rates is insignificant.

Run	Weisz Modulus	Run	Weisz Modulus	Run	Weisz Modulus	Run	Weisz Modulus
1	6.96E-03	10	7.05E-03	19	2.13E-02	28	3.76E-02
2	7.54E-03	11	1.92E-02	20	2.01E-02	29	3.66E-02
3	7.78E-03	12	2.56E-02	21	1.96E-02	30	6.96E-02
4	1.01E-02	13	2.53E-02	22	3.44E-02	31	2.10E-01
5	6.12E-03	14	2.39E-02	23	4.20E-02	32	1.65E-01
6	7.20E-03	15	2.18E-02	24	4.67E-02	33	9.82E-02
7	8.68E-03	16	1.91E-02	25	1.39E-01	34	1.41E-01
8	6.87E-03	17	2.12E-02	26	3.69E-02	35	7.54E-02
9	6.58E-03	18	2.02E-02	27	3.83E-02	36	1.09E-01

Table 5-4: Parameter estimates as a function of run number during a sequential design of kinetic experiments based on D-optimal criteria using Equation 3.10 as response model for 20Fe1K1Pt-ALa-mon-507.

run	A1 (mol/kg-hr)	Ea (J/mol)	A2 (atm^{-1})	ΔH (J/mol)
22	9.19E+05	6.17E+04	4.42E-03	-1.33E+04
23	7.62E+05	6.05E+04	4.48E-03	-1.38E+04
24	1.04E+06	6.16E+04	2.01E-03	-1.75E+04
25	1.01E+06	6.10E+04	2.19E-03	-1.76E+04
26	1.09E+06	6.13E+04	1.90E-03	-1.81E+04
27	1.17E+06	6.20E+04	1.42E-03	-1.86E+04
28	1.20E+06	6.24E+04	1.27E-03	-1.86E+04
30	1.19E+06	6.19E+04	1.02E-03	-2.01E+04
31	1.25E+06	6.15E+04	1.12E-03	-2.04E+04
32	1.25E+06	6.15E+04	1.12E-03	-2.04E+04

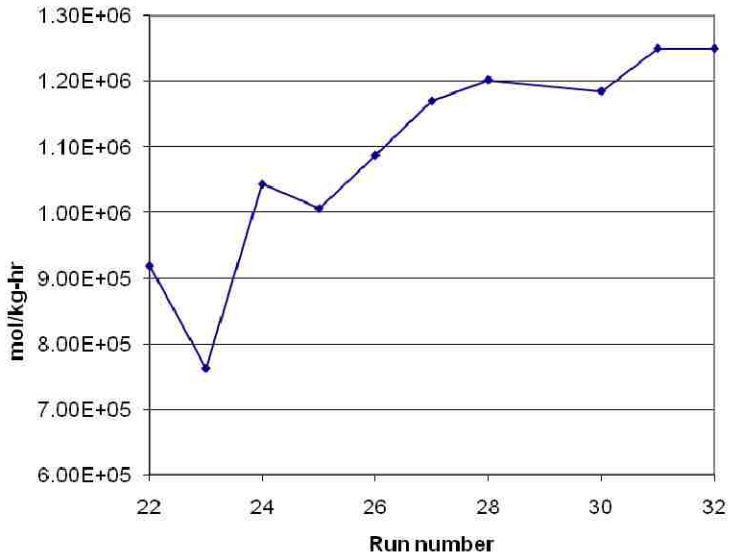

Figure 5-2: Estimated value of apparent pre-exponential factor (numerator) during sequential design of experiment based on D-Optimal criteria using Equation 3.10 as the response model for 20Fe1K1Pt-ALa-mon-507.

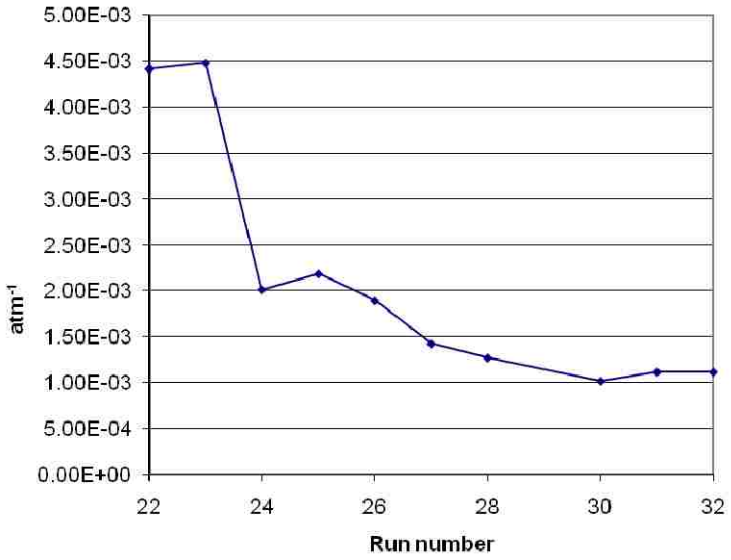

Figure 5-3: Estimated value of the apparent pre-exponential factor (denominator) during sequential design of experiment based on D-Optimal criteria using Equation 3.10 as the response model for 20Fe1K1Pt-ALa-mon-507.

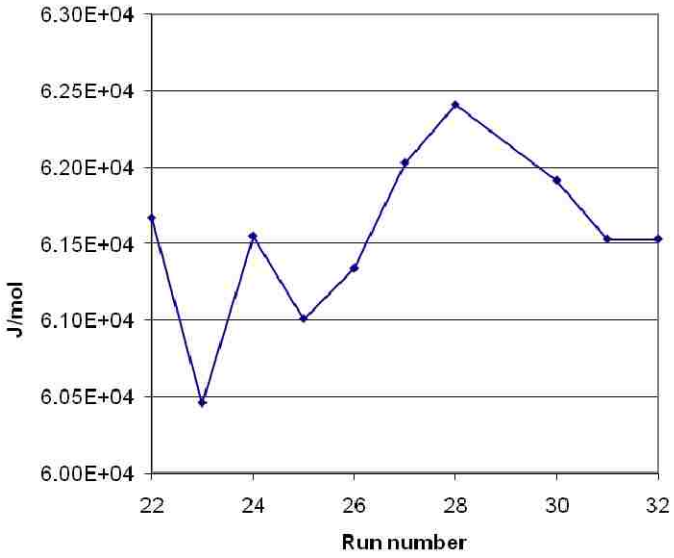

Figure 5-4: Estimated value of the apparent activation energy (numerator) during sequential design of experiment based on D-Optimal criteria using Equation 3.10 as the response model for 20Fe1K1Pt-ALa-mon-507.

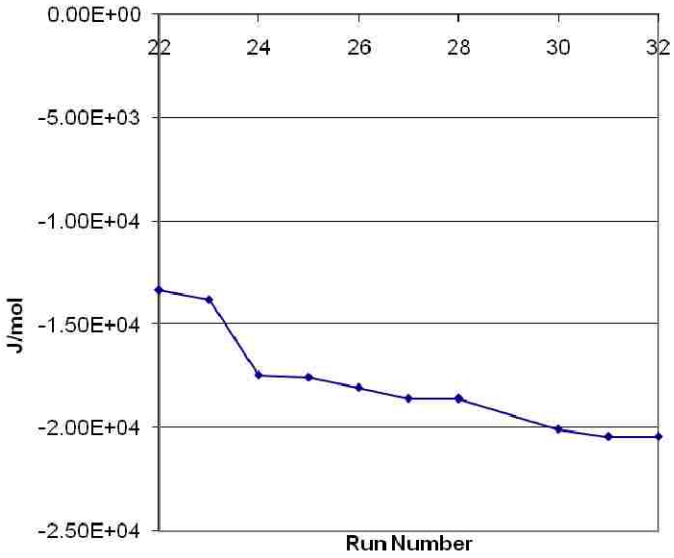

Figure 5-5: Estimated value of the apparent adsorption enthalpy (denominator) during sequential design of experiment based on D-Optimal criteria using Equation 3.10 as the response model for 20Fe1K1Pt-ALa-mon-507.

5.1.3 Steady-state macrokinetic models for 20Fe1K1Pt-ALa-mon-507

Four different Langmuir-Hinshelwood (LH) type rate expressions were developed by assuming various sequences of elementary steps and rate determining steps respectively. Thereafter, transition state theory was used to estimate the values of the apparent pre-exponential factors corresponding to these rate expressions. Multi-response nonlinear regression was used to fit the observed rates of CO disappearance and CO_2 formation (response variables) with reactor temperature, partial pressures of CO and H_2 as dependent variables. During the regression process, the estimated values of apparent pre-exponential-factors were constrained to lie within an order of magnitude of those estimated from transition state theory. The goodness of fit and 95% confidence were calculated using Polymath based on the converged parameter values. Derivation of the LH type rate expressions and calculation of apparent pre-exponential factors for the models are presented in the Appendix A.5.

5.1.3.1 Model 1

Model 1 is derived from the carbide mechanism, with the assumption that the rates of CO disappearance, hydrocarbon formation, and CO_2 formation are determined by the steps involving carbon hydrogenation and water formation (i.e. the reaction of adsorbed OH and H to form water). Additionally, surface carbon is assumed to be the most abundant surface intermediate (MASI). The set of elementary steps used in deriving this model is shown in Equation 5.1 while the LH type rate expression for this model is shown in Equation 5.2. During the nonlinear regression analysis, the rate

constants were written in Arrhenius form to enable the estimation of both the activation energies/heats of adsorption and pre-exponential factors.

Since the model assumes a series relationship between the disappearance of CO and the formations of hydrocarbons and CO_2, it follows that the rate of hydrocarbon formation and CO_2 formation is obtained by multiplying Equation 5.2 by the appropriate selectivity or stoichiometric ratio for this species from the overall reaction stoichiometry, if known.

$$\left.\begin{array}{l} CO_g + * \leftrightarrow CO*.....(1) \\ H_{2_{(g)}} + 2* \leftrightarrow 2H*.....(2) \\ CO* + * \leftrightarrow C* + O*.....(3) \\ C* + H* \rightarrow CH* + *...(4)(r.d.s.) \\ O* + H* \leftrightarrow OH* + *.....(5) \\ OH* + H* \rightarrow H_2O_{(g)} + 2*...(6)(r.d.s.) \end{array}\right\} \quad (5.1)$$

$$-r_{CO} = \frac{AP_{CO}^{1/2}P_{H_2}^{3/4}}{\left(1 + BP_{CO}^{1/2}P_{H_2}^{1/4}\right)^2} \Rightarrow A = \left(k_4 k_6 K_5 K_1\right)^{1/2} K_2^{3/4} \quad (5.2)$$

Figure 5-6 and Figure 5-7 show parity plots for both CO and CO_2 rates obtained with this model, while Table 5-5 shows the model parameters.

The estimated apparent pre-exponential factors shown in Table 5-5 are within order of magnitude of those calculated from transition state theory (see Appendix A.5), for the numerator and denominator kinetic constants of 2.0 x 10^4 $atm^{-1.25}s^{-1}$ and 4.5 x 10^{-7} $atm^{-0.75}$ respectively (since it was constrained to be consistent with theory). Similarly, the estimated average CO_2 selectivity of 0.326 is approximately equal to that observed experimentally.

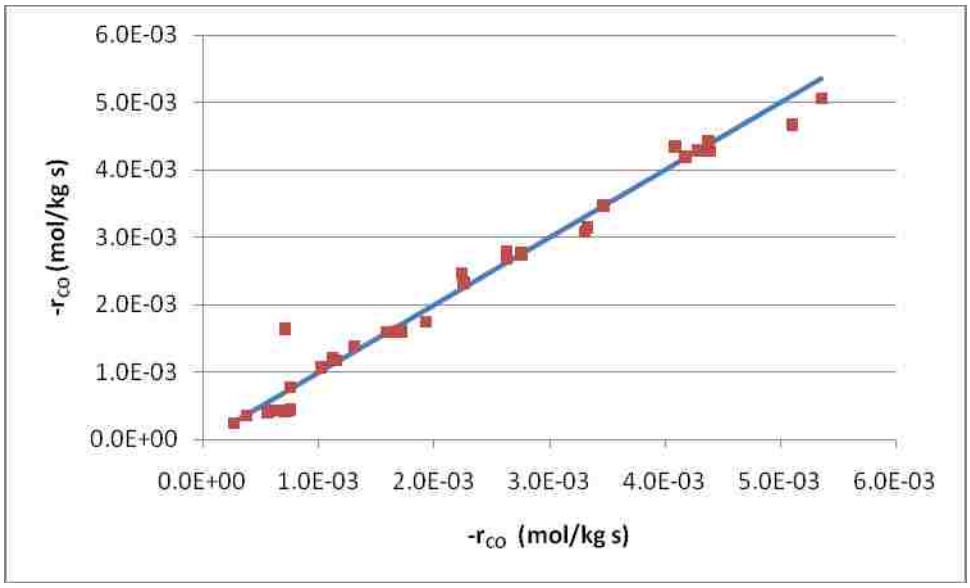

Figure 5-6: Parity plot for $-r_{CO}$ (mol/kg s) for 20Fe1K1Pt-ALa-mon-507 based on Equation 5.2.

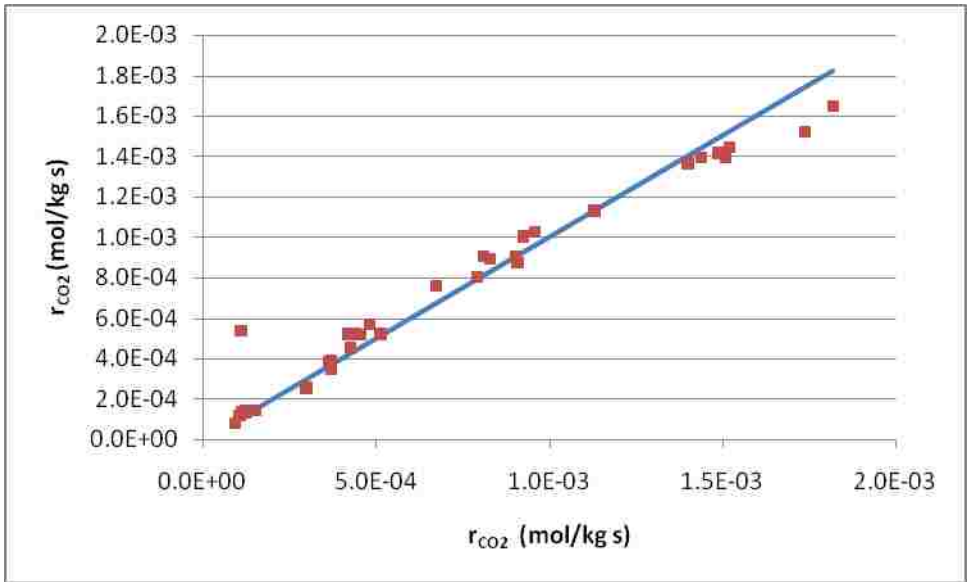

Figure 5-7: Parity plot for r_{CO2} (mol/kg s) for 20Fe1K1Pt-ALa-mon-507 based on Equation 5.2.

Table 5-5: Estimated kinetic parameters for Model 1 (Equation 5.2) above using 20Fe1K1Pt-ALa-mon-507 as catalyst. A_A and Ea_A are the apparent pre-exponential factor and activation energy, respectively, corresponding to the rate constant A, while A_B and ΔH_B are the pre-exponential factor and heat of adsorption for the rate coefficient B. A_3 is estimated from CO_2 selectivity.

Parameter	**Estimate**	**95% confidence interval**
A_A (mol/kg-s-atm$^{1.25}$)	1.0E5	4.66E5
A_B (atm$^{-0.75}$)	2.12E-7	2.02E-06
Ea_A (J/mol)	8.22E4	1.74E4
ΔH_B (J/mol)	-5.89E4	3.878E3
A_3(CO_2 Selectivity)	0.326	N/A
Correlation coefficient R^2	0.98	

5.1.3.2 Model 2

This model was derived from the carbide mechanism with similar rate determining steps as in Model 1 except that water is formed from the reaction of two adsorbed OH species. This step and the step involving carbon hydrogenation were assumed to be the rate determining steps. As in Section 5.1.3.1, carbon was still assumed to be the MASI. The elementary steps and the LH type rate expression for this model are shown in Equation 5.3 and Equation 5.4 respectively.

$$\left.\begin{aligned} &CO_g + * \leftrightarrow CO*.....(1)\\ &H_{2_{(g)}} + 2* \leftrightarrow 2H*.....(2)\\ &CO* + * \leftrightarrow C* + O*.....(3)\\ &C* + H* \rightarrow CH* + *...(4)(r.d.s.)\\ &O* + H* \leftrightarrow OH* + *.....(5)\\ &OH* + OH* \rightarrow H_2O_{(g)} + O* + *...(6)(r.d.s.) \end{aligned}\right\} \quad (5.3)$$

$$-r_{CO} = \frac{CP_{CO}^{2/3}P_{H_2}^{2/3}}{\left(1 + DP_{CO}^{2/3}P_{H_2}^{1/6}\right)^2} \Rightarrow C = k_4^{2/3}k_6^{1/3}K_5^{2/3}K_1^{2/3}K_2^{2/3} \quad (5.4)$$

Figure 5-8 and Figure 5-9 show the parity plots for the rates of CO disappearance and CO_2 formation respectively, while Table 5-6 lists the estimated model parameters.

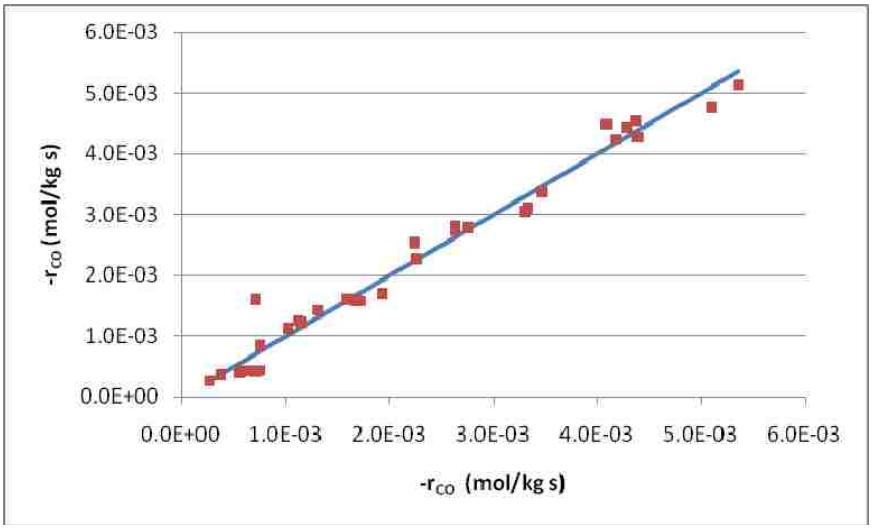

Figure 5-8: Parity plot for $-r_{CO}$ (mol/kg s) for 20Fe1K1Pt-ALa-mon-507 based on Equation 5.4.

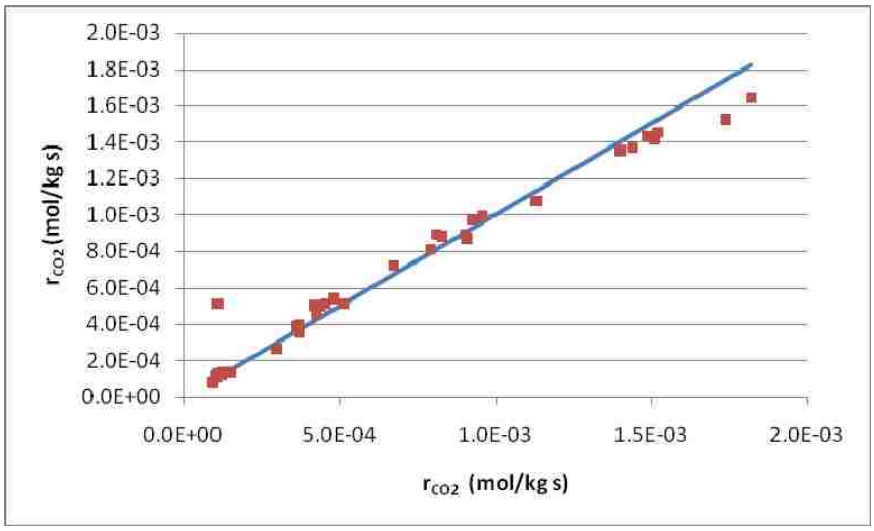

Figure 5-9: Parity plot for r_{CO2} (mol/kg s) for 20Fe1K1Pt-ALa-mon-507 based on Equation 5.4

Table 5-6: Estimated kinetic parameters for Model 2 (Equation 5.4) above using 20Fe1K1Pt-ALa-mon-507 as the catalyst. A_C and Ea_C are the apparent pre-exponential factor and activation energy corresponding to the rate constant C, while A_D and ΔH_D are the pre-exponential factor and heat of adsorption for the rate constant D. A_3 is estimated from CO_2 selectivity.

Parameter	**Value**	**95% confidence**
A_C (mol/kg-s-atm$^{4/3}$)	1.0E5	1.89E5
A_D (atm$^{-5/6}$)	1.32E-6	3.78E-5
Ea_C (J/mol)	8.12E4	8.16E1
ΔH_D (J/mol)	-5.22E4	1.14E2
A_3(CO_2 Selectivity)	0.32	N/A
Correlation coefficient R^2	0.98	

As with Model 1, the estimated apparent pre-exponential factors shown in Table 5-6 are within an order of magnitude of those calculated from transition state theory (see Appendix A.5), for the numerator and denominator kinetic constants of 1.7 x 10^4 $atm^{-4/3}s^{-1}$ and 4.5 x 10^{-7} $atm^{-5/6}$ respectively. Similarly, the estimated average CO_2 selectivity of 0.326 is approximately equal to that observed experimentally.

5.1.3.3 Model 3

Model 3 is based on a formyl mechanism, i.e. adsorbed H and CO react to form a CHO intermediate, which is further hydrogenated to form CH and OH species. The basic assumptions for this model are (1) hydrogenation of CHO to form CH and OH species as the rate determining step, and (2) adsorbed CO as MASI. The elementary steps and the corresponding LH type rate expression for this model are shown in Equation 5.5 and Equation 5.6 respectively.

$$\left.\begin{aligned} &CO_g + * \leftrightarrow CO*.....(1)\\ &H_{2(g)} + 2* \leftrightarrow 2H*.....(2)\\ &CO* + H* \leftrightarrow CHO* + *....(3)\\ &CHO* + H* \rightarrow CH* + OH*...(4)(r.d.s.) \end{aligned}\right\} \quad (5.5)$$

$$-r_{CO} = \frac{EP_{CO}P_{H_2}}{\left(1 + K_1P_{CO}\right)^2} \Rightarrow E = k_4K_3K_2K_1 \quad (5.6)$$

Figure 5-10 and Figure 5-11 show the parity plots for the rates of CO disappearance and CO_2 formation respectively, while Table 5-7 shows the estimated model parameters.

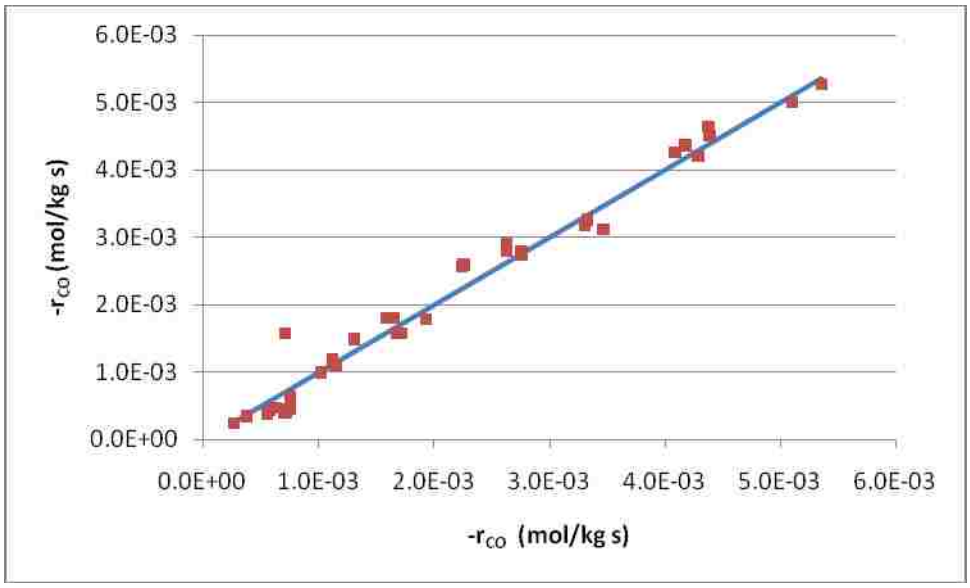

Figure 5-10: Parity plot for $-r_{CO}$ (mol/kg s) for 20Fe1K1Pt-ALa-mon-507 based on Equation 5.6

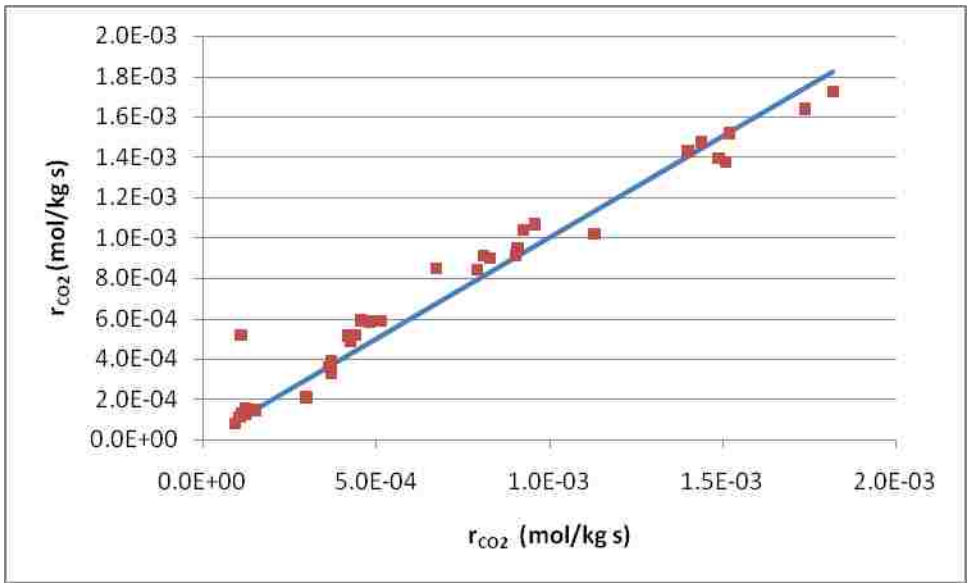

Figure 5-11: Parity plot for r_{CO2} (mol/kg s) for 20Fe1K1Pt-ALa-mon-507 based on Equation 5.6

Table 5-7: Estimated kinetic parameters for Model 3 (Equation 5.6) above using 20Fe1K1Pt-ALa-mon-507 as catalyst. A_E and Ea_E are the apparent pre-exponential factor and activation energy corresponding to the rate constant E, while A_F and ΔH_F are the pre-exponential factor and heat of adsorption for the rate constant F. A_3 is the estimated CO_2 selectivity.

Parameter	**Value**	**95% confidence interval**
A_E (mol/kg-s-atm^2)	4.47×10^{-1}	5.46×10^{1}
A_F (atm^{-1})	9.69×10^{-9}	1.2×10^{-4}
Ea_E (J/mol)	3.05×10^{4}	1.64×10^{4}
ΔH_F (J/mol)	-7.56×10^{4}	1.34×10^{3}
A_3(CO_2 Selectivity)	0.32	N/A
Correlation coefficient R^2	0.98	

As with Models 1 and 2, the parity plots for both CO and CO_2 show very good fits. Moreover, the estimated pre-exponential factors are within an order of magnitude when compared to those calculated from transition state theory (2.2×10^{-2} atm^{-2} s^{-1} and 4.3×10^{-9} atm^{-1}; see Appendix A.5). However, the estimated activation energy of 30.5 kJ/mol was much smaller than those estimated for Models 1 and 2 above. Nevertheless, the estimated CO_2 selectivity of 0.32 was similar to the average observed CO_2 selectivity (see Table 5-1).

5.1.3.4 Model 4

This model assumes that FTS occurs through two parallel mechanisms – carbide and formyl mechanisms respectively. As such, the rate of CO disappearance is a summation of two parallel mechanisms. For the carbide mechanism, CO dissociation is

assumed to be the rate determining step while for the formyl mechanism, the reaction of CHO with H to form CH and OH is assumed to be the rate determining step similar to Model 3. Furthermore, CO_2 was assumed to be formed through the carbide mechanism alone. The elementary steps and LH type rate expression for the disappearance of CO are shown in Equations 5.7 and 5.8, respectively, while the LH rate expression for the formation of CO_2 is shown in Equation 5.9.

$$\left.\begin{array}{l} CO_g + * \leftrightarrow CO*.....(1) \\ H_{2_{(g)}} + 2* \leftrightarrow 2H*.....(2) \\ CO* + H* \leftrightarrow CHO* + *....(3) \\ CHO* + H* \rightarrow CH* + OH*...(4)(r.d.s.) \\ CO* + * \rightarrow C* + O*.....(5)(r.d.s.) \end{array}\right\} \quad (5.7)$$

$$-r_{CO} = \frac{EP_{CO}P_{H_2} + FP_{CO}}{\left(1 + K_1 P_{CO}\right)^2} \Rightarrow E = k_4 K_3 K_1 K_2 \Rightarrow F = k_5 K_1 \quad (5.8)$$

$$r_{CO_2} = \frac{FP_{CO}}{\left(1 + K_1 P_{CO}\right)^2} \Rightarrow F = k_5 K_1 \quad (5.9)$$

In fitting Equations 5.8 and 5.9 to the data, *F* was multiplied by a constant to account for the stoichiometry resulting from the CO dissociation step in terms of the overall reaction stoichiometry. Since this value is unknown, it was estimated during the regression.

Figure 5-12 and Figure 5-13 show the parity plots for the rates of CO disappearance and CO_2 formation respectively, while estimated model parameters are listed in Table 5-8.

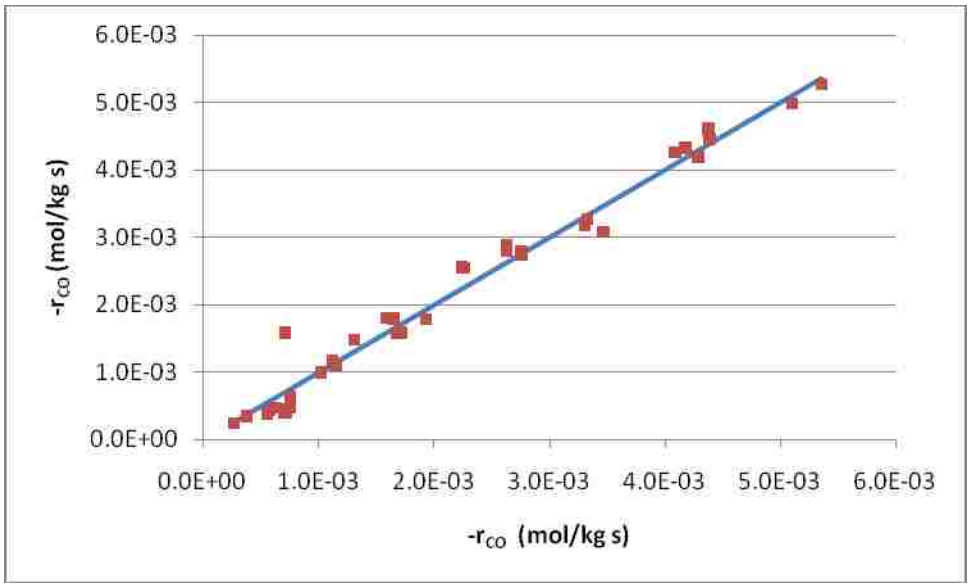

Figure 5-12: Parity plot for $-r_{CO}$ (mol/kg s) for 20Fe1K1Pt-ALa-mon-507 based on Equation 5.8.

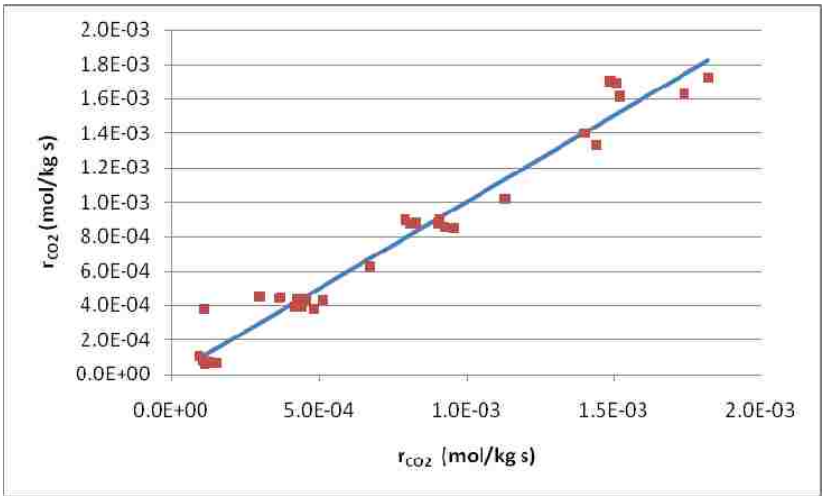

Figure 5-13: Parity plot for r_{CO2} (mol/kg s) for 20Fe1K1Pt-ALa-mon-507 based on Equation 5.9.

Table 5-8: Estimated kinetic parameters for Model 4 (Equations 5.8 and 5.9) above using 20Fe1K1Pt-ALa-mon-507 as the catalyst. A_E and Ea_E are the apparent pre-exponential factor and activation energy corresponding to the rate constant E, while A_F and Ea_F are the pre-exponential factor and heat of adsorption for the rate constant F. A_1 and ΔH_1 are the pre-exponential factor and heat of adsorption for the constant K_1. A_3 iand A_4 are factors to account for selectivity for each reaction pathway.

Parameter	Value
A_E (mol/kg-s-atm^2)	6.54E-1
A_F (mol/kg-s-atm)	3.81E4
A_1 (atm^{-1})	1.059E-8
Ea_E (J/mol)	3.23E4
Ea_F (J/mol)	7.74E4
ΔH_1 (J/mol)	-7.51E4
A_3(F factor for CO)	1.7
A_4(F factor for CO2)	9.5E-8
Correlation coefficient R^2	0.98

As with the previous models, the parity plots for both CO and CO_2 showed very good fits. Moreover, the estimated pre-exponential factors are within an order of magnitude when compared to those calculated from transition state theory

5.1.4 Validation of macrokinetic model

Using a FTS fixed-bed reactor (FBR) code for Fe catalyst developed in the BYU Catalysis lab [165], the accuracy of the kinetic models presented in the previous section 5.1.3 was validated against published FTS data on Fe catalysts for pilot and demo plants respectively available largely in [7] or in references cited therein.

The procedure for determining the best match of reported and calculated output/performance parameters was as follows: (1) specified operating parameters and process characteristics were entered into the input of the FBR design code; (2) unspecified input/operating parameters and reactor/-catalyst characteristics needed for the FBR design code were chosen based on reasonable values from the literature or based on experience; (3) the code was run to determine if calculated performance parameters could be obtained in reasonable agreement with reported parameters; and (4) based on the comparison, unspecified input parameters were adjusted to enable better matching of the outputs. Table 5-9 shows calculated plant input/output parameters using Model 1 versus those reported for both FTS pilot and demo plants.

5.2 Development of a Microkinetic Model With Data from Steady State Experiments with 20Fe1K1Pt-ALa-mon-507

Steady-state kinetic data collected at conditions similar to industrial FTS operations in Table 5-1 were used to develop a microkinetic model. C, O, and H binding energies determined from these data were then used in a UBI-QEP framework to determine activation energies of plausible elementary reactions that occur during FTS.

The procedure for estimating the binding energies of C, O, and H respectively was (a) derive a LH type rate expression, (b) guess the values of C, O, and H respective binding energies and the corresponding apparent pre-exponential factors, (c) use UBI-QEP to calculate the activation energies for the elementary steps in the reaction sequence used to derive the LH type rate expression, (d) calculate the apparent activation energies

Table 5-9: Validation of the Fe kinetic model using data from pilot and demonstration plant facilities [Wang et al., 2003] and Fe fixed bed FTS reactor design code developed at BYU catalysis lab. The kinetic model used in the simulations was Model 1 [165].

Parameter	Fe/K/Cu (Pilot Plant)		Fe/K/Cu (Demo Plant)	
	Reported	**Assumed/ Calculated**	**Reported**	**Assumed/ Calculated**
Input/Operating Parameters				
Syngas flowrate (SCFH)	8,822		132,328	
% CO (% CO_2)	14.1 (22.7)		14.1 (22.7)	
H_2/CO Ratio	3.48		3.48	
Inlet Temp (K)	515	520	–	518.2
Pressure in (bar)	25		25.2	
Recycle Ratio	3.5		3.3	
CO conversion (%)	70		74	
C_{2+} Selectivity		65.5		65.5
CH_4 Selectivity		4.5		4.5
CO_2 Selectivity (% of CO converted)		30.0		30.0
Reactor/Catalyst Characteristics				
Tube diameter (cm)	3.2		3.8	
Number of tubes	114		1,327	
Cooling water Temp (K)	523		518.2	
Catalyst particle diameter (mm)	2.5		2.5	
Bed void fraction	–	0.44	–	0.35
Catalyst activity	–	1.31	–	2.50
Output/Performance Parameters				
Effectiveness factor	–	0.35	–	0.55
Space velocity (h^{-1})	**425**	**430**	**324**	**219**
Pressure drop (atm)	**–**	**0.03**	**-**	**0.04**
Tube length (m)	**4.0**	**4.0**	**8.0**	**6.9**
Catalyst charge (m^3)	**0.37**	**0.37**	**10.5**	**10.4**
Catalyst productivity (g_{C5+}/g_{cat}-h)	**0.021**	**0.025**	**-**	**0.014**
Maximum Temp (K)	**518**	**529**	**523**	**523**

and heats of adsorption from the calculated activation energies for the elementary steps, (e) determine the rates of CO conversion and CO_2 formation from the LH expression, (f) compare the calculated rates to the experimentally observed rates and compute the errors, (g) minimize the errors by changing the guessed values of binding energies of C, O, and H and the apparent pre-exponential factors. The values of the apparent pre-exponential factors were constrained to lie within an order of magnitude from those estimated from transition state theory shown in Appendix A.5.

Using the LH type expression developed in Section 5.1.3.1 (Model 1), the above procedure was used to estimate binding energies of C, O, and H of 629 kJ/mol, 624 kJ/mol and 244 kJ/mol respectively. The estimated binding energies were then used in the UBI-QEP framework to calculate the activation energies of the elementary reaction steps in FTS up to the formation of C_2 products shown in Table 5-10. The apparent activation energy and enthalpy of adsorption for Model 1 calculated from the activation energies for the relevant elementary steps are 82.1 kJ/mol and -54.8 kJ/mol. These values and the estimated pre-exponential factors are similar to the estimated parameters for Model 1 listed in Table 5-5.

The activation energies of 151 kJ/mol and 121 kJ/mol for C hydrogenation to CH and for OH hydrogenation to H_2O(g) in are consistent with the assumption that these two steps are the rate determining since they had the highest activation energies; nevertheless, the activation energy for the O hydrogenation to OH is 123 kJ/mol and thus could also be co-rate-determining. The algorithm for implementing the modeling described above is illustrated in Appendix A.10.

Table 5-10: Activation energies for plausible elementary reactions in FTS calculated using UBI-QEP method based on estimated binding energies of C, O, and H by using Model 1 to fit steady-state kinetic data for 20Fe1K1Pt-ALa-mon-507 catalyst.

Rxn #	Reactions	Forward activation energy (J/mol)	Reverse activation energy (J/mol)
1	$H_2(g) + 2* = 2H*$	2.16E+04	7.59E+04
2	$CO(g) + * = CO*$	0.00E+00	9.82E+04
3	$CO* + * = C* + O*$	1.17E+05	1.97E+05
4	$C* + H* = CH* + *$	1.51E+05	2.51E+04
5	$CH* + H* = CH_2* + *$	4.79E+04	1.05E+05
6	$CH_2* + H* = CH_3* + *$	1.99E+04	1.12E+05
7	$CH_3* + H* = CH_4(g) + 2*$	0.00E+00	2.87E+04
8	$O* + H* = OH* + *$	1.23E+05	5.23E+04
9	$OH* + H* = H_2O*$	3.92E+04	1.08E+05
10	$H_2O* = H_2O(g) + *$	1.90E+05	0.00E+00
11	$CO* + O* = CO_2* + *$	1.41E+05	0.00E+00
12	$CO_2* = CO_2(g) + *$	4.50E+04	0.00E+00
13	$CO* + H* = CHO* + *$	1.04E+05	0.00E+00
14	$CHO* + H* = CH_2O* + *$	3.61E+04	6.34E+04
15	$CH_2O* + H* = CH_2* + OH*$	7.20E+04	8.88E+04
16	$CH_2O* + H* = CH_3O* + *$	0.00E+00	1.10E+05
17	$CH_3O* + * = CH_3* + O*$	5.48E+04	7.23E+04
18	$CO* + H* = C* + OH*$	1.12E+05	1.21E+05
19	$OH* + H* = H_2O(g) + 2*$	1.21E+05	0.00E+00
20	$OH* + OH* = H_2O* + O*$	2.89E+03	1.43E+05
21	$CHO* + H* = CH* + OH*$	1.04E+05	9.06E+04
22	$CH* + CH* = C_2H_2*$	0.00E+00	2.08E+05
23	$CH_2* + CH_2* = C_2H_4*$	0.00E+00	1.71E+05
24	$CH* + CH_2* = C_2H_3*$	3.02E+04	1.37E+05

5.3 Results of Steady-State Kinetic Experiments on 99Fe1ALa-mon-907

Data from statistically designed steady-state kinetic experiments for 99Fe1ALa-mon-907 (monolith # 1) are shown on Table 5-11. The Data were collected as described in section 3.7.1. As in the study of 20Fe1K1Pt-ALa-mon-507, the stability of the catalyst at each temperature was monitored by periodically returning to a standard inlet composition (44 mL/min He, 74 mL/min CO/Ar, and 130 mL/min H_2). Data from Runs 1, 6, and 10 at 493 K and from Runs 11 and 16 at 513 K were run at this feed composition. Standard deviations in the rate of CO conversion at this standard composition and 493 K and 513 K were 3.6×10^{-4} and 6.2×10^{-4} respectively, which are within experimental error, indicating no significant loss of catalyst activity during the study.

Effects of pore diffusion were not calculated because of the difficulty in determining the thickness of the catalyst layer on the monolith. However, based on the method of preparation, the catalyst thickness for 99Fe1ALa-mon-907 is likely to be smaller than that of 20Fe1K1Pt-ALa-mon-507. Since the kinetic tests for 20Fe1K1Pt-ALa-mon-507 involved negligible pore diffusion resistance, it is safe to assume that intra-particle mass transfer resistance was negligible for the kinetic tests for 99Fe1ALa-mon-907.

5.3.1 Development of a microkinetic model for 99Fe1ALa-mon-907 based on steady-state kinetic data

The kinetic data presented in Table 5-11 were used to develop a microkinetic model as described in Section 5.2 above.

Table 5-11: Kinetic data obtained during statistically designed steady-state kinetic experiment for 99Fe1ALa-mon-907. Pressures are in atm absolute.

Run	Temp (K)	$V_{CO}o$ (mL/min) @s.t.p.	$V_{H2}o$ (mL/min) @s.t.p.	V_{Inert} (mL/min) @s.t.p.	P_{TOT} (atm)	P_{CO} (atm)	P_{H2} (atm)	P_{CO2} (atm)	P_{CH4} (atm)	P_{H2O} (atm)	$-r_{CO}$ (mol/kg-s)	r_{C2+} (mol/kg-s)	r_{CO2} (mol/kg-s)	X_{CO} (%)	X_{H2} (%)	Sel_{CH4} (%)	Sel_{CO2} (%)
1	493	65.3	130	52.7	21.4	4.9	10.1	0.1	0.1	0.8	2.3E-03	1.9E-03	1.5E-04	16.3	12.6	9.9	6.6
2	493	28.3	60	14.7	20.9	4.1	10.0	0.2	0.2	1.6	2.0E-03	1.6E-03	1.8E-04	32.6	22.4	8.0	9.2
3	493	36.2	91	36.8	21.0	3.7	10.1	0.1	0.1	1.0	1.9E-03	1.6E-03	1.5E-04	24.7	17.1	10.5	7.9
4	493	17.7	52	185.3	21.5	1.2	3.4	0.1	0.0	0.3	9.3E-04	6.7E-04	1.4E-04	24.7	25.6	12.8	14.9
5	493	38.9	90	121.1	21.2	2.9	6.6	0.1	0.1	0.4	1.2E-03	9.4E-04	1.3E-04	14.9	17.8	13.2	10.4
6	493	65.3	130	52.7	20.7	4.9	10.1	0.1	0.1	0.6	1.7E-03	1.4E-03	1.3E-04	12.2	8.7	12.8	7.6
7	493	31.8	72	21.2	21.1	4.0	10.4	0.1	0.1	1.3	1.9E-03	1.6E-03	1.6E-04	28.6	17.3	9.2	8.3
8	493	30.0	68	34.0	21.5	4.0	9.7	0.1	0.1	0.9	1.5E-03	1.1E-03	1.5E-04	22.7	16.7	11.1	10.0
9	493	31.8	65	41.2	21.2	4.1	8.7	0.1	0.1	0.8	1.3E-03	1.0E-03	1.4E-04	19.7	17.0	11.2	10.9
10	493	65.3	130	52.7	20.9	4.9	10.3	0.0	0.1	0.5	1.6E-03	1.3E-03	1.2E-04	11.5	7.2	13.1	7.3
11	513	65.3	130	52.7	21.4	4.4	9.6	0.2	0.2	1.1	3.6E-03	2.7E-03	5.0E-04	25.7	18.7	10.7	13.9
12	513	28.3	60	14.7	21.2	3.7	9.7	0.4	0.2	1.8	2.5E-03	1.9E-03	3.9E-04	42.0	27.9	8.8	15.3
13	513	36.2	91	36.8	21.5	3.5	10.2	0.2	0.2	1.2	2.4E-03	1.8E-03	3.2E-04	31.5	19.7	12.1	13.2
14	513	26.5	60	43.5	21.2	3.0	7.9	0.3	0.2	1.1	2.0E-03	1.4E-03	3.4E-04	34.8	24.9	11.0	17.2
15	513	38.9	90	121.1	21.5	2.7	6.6	0.1	0.1	0.5	1.8E-03	1.3E-03	2.8E-04	22.3	17.8	13.2	15.3
16	513	65.3	130	52.7	21.4	4.6	10.3	0.1	0.1	0.9	2.7E-03	2.1E-03	2.8E-04	19.3	9.6	11.9	10.6
17	513	32.7	65	221.3	21.4	1.9	3.5	0.1	0.1	0.2	1.2E-03	7.7E-04	2.5E-04	17.0	22.6	13.7	21.4
18	513	61.8	124	18.2	21.1	5.4	10.8	0.2	0.2	1.3	3.1E-03	2.4E-03	3.1E-04	23.3	23.3	11.2	10.2

Using the LH type expression developed in Section 5.1.3.1 (Model 1), binding energies of C, O, and H were estimated to be 747 kJ/mol, 481 kJ/mol and 270 kJ/mol respectively. These estimated binding energies were used in the UBI-QEP framework to calculate activation energies of the elementary reaction steps in FTS up to the formation of C_2 products (see Table 5-12). The apparent activation energy and heat of adsorption for Model 1 calculated from the activation energies for the relevant elementary steps are 55.0 kJ/mol and -23.1 kJ/mol respectively (see Table 5-13). Parity plots for r_{CO} and r_{CO2} are shown on Figure 5-14 and Figure 5-15, respectively.

The estimated apparent pre-exponential factors shown in Table 5-13 are within two orders of magnitude of those calculated from transition state theory (see Appendix A.5), for the numerator and denominator kinetic constants of 2.0×10^{4} $atm^{-1.25}s^{-1}$ and 4.5×10^{-7} $atm^{-0.75}$ respectively. Similarly, the estimated average CO_2 selectivity of 0.17 is approximately equal to that observed experimentally. The correlation coefficient of 0.81 obtained for this catalyst was less than 0.98 obtained for 20Fe1K1Pt-ALa-mon-507 probably due to less number of data points.

The LH type expression developed in Section 5.1.3.4 (Model 4) was also used to estimate the binding energies of C, O, and H; thereafter, the activation energies of plausible *elementary* steps occurring during FTS on Fe catalyst was calculated using UBI-QEP method. The binding energies of C, O, and H were estimated to be 497 kJ/mol, 766 kJ/mol and 270 kJ/mol respectively.

Table 5-12: Activation energies for plausible elementary reactions in FTS calculated using UBI-QEP method based on estimated binding energies of C, O, and Hof 7.47 x 10^5 J/mol, 4.81 x 10^5 J/mol, and 2.7 x 10^5 J/mol respectively by using Model 1 to fit steady-state kinetic data for 99Fe1ALa-mon-907 catalyst.

Rxn #	Reactions	Forward activation energy (J/mol)	Reverse activation energy (J/mol)
1	$H_2(g) + 2* = 2H*$	3.83E+04	5.31E+04
2	$CO(g) + * = CO*$	0.00E+00	9.47E+04
3	$CO* + * = C* + O*$	1.42E+05	1.52E+05
4	$C* + H* = CH* + *$	1.35E+05	3.01E+04
5	$CH* + H* = CH_2* + *$	3.22E+04	1.12E+05
6	$CH_2* + H* = CH_3* + *$	4.49E+03	1.19E+05
7	$CH_3* + H* = CH4(g) + 2*$	0.00E+00	4.01E+04
8	$O* + H* = OH* + *$	1.01E+05	6.00E+04
9	$OH* + H* = H_2O*$	1.58E+04	1.16E+05
10	$H_2O* = H_2O(g) + *$	1.52E+05	0.00E+00
11	$CO* + O* = CO_2* + *$	8.52E+04	0.00E+00
12	$CO_2* = CO_2(g) + *$	3.70E+04	0.00E+00
13	$CO* + H* = CHO* + *$	8.69E+04	0.00E+00
14	$CHO* + H* = CH_2O* + *$	2.19E+04	7.21E+04
15	$CH_2O* + H* = CH_2* + OH*$	8.39E+04	6.41E+04
16	$CH_2O* + H* = CH_3O* + *$	0.00E+00	9.40E+04
17	$CH_3O* + * = CH_3* + O*$	5.91E+04	6.17E+04
18	$CO* + H* = C* + OH*$	1.21E+05	8.98E+04
19	$OH* + H* = H_2O(g) + 2*$	5.14E+04	0.00E+00
20	$OH* + OH* = H_2O* + O*$	0.00E+00	1.41E+05
21	$CHO* + H* = CH* + OH*$	1.39E+05	3.19E+04
22	$CH* + CH* = C_2H_2*$	1.14E+05	1.43E+05
23	$CH_2* + CH_2* = C_2H_4*$	6.77E+04	1.17E+05
24	$CH* + CH_2* = C_2H_3*$	1.22E+05	9.27E+04

Table 5-13: Estimated kinetic parameters for Equation 5.2 using the microkinetic model shown on Table 5-12 for 99Fe1ALa-mon-907 catalyst. A_A and Ea_A are the apparent pre-exponential factor and activation energy corresponding to the rate constant A, while A_B and ΔH_B are the pre-exponential factor and heat of adsorption for the rate constant F. A_3 is the estimated CO_2 selectivity.

Parameter	Value	95% confidence
Ea_A (J/mol)	5.50E+04	2.03E+04
ΔH_B (J/mol)	-2.31E+04	3.69E+04
A_A (mol/kg s $atm^{1.25}$)	1.00E+02	2.31
A_B ($atm^{-0.75}$)	5.18E-09	3.87E-04
A_3 (CO_2 Selectivity)	1.17E-01	N/A
R^2	8.10E-01	

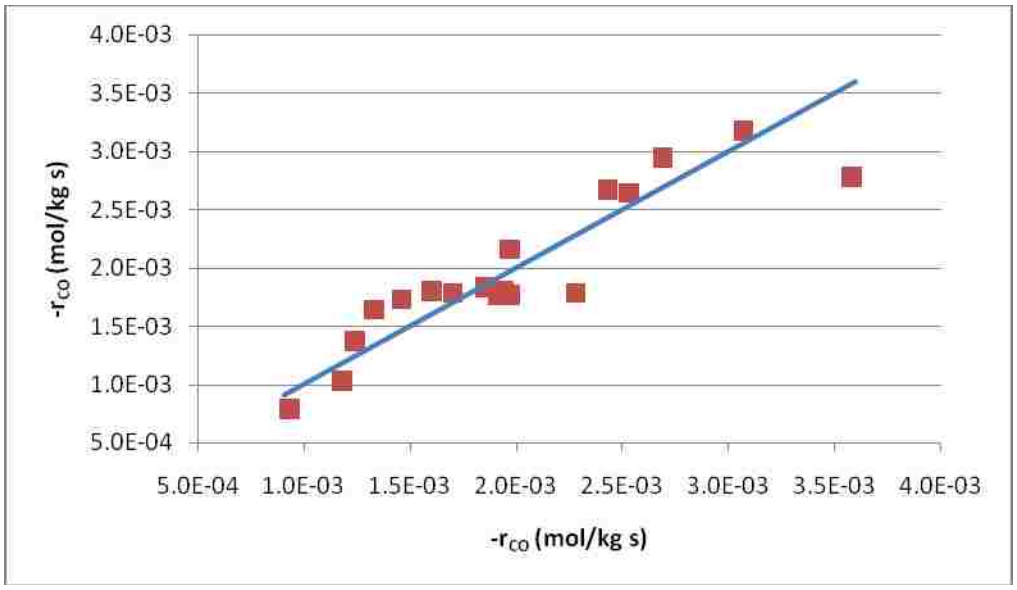

Figure 5-14: Parity plot for $-r_{CO}$ (mol/kg s) for 99Fe1ALa-mon-907 based on Equation 5.2 and microkinetic model shown in Table 5-12.

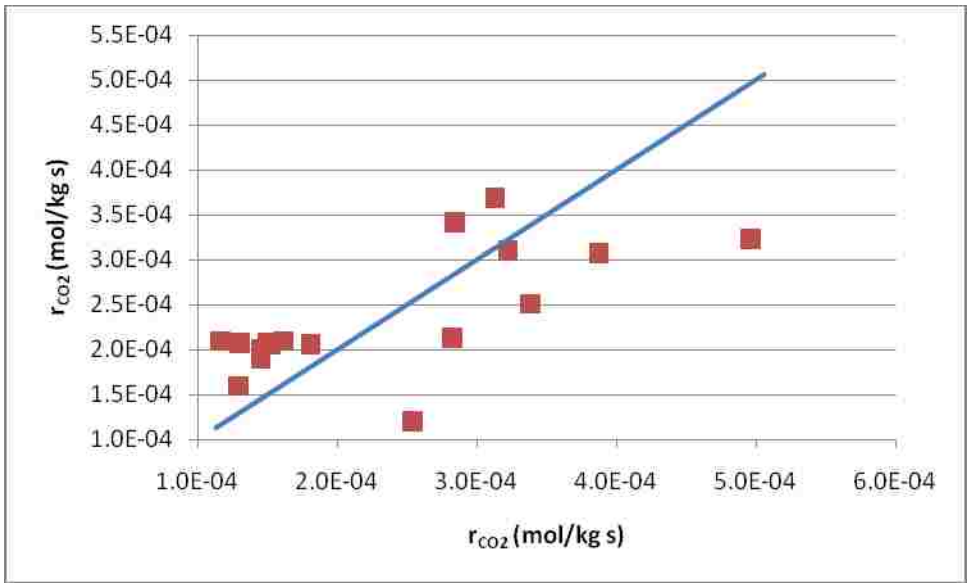

Figure 5-15: Parity plot for r_{CO2} (mol/kg s) for 99Fe1ALa-mon-907 based on Equation 5.2 and microkinetic model shown in Table 5-12.

The calculated activation energies for plausible elementary steps in FTS based on Model 4 and the UBI-QEP method are tabulated on Table 5-14 while the calculated apparent activation energies for Model 4 and estimated apparent pre-exponential factors for the same model are tabulated on Table 5-15. The corresponding parity plots for r_{CO} and r_{CO2} are shown in Figure 5-16 and Figure 5-17, respectively.

The parity plots for the rates of CO and CO_2 respectively for 20Fe1K1Pt-ALA-mon-507 showed better fits than those for 99Fe1Ala-mon-907 probably due to higher variability in the observed rates due to temperature fluctuations. As in 5.1, the correlation coefficients for the fits with Models 1 and 2 are statistically indistinguishable and as such cannot be used in this case to discriminate against either of the models. Additional discussion on this subject is provided in Chapter 6.

Table 5-14: Activation energies for FTS on 99Fe1ALa-307 catalyst based on analysis of steady state kinetic data from the Berty reactor. The activation energies were calculated with the UBI-QEP method with C, O, and H binding energies of 7.47 x 10^5 J/mol, 4.81 x 10^5 J/mol, and 2.7 x 10^5 J/mol respectively. The "=" sign implies that the reaction is reversible.

Rxn #	Reactions	Forward activation energy (J/mol)	Reverse activation energy (J/mol)
1	$H_2(g) + 2* = 2H*$	1.01E+02	1.05E+05
2	$CO(g) + * = CO*$	0.00E+00	6.48E+04
3	$CO* + * = C* + O*$	8.91E+04	2.13E+05
4	$C* + H* = CH* + *$	1.54E+05	2.12E+04
5	$CH* + H* = CH_2* + *$	4.20E+04	9.91E+04
6	$CH_2* + H* = CH_3* + *$	6.60E+03	1.07E+05
7	$CH_3* + H* = CH4(g) + 2*$	0.00E+00	4.50E+04
8	$O* + H* = OH* + *$	1.58E+05	4.12E+04
9	$OH* + H* = H_2O*$	6.96E+04	1.05E+05
10	$H_2O* = H_2O(g) + *$	3.04E+05	0.00E+00
11	$CO* + O* = CO_2* + *$	2.29E+05	0.00E+00
12	$CO_2* = CO_2(g) + *$	6.67E+04	0.00E+00
13	$CO* + H* = CHO* + *$	1.53E+05	0.00E+00
14	$CHO* + H* = CH_2O* + *$	2.32E+04	5.54E+04
15	$CH_2O* + H* = CH_2* + OH*$	4.43E+04	9.58E+04
16	$CH_2O* + H* = CH_3O* + *$	0.00E+00	1.65E+05
17	$CH_3O* + * = CH_3* + O*$	5.58E+04	3.68E+04
18	$CO* + H* = C* + OH*$	1.21E+05	1.27E+05
19	$OH* + H* = H_2O(g) + 2*$	2.69E+05	0.00E+00
20	$OH* + OH* = H_2O* + O*$	3.26E+04	1.85E+05
21	$CHO* + H* = CH* + OH*$	7.91E+04	1.06E+05
22	$CH* + CH* = C_2H_2*$	0.00E+00	2.78E+05
23	$CH_2* + CH_2* = C_2H_4*$	0.00E+00	2.25E+05
24	$CH* + CH_2* = C_2H_3*$	0.00E+00	1.82E+05

Table 5-15: Estimated parameters for Langmuir-Hinshelwood rate expression (Equation 5-5) based on the microkinetic model below (Table 5-14) for 99Fe1ALa-mon-907

Parameter	Value	95% Confidence interval
Ea_1 (J/mol)	6.21E+04	1.32E+07
Ea_2 (J/mol)	2.43E+04	1.70E+05
ΔH_{CO} (J/mol)	-6.48E+04	1.34E+04
A_1 (mol/kg s)	1.68E-01	2.00E+03
A_2 (mol/kg s)	2.64E-01	25.9
A_{CO} (atm)	9.88E-09	1.20E-04
$CO_{2selectivity}$	1.17E-01	N/A
R^2	8.20E-01	

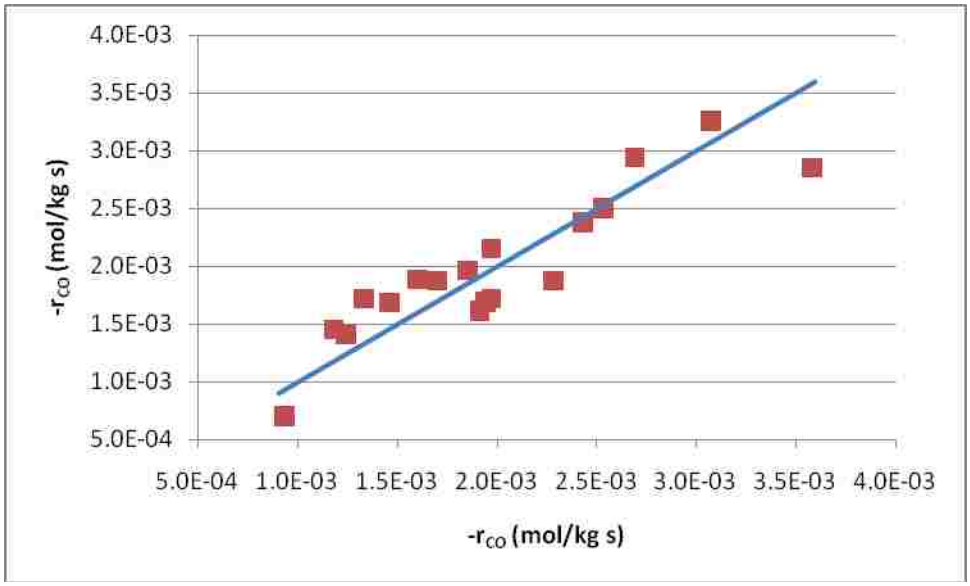

Figure 5-16: Parity plot showing observed rate of CO disappearance vs model predicted rate of CO disappearance using the activation energies of the elementary steps shown in Table 5-5 to calculate an apparent activation energies and heat of adsorption for the dual rate mechanism with the assumption that CO was the most abundant surface intermediate for 99Fe1ALa-mon-907 catalyst.

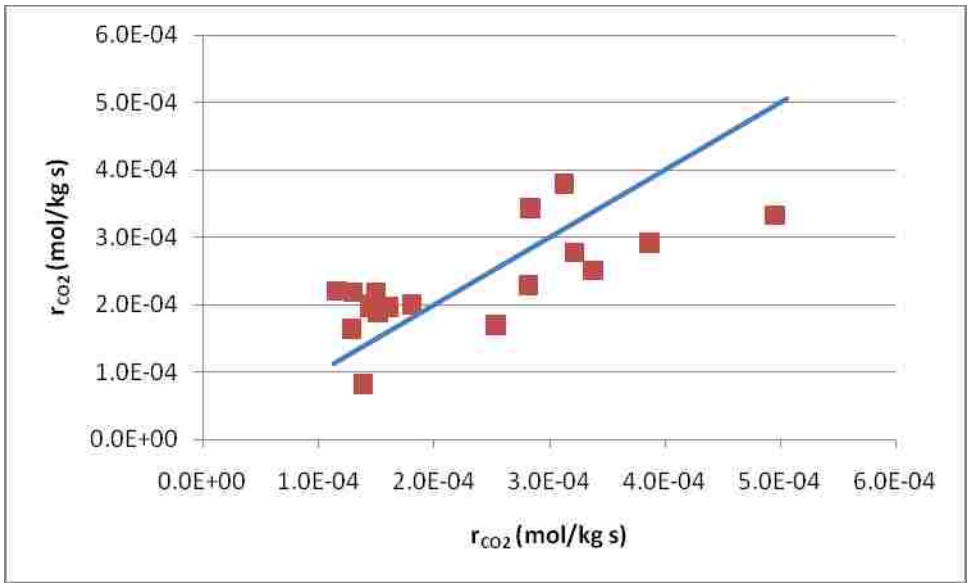

Figure 5-17: Parity plot showing observed rate of CO_2 formation vs model predicted rate of CO_2 formation using the activation energies of the elementary steps shown in Table 5-5 to calculate an apparent activation energies and heat of adsorption for the dual rate mechanism with the assumption that CO was the most abundant surface intermediate for 99Fe1ALa-mon-907 catalyst.

6. Chapter 6: Discussion

This dissertation work was part of a larger study funded by department of energy (DOE) in which the effects of promoters (e.g. K, Pt) on Fe catalyst were examined. However, due to time constraints, this work focused on only unsupported, unpromoted Fe and K, Pt promoted Fe supported on Al_2O_3. The larger study provides additional qualitative mechanistic information on promoted, unsupported Fe and unpromoted, supported Fe catalysts.

This chapter focuses on addressing the implications of the results presented in this work and the limitations thereof.

6.1 Catalyst Selection, Preparation, and Characterization

Two important classes of Fe catalysts were chosen for this study: (1) unsupported Fe representative of catalysts used in fixed-bed FTS, and (2) Al_2O_3 supported Fe representative of new attrition-resistant catalysts suitable for use in studying FTS reactions.

While more sophisticated methods for preparing stable, high surface area precipitated Fe FTS catalysts have been reported in the literature [141-143] for which BET surface areas range from 83 to 179 m^2/g, the emphasis in this study was however, on the preparation of stable Fe catalysts suitable for kinetic studies. Moderately-high BET

surface area of 86.8 m^2/g for the precipitated 99% Fe prepared in this study was adequate for evaluating desorption and reaction studies, while also favoring catalyst stability.

CO chemisorption was used as a measure of active site density because (1) CO chemisorption is an important, fundamental step in FTS mechanism and (2) evidence from previous spectroscopic studies [166] indicated that for moderately dispersed Fe (as in this study), the adsorption stoichiometry is one CO molecule per Fe site at room temperature. This suggested stoichiometry is also consistent with recent DFT studies [89, 167, 168]. Therefore, metal dispersion reported for the catalysts prepared in this study were based on CO uptake assuming a CO-metal adsorption stoichiometry of 1:1 at room temperature. Nevertheless, the broad-overlapping TPD thermogram observed for the 20% Fe catalyst suggests the existence of different CO adsorption sites and possible adsorbate species. Accordingly, the dispersions reported in this study are only approximate values and should be cross-checked with H_2 chemisorption uptake. CO uptake for 99Fe1ALa-mon-907 was about 5 times higher than that of 99Fe1ALa-307, though both catalysts were of similar composition. This disparity may be due to the difference in their preparation procedures, which may have affected the crystallite sizes: while 99Fe1ALa-307 was prepared by co-precipitation method, 99Fe1ALa-mon-907 was prepared by dipping the blank monolith in a melt of the nitrate precursors.

6.2 CO TPD

In a review article on TPD, Falconer et al. [124] presented various classical techniques for obtaining adsorbate heat of adsorption from TPD thermograms. The mathematical derivation of these techniques assumes that the adsorbate does not undergo additional reaction and that the fraction of vacant site (θ_v) is given by Equation 6.1,

$$\theta_v = 1 - \theta_A \tag{6.1}$$

where (θ_A) is the fractional coverage of adsorbate A. Equation 6.1 is valid for TPD if the adsorbate does not undergo further reaction other than desorbing as in the case of hydrogen. However, during CO TPD at atmospheric pressure, adsorbed CO not only desorbs but also undergoes additional reactions including dissociation to C and O, and reaction with adsorbed O to form CO_2. This is evident in the TPD thermograms for both 99% Fe and 20% Fe. As such, the vacant site fractional concentration cannot be predicted by Equation 6.1 and hence the classical method for obtaining heats of adsorption from TPD data may not accurately give the CO heat of adsorption from the analysis of CO TPD data obtained at atmospheric pressure. This possibly explains the reason why the trend in CO heats of adsorption as a function of coverage observed in this study was opposite to that expected when the classical method was used to determine CO heat of adsorption from CO TPD thermogram for the 20% Fe catalyst.

Mathematical models for TPD profiles at atmospheric pressure where re-adsorption is likely have been published [11, 121, 126]. These models were developed for cases where the adsorbate does not undergo further reaction (single adsorbate systems) and as such, the vacant site is given by Equation 6.1. Hence, they suffer the same limitations as the classical methods described previously. The microkinetic model for CO TPD on polycrystalline Fe catalyst presented in this work is a novel fundamental approach which accurately accounts for the coverages of all species present during CO TPD on Fe catalyst and enables estimation of the pre-exponential factors and activation energies for both forward and reverse steps for the elementary reactions occurring during

CO TPD on polycrystalline Fe at atmospheric pressure. Moreover, it does not assume that quasi-equilibrium conditions exist between the gas-phase and the adsorbate.

In developing the microkinetic model for CO TPD, a PFR reactor model was assumed. However, significant deviations from plug flow with significant dispersion were evident from tracer measurements. An attempt was made at modeling the TPD with a dispersion model but such a model increased the "stiffness" of the differential equations, making them too difficult to solve numerically. Hence the accuracy of the TPD microkinetic model is limited somewhat by deviations from ideal reactor flow. Nevertheless, the tracer profile is qualitatively closer to plug flow than mixed flow. Moreover, the deviations are not large enough to invalidate the results.

Although Langmuir isotherm assumes that heat of adsorption is independent of coverage, this is only valid for a unity desorption order. For non-unity desorption orders, it has been found that heat of adsorption is a function of coverage and has led to the development of other isotherms such as Temkin, and Freundlich isotherms to account for this coverage dependence [115] on the heat of adsorption. The CO TPD microkinetic model presented here, based on the Langmuir isotherm, does not take into consideration the variation of the heat of adsorption with coverage. Therefore, the resulting values of heats of adsorption from this microkinetic model are average values.

Kanervo et al. analyzed the effect effects of pore diffusion on TPD and suggested that pore diffusion resistance was negligible if (1) catalyst average particle size was less than 0.004 cm; (2) catalyst loading was greater than 150 mg; and (3) carrier gas flows was below 20 mL/min. For the TPD experiment reported in this work, these conditions were satisfied, hence justifying the omission of the effect of a pore diffusion model.

From a DFT study on CO adsorption and dissociation on Fe(100), Curulla-Ferre et al. reported a heat of adsorption for a 0.5 ML coverage of 183 kJ/mol for ontop and 172.8 kJ/mol for the bridged configurations and an activation energy of dissociation of 139 kJ/mol [169]. On the other hand, Vink et al. reported an experimental CO heat of adsorption of 100 kJ/mol ± 5 kJ/mol for Fe(100) at the zero coverage limit [170]. The heat of CO adsorption on polycrystalline Fe at zero coverage limit was estimated from this study to be 91.6 kJ/mol and 64.8 kJ/mol from ITH and FTS models respectively, while a mean value of 50.0 kJ/mol was estimated from TPD. Also, an activation energy for CO dissociation of 89.4 kJ/mol, and an activation energy for C and O recombination of 190 kJ/mol for polycrystalline Fe were estimated from the TPD model of this work. The existence of sites of varying coordination is typically prevalent in polycrystalline materials compared to well defined, smooth single crystal surfaces. Hence enthalpies of adsorption/activation energies observed for polycrystalline surfaces will differ from those of well defined single crystal surfaces. The difference in the CO heat of adsorption estimated from the three models was probably due to differences in carbon coverage and possible site rearrangement during FTS [7, 63, 171].

The carbon coverage profile predicted by the microkinetic model of this work (see Figure 4-9) indicates that the surface C fractional coverage of the Fe catalyst surface is at least 0.1 at the end of the desorption experiment. This is logical since the only way for C to leave the catalyst surface will be by reaction with O. However, some of the O formed during CO dissociation to C and O, reacts with adsorbed CO to form CO_2, hence creating a surface deficient in O.

6.3 Hydrogenation Experiments

The methane mole fraction verses temperature profiles during TPH for both 99Fe1ALa-307 and 20Fe1K1Pt-ALa-705 shown in Figure 4-12 and Figure 4-14 are characterized by multiple overlapping peaks and shifting peak maxima as FTS temperature was increased from 398 K to 493 K. Similar observations were made for CO mole fraction profiles as shown in Figure 4-13 and Figure 4-15. Xu and Bartholomew [30] observed similar trends during their TPH study on silica supported Fe after pretreatment in H_2 and concluded that at least four forms of carbon (which they identified as carbidic, amorphous, carbide, and graphitic) were formed on Fe surface during FTS. The ease of hydrogenation of these forms of carbon decreases in the order carbidic, amorphous, and graphitic. Eliason and Bartholomew [172] made similar observations in their TPH studies and their studies of deactivation of Fe catalyst during FTS. The observed shifts in CH_4 peak maxima during TPH after FTS for 5 min from 398 K to 493 K respectively suggest that CH_4 formation via hydrogenation of carbon species is not a single order reaction. Indeed, it can be inferred from the significant initial CO coverage that CH_4 is formed through parallel hydrogenations of CO and carbon species. Similarly, it can also be inferred that the methane produced within the first 4000 s of ITH is mostly from hydrogenation of carbidic carbon and adsorbed CO. The observed approach of the methane profile to a steady-state value after about 4000 s during ITH is likely due to the slow hydrogenation of amorphous, carbide, and perhaps graphitic forms of carbon since these carbon forms are much more difficult to hydrogenate at lower temperatures. The foregoing analysis perhaps explains why the ITH model presented in this work does not accurately predict CH_4 mole fraction profiles after about 4000 s because the model assumes only one form of carbon (carbidic carbon) to be present.

Examination of the net turnover frequency profile during ITH shown in Figure 4-27, for the elementary reaction shown in Equation 6.2, and the net turnover frequency shown in Figure 4-28, for the elementary reaction shown in Equation 6.3, shows that while the net turnover frequency for Reaction 6.2 rises quickly to a maximum value of about 2.7 x 10^{-5} s^{-1} within the first 4000 s, the net turnover frequency for Reaction 6.3 only rises to an approximate maximum value of 2.0 x 10^{-9} s^{-1}.

$$C* + H* \leftrightarrow CH* + * \tag{6.2}$$

$$CO* + H* \leftrightarrow CHO* + * \tag{6.3}$$

This suggests that although the CH_4 formation occurs via parallel reaction mechanisms, the contribution from the carbide mechanism is more significant than the contribution from the formyl mechanism. Similarly, examination of Figure 4-31 shows that direct CO dissociation is more favorable than hydrogen assisted CO dissociation during the early seconds of ITH. Although, the formyl mechanism does not play a significant role in hydrocarbon formation during FTS on Fe catalyst especially at low reaction temperatures, its contribution to hydrocarbon formation will become more significant at higher reaction temperatures because of the zero activation energy for the reverse reaction in Equation 6.3. Additionally, the formyl mechanism is perhaps a principal route for the formation of oxygenated compounds during FTS.

The accuracy of the microkinetic model presented here is limited to the accuracy of (1) the UBI-QEP formalism in calculating activation energies for elementary surface reactions; (2) transition state theory in predicting pre-exponential factors for elementary reactions considered in this model; (3) the reactor flow profile; and (4) errors in estimating the binding energies of C, H, and O. Additionally, heats of adsorption

calculated from the UBI-QEP formalism are only for the zero coverage limit, and would probably be different at higher coverages. While Aghalayam et al. [17] have suggested rigorous ways to account for coverage dependence in UBI-QEP, such a method was not utilized in this model due to its complexity and necessary limitations on time to conduct the present study. Nevertheless, multiplication of the forward pre-exponential factor calculated from transition state theory for either C hydrogenation or CO desorption step by a constant achieves essentially the same result as the sensitivity analysis proposed by Aghalayam et al. in their work on the construction and optimization of complex surface reaction mechanisms [17].

6.4 Steady-State Kinetic Experiments and Overall Microkinetic Model Formulation

The four LH type rate expressions developed in Chapter five fit the observed CO and CO_2 steady-state rate data well despite the assumption of different rate determining steps. This illustrates that obtaining a good data fit to an LH expression does not necessarily mean that the mechanism and underlying assumptions used to derive such a model are correct. However, building on the conclusions in the previous section of a parallel mechanism during FTS, it appears that LH type expressions derived from either the carbide or formyl mechanisms will produce good fits of the steady-state kinetic data with the error distributed across the estimated constants since both paths appear to play a role in FTS reaction on Fe.

Although the microkinetic models presented in Chapter four showed similar mechanisms to those in Chapter five, the activation energies for some of the elementary steps differed. The activation energies calculated in Chapter five using steady-state FTS

data at conditions similar to industrial operating conditions are probably more accurate than those calculated from the ITH experiments since the correct reactor flow model was unknown and the experimental conditions were not close to industrial FTS operation conditions. The optimized respective binding energies for C, O, and H from the various techniques used in this study and those from literature are shown in Table 6-1.

Table 6-1: Summary of optimized binding energies of C, O, and H from the techniques used in this study and those from literature.

	Binding Energies (kJ/mol)			**Comment**
	C	**O**	**H**	
Analysis of steady-state kinetic data for 20Fe1K1Pt-ALa-mon-507	629	624	244	
Analysis of steady-state kinetic data for 99Fe1ALa-mon-907	747	481	270	
Analysis of ITH data for 99Fe1ALa-307	605	450	250	
Analysis of ITH data for 20Fe1K1Pt-ALa-705	399	734	265	
Jiang et al. [163]	765 - 552	-	-	at 0.11 ML to 1 ML on Fe(110)
Blonski et al. [164]	-	628 - 290		from clean surface to 0.75 ML on Fe(110)
Storsaeter et al. [16]	678	485	251	On Co single crystal

The model from this work teaches that hydrocarbon formation during FTS on Fe catalyst occurs through parallel mechanisms (carbide and formyl). It also teaches that hydrocarbon formation via the carbide mechanism is more significant in unpromoted Fe

catalysts than in a supported K promoted Fe catalysts. On Co catalyzed FTS, Storaeter et al. [84] proposed a dual mechanism with hydrocarbon formation via formyl network as more significant than hydrocarbon formation via carbide mechanism. However, they also suggested that the mechanism for Co catalyzed FTS would be different from that of Fe catalyzed FTS since the product distributions from Co and Fe catalysts differ.

An average CO_2 selectivity of 0.30 was observed for the K promoted Fe catalyst compared to 0.17 observed for the un-promoted Fe catalyst. Li et al. [27] observed that K promotion increases the rate of water-gas-shift reaction, evidenced by the increase in CO_2 production. In the microkinetic model, for the K promoted Fe tabulated on Table 5-10, the forward activation energy for the formation of adsorbed CO_2 from the reaction of adsorbed CO and O was found to be 141 kJ/mol while that for the desorption of adsorbed CO_2 was 45 kJ/mol. By comparison, from Table 5-14, the forward activation energy for the formation of adsorbed CO_2 from adsorbed CO and O for unpromoted Fe was found to be 229 kJ/mol while that for the desorption of adsorbed CO_2 was 66.7 kJ/mol. The calculated activation energies for the reverse reactions for the elementary steps above were all found to equal zero. If CO_2 is formed only through the mechanisms considered in this work, then it follows that the difference in the CO_2 selectivity for K-promoted Fe and that of unpromoted Fe is due to the lower activation barriers in the formation and desorption of CO_2.

The activation energy for C hydrogenation to CH is 151 kJ/mol for K-promoted Fe and 154 kJ/mol for unpromoted Fe. For both catalysts, C hydrogenation is the rate determining step as opposed to the rate of CO dissociation, although the rate determining step may differ on Co and Ru catalyzed FTS reactions. The coupling reactions (1) CH –

CH; (2) $CH_2 – CH_2$; and (3) $CH – CH_2$ are non-activated for unpromoted Fe, while the third coupling step 3 has an activation energy of 30.2 kJ/mol on supported Fe/K. On the other hand, coupling step 1 has the highest reverse activation energies of 278 kJ/mol and 208 kJ/mol for unpromoted and K- promoted Fe catalysts respectively. Therefore, if the pre-exponential factors for these steps are equal, it follows that CH – CH coupling will proceed faster than $CH_2 – CH_2$ coupling or $CH – CH_2$ coupling since it is less reversible. This result is supported by the recent work on FTS mechanism on Co by Jun Cheng et al. [135] from DFT studies. Nevertheless, DFT calculations on F(100) by Lo et al. [87], suggest that the most favorable C_2 species on the Fe(100) surface are those containing acethylenic carbon i.e. $C – CH$, $C – CH_2$, and $C – CH_3$. Formation of these species was not investigated in this model, although the C_2 species investigated in this study could easily re-arrange to those species proposed by Lo et al. via hydride shifts.

The FTS microkinetic model presented in this work is incomplete, since it does not describe the formation of C_{3+} species, nevertheless, it can be extended to include the formation of higher hydrocarbons by applying the Evans – Polanyi correlation [11] to each family of reactions in this model. Because of the non-inclusion of the formation of higher hydrocarbons in the microkinetic model presented in this work, the overall FTS reaction rate can be determined from a LH type rate expression where the apparent kinetic constants (activation energies and pre-exponential factors) are obtained by combining the kinetic constants of the individual elementary reactions relevant to the derivation of LH type expression. Selectivity models will still be required to predict selectivity of higher hydrocarbons. Kinetic constants for a LH type expression derived in this manner are more accurate and will be thermodynamically consistent since it was

based on a more realistic chemistry on a molecular level. Although previous FTS kinetic studies based on LH type rate expressions have been reported [8, 33, 34, 55, 99, 100, 173-175], values of the kinetic constants were estimated arbitrarily without theoretical underpinnings, as such, they were not able to provide the activation energies and pre-exponential factors for the elementary steps used in the derivation of the LH type rate model. However, the approach used in this study provides LH type rate model with the kinetic constants are estimated on the fundamental chemistry and reactivity.

As stated in Chapter 2, kinetic studies of Fe catalyzed FTS did not start with this work. However, this work provides a robust FTS model with kinetic parameters for the relevant early elementary steps in FTS on Fe catalyst at conditions similar to industrial operations.

6.5 Thermodynamic Consistency

The activation energies and pre-exponential factors estimated in the ITH and FTS microkinetic models are thermodynamically consistent. Enthalpic consistency was guaranteed since this is inherent in the UBI-QEP formalism, while entropic consistency is also guaranteed by virtue of calculating the pre-exponential factors from transition state theory.

7. Chapter 7: Summary, Conclusion, Recommendations, and Future Work

In this chapter, a summary of the findings and limitations of this study are presented. Recommendations on how to overcome these limitations are suggested along with possibilities of future research work.

7.1 Summary

Fischer-Tropsch synthesis (FTS), developed in the early 1900's, is defined as the catalytic conversion of H_2 and CO to hydrocarbons and oxygenates with the production of H_2O and CO_2. Accurate microkinetic modeling can in principle provide insights into catalyst design, and the role of promoters. This work focused on gaining an understanding of the chemistry of the kinetically relevant steps in FTS on Fe catalyst, and developing a microkinetic model that described FTS reaction kinetics.

Stable supported/K-promoted and unsupported Fe catalysts were prepared and characterized. Transient experiments including temperature programmed desorption (TPD), temperature programmed hydrogenation (TPH), and isothermal hydrogenation (ITH) provided insights into the chemistry and energetics of the early elementary reactions in FTS on Fe catalysts. Microkinetic models of CO TPD, ITH, and FTS were developed for Fe catalyst by combining transition state theory and UBI-QEP formalism. These models support the conclusion that hydrocarbon formation occurs on Fe via a dual

mechanism – involving surface carbide and formyl intermediates; nevertheless, hydrocarbon formation is more favorable via the carbide mechanism. The heat of CO adsorption on polycrystalline Fe at zero coverage was estimated to be -91.6 kJ/mol and -64.8 kJ/mol from ITH and FTS models respectively while a mean value of -50.0 kJ/mol was estimated from TPD model. The activation energy for CO dissociation at zero coverage was estimated to be 117 kJ/mol form ITH and FTS models while an average activation energy for CO dissociation of 89.4 kJ/mol was estimated from TPD microkinetic model. Carbon hydrogenation was found to be the rate determining step in the carbide mechanism.

Statistically designed steady-state kinetic experiments at conditions similar to industrial operating conditions were used to obtain rate data. The rate data were used to develop a microkinetic model of FTS. FTS and ITH appear to follow similar reaction pathways, although the energetics are slightly different. In both cases, hydrocarbon formation via carbide mechanism was more favorable than via a formyl intermediate while carbon hydrogenation was the rate determining step.

Promotion of Fe with K does not alter Fischer-Tropsch synthesis reaction pathways but does alter the energetics for the steps leading to the formation of CO_2 this phenomenon accounts for the CO_2 selectivity of 0.3 observed for K promoted Fe against 0.17 observed for un-promoted Fe. A Langmuir Hinshelwood rate expression derived from the microkinetic model was put into a fixed bed FTS reactor design code. Calculated reactor sizes, throughput, temperature profiles and conversions are similar to those of pilot and demonstration FTS reactors with similar feed rates and compositions.

The accuracy of the microkinetic model presented here is limited by the accuracy of (1) the UBI-QEP formalism in calculating activation energies for elementary surface reactions; (2) transition state theory in predicting pre-exponential factors for elementary reactions considered in this model; (3) the reactor flow profile; and (4) errors in estimating the binding energies of C, H, and O respectively. Similarly, heats of adsorption calculated from the UBI-QEP formalism are only for the zero coverage limit, and would probably be different at higher coverages. Additionally, the models are limited to the formation of hydrocarbons with carbon number less than or equal to two, although they can easily be extended to include higher hydrocarbons and oxygenates. A comprehensive description of the effects of support and promoters is not available from the present microkinetic model, although it provides some insights regarding the formation of CO_2 and the effects of potassium promotion on selectivity. It is expected that further model development will expand understanding of the effects of support and promoters on Fe FTS activity and product selectivity.

7.2 Conclusion

A technique involving relatively modest computing time and programming on an HP desktop computer was combined with unsteady-state and steady-state kinetic experiments to develop microkinetic models for FTS on Fe catalyst. The models are limited to hydrocarbons with carbon number less than or equal to two, and CO2, but they can be extended to include the formation of higher hydrocarbons and oxygenated compounds. The models provide insights into the FTS mechanism, e.g. that hydrocarbon formation occurs via a dual path mechanism, although the carbide mechanism route

appears to be more favorable. Insight into the effects of K promotion on CO_2 selectivity is also provided by the model.

A Langmuir Hinshelwood type rate expression derived from the microkinetic model when incorporated into a fixed-bed FTS reactor design code enabled calculation of reactor sizes, throughput, temperature profiles and conversion similar to those of pilot and demonstration FTS reactors with similar feed rates and composition.

7.3 Recommendation

1. As the FTS model presented here is limited to formation of hydrocarbons with carbon number less than or equal to two, extension of the model to include formation of higher hydrocarbons and oxygenates is recommended, since such a model would enable prediction of product selectivity in FTS.

2. The robustness of the model could be improved by coupling the methods used to develop this model to more robust theory (e.g. DFT) and experimental techniques (e.g. steady-state isotopic transient kinetic analysis, IR, and Raman). In situ spectroscopic methods such as infra red and Raman can be used to directly measure surface coverages of intermediates on the catalytic surface at industrial process conditions as well as determine CO adsorption stoichiometry.

3. Surface restructuring and the effects of C and O coverages on the enthalpy of CO adsorption need to be investigated. Performing CO TPD in situ at industrial operating conditions (20 – 30 atm and 220 – 260 K) after FTS could

4. Further studies on the effects of support and promoters on FTS activity and selectivity should be pursued, since they could provide a scientific basis for advances in catalyst design.

5. Obtaining additional rate data from lab, pilot, and demonstration plants including accurate measurements of the product distributions is a high priority. Such data can be used in improving and validation microkinetic models.

6. Efforts to produce standard Fe FTS catalyst for comparative studies among different labs should be further encouraged. Data from such catalyst could be used in mechanistic studies to minimize errors in the predicted energetics since the mode of catalyst preparation affects surface heterogeneity which in turn affects the energetics and product selectivity.

8. References

1. *Petroleum and Other Liquid Fuels*, D.o. Energy, Editor. 2007, Energy Information Administration. p. 29-48.

2. Shin, M.W., D. Shin, S.H. Choi, E.S. Yoon, and C. Han, *Optimization of the Operation of Boil-Off Gas Compressors at a Liquified Natural Gas Gasification Plant*. 2007. p. 6540-6545.

3. Suzuki, S., T. Sasaki, T. Kojima, M. Yamamura, and T. Yoshinari, *New Process Development of Natural Gas Conversion Technology to Liquid Fuels via OCM Reaction*. 1996. p. 531-536.

4. Wender, I. and B.H. Davis, *Symposium on Synthesis Gas Chemistry: An Introduction.* Energy & Fuels, 1996. **10**(3): p. 519-519.

5. Wang, Z.X., T. Dong, L.X. Yuan, T. Kan, X.F. Zhu, Y. Torimoto, M. Sadakata, and Q.X. Li, *Characteristics of Bio-Oil-Syngas and Its Utilization in Fischer-Tropsch Synthesis.* Energy & Fuels, 2007. **21**(4): p. 2421-2432.

6. Rofer-DePoorter, C.K., *A comprehensive mechanism for the Fischer-Tropsch synthesis.* Chem. Rev., 1981. **81**(5): p. 447-474.

7. Bartholomew, C.H. and R.J. Farrauto, *Fundamentals of Industrial Catalytic Processes*. 2nd ed. 2006, Jew Jersey: John Wiley & Sons, Inc.

8. Bukur, D.B., X. Lang, and L. Nowicki, *Comparative Study of an Iron Fischer-Tropsch Catalyst Performance in Stirred Tank Slurry and Fixed-Bed Reactors.* Ind. Eng. Chem. Res., 2005. **44**(16): p. 6038-6044.

9. Spivey, J.J. and K.M. Dooley, eds. *Catalysis*. Specialist Periodical Reports. Vol. 19. 2006, The Royal Society of Chemistry: Cambridge.

10. Huber, G., *Intrinsic Kinetics of Pt Promoted Co/SiO_2 Fischer-Tropsch Synthesis Catalysts*, in *Chemical Engineering*. 2000, Brigham Young University: Provo.

11. Dumesic J. A., R.D.F., Aparicio L. M., Rekoske J. E., Trevino A. A., *The Microkinetics of Heterogeneous Catalysis*. ACS Professional Reference Book. 1993, Washinton, DC: American Chemical Society.

12. Van Dijk, H.A.J., *The Fischer-Tropsch synthesis: A mechanistic study using transient isotopic tracing*, in *Chemical Engineering*. 2001, Technische Universiteit: Eindhonen.

13. Van Dijk, H.A.J., J.H.B.J. Hoebink, and J.C. Schouten, *A mechanistic study of the Fischer-Tropsch synthesis using transient isotopic tracing. Part-1: Model identification and discrimination.* Topics in Catalysis, 2003. **26**(Nos. 1-4): p. 111-119.

14. Van Dijk, H.A.J., J.H.B.J. Hoebink, and J.C. Schouten, *A mechanistic study of the Fischer-Tropsch synthesis using transient isotopic tracing. Part 2: Model quantification.* Topics in Catalysis, 2003. **26**(Nos. 1-4): p. 163-171.

15. Adesina A. A., *Hydrocarbon synthesis via Fischer-Tropsch reaction: Travails and triumphs.* Applied Catalysis A: General, 1996. **138**: p. 345-367.

16. Storsaeter, S., D. Chen, and A. Holmen, *Microkinetic modeling of the formation of C_1 and C_2 products in the Fischer-Tropsch synthesis over cobalt catalysts.* Surface Science, 2006. **600**: p. 2051-2063.

17. Preeti Aghalayam, Y.K.P.D.G.V., *Construction and optimization of complex surface-reaction mechanisms.* AiChE Journal, 2000. **46**(10): p. 2017-2029.

18. Fishtik, I., C.A. Callaghan, and R. Datta, *Reaction network analysis. The kinetics and mechanism of water-gas-shift reaction on Cu(111)*, in *Theoretical and Computation Chemistry*, J. Leszczynski, Editor. 2004.

19. Critchfield, B., *Statistical Methods for Kinetic Modeling of Fischer-Tropsch Synthesis on a supported Iron Catalyst*, in *Chemical Engineering*. 2006, Brigham Young University: Provo.

20. Yang, J., Y. Liu, J. Chang, Y.N. Wang, L. Bai, Y.Y. Xu, H.W. Xiang, Y.W. Li, and B. Zhong, *Detailed Kinetics of Fischer-Tropsch Synthesis on an Industrial Fe-Mn Catalyst.* Ind. Eng. Chem. Res., 2003. **42**(21): p. 5066-5090.

21. O'Brien, R.J., L. Xu, S. Bao, A. Raje, and B.H. Davis, *Activity, selectivity and attrition charactersistics of supported iron Fischer-Tropsch catalysts.* Applied Catalysis A: General, 2000. **196**(2): p. 173-178.

22. Ali S. H. and J.G. Goodwin , Jr,, *Impact of readsorption effects and their removal from surface reaction parameters obtained by isotopic transient kinetic analysis: Methanol synthesis on Pd/SiO_2.* Journal of Catalysis, 1997(171): p. 339-344.

23. Ali, S.H., B. Chen, and J.G. Goodwin, Jr, *Zr promotion of Co/SiO_2 for Fischer-Tropsch synthesis.* Journal of Catalysis, 1995. **157**: p. 35-41.

24. Jacobs, G., Y. Ji, B.H. Davis, D. Cronauer, A.J. Kropf, and C.L. Marshall, *Fischer-Tropsch synthesis: Temperature programmed EXAFS/XANES*

investigation of the influence of support type, cobalt loading, and noble metal promoter addition to the reduction behavior of cobalt oxide particles Applied Catalysis A: General, 2007.

25. Kogelbauer, A., J.J.G. Goodwin, and R. Oukaci, *Ruthenium Promotion of Co/Al_2O_3 Fischer-Tropsch Catalysts.* Journal of Catalysis, 1996. **160**(1): p. 125-133.

26. Li, S., W. Ding, G.D. Meitzner, and E. Iglesia, *Spectroscopic and Transient Kinetic Studies of Site Requirements in Iron-Catalyzed Fischer-Tropsch Synthesis.* J. Phys. Chem. B, 2002. **106**(1): p. 85-91.

27. Li, S., A. Li, S. Krishnamoorthy, and E. Iglesia, *Effects of Zn, Cu, and K Promoters on the Structure and on the Reduction, Carburization, and Catalytic Behavior of Iron-Based Fischer–Tropsch Synthesis Catalysts.* Catalysis Letters, 2001. **77**(4): p. 197-205.

28. Rankin, J.L. and C.H. Bartholomew, *Effects of calcination on the CO hydrogenation activity/selectivity properties of potassium-promoted iron/silica.* Journal of Catalysis, 1986. **100**(2): p. 526-532.

29. Rankin, J.L. and C.H. Bartholomew, *Effects of potassium and calcination pretreatment on the adsorption and chemical/physical properties of Fe/SiO2.* Journal of Catalysis, 1986. **100**(2): p. 533-540.

30. Xu, J. and C.H. Bartholomew, *Temperature-Programmed Hydrogenation (TPH) and in Situ Mössbauer Spectroscopy Studies of Carbonaceous Species on Silica-Supported Iron Fischer-Tropsch Catalysts.* J. Phys. Chem. B, 2005. **109**(6): p. 2392-2403.

31. Xu, J., C.H. Bartholomew, J. Sudweeks, and D.L. Eggett, *Design, Synthesis, and Catalytic Properties of Silica-Supported, Pt-Promoted Iron Fischer–Tropsch Catalysts.* Topics in Catalysis, 2003. **26**(1): p. 55-71.

32. Stockwell, D.M., D. Bianchi, and C.O. Bennett, *Carbon pathways in methanation and chain growth during the Fischer-Tropsch synthesis on Fe/Al2O3.* Journal of Catalysis, 1988. **113**(1): p. 13-24.

33. Brady, R.C., III and R. Pettit, *Mechanism of the Fischer-Tropsch reaction. The chain propagation step.* Journal of the American Chemical Society, 1981. **103**(5): p. 1287-1289.

34. Lox, E.S. and G.F. Froment, *Kinetics of the Fischer-Tropsch reaction on a precipitated promoted iron catalyst. 1. Experimental procedure and results.* Ind. Eng. Chem. Res., 1993. **32**(1): p. 61-70.

35. Rohr, F., O.A. Lindvag, A. Holmen, and E.A. Blekkan, *Fischer-Tropsch synthesis over cobalt catalysts supported on zirconia-modified alumina.* Catalysis Today, 2000. **58**(4): p. 247-254.

36. van Dijk, H.A.J., *The Fischer-Tropsch synthesis: a mechanistic study using transient isotopic tracing*. 2001, Technical University Eindhoven: Eindhoven, Neth.

37. Friedel, R.A. and R.B. Anderson, *Composition of synthetic liquid fuels. I. Product distribution and analysis of C5-C8 paraffin isomers from cobalt catalyst.* Journal of the American Chemical Society, 1950. **72**: p. 1212-1215.

38. Bertole, C.J., G. Kiss, and C.A. Mims, *The effect of surface-active carbon on hydrogenation selectivity in cobalt-catalyzed Fischer-Tropsch synthesis.* Journal of Catalysis, 2004. **223**: p. 309-318.

39. Bertole, C.J., C.A. Mims, and G. Kiss, *The effect of water on the cobalt-catalyzed Fischer-Tropsch synthesis.* Journal of Catalysis, 2002. **210**: p. 84-96.

40. Bertole, C.J., C.A. Mims, G. Kiss, and P. Joshi, *Site rectivity of Fischer-Tropsch synthesis catalysts studied by ^{12}CO to ^{13}CO isotope transients.* Studies in surface science and catalysis, 2001. **136**(Natural gas conversion VI): p. 369-374.

41. Buchang, S. and B.H. Davis, *Fischer-Tropsch synthesis: accounting for chain-length related phenomena.* Applied Catalysis A: General, 2004. **277**: p. 61-69.

42. Mims, C.A. and C.J. Bertole, *Surface carbon coverage and selectivity in TF synthesis: a simple model for selectivity correlations.* Studies in surface science and catalysis, 2001. **136**(Natural Gas Conversion VI): p. 375-380.

43. Novak, S., R.J. Madon, and H. Suhl, *Models of hydrocarbon product distributions in Fischer-Tropsch synthesis. I.* Journal of Chemical Physics, 1981. **74**(11): p. 6083-6091.

44. Shi, B. and B.H. Davis, *^{13}C-tracer study of the Fischer-Tropsch synthesis: another interpretation.* Catalysis Today, 2000. **58**: p. 255-261.

45. Madon, R.J. and W.F. Taylor, *Fischer_Tropsch synthesis on a presipitated iron catalyst.* Journal of Catalysis, 1981. **69**(1): p. 32-43.

46. Iglesia, E., S.C. Reyes, and R.J. Madon, *Transport-enhanced α-olefin readsorption pathways in ruthenium-catalyzed hydrocarbon synthesis.* Journal of Catalysis, 1991. **129**(1): p. 238-256.

47. Madom, R.J. and E. Iglesia, *The importance of olefin readsorption and hydrogen/carbon monoxide reactant ratio for hydrocarbon chain growth on ruthenium catalysts.* Journal of Catalysis, 1993. **139**(2): p. 576-590.

48. Madon, R.J., S.C. Reyes, and E. Iglesia, *Primary and secondary reaction pathways in ruthenium-catalyzed hydrocarbon synthesis.* Journal of Physical Chemistry, 1991. **95**(20): p. 7795-7804.

49. Van der Laan, G.P. and A.A.C.M. Beenackers, *Kinetics and selectivity of the Fishcher-Tropsch synthesis: a literature review.* Catalysis Review -Science and Engineering, 1999. **41**(3 & 4): p. 255-318.

50. Komaya, T. and A. Bell, *Estimates of rate coefficients for elementary processes occuring during Fischer-Tropsch synthesis over Ru/TiO_2.* Journal of Catalysis, 1994. **146**(1): p. 237-248.

51. Kuipers, E.W., C. Scheper, J.H. Wilson, I.H. Vinkenburg, and H. Oosterbeek, *Non-ASF product distributions due to secondary reactions during Fischer-Tropsch synthesis.* Journal of Catalysis, 1996. **158**(1): p. 288-300.

52. Dictor, R.A. and A.T. Bell, *An explanation for deviations of Fischer-Tropsch products from a Schulz-Flory distribution.* Industrial & Engineering Chemistry Process Design and Development, 1983. **22**(4): p. 678-681.

53. Komaya, T. and A.T. Bell, *Estimates of rate coefficients for elementary processes occurring during Fischer-Tropsch synthesis over Ru/TiO2.* Journal of Catalysis, 1994. **146**(1): p. 237-248.

54. van der Laan, G.P. and A.A.C.M. Beenackers, *Hydrocarbon Selectivity Model for the Gas-Solid Fischer-Tropsch Synthesis on Precipitated Iron Catalysts.* Ind. Eng. Chem. Res., 1999. **38**(4): p. 1277-1290.

55. Das, T.K., W.A. Conner, J. Li, G. Jacobs, M.E. Dry, and B.H. Davis, *Fischer-Tropsch Synthesis: Kinetics and Effect of Water for a Co/SiO_2 Catalyst.* Energy & Fuels, 2005. **19**(4): p. 1430-1439.

56. Bartholomew, C.H. and R.B. Pannell, *The stoichiometry of hydrogen and carbon monoxide chemisorption on alumina- and silica-supported nickel.* Journal of Catalysis, 1980. **65**(2): p. 390-401.

57. Bridge, M.E., C.M. Comrie, and R.M. Lambert, *Hydrogen chemisorption and the carbon monoxide-hydrogen interaction on cobalt (0001).* Journal of Catalysis, 1979. **58**(1): p. 28-33.

58. Christmann, K., O. Schober, G. Ertl, and M. Neumann, *Adsorption of hydrogen on nickel single crystal surfaces.* Journal of Chemical Physics, 1974. **60**(11): p. 4528-4540.

59. Bajusz, I.G. and J.G. Goodwin, Jr, *Hydrogen and temperature effects on the coverage and activities of surface intermediates during methanation on Ru/SiO_2.* Journal of Catalysis, 1997. **169**(1): p. 157-165.

60. Baro, A.M. and W. Erley, *The Chemisorption of Hydrogen on a (110) Iron Crystal Studied by Vibrational Spectroscopy (Eels).* Surface Science, 1981. **112**(1-2): p. L759-L764.

61. Zowtiak, J.M., *Metal-Support Interactions in Cobalt Catalysts: Their Effects on Adsorption/Desorption kinetics for Hydrogen and Carbon Monoxide*, in *Chemical Engineering*. 1983, Brigham Young University: Provo.

62. Mavrikakis, M., J.A. Dumesic, G.A. Gokhale, R.P. Nabar, C.H. Bartholomew, H. Zou, and B. Critchfield, *Atomic-Scale Design of Iron Fischer-Tropsch Catalysts: A Combined Computational Chemistry, Experimental, and Microkinetic Modeling Approach*. 2005.

63. Bromfield, T.C., D.C. Ferré, and J.W. Niemantsverdriet, *A DFT Study of the Adsorption and Dissociation of CO on Fe(100): Influence of Surface Coverage on the Nature of Accessible Adsorption States.* ChemPhysChem, 2005. **6**(2): p. 254-260.

64. Burke, M.L. and R.J. Madix, *Effect of CO on hyrogen thermal desorption from Fe(100).* Surface Science, 1990. **237**: p. 20-34.

65. Curulla-Ferre, D., A. Govender, T.C. Bromfield, and J.W. Niemantsverdriet, *A DFT study of the adsorption and dissociation of CO on sulfur-precovered Fe(100).* Journal of Physical Chemistry B, 2006. **110**(28): p. 13897-13904.

66. Huang, D.M., D.B. Cao, Y.W. Li, and H. Jiao, *Density Function Theory Study of CO Adsorption on Fe_3O_4(111) Surface.* J. Phys. Chem. B, 2006. **110**(28): p. 13920-13925.

67. Jenkins, S.J., *Dissociative adsorption and adsorbate-induced reconstruction on Fe{2 1 1}.* Surface Science, 2006. **600**(7): p. 1431-1438.

68. Jiang, D.E. and E.A. Carter, *Adsorption and dissociation of CO on Fe(1 1 0) from first principles.* Surface Science, 2004. **570**(3): p. 167-177.

69. Jiang, M., N. Koizumi, and M. Yamada, *Adsorption Properties of Iron and Iron-Manganese Catalysts Investigated by in-situ Diffuse Reflectance FTIR Spectroscopy.* J. Phys. Chem. B, 2000. **104**(32): p. 7636-7643.

70. Mehandru, S.P. and A.B. Anderson, *Binding and orientations of CO on Fe(110), (100), and (111): A surface structure effect from molecular orbital theory.* Surface Science, 1988. **201**(1-2): p. 345-360.

71. Stibor, A., G. Kresse, A. Eichler, and J. Hafner, *Density functional study of the adsorption of CO on Fe(1 1 0).* Surface Science, 2002. **507-510**: p. 99-102.

72. Bian, G., A. Oonuki, Y. Kobayashi, N. Koizumi, and M. Yamada, *Syngas adsorption on precipitated iron catalysts reduced by H2, syngas or CO and on*

those used for high-pressure FT synthesis by in situ diffuse reflectance FTIR spectroscopy. Applied Catalysis A: General, 2001. **219**(1-2): p. 13-24.

73. Broden, G., T.N. Rhodin, C. Brucker, R. Benbow, and Z. Hurych, *Synchrotron radiation study of chemisorptive bonding of CO on transition metals -- Polarization effect on Fe(100).* Surface Science, 1976. **59**(2): p. 593-611.

74. Joyner, R.W., *Electron spectroscopy applied to the study of reactivity at metal surfaces -- A review.* Surface Science, 1977. **63**: p. 291-314.

75. Joyner, R.W. and M.W. Roberts, *Oxygen (1s) binding energies in carbon monoxide adsorption on metals.* Chemical Physics Letters, 1974. **29**(3): p. 447-448.

76. Broden, G., G. Gafner, and H.P. Bonzel, *CO adsorption on potassium promoted Fe(110).* Surf. Sci., 1979. **84**: p. 295-314.

77. Ahlafi, H., M. Nawdali, and D. Bianchi, *Hydrogenation of carbonaceous adsorbed species formed during the CO/H2 reaction on a Ru/Al2O3 catalyst: experimental and kinetic modeling.* Studies in surface science and catalysis, 1999. **122**: p. 419-422.

78. Nawdali, M., H. Ahlafi, G.M. Pajonk, and D. Bianchi, *Elementary steps involved in the hydrogenation of the linear CO species adsorbed on a Ru/Al2O3 catalyst.* Journal of Molecular Catalysis A: Chemical, 2000. **162**(1-2): p. 247-256.

79. Shustorovich, E. and A.T. Bell, *Analysis of CO hydrogenation pathways using the bond-order-conservation method.* Journal of Catalysis, 1988. **113**(2): p. 341-352.

80. Wang, H., J. Liu, J. Xu, J. Fu, Z. Lin, H. Zhang, and K. Tsai, *Pathway for cleavage of the C-O bond in syngas conversion to ethanol over rhodium catalysts.* Fenzi Cuihua, 1994. **8**(2): p. 111-116.

81. Zhang, Z.L., A. Kladi, and X.E. Verykios, *Surface Species Formed During CO and CO2 Hydrogenation over Rh/TiO2 (W6+) Catalysts Investigated by FTIR and Mass-Spectroscopy.* Journal of Catalysis, 1995. **156**(1): p. 37-50.

82. Bonzel, H.P. and H.J. Krebs, *On the chemical nature of the carbonaceous deposits on iron after CO hydrogenation.* Surface Science, 1980. **91**(2-3): p. 499-513.

83. Rabo, J.A., A.P. Risch, and M.L. Poutsma, *Reactions of carbon monoxide and hydrogen on Co, Ni, Ru, and Pd metals.* Journal of Catalysis, 1978. **53**(3): p. 295-311.

84. Storsaeter, S., D. Chen, and A. Holmen, *Microkinetic modelling of the formation of C1 and C2 products in the Fischer-Tropsch synthesis over cobalt catalysts.* Surface Science, 2006. **600**(10): p. 2051-2063.

85. McCarty, J.G. and H. Wise, *Hydrogenation of surface carbon on alumina-supported nickel.* Journal of Catalysis, 1979. **57**(3): p. 406-416.

86. Iglesia, E. *Fischer-Tropsch Synthesis Catalysis: Low-Temperature Fe Catalysts and the Mechanism for CO Dissociation on Fe and Co*. in *20th NAM of the Catalysis Society*. 2007. Houston, Texas.

87. Lo, J.M.H. and T. Ziegler, *Theoretical Studies of the Formation and Reactivity of C2 Hydrocarbon Species on the Fe(100) Surface.* J. Phys. Chem. C, 2007. **111**(35): p. 13149-13162.

88. Fischer, F. and H. Tropsch, *The synthesis of petroleum at atmospheric pressures from gasification products of coal.* Brennstoff-Chemie, 1926. **7**: p. 97-104.

89. Mavrikakis, M. and A.A. Gokhale, *Early Fischer-Tropsch steps on Fe(110) and Co(0001) surfaces: Comparative DFT studies.* Abstracts of Papers of the American Chemical Society, 2005. **229**: p. U861-U861.

90. Storch, H.H., N. Golumbic, and R.B. Anderson, *The Fischer-Tropsch Synthesis and Related Synthesis*. 1951, New York: John Wiley.

91. Kummer, J.T., H.H. Podgurski, W.B. Spencer, and P.H. Emmett, *Mechanism studies of the Fischer-Tropsch synthesis. The addition of radioactive alcohol.* Journal of the American Chemical Society, 1951. **73**: p. 564-569.

92. Pichler, H. and H. Schulz, *Recent results in the synthesis of hydrocarbons from carbon monoxide and hydrogen.* Chemie Ingenieur Technik, 1970. **42**(18): p. 1162-1174.

93. Davidson, P.J., M.F. Lappert, and R. Pearce, *Metal .sigma.-hydrocarbyls, MRn. Stoichiometry, structures, stabilities, and thermal decomposition pathways.* Chem. Rev., 1976. **76**(2): p. 219-242.

94. Brown, S.L. and S.G. Davis, *Reductive polymerization of carbon monoxide: synthesis of entirely CO-derived pentanoic acid.* J. Chem. Soc. Chem. Comm., 1986(84-85): p. 84.

95. Belambe, A.R., R. Oukaci, and J.G. Goodwin, Jr, *Effect of pretreatment on the activity of a Ru-promoted Co/Al_2O_3 Fischer-Tropsch catalyst.* Journal of Catalysis, 1997. **166**: p. 8-15.

96. Froseth, V., S. Storsaeter, O. Borg, E.A. Blekkan, M. Ronning, and A. Holmen, *Steady state isotopic transient kinetic analysis (SSITKA) of CO hydrogenation on different Co catalysts.* Applied Catalysis A: General, 2005. **289**: p. 10-15.

97. Rohr, F., O.A. Lindvag, A. Holmen, and E.A. Blekkan, *Fischer-Tropsch synthesis over cobalt catalysts supported on zirconia-modified alumina.* Catalysis Today, 2000. **58**: p. 247-254.

98. Wan, H.-J., B.-S. Wu, C.-H. Zhang, H.-W. Xiang, Y.-W. Li, B.-F. Xu, and F. Yi, *Study on Fe-Al_2O_3 interaction over precipitated iron catalyst for Fischer-Tropsch synthesis.* Catalysis Communications, 2007. **8**(10): p. 1538-1545.

99. Chang, J., L. Bai, B. Teng, R. Zhang, J. Yang, Y. Xu, H. Xiang, and Y. Li, *Kinetic modeling of Fischer-Tropsch synthesis over Fe-Cu-K-SiO2 catalyst in slurry phase reactor.* Chemical Engineering Science, 2007. **62**(18-20): p. 4983-4991.

100. Botes, F.G., *Water-gas-shift kinetics in the iron-based low-temperature Fischer-Tropsch synthesis.* Applied Catalysis A: General, 2007. **328**(2): p. 237-242.

101. Hayakawa, H., H. Tanaka, and K. Fujimoto, *Studies on catalytic performance of precipitated iron/silica catalysts for Fischer-Tropsch Synthesis.* Applied Catalysis A: General, 2007. **328**(2): p. 117-123.

102. Ion Iliuta, F.L.J.A.N.D.D.S., *Multicomponent multicompartment model for Fischer-Tropsch SCBR.* AiChE Journal, 2007. **53**(8): p. 2062-2083.

103. Wan, H.-J., B.-S. Wu, X. An, T.-Z. Li, Z.-C. Tao, H.-W. Xiang, and Y.-W. Li, *Effect of $A1_2O_3$ Binder on the Precipitated Iron-Based Catalysts for Fischer-Tropsch Synthesis.* Journal of Natural Gas Chemistry, 2007. **16**(2): p. 130-138.

104. Ma, W., E.L. Kugler, and D.B. Dadyburjor, *Potassium Effects on Activated-Carbon-Supported Iron Catalysts for Fischer-Tropsch Synthesis.* Energy & Fuels, 2007. **21**(4): p. 1832-1842.

105. Teng, B.-T., J. Chang, J. Yang, G. Wang, C.-H. Zhang, Y.-Y. Xu, H.-W. Xiang, and Y.-W. Li, *Water gas shift reaction kinetics in Fischer-Tropsch synthesis over an industrial Fe-Mn catalyst.* Fuel, 2005. **84**(7-8): p. 917-926.

106. Chen, C.-S., W.-H. Cheng, and S.-S. Lin, *Study of reverse water gas shift reaction by TPD, TPR and CO2 hydrogenation over potassium-promoted Cu/SiO2 catalyst.* Applied Catalysis A: General, 2003. **238**(1): p. 55-67.

107. Capek, P. and K. Klusacek, *Dynamic kinetic model of the water-gas shift reaction using unsteady kinetic experiments.* Chemical Engineering Science, 1994. **49**(24, Part 1): p. 4095-4102.

108. Rhodes, C., G.J. Hutchings, and A.M. Ward, *Water-gas shift reaction: finding the mechanistic boundary.* Catalysis Today, 1995. **23**(1): p. 43-58.

109. Davis, B.H., M. Luo, and D. Devilliers. *Fischer-Tropsch synthesis: Are common sites responsible for FTS and water-gas shift (WGS)?* in *227th ACS National Meeting*. 2004. Anaheim, CA, USA.

110. Luo, M., D. Devilliers, R.J. O'Brien, S. Bao, and B.H. Davis, *Fischer-Tropsch synthesis: are common sites responsible for FTS and water-gas shift (WGS)?* Vol.

49. 2004: American Chemical Society, Division of Petroleum Chemistry. 172-174.

111. Shustorovich, E., *Metal effects in the Fischer-Tropsch synthesis: Bond-order-conservation-morse-potential approach.* Catalysis Letters, 1990. **7**(1): p. 107-118.

112. Shustorovich, E. and A.T. Bell, *An analysis of Fischer-Tropsch synthesis by the bond-order-conservation-Morse-potential approach.* Surface Science, 1991. **248**(3): p. 359-368.

113. Shustorovich, E. and H. Sellers, *The UBI-QEP method: a practical theoretical approach to understanding chemistry on transition metal surfaces.* Surface Science Reports, 1998. **31**: p. 1-119.

114. Efstathiou, A.M. and X.E. Verykios, *Transient methods in heterogeneous catalysis: Experimental features and application to study mechanistic aspects of the CH_4/O_2 (OCM), NH_3/O_2 and NO/He reactions.* Applied Catalysis A: General, 1997. **151**: p. 109-116.

115. Masel, R.I., *Principles of Adsorption and Reaction on Solid Surfaces*. Wiley series in chemical engineering. 1996, New York: John Wiley & Sons, Inc.

116. Shannon, S.L. and J.G. Goodwin, Jr, *Characterization of catalytic surfaces by isotopic-transient kinetics during steady-state reaction.* Chemical Reviews, 1995. **95**: p. 677-695.

117. Levine, I.N., *Quantum Chemistry*. 5th ed. 1999: Prentice Hall.

118. Redhead, P.A., *Thermal desorption of gases.* Vacuum, 1962. **12**(4): p. 203-211.

119. Amenomiya, Y. and R.J. Cvetanovic, *Application of flash-desorption method to catalyst studies. I. Ethylene--Alumina system.* J. Phys. Chem, 1963. **67**(1): p. 144-147.

120. Gorte, R.J., *Temperature-programmed desorption for the characterization of oxide catalysts.* Catalysis Today, 1996. **28**(4): p. 405-414.

121. Kanervo, J.M., T.J. Keskitalo, R.I. Slioor, and A.O.I. Krause, *Temperature-programmed desorption as a tool to extract quantitative kinetic or energetic information for porous catalysts.* Journal of Catalysis, 2006. **238**(2): p. 382-393.

122. Daniela Fenske, W.-L.Y.S.N.D.H.D.G.H.B.T.K.K.A.-S., *Pitfalls in Interpreting Temperature Programmed Desorption Spectra of Alloys: The CO/CoPt Puzzle*. 2007. p. 654-656.

123. Falconer, J.L. and R.J. Madix, *Desorption rate isotherms in flash desorption analysis.* Journal of Catalysis, 1977. **48**(1-3): p. 262-268.

124. Falconer, J.L. and J.A. Schwarz, *Temperature-programmed desorption and reaction: Applications to supported catalysts.* Catalysis Review -Science and Engineering, 1983. **25**(2): p. 141-227.

125. Ibok, E.E. and D.F. Ollis, *Temperature-programmed desorption from porous catalysts: Shape index analysis.* Journal of Catalysis, 1980. **66**(2): p. 391-400.

126. Kanervo, J.M., K.M. Reinikainen, and A.O.I. Krause, *Kinetic analysis of temperature-programmed desorption.* Applied Catalysis A: General, 2004. **258**(2): p. 135-144.

127. Lai, F., D.W. Kim, O.S. Alexeev, G.W. Graham, M. Shelef, and B.C. Gates, *Temperature-programmed desorption of hydrogen from γ-Al_2O_3- supported platinum catalysis with and without tungsten.* Phys. Chem. Chem. Physis, 2000. **2**: p. 1997-2003.

128. van Bavel, A.P., D. Curulla Ferre, and J.W. Niemantsverdriet, *Simulating temperature programmed desorption directly from density functional calculations: How adsorbate configurations relate to desorption features.* Chemical Physics Letters, 2005. **407**(1-3): p. 227-231.

129. Lear, T., N.G. Hamilton, and D. Lennon, *The application of temperature-programmed desorption, adsorption isotherms and temperature-programmed oxidation to investigate the interaction of CO with alumina-supported palladium catalysts.* Catalysis Today, 2007. **126**(1-2): p. 219-227.

130. Fernandes, F.A.N., *Modeling and Product Grade Optimization of Fischer-Tropsch Synthesis in a Slurry Reactor.* Ind. Eng. Chem. Res., 2006. **45**(3): p. 1047-1057.

131. Sakakini, B.H. and A.S. Verbrugge, *Temperature-programmed surface reaction as a means of characterizing supported-metal catalysts and probing their surface reactivity.* J. Chem. Soc., Faraday Trans., 1997. **93**(8): p. 1637-1640.

132. Ahlafi, H., M. Nawdali, A.K. Bencheikh, and D. Bianchi, *Isothermal hydrogenation of carbon species adsorbed on Ru/Al_2O_3 catalyst after CO adsorption and CO/H_2.* Bulletin des Societes Chimiques Belges, 1997. **106**(5): p. 245-252.

133. Davis, M.E. and R.J. Davis, *Fundamentals of Reaction Engineering*. 1st ed. 2003, New York: McGraw-Hill.

134. Norskov, J.K., M. Scheffler, and H. Toulhoat, *Density functional theory in surface science and heterogeneous catalysis.* MRS Bulletin, 2006. **31**(9): p. 669-674.

135. Cheng, J., X.-Q. Gong, P. Hu, C.M. Lok, P. Ellis, and S. French, *A quantitative determination of reaction mechanisms from density functional theory*

calculations: Fischer-Tropsch synthesis on flat and stepped cobalt surfaces. Journal of Catalysis, 2008. **254**(2): p. 285-295.

136. Norskov, J.K., T. Bligaard, A. Logadottir, S. Bahn, L.B. Hansen, M. Bollinger, H. Bengaard, B. Hammer, Z. Sljivancanin, M. Mavrikakis, Y. Xu, S. Dahl, and C.J.H. Jacobsen, *Universality in heterogeneous catalysis.* J. Catal., 2002. **209**(2): p. 275-278.

137. Shustorovich, E. and H. Sellers, *The UBI-QEP method: A practical theoretical approach to understanding chemistry on transition metal surfaces.* Surface Science Reports, 1998. **31**(1-3): p. 1-119.

138. Shustorovich, E. and A.V. Zeigarnik, *The UBI-QEP treatment of polyatomic molecules without bond-energy partitioning.* Surface Science, 2003. **527**(1-3): p. 137-148.

139. Mhadeshwar, A.B., H. Wang, and D.G. Vlachos, *Thermodynamic Consistency in Microkinetic Development of Surface Reaction Mechanisms*. 2003. p. 12721-12733.

140. Jothimurugesan, K., J.G. Goodwin, and S.K. Gangwal, *Attrition-resistant bulk iron catalysts for Fischer-Tropsch reaction in slurry reactors and fluidized-bed reeactors*, A. PCT Int, Editor. 2002: USA.

141. Sudsakorn, K., J.G. Goodwin, K. Jothimurugesan, and A.A. Adeyiga, *Preparation of Attrition-Resistant Spray-Dried Fe Fischer-Tropsch Catalysts Using Precipitated SiO_2.* Ind. Eng. Chem. Res., 2001. **40**(22): p. 4778-4784.

142. Zhao, R., J.G. Goodwin, K. Jothimurugesan, S.K. Gangwal, and J.J. Spivey, *Spray-Dried Iron Fischer-Tropsch Catalysts. 1. Effect of Structure on the Attrition Resistance of the Catalysts in the Calcined State.* Ind. Eng. Chem. Res., 2001. **40**(4): p. 1065-1075.

143. Zhao, R., J.G. Goodwin, K. Jothimurugesan, S.K. Gangwal, and J.J. Spivey, *Spray-Dried Iron Fischer-Tropsch Catalysts. 2. Effect of Carburization on Catalyst Attrition Resistance.* Ind. Eng. Chem. Res., 2001. **40**(5): p. 1320-1328.

144. Campos, A., J.J. Spivey, A. Roy, N. Lohitharn, J. Goodwin, E. Lotero, and H. Lamb, *Characterization of Mo additions in iron-based Fischer-Tropsch catalysts using X-ray absorption spectroscopy and X-ray diffraction.* Nuclear Instruments and Methods in Physics Research Section A: Accelerators, Spectrometers, Detectors and Associated Equipment, 2007. **582**(1): p. 236-238.

145. Tao, Z., Y. Yang, M. Ding, T. Li, H. Xiang, and Y. Li, *Effect of calcination behaviors on precipitated iron–manganese Fischer–Tropsch synthesis catalyst.* Catalysis Letters, 2007. **117**(3): p. 130-135.

146. Hou, W., B. Wu, X. An, T. Li, Z. Tao, H. Zheng, H. Xiang, and Y. Li, *Effect of the Ratio of Precipitated SiO2 to Binder SiO2 on Iron-based Catalysts for Fischer–Tropsch Synthesis.* Catalysis Letters, 2007. **119**(3): p. 353-360.

147. Hayakawa, H., H. Tanaka, and K. Fujimoto, *Preparation of a new precipitated iron catalyst for Fischer-Tropsch synthesis.* Catalysis Communications, 2007. **8**(11): p. 1820-1824.

148. Wu, B., L. Tian, H. Xiang, Z. Zhang, and Y.-W. Li, *Novel precipitated iron Fischer–Tropsch catalysts with Fe_3O_4 coexisting with α-Fe_2O_3.* Catalysis Letters, 2005. **102**(3): p. 211-218.

149. Yang, Y., H.-W. Xiang, L. Tian, H. Wang, C.-H. Zhang, Z.-C. Tao, Y.-Y. Xu, B. Zhong, and Y.-W. Li, *Structure and Fischer-Tropsch performance of iron-manganese catalyst incorporated with SiO_2.* Applied Catalysis A: General, 2005. **284**(1-2): p. 105-122.

150. Tijburg, I.I.M., J.W. Geus, and H.W. Zandbergen, *Application of Lanthanum to Pseudo-Boehmite and γ-Al_2O_3.* Journal of Materials Science, 1991. **26**: p. 6479-6486.

151. Nijhuis, T.A., A.E.W. Beers, T. Vergunst, I. Hoek, F. Kapteijn, and J.A. Moulijn, *Preparation of monolithic catalysts.* Catalysis Review -Science and Engineering, 2001. **43**(4): p. 345 - 380.

152. Retallick, W.B., *Catalyst support with three-way washcoat layer for exhaust gas treatment*, in *US Patent US 4762567*, U. W. R. Grace and Co., Editor. 1988: United States. p. 19pp.

153. Juusola, J.A., D.W. Bacon, and J. Downie, *Sequential statistical design strategy in an experimental kinetic study.* Can. J. Chem. Eng., 1972. **50**: p. 796.

154. Lawson, J. and J. Erjavec, *Modern Statistics for Engineering and Quality Improvement*. 2001, Pacific Grove: Duxbury Thomson Learning.

155. Forzatti, P., G. Buzzi-Ferraris, P. Canu, and E. Tronconi, *Sequential desgn of experiments. I. A review of the procedures for discriminating between rival models.* Quaderni dell'Ingegnere Chimico Itanliano, 1986. **22**(2): p. 8-11.

156. Forzatti, P., G. Buzzi-Ferraris, P. Canu, and E. Tronconi, *Sequential design of experiments. II. A review of the procedures for increasing the precision of the parameter estimates.* Quaderni dell'Ingegnere Chimico Itanliano, 1987. **23**(3-4): p. 10-15.

157. Press, W.H., S.A. Teukolsky, W.T. Vetterling, and B.P. Flannery, *Numerical Recipes in Fortran 77*. Second ed. The Art of Scientific Computing. Vol. 1. 2001, New York: Cambridge University Press.

158. Brown, E.R., J.E. Bjarnason, A.M. Fedor, and T.M. Korter, *On the strong and narrow absorption signature in lactose at 0.53 THz.* Applied Physics Letters, 2007. **90**(6): p. N.PAG-N.PAG.

159. Ryvola, R. and M. Mashlan, *Mossbauer spectra processing using neutral networks.* Czechosloavak Journal of Physics, 2005. **55**(7): p. 865-874.

160. Zhang, B., Z. Quan, T. Zhang, T. Guo, and S. Mo, *Effect of oxygen gas and annealing treatment for magnetically enhanced reactive ion etched $(Ba_{0.65},Sr_{0.35})TiO_3$ thin films.* Journal of Applied Physics, 2007. **101**(1): p. 014107-8.

161. Brown, P.N., A.C. Hindmarsh, and G.C. Byrne, *Variable-coefficient Ordinary Differential Equation solver, with fixed-leading-coefficient implementation*, Lawrence Livermore National Laboratory Livermore, CA 94551.

162. Boggs, P.T., R.H. Byrd, J.E. Rogers, and R.B. Schnabel, *ODRPACK version 2.01 software for weighted orthogonal distance regression*. 1992, National Institute of Standards and Technology: Boulder, CO.

163. Jiang, D.E. and E.A. Carter, *Carbon atom adsorption on and diffusion into Fe(110) and Fe(100) from first principles.* Phys. Rev. B, 2005. **71**(045402): p. 6 pages.

164. Blonski, P., A. Kiejna, and J. Hafner, *Oxygen adsorption on the clean and O-precovered Fe(110) and (100) surfaces.* J. Phys.: Condens. Matter, 2007. **19**(096011): p. 8pp.

165. Bartholomew, C.H., W.C. Hecker, K. Brunner, J. Bell, and D. Tree, *Fischer-Tropsch Fixed Bed Reactor Models and Data for Co and Fe Catalysts*. 2007, Brigham Young University: Provo, Utah.

166. Cuesta, A. and C. Gutierrez, *Study by Fourier Transform Infrared Spectroscopy of the Electroadsorption of CO on the Ferrous Metals. 1. Iron.* Journal of Physical Chemistry, 1996. **100**(30): p. 12600-12608.

167. Abild-Pedersen, F. and M.P. Andersson, *CO adsorption energies on metals with correction for high coordination adsorption sites - A density functional study.* Surface Science, 2007. **601**(7): p. 1747-1753.

168. Mavrikakis, M., M. Baumer, H.J. Freund, and J.K. Norskov, *Structure sensitivity of CO dissociation on Rh surfaces.* Catalysis Letters, 2002. **81**(3-4): p. 153-156.

169. Curulla-Ferre, D., A. Govender, T.C. Bromfield, and J.W. Niemantsverdriet, *A DFT Study of the Adsorption and Dissociation of CO on Sulfur-Precovered Fe(100).* J. Phys. Chem. B, 2006. **110**(28): p. 13897-13904.

170. Vink, T.J., O.L.J. Gijzeman, and J.W. Geus, *CO interaction with Fe(100): Effects of carbon and oxygen adlayers on co adsorption isotherms.* Surface Science, 1985. **150**(1): p. 14-23.

171. Kubota, J., E. Yoda, N. Ishizawa, A. Wada, K. Domen, and S.S. Kano, *Site-Hopping of Adsorbed CO in c(4 x 2)-CO/Ni(111) by Laser-Induced Temperature Jump: Time-Resolved Sum-Frequency Generation Observation.* J. Phys. Chem. B, 2003. **107**(38): p. 10329-10332.

172. Eliason, S.A. and C.H. Bartholomew, *Reaction and deactivation kinetics for Fischer-Tropsch synthesis on unpromoted and potassium-promoted iron catalysts.* Applied Catalysis A: General, 1999. **186**(1-2): p. 229-243.

173. Davis, B.H., *Fischer-Tropsch synthesis: current mechanism and futuristic needs.* Fuel Processing Technology, 2001. **71**(1-3): p. 157-166.

174. van der Laan, G.P. and A.A.C.M. Beenackers, *Intrinsic kinetics of the gas-solid Fischer-Tropsch and water gas shift reactions over a precipitated iron catalyst.* Applied Catalysis A: General, 2000. **193**(1-2): p. 39-53.

175. Yates, I.C. and C.N. Satterfield, *Intrinsic kinetics of the Fischer-Tropsch synthesis on a cobalt catalyst.* Energy & Fuels, 1991. **5**(1): p. 168-173.

A. Appendix

A.1 Mathcad Worksheet for Determining the Amounts of $Fe(NO_3)_3.9H_2O$, $Al(NO_3)_3.9H_2O$, NH_4OH, and H_2O Required to Prepare 99%Fe, 1% Al_2O_3 by Method of Co-Precipitation

$Mw_{Fe} := 55.85 \cdot \frac{gm}{mol}$ $Mw_{Al} := 26.98 \cdot \frac{gm}{mol}$ $Mw_{O} := 16 \cdot \frac{gm}{mol}$

$Mw_{N} := 14.01 \cdot \frac{gm}{mol}$ $Mw_{H} := 1.008 \cdot \frac{gm}{mol}$ $Mw_{Fe2O3} := 2 \cdot Mw_{Fe} + 3 \cdot Mw_{O}$

$Mw_{Al2O3} := 2 \cdot Mw_{Al} + 3 \cdot Mw_{O}$ $Mw_{AlOH3} := Mw_{Al} + 3 \cdot (Mw_{O} + Mw_{H})$

$Mw_{FeOH3} := Mw_{Fe} + 3 \cdot (Mw_{O} + Mw_{H})$ $Mw_{Al2O3} = 0.102 \frac{kg}{mol}$

$Mw_{Fe2O3} = 0.16 \frac{kg}{mol}$ $Mw_{FeOH3} = 0.107 \frac{kg}{mol}$

$Mw_{AlOH3} = 0.078 \frac{kg}{mol}$ Let Molecular weight of $Fe(NO_3)_3.9H_2O = Mw_A$

$Mw_{A} := Mw_{Fe} + 3 \cdot (Mw_{N} + 3 \cdot Mw_{O}) + 9 \cdot (2 \cdot Mw_{H} + Mw_{O})$

$Mw_{A} = 0.404 \frac{kg}{mol}$

Let Molecular weight of $Al(NO_3)_3.9H_2O = Mw_B$

$Mw_{B} := Mw_{Al} + 3 \cdot (Mw_{N} + 3 \cdot Mw_{O}) + 9 \cdot (2 \cdot Mw_{H} + Mw_{O})$

Molecular weight of $Al(NO_3)_3.9H_2O$ becomes:

$$Mw_B = 0.375 \frac{kg}{mol}$$

Desired weight of catalyst: $Wt_{cat} := 50 \cdot gm$

Since Fe is 99%, therefore wt of Fe in catalyst is:

$Wt_{Fe} := 0.99 \cdot Wt_{cat}$ $Wt_{Al2O3} := 0.01 \cdot Wt_{cat}$

$Wt_{Fe} = 0.05 kg$ $Wt_{Al2O3} = 5 \times 10^{-4} kg$

$$Wt\_fraction\_Al\_in\_Al2O3 := \frac{2 \cdot Mw_{Al}}{Mw_{Al2O3}}$$

$Wt\_fraction\_Al\_in\_Al2O3 = 0.529$

$Wt_{Al} := Wt_{Al2O3} \cdot Wt\_fraction\_Al\_in\_Al2C$

$Wt_{Al} = 2.646 \times 10^{-4} kg$

$$Wt\_fraction\_Fe\_in\_A := \frac{Mw_{Fe}}{Mw_A}$$ $Wt\_fraction\_Fe\_in\_A = 0.138$

$$Wt\_fraction\_Al\_in\_B := \frac{Mw_{Al}}{Mw_B}$$ $Wt\_fraction\_Al\_in\_B = 0.072$

$$Wt\_A\_required := \frac{Wt_{Fe}}{Wt\_fraction\_Fe\_in\_A}$$ $Wt\_A\_required = 0.358 kg$

Weight of $Al(NO_3)_3.9H_2O$ required is:

$$Wt\_B\_required := \frac{Wt_{Al}}{Wt\_fraction\_Al\_in\_}$$

$$Wt\_B\_required = 3.679 \times 10^{-3}\,kg$$

Calculate the amount of water needed

$$Moles_{Fe} := \frac{Wt_{Fe}}{Mw_{Fe}}$$

$$Moles_{Al} := \frac{Wt_{Al}}{Mw_{Al}}$$

$$Moles_{Fe} = 0.886\,mol$$

$$Moles_{Al} = 9.808 \times 10^{-3}\,mol$$

$$Total\_moles\_cations = Moles_{Fe} + Moles_{Al}$$

$$Total\_moles\_cations = 0.896\,mol$$

Hence to make a 1M (1mol/L) solution of cations, total volume of water is:

$$Vol\_H2O\_total := \frac{Total\_moles\_cation}{1 \cdot \frac{mol}{L}}$$

$$Vol\_H2O\_total = 0.896\,L$$

$$Conc\_cations := \frac{Total\_moles\_cation}{Vol\_H2O\_total}$$

$$Conc\_cations = 1 \cdot \frac{mol}{L}$$

$$Wt\_fraction\_of\_H2O\_in\_A = \frac{9 \cdot \left(2 \cdot Mw_H + Mw_O\right)}{Mw_A}$$

$$Wt\_fraction\_of\_H2O\_in\_A = 0.401$$

$$Wt\_fraction\_of\_H2O\_in\_B = \frac{9 \cdot \left(2 \cdot Mw_H + Mw_O\right)}{Mw_B}$$

Weight fraction of H_2O in $Al(NO_3)_3.9H_2O$ is

Wt_fraction_of_H2O_in_B = 0.432

Wt_H2O_from_A := Wt_fraction_of_H2O_in_A Wt_A_required

Wt_H2O_from_A = 0.144 kg

Wt_H2O_from_B := Wt_fraction_of_H2O_in_B Wt_B_required

Wt_H2O_from_B = 1.59×10^{-3} kg

Wt_H2O_from_A_and_B := Wt_H2O_from_A + Wt_H2O_from_B

Wt_H2O_from_A_and_B = 0.145 kg

Therefore, volume of water from A and B

$$Vol\_H2O\_from\_A\_and\_B := \frac{Wt\_H2O\_from\_A\_and\_B}{1 \cdot \frac{gm}{cm^3}}$$

Vol_H2O_from_A_and_B = 0.145 L

Hence

Actual_vol_water_to_add := Vol_H2O_total − Vol_H2O_from_A_and_B

Actual_vol_water_to_add = 0.751 L

Calculation of NH_4OH concentration and preparation

Compute molecular weight of NH_4OH:

$$Mw_{NH4OH} := Mw_N + 4 \cdot Mw_H + Mw_O + Mw_H$$

$$Mw_{NH4OH} = 0.035 \frac{kg}{mol}$$

Moles_NH4_required := 3.2·Total_moles_cation

Moles_NH4_required = 2.868 mol

NH_4OH solution assay: NH_3 = 29.7%, sg = 0.9

$$sg_{NH4OH} := 0.9 \frac{gm}{cm^3}$$

NH3_fraction_in_solution := 0.297

$$Mw_{NH3} := 17 \cdot \frac{gm}{mol}$$

$$Vol\_conc\_NH4OH\_required := \frac{Moles\_NH4\_required \, Mw_{NH3}}{sg_{NH4OH} \cdot NH3\_fraction\_in\_solution}$$

Vol_conc_NH4OH_required = 0.182 L

To make 4M solution of NH4OH, volume of water required is:

$$vol\_water\_total := \frac{Moles\_NH4\_required}{4 \cdot \frac{mol}{L}}$$

vol_water_total = 0.717 L

vol_water_in_NH4OH := (1 − NH3_fraction_in_solution)·Vol_conc_NH4OH_required

Volume of water in NH_4OH solution is:

vol_water_in_NH4OH= 0.128L

Hence volume of water to be added to 0.182L of conc NH_4OH is:

Vol_water_to_be_added_to_conc_NH4OH:= vol_water_total− vol_water_in_NH4OH

Vol_water_to_be_added_to_conc_NH4OH= 0.589L

A.2 Calculation of Percent Weight Loss for the Various Oxides of Iron Due to Reduction to Fe Metal by H_2

A.2.1 Reduction of Fe_3O_4

The stoichiometric equation for the reaction is:

$$Fe_3O_4 + 4H_2 \rightarrow 3Fe + 4H_2O \quad \text{(A.1)}$$

$$\%Weight\_loss = \frac{4 \times atomic\_mass\_of\_oxygen \times 100}{molecular\_weight\_of\_Fe_3O_4} = 27.642\% \quad \text{(A.2)}$$

A.2.2 Reduction of Fe_2O_3

The stoichiometric equation for the reaction is:

$$Fe_2O_3 + 3H_2 \rightarrow 2Fe + 3H_2O \quad \text{(A.3)}$$

$$\%Weight\_loss = \frac{3 \times atomic\_mass\_of\_oxygen \times 100}{molecular\_weight\_of\_Fe_2O_3} = 30.058\% \quad (A.4)$$

A.2.3 Reduction of FeO

The stoichiometric equation for this reaction is:

$$FeO + H_2 \rightarrow Fe + H_2O \quad (A.5)$$

$$\%Weight\_loss = \frac{atomic\_mass\_of\_oxygen \times 100}{molecular\_weight\_of\_FeO} = 22.27\% \quad (A.6)$$

A.3 Mathcad Worksheet for Calculating EOR, CO Uptake, and %Dispersion for 20Fe1K1Pt-ALa-mon-507

A.3.1 EOR

%Fe2O3_in_monolith_after_calcination := 5.507%

Wt_Fe2O3_in_precusor := %Fe2O3_in_monolith_after_calcination·Wt_of_sample_loaded_into_TG
Wt_of_sample_loaded_into_TGA := 31.859·mg

Wt_Fe2O3_in_precusor = 1.754·mg

Wt_gained_after_Oxygen_titration := 0.481·mg

Let x = wt of Fe after reduction and y = wt of Fe_2O_3 formed after oxygen titration
The the equation of reaction is: $4Fe + 3O_2 = 2Fe_2O_3$
1 mole of Fe will produce 0.5 moles of Fe_2O_3

$$Mole\_Fe\_consumed = \frac{x}{Mw\_Fe}$$

$$\text{Mole\_Fe2O3\_produced} = \frac{0.5 \cdot x}{\text{Mw\_Fe}}$$

$$\text{Wt\_Fe2O3\_produced} = \frac{0.5 \cdot x}{\text{Mw\_Fe}} \cdot \text{Mw\_Fe2O3}$$

Therefore wt gained after oxygen titration is:

$$\text{Wt\_gained\_after\_Oxygen\_titration} = \text{Wt\_Fe2O3} - \text{Wt\_Fe}$$

$$\text{Wt\_gained\_after\_Oxygen\_titration} = \frac{0.5 \cdot x}{\text{Mw\_Fe}} \cdot \text{Mw\_Fe2O3} - x$$

$$\text{Wt\_gained\_after\_Oxygen\_titration} = x\left(\frac{0.5}{\text{Mw\_Fe}} \cdot \text{Mw\_Fe2O3} - 1\right)$$

$$x := \frac{\text{Wt\_gained\_after\_Oxygen\_titrati}}{\left(\frac{0.5\text{Mw\_Fe2O3}}{\text{Mw\_Fe}} - 1\right)}$$

$$x = 1.119 \cdot \text{mg}$$

$$y := \frac{0.5 \cdot x}{\text{Mw\_Fe}} \cdot \text{Mw\_Fe2O3}$$

$$y = 1.6 \cdot \text{mg}$$

$$\text{EOR} := \frac{y}{\text{Wt\_Fe2O3\_in\_precuso}}$$

$$\text{EOR} = 91.208 \cdot \%$$

A.3.2 CO uptake and % dispersion

$$Mw\_CO := 28 \cdot \frac{gm}{mol}$$

$$Wt\_of\_CO\_adsorbed := (1.00106 \cdot 31.175 - 31.175) \cdot mg$$

$$Wt\_of\_CO\_adsorbed = 0.033 \cdot mg$$

$$Mole\_of\_CO\_adsorbed := \frac{Wt\_of\_CO\_adsorbed}{Mw\_CO}$$

$$Mole\_of\_CO\_adsorbed = 1.18 \times 10^{-6}\, mol$$

$$\%monolith := 78.43\%$$

$$\%Metal\_loading = 17.86\%$$

$$Initial\_wt\_of\_sample\_loaded\_in\_TGA = 31.859 \cdot mg$$

$$Wt\_of\_Monolith := \%monolith \cdot Initial\_wt\_of\_sample\_loaded\_in\_T$$

$$Wt\_of\_Monolith = 24.99 \cdot mg$$

$$Wt\_after\_reduction := 0.97245 \cdot Initial\_wt\_of\_sample\_loaded\_in\_T$$

$$Wt\_after\_reduction = 30.981 \cdot mg$$

$$Catalyst\_wt\_monolith\_free\_basis\_after\_reduction = Wt\_after\_reduction - Wt\_of\_Monolit$$

$$Catalyst\_wt\_monolith\_free\_basis\_after\_reduction = 5.991 \cdot mg$$

$$CO\_Uptake := \frac{Mole\_of\_CO\_adsorbed}{Catalyst\_wt\_monolith\_free\_basis\_after\_reduct}$$

$$CO\_Uptake = 196.982 \cdot \frac{\mu mol}{gm}$$

$$C2 := 1.12 \cdot \frac{gm}{\mu mol}$$

$$\%D := \frac{C2 \cdot CO\_Uptake}{\%Metal\_loading \cdot 100 \cdot EOR}$$

$$\%D = 13.54$$

A.4 Sample Calculation of Activation Energies for a Reversible Elementary Reaction Using the UBI-QEP Method

To illustrate the use of the UBI-QEP method in calculating the activation energies for the forward and reverse steps of elementary reactions, consider the CO dissociation reaction on Fe ($CO* + * \leftrightarrow C* + O*$). If the atomic binding energies of C and O are 118.706 kcal/mol and 159.31 kcal/mol respectively, for a coordination number (n) of 3; from Equation 2.35 the metal heat of adsorption for C is

$Q_{0C} = Q_C/(2-1/n) = 118.706/(2-1/3)$ = 71.224 kcal/mol while that for O is

$Q_{0O} = Q_O/(2-1/n) = 159.31/(2-1/3)$ = 95.586 kcal/mol. The Heat of adsorption of CO (Q_{CO}) is calculated from Equation 2.36

$Q_{CO} = Q_{0C}^2/(Q_{0C} + D_{CO}) = 71.224^2/(71.224 + 257)$ = 15.455 kcal/mol. The net reaction enthalpy (ΔH) is calculated from Equation

2.46: $\Delta H = D_{CO} + Q_{CO} - Q_C - Q_O = 257 + 15.455 - 118.709 - 159.31$ = -5.561 kcal/mol.

The forward activation energy for the dissociation step (E_f) is calculated from Equation

2.47: $E_f = 0.5\left(\Delta H + \frac{Q_C Q_O}{Q_C + Q_O}\right) = 0.5\left(-5.561 + \frac{118.706 \times 159.31}{118.706 + 159.31}\right)$ = 31.23 kcal/mol =

131 kJ/mol. The reverse activation energy (E_r) is calculated from Equation 2.48:

$E_r = E_f - \Delta H = 31.23 - (-)5.561$ = 36.791 kcal/mol = 154 kJ/mol

A.5 Derivation of LH Type Macrokinetic Models

Model 1:

1 $$CO_g + * \leftrightarrow CO*$$ (A.7)

2 $$H_{2g} + 2* \leftrightarrow 2H*$$ (A.8)

3 $$CO* + * \leftrightarrow C* + O*$$ (A.9)

4 $$C* + H* \rightarrow CH* + *$$ (A.10) rds

5 $$O* + H* \leftrightarrow OH* + *$$ (A.11)

6 $$OH* + H* \rightarrow H_2O_g + 2*$$ (A.12) rds

7 $$-r_{CO} = r_4 = r_6 = k_4\theta_C\theta_H = k_6\theta_{OH}\theta_H$$ (A.13)

From Equation (A.7):

8 $$\theta_{CO} = K_1 P_{CO}\theta_V$$ (A.14)

From Equation (A.8):

9 $$\theta_H = K_2^{1/2} P_{H_2}^{1/2}\theta_V$$ (A.15)

From Equation (A.9):

10 $$k_3\theta_{CO}\theta_V = k_{-3}\theta_C\theta_O \Rightarrow \theta_C = \frac{K_3\theta_{CO}\theta_V}{\theta_O}$$ (A.16)

From Equation (A.11):

11 $$k_5\theta_O\theta_H = k_{-5}\theta_{OH}\theta_V \Rightarrow \theta_O = \frac{k_{-5}\theta_{OH}\theta_V}{k_5\theta_H}$$ (A.17)

From Equation (A.13)

12 $$k_4\theta_C\theta_H = k_6\theta_{OH}\theta_H \Rightarrow \theta_{OH} = \frac{k_4\theta_C}{k_6} \Rightarrow \theta_O = \frac{k_{-5}k_4\theta_C\theta_V}{k_5k_6\theta_H}$$ (A.18)

13 $$\therefore \theta_C = \frac{K_3k_5k_6\theta_{CO}\theta_H\theta_V}{k_4k_{-5}\theta_C\theta_V} \Rightarrow \theta_C = \left(\frac{K_3K_5k_6\theta_{CO}\theta_H}{k_4}\right)^{1/2}$$ (A.19)

Therefore,

14 $$-r_{CO} = k_4\left(\frac{K_3K_5k_6\theta_{CO}\theta_H}{k_4}\right)^{1/2}\theta_H = \left(k_4k_6K_5K_1\right)^{1/2}K_2^{3/4}P_{CO}^{1/2}P_{H_2}^{3/4}\theta_V^2 \quad \text{(A.20)}$$

If carbon is the most abundant surface intermediate, then the site balance becomes:

15 $$1 = \theta_V + \theta_C = \theta_V + \left(\frac{k_6K_3K_5K_1}{k_4}\right)^{1/2}K_2^{1/4}P_{CO}^{1/2}P_{H_2}^{1/4}\theta_V \quad \text{(A.21)}$$

16 $$\Rightarrow \theta_V = \frac{1}{1+BP_{CO}^{1/2}P_{H_2}^{1/4}} \Rightarrow B = \left(\frac{k_6K_3K_5K_1}{k_4}\right)^{1/2}K_2^{1/4} \quad \text{(A.22)}$$

17 $$-r_{CO} = \frac{AP_{CO}^{1/2}P_{H_2}^{3/4}}{\left(1+BP_{CO}^{1/2}P_{H_2}^{1/4}\right)^2} \Rightarrow A = \left(k_4k_6K_5K_1\right)^{1/2}K_2^{3/4} \quad \text{(A.23)}$$

Model 2:

18 $$C* + H* \rightarrow CH* + * \quad \text{(A.24) rds}$$

19 $$OH* + OH* \rightarrow H_2O_g + O* + * \quad \text{(A.25) rds}$$

20 $$-r_{CO} = r_{18} = r_{19} = k_{18}\theta_C\theta_H = k_{19}\theta_{OH}^2 \quad \text{(A.26)}$$

From Equation (A.26);

21 $$k_{18}\theta_C\theta_H = k_{19}\theta_{OH}^2 \Rightarrow \theta_{OH} = \left(\frac{k_{18}\theta_C\theta_H}{k_{19}}\right)^{1/2} \quad \text{(A.27)}$$

22 $$\therefore \theta_O = \frac{k_{-5}\left(\frac{k_{18}\theta_C\theta_H}{k_{19}}\right)^{1/2}\theta_V}{k_5\theta_H} \Rightarrow \theta_C = \frac{K_3K_5\theta_{CO}\theta_H}{\left(\frac{k_{18}\theta_C\theta_H}{k_{19}}\right)^{1/2}} \quad \text{(A.28)}$$

23 $$\theta_C = \frac{k_{19}^{1/3}K_3^{2/3}K_5^{2/3}\theta_{CO}^{2/3}\theta_H^{1/3}}{k_{18}^{1/3}} = k_{18}^{-1/3}k_{19}^{1/3}K_5^{2/3}K_1^{2/3}K_2^{1/6}P_{CO}^{2/3}P_{H_2}^{1/6}\theta_V \quad \text{(A.29)}$$

Therefore,

24 $$-r_{CO} = k_{18}k_{18}^{-1/3}k_{19}^{1/3}K_5^{2/3}K_1^{2/3}K_2^{1/6}P_{CO}^{2/3}P_{H_2}^{1/6}\theta_V K_2^{1/2}P_{H_2}^{1/2}\theta_V \quad \text{(A.30)}$$

If we assume that carbon is the most abundant surface intermediate, then from site balance,

25 $$\theta_V = \frac{1}{1+DP_{CO}^{2/3}P_{H_2}^{1/6}} \Rightarrow D = k_{18}^{-1/3}k_{19}^{1/3}K_5^{2/3}K_1^{2/3}K_2^{1/6} \quad \text{(A.31)}$$

Hence,

26 $$-r_{CO} = \frac{CP_{CO}^{2/3} P_{H_2}^{2/3}}{\left(1 + DP_{CO}^{2/3} P_{H_2}^{1/6}\right)^2} \Rightarrow C = k_{18}^{2/3} k_{19}^{1/3} K_5^{2/3} K_1^{2/3} K_2^{2/3}$$ (A.32)

Model 3:

27 $$CO* + H* \leftrightarrow CHO* + *$$ (A.33)

28 $$CHO* + H* \rightarrow CH* + OH*$$ (A.34) rds

29 $$CO* + * \rightarrow C* + O*$$ (A.35) rds

30 $$-r_{CO} = r_{28} + r_{29} = k_{28}\theta_{CHO}\theta_H + k_{29}\theta_{CO}\theta_V$$ (A.36)

From Equation (A.33),

31 $$k_{27}\theta_{CO}\theta_H = k_{-27}\theta_{CHO}\theta_V \Rightarrow \theta_{CHO} = \frac{K_{27}\theta_{CO}\theta_H}{\theta_V}$$ (A.37)

32 $$r_{28} = k_{28}\frac{K_{27}\theta_{CO}\theta_H^2}{\theta_V} = k_{28}K_{27}K_1K_2P_{CO}P_{H_2}\theta_V^2$$ (A.38)

33 $$r_{29} = k_{29}\theta_{CO}\theta_V = k_{29}K_1P_{CO}\theta_V^2$$ (A.39)

Therefore,

34 $$-r_{CO} = k_{28}K_{27}K_1K_2P_{CO}P_{H_2}\theta_V^2 + k_{29}K_1P_{CO}\theta_V^2$$ (A.40)

If we assume that adsorbed CO is the most abundant surface intermediate, then;

35 $$\theta_V = \frac{1}{1 + K_1P_{CO}}$$ (A.41)

Therefore,

36 $$-r_{CO} = \frac{EP_{CO}P_{H_2} + FP_{CO}}{\left(1 + K_1P_{CO}\right)^2} \Rightarrow E = k_{28}K_{27}K_1K_2 \Rightarrow F = k_{29}K_1$$ (A.42)

Estimation of rate constants from transition state theory

We can use Transition state theory to estimate the pre-exponential factors at 483K. Below are estimates of the pre-exponential factors where the subscript c represents the pre-exponential factor for the specified rate constants.

37 $$K_{1_c} = \frac{k_{1_c}}{k_{-1_c}} = \frac{4.256\times10^4\left(atm\cdot s\right)^{-1}}{1.0\times10^{13}s^{-1}} = 4.256\times10^{-9}atm^{-1}$$ (A.43)

$$K_{2_C} = \frac{k_{2_C}}{k_{-2_C}} = \frac{2.2\times10^6\left(atm\cdot s\right)^{-1}}{1.9\times10^{13}s^{-1}} = 1.1\times10^{-7}atm^{-1}$$

38 $$K_{27C} = \frac{k_{27_C}}{k_{-27_C}} = \frac{1.7\times10^{14}s^{-1}}{1.0\times10^{13}s^{-1}} = 17$$ (A.44)

$$E_c = \left(\frac{2.7\times10^{12}}{s}\right)(17)\left(\frac{1.1\times10^{-7}}{atm}\right)\left(\frac{4.256\times10^{-9}}{atm}\right) = \frac{2.15\times10^{-2}}{atm^2 s}$$

39 $$F_c = \left(1.0\times10^{13}\,s^{-1}\right)\left(4.256\times10^{-9}\,atm^{-1}\right) = 4.256\times10^{4}\left(atm\cdot s\right)^{-1} \quad \text{(A.45)}$$

40 $$C_c = \left(\frac{1.4\times10^{14}}{s}\right)^{2/3}\left(\frac{1.0\times10^{13}}{s}\right)^{1/3}(11)^{2/3}\left(\frac{4.256\times10^{-9}}{atm}\right)^{2/3}\left(\frac{1.1\times10^{-7}}{atm}\right)^{2/3} = \frac{1.732\times10^{4}}{atm^{4/3}s} \quad \text{(A.46)}$$

41 $$D_c = \left(\frac{1.4\times10^{14}}{s}\right)^{-1/3}\left(\frac{1.0\times10^{13}}{s}\right)^{1/3}\left(\frac{4.256\times10^{-9}}{atm}\right)^{2/3}\left(\frac{1.1\times10^{-7}}{atm}\right)(10)^{2/3} = 1.2\times10^{-7}\,atm^{-5/6} \quad \text{(A.47)}$$

42 $$A_c = \left(\frac{1.4\times10^{14}}{s}\right)^{1/2}(16.4)^{1/2}(11)^{1/2}\left(\frac{1.1\times10^{13}}{s}\right)^{1/2}\left(\frac{4.256\times10^{-9}}{atm}\right)^{1/2}\left(\frac{1.1\times10^{-7}}{atm}\right)^{3/4} = \frac{2.0\times10^{4}}{atm^{1.25}s} \quad \text{(A.48)}$$

43 $$B_C = (0.164)^{1/2}(11)^{1/2}\left(\frac{1.1\times10^{13}\,s^{-1}}{1.4\times10^{14}\,s^{-1}}\right)^{1/2}\left(\frac{4.256\times10^{-9}}{atm}\right)^{1/2}\left(\frac{1.1\times10^{-7}}{atm}\right)^{1/4} = 4.47\times10^{-7}\,atm^{-0.75} \quad \text{(A.49)}$$

A.6 Catalyst Preparation

See Reference [19] for support prepation and washcoating procedure used during the preparation of 20Fe1K1Pt-ALa-mon-507.

A.7 Fortran Code for Modeling CO TPD and Estimating Kinetic Parameters for the Elementary Steps

The sample Fotran code listed below are only driver programs for calling DODRPACK and DVODE. Both DODRPACK and DVODE programs are not included here since they are available online for free at http://www.netlib.org/odrpack/ and https://computation.llnl.gov/casc/software.html respectively.

```
      PROGRAM SAMPLE

C  ODRPACK ARGUMENT DEFINITIONS
C       ==> FCN       NAME OF THE USER SUPPLIED FUNCTION SUBROUTINE
C       ==> N         NUMBER OF OBSERVATIONS
C       ==> M         COLUMNS OF DATA IN THE EXPLANATORY VARIABLE
C       ==> NP        NUMBER OF PARAMETERS
C       ==> NQ        NUMBER OF RESPONSES PER OBSERVATION
C      <==> BETA      FUNCTION PARAMETERS
```

```
C      ==> Y        RESPONSE VARIABLE
C      ==> LDY      LEADING DIMENSION OF ARRAY Y
C      ==> X        EXPLANATORY VARIABLE
C      ==> LDX      LEADING DIMENSION OF ARRAY X
C      ==> WE       "EPSILON" WEIGHTS
C      ==> LDWE     LEADING DIMENSION OF ARRAY WE
C      ==> LD2WE    SECOND DIMENSION OF ARRAY WE
C      ==> WD       "DELTA" WEIGHTS
C      ==> LDWD     LEADING DIMENSION OF ARRAY WD
C      ==> LD2WD    SECOND DIMENSION OF ARRAY WD
C      ==> IFIXB    INDICATORS FOR "FIXING" PARAMETERS (BETA)
C      ==> IFIXX    INDICATORS FOR "FIXING" EXPLANATORY VARIABLE (X)
C      ==> LDIFX    LEADING DIMENSION OF ARRAY IFIXX
C      ==> JOB      TASK TO BE PERFORMED
C      ==> NDIGIT   GOOD DIGITS IN SUBROUTINE FCN RESULTS
C      ==> TAUFAC   TRUST REGION INITIALIZATION FACTOR
C      ==> SSTOL    SUM OF SQUARES CONVERGENCE CRITERION
C      ==> PARTOL   PARAMETER CONVERGENCE CRITERION
C      ==> MAXIT    MAXIMUM NUMBER OF ITERATIONS
C      ==> IPRINT   PRINT CONTROL
C      ==> LUNERR   LOGICAL UNIT FOR ERROR REPORTS
C      ==> LUNRPT   LOGICAL UNIT FOR COMPUTATION REPORTS
C      ==> STPB     STEP SIZES FOR FINITE DIFFERENCE DERIVATIVES WRT BETA
C      ==> STPD     STEP SIZES FOR FINITE DIFFERENCE DERIVATIVES WRT DELTA
C      ==> LDSTPD   LEADING DIMENSION OF ARRAY STPD
C      ==> SCLB     SCALE VALUES FOR PARAMETERS BETA
C      ==> SCLD     SCALE VALUES FOR ERRORS DELTA IN EXPLANATORY VARIABLE
C      ==> LDSCLD   LEADING DIMENSION OF ARRAY SCLD
C     <==> WORK     DOUBLE PRECISION WORK VECTOR
C      ==> LWORK    DIMENSION OF VECTOR WORK
C     <==  IWORK    INTEGER WORK VECTOR
C      ==> LIWORK   DIMENSION OF VECTOR IWORK
C     <==  INFO     STOPPING CONDITION

C  PARAMETERS SPECIFYING MAXIMUM PROBLEM SIZES HANDLED BY THIS DRIVER
C     MAXN          MAXIMUM NUMBER OF OBSERVATIONS
C     MAXM          MAXIMUM NUMBER OF COLUMNS IN EXPLANATORY VARIABLE
C     MAXNP         MAXIMUM NUMBER OF FUNCTION PARAMETERS
C     MAXNQ         MAXIMUM NUMBER OF RESPONSES PER OBSERVATION

C  PARAMETER DECLARATIONS AND SPECIFICATIONS
      INTEGER    LDIFX,LDSCLD,LDSTPD,LDWD,LDWE,LDX,LDY,LD2WD,LD2WE,
     +           LIWORK,LWORK,MAXM,MAXN,MAXNP,MAXNQ
      PARAMETER (MAXM=5,MAXN=10000,MAXNP=40,MAXNQ=5,
     +           LDY=MAXN,LDX=MAXN,
     +           LDWE=MAXN,LD2WE=MAXNQ,LDWD=MAXN,LD2WD=1,
     +           LDIFX=MAXN,LDSCLD=1,LDSTPD=1,
     +           LWORK=18 + 11*MAXNP + MAXNP**2 + MAXM + MAXM**2 +
     +                 4*MAXN*MAXNQ + 6*MAXN*MAXM + 2*MAXN*MAXNQ*MAXNP +
     +                 2*MAXN*MAXNQ*MAXM + MAXNQ**2 +
     +                 5*MAXNQ + MAXNQ*(MAXNP+MAXM) + LDWE*LD2WE*MAXNQ,
     +           LIWORK=20+MAXNP+MAXNQ*(MAXNP+MAXM))

C  VARIABLE DECLARATIONS
      INTEGER          I,INFO,IPRINT,J,JOB,L,LUNERR,LUNRPT,M,MAXIT,N,
     +                 NDIGIT,NP,NQ
      INTEGER          IFIXB(MAXNP),IFIXX(LDIFX,MAXM),IWORK(LIWORK)
      DOUBLE PRECISION PARTOL,SSTOL,TAUFAC
      DOUBLE PRECISION BETA(MAXNP),SCLB(MAXNP),SCLD(LDSCLD,MAXM),
     +                 STPB(MAXNP),STPD(LDSTPD,MAXM),
     +                 WD(LDWD,LD2WD,MAXM),WE(LDWE,LD2WE,MAXNQ),
     +                 WORK(LWORK),X(LDX,MAXM),Y(LDY,MAXNQ)
      EXTERNAL         FCN
```

```
       COMMON /DVOD01/ ACNRM, CCMXJ, CONP, CRATE, DRC, EL(13),
      1                ETT, ETAMAX, H, HMIN, HMXI, HNEW, HSCAL, PRL1,
      2                RC, RL1, TAU(13), TQ(5), TN, UROUND,
      3                ICF, INIT, IPUP, JCUR, JSTART, JSV, KFLAG, KUTH,
      4                L, LMAX, LYH, LEWT, LACOR, LSAVF, LWM, LIWM,
      5                LOCJS, MAXORD, METH, MITER, MSBJ, MXHNIL, MXSTEP,
      6                N, NEWH, NEWQ, NHNIL, NQ, NQNYH, NQWAIT, NSLJ,
      7                NSLP, NYH
       COMMON /DVOD02/ HU, NCFN, NETF, NFE, NJE, NLU, NNI, NQU, NST

C  SPECIFY DEFAULT VALUES FOR DODRC ARGUMENTS
      WE(1,1,1)  = -1.0D0
      WD(1,1,1)  = -1.0D0
      IFIXB(1)   = -1



      IFIXX(1,1) = -1
      JOB        = -1
      NDIGIT     = -1
      TAUFAC     = -1.0D0

C      SSTOL      = -1.0D0
C      PARTOL     = -1.0D0
       SSTOL=1.0D-20
       PARTOL=1.0D-30
C      MAXIT      = -1
       MAXIT      = 1000
      IPRINT     = -1
      LUNERR     = -1
      LUNRPT     = -1
      STPB(1)    = -1.0D0
      STPD(1,1)  = -1.0D0
      SCLB(1)    = -1.0D0
      SCLD(1,1)  = -1.0D0

C  SET UP ODRPACK REPORT FILES
      LUNERR  =   9
      LUNRPT  =   9
      OPEN (UNIT=9,FILE='REPORT3')

C  READ PROBLEM DATA
      OPEN (UNIT=5,FILE='DATA3')

      READ (5,FMT=*) N,M,NP,NQ
      READ (5,FMT=*) (BETA(I),I=1,NP)
      DO 10 I=1,N
         READ (5,FMT=*) (X(I,J),J=1,M),(Y(I,L),L=1,NQ)

   10 CONTINUE

C  SPECIFY TASK AS EXPLICIT ORTHOGONAL DISTANCE REGRESSION
C                  WITH CENTRAL DIFFERENCE DERIVATIVES
C                  COVARIANCE MATRIX CONSTRUCTED WITH RECOMPUTED DERIVATIVES
C                  DELTA INITIALIZED BY USER
C                  NOT A RESTART
C  AND INDICATE LONG INITIAL REPORT
C               NO ITERATION REPORTS
C               LONG FINAL REPORT
C      JOB     = 01010
c      IPRINT  = 2002
       JOB     = 00002
      IPRINT  = 2222
```

```
C
C  INITIALIZE DELTA, AND SPECIFY FIRST DECADE OF FREQUENCIES AS FIXED
C      DO 20 I=1,N
C         IF (X(I,1).LT.100.0D0) THEN
C            WORK(I)    = 0.0D0
C            IFIXX(I,1) = 1
C         ELSE IF (X(I,1).LE.150.0D0) THEN
C            WORK(I)    = 0.0D0
C            IFIXX(I,1) = 1
C         ELSE IF (X(I,1).LE.1000.0D0) THEN
C            WORK(I)    = 25.0D0
C            IFIXX(I,1) = 1
C         ELSE IF (X(I,1).LE.10000.0D0) THEN
C            WORK(I)    = 560.0D0
C            IFIXX(I,1) = 1
C         ELSE IF (X(I,1).LE.100000.0D0) THEN
C            WORK(I)    = 9500.0D0
C            IFIXX(I,1) = 1
C         ELSE
C            WORK(I) = 144000.0D0
C            IFIXX(I,1) = 1

C   20 CONTINUE

C  SET WEIGHTS
C      DO 30 I=1,N
C         IF (X(I,1).EQ.100.0D0 .OR. X(I,1).EQ.150.0D0) THEN
C            WE(I,1,1) = 0.0D0
C            WE(I,1,2) = 0.0D0
C            WE(I,2,1) = 0.0D0
C            WE(I,2,2) = 0.0D0
C         ELSE
C            WE(I,1,1) =   559.6D0
C            WE(I,1,2) = -1634.0D0
C            WE(I,2,1) = -1634.0D0
C            WE(I,2,2) =  8397.0D0
C         END IF
C         WD(I,1,1)    =  (1.0D-4)/(X(I,1)**2)
C            WD(I,1,1)=0.0D0
C   30 CONTINUE
C      DO 40 I=1,N
C            WE(I,1,1)=1.0D0
C            WE(I,1,2)=1.0D0
C            WE(I,1,3)=1.0D0
C            WE(I,2,1)=1.0D0
C            WE(I,2,2)=1.0D0
C            WE(I,2,3)=1.0D0
C            WE(I,3,1)=1.0D0
C            WE(I,3,2)=1.0D0
C            WE(I,3,3)=1.0D0
C 40   CONTINUE


C  COMPUTE SOLUTION
      CALL DODRC(FCN,
     +           N,M,NP,NQ,
     +           BETA,
     +           Y,LDY,X,LDX,
     +           WE,LDWE,LD2WE,WD,LDWD,LD2WD,
     +           IFIXB,IFIXX,LDIFX,
     +           JOB,NDIGIT,TAUFAC,
     +           SSTOL,PARTOL,MAXIT,
     +           IPRINT,LUNERR,LUNRPT,
```

```
     +           STPB,STPD,LDSTPD,
     +           SCLB,SCLD,LDSCLD,
     +           WORK,LWORK,IWORK,LIWORK,
     +           INFO)
      END
C  COMPUTE SOLUTION
C      CALL DODR(FCN,
C     +           N,M,NP,NQ,
C     +           BETA,
C     +           Y,LDY,X,LDX,
C     +           WE,LDWE,LD2WE,WD,LDWD,LD2WD,
C     +           JOB,
C     +           IPRINT,LUNERR,LUNRPT,
C     +           WORK,LWORK,IWORK,LIWORK,
C     +           INFO)
C      END


      SUBROUTINE FCN(N,M,NP,NQ,
     +               LDN,LDM,LDNP,
     +               BETA,XPLUSD,
     +               IFIXB,IFIXX,LDIFX,
     +               IDEVAL,F,FJACB,FJACD,
     +               ISTOP)

C  SUBROUTINE ARGUMENTS
C      ==> N        NUMBER OF OBSERVATIONS
C      ==> M        NUMBER OF COLUMNS IN EXPLANATORY VARIABLE
C      ==> NP       NUMBER OF PARAMETERS
C      ==> NQ       NUMBER OF RESPONSES PER OBSERVATION
C      ==> LDN      LEADING DIMENSION DECLARATOR EQUAL OR EXCEEDING N
C      ==> LDM      LEADING DIMENSION DECLARATOR EQUAL OR EXCEEDING M
C      ==> LDNP     LEADING DIMENSION DECLARATOR EQUAL OR EXCEEDING NP
C      ==> BETA     CURRENT VALUES OF PARAMETERS
C      ==> XPLUSD   CURRENT VALUE OF EXPLANATORY VARIABLE, I.E., X + DELTA
C      ==> IFIXB    INDICATORS FOR "FIXING" PARAMETERS (BETA)
C      ==> IFIXX    INDICATORS FOR "FIXING" EXPLANATORY VARIABLE (X)
C      ==> LDIFX    LEADING DIMENSION OF ARRAY IFIXX
C      ==> IDEVAL   INDICATOR FOR SELECTING COMPUTATION TO BE PERFORMED
C     <==  F        PREDICTED FUNCTION VALUES
C     <==  FJACB    JACOBIAN WITH RESPECT TO BETA
C     <==  FJACD    JACOBIAN WITH RESPECT TO ERRORS DELTA
C     <==  ISTOP    STOPPING CONDITION, WHERE
C                     0 MEANS CURRENT BETA AND X+DELTA WERE
C                       ACCEPTABLE AND VALUES WERE COMPUTED SUCCESSFULLY
C                     1 MEANS CURRENT BETA AND X+DELTA ARE
C                       NOT ACCEPTABLE;  ODRPACK SHOULD SELECT VALUES
C                       CLOSER TO MOST RECENTLY USED VALUES IF POSSIBLE
C                    -1 MEANS CURRENT BETA AND X+DELTA ARE
C                       NOT ACCEPTABLE;  ODRPACK SHOULD STOP

C  INPUT ARGUMENTS, NOT TO BE CHANGED BY THIS ROUTINE:
      INTEGER          I,IDEVAL,ISTOP,LDIFX,LDM,LDN,LDNP,M,N,NP,NQ
      DOUBLE PRECISION BETA(NP),XPLUSD(LDN,M),FFNEW(LDN,NQ),T
      INTEGER          IFIXB(NP),IFIXX(LDIFX,M),NEWN,LLDN,NNQ
C  OUTPUT ARGUMENTS:
      DOUBLE PRECISION F(LDN,NQ),FJACB(LDN,LDNP,NQ),FJACD(LDN,LDM,NQ)
       DOUBLE PRECISION BETA_THETA1,BETA_THETA2
       DOUBLE PRECISION FYYCO(LDN),FYYCO2(LDN),X_TOUT(LDN)
C  LOCAL VARIABLES
C      DOUBLE PRECISION FREQ,PI,OMEGA,CTHETA,STHETA,THETA,PHI,R
C      INTRINSIC        ATAN2,EXP,SQRT
```

```
C
C  CHECK FOR UNACCEPTABLE VALUES FOR THIS PROBLEM
      DO  I=1,N
         IF (XPLUSD(I,1).LT.296.0D0) THEN
            ISTOP = 1
            RETURN
         END IF
       ENDDO
       DO 10 I =1,NP
             IF(BETA(I).LT.0.0D0)THEN
                   ISTOP=1
                   RETURN
             ENDIF
   10 CONTINUE

       BETA_THETA1 = BETA(20)
         IF (BETA_THETA1.GT.1.0D0) THEN
            ISTOP = 1
            RETURN
         END IF



      ISTOP = 0


C  COMPUTE PREDICTED VALUES
      IF (MOD(IDEVAL,10).GE.1) THEN

         KKK = KKK+1
             KKKK=0


       DO I = 1,LDN
             X_TOUT(I) = XPLUSD(I,1)
       END DO
       N_DIM = LDN
       CALL DVODE_DRIVER(BETA,FYYCO,FYYCO2,X_TOUT,N_DIM)



          DO 100 I = 1,LDN
C                  TOUT=XPLUSD(I,1)

C                  CALL DVODE_DRIVER(YY,BETA,TOUT,IEYCO,IEYCO2)
C                        F(I,1)=YY(IEYCO)
C                        F(I,2)=YY(IEYCO2)
C                        F(I,3)=YY(3)

                         F(I,1) = FYYCO(I)
                         F(I,2) = FYYCO2(I)
                         WRITE(*,*)KKK,I
 100    CONTINUE

      END IF
       ISTOP = 0
      RETURN
      END

C      SUBROUTINE DVODE_DRIVER(YY,BETA,TOUT,IEYCO,IEYCO2)
       SUBROUTINE DVODE_DRIVER(BETA,FYYCO,FYYCO2,X_TOUT,N_DIM)
       EXTERNAL FEX, JEX
      DOUBLE PRECISION ATOL, RPAR, RTOL, RWORK, TT, TOUT, YY,BETA
```

```
C
C
      DIMENSION YY(80), ATOL(80), RWORK(59352), IIWRK(200),BETA(20)
       DOUBLE PRECISION THETA_V_1_1,THETA_V_2_2

       DOUBLE PRECISION FYYCO(N_DIM),FYYCO2(N_DIM),X_TOUT(N_DIM)

       DOUBLE PRECISION A1_F,A1_R,E1_F,E1_R,A2_F,A2_R,E2_F,E2_R,A3_F,
       1A3_R,E3_F,E3_R,A4_F,A4_R,E4_F,E4_R,BETA_T,YCO_MAX,YCO2_MAX

       DOUBLE PRECISION DISP_CAT,CAT_MW,CAT_LOADING,T_EMP,RG,
       1PTOT,EB,TAU_T,RHOB,N_GAS_PHASE_SPECIES,YH2_0

       DOUBLE PRECISION RR1,RR2,RR3,RR4,THETA_V_1,DENOM1

       DOUBLE PRECISION B1_F,B1_R,EA1_F,EA1_R,B2_F,B2_R,EA2_F,EA2_R,B3_F,
       1B3_R,EA3_F,EA3_R,B4_F,B4_R,EA4_F,EA4_R

       DOUBLE PRECISION SPACE_STEP

       COMMON/UCHENNA/A1_F,A1_R,E1_F,E1_R,A2_F,A2_R,E2_F,E2_R,A3_F,
       1A3_R,E3_F,E3_R,A4_F,A4_R,E4_F,E4_R,BETA_T,YCO_MAX,YCO2_MAX

       COMMON /UCHENNA2/DISP_CAT,CAT_MW,CAT_LOADING,T_EMP,RG,
       1PTOT,EB,TAU_T,RHOB,N_GAS_PHASE_SPECIES,YH2_0

       COMMON/UCHENNA3/B1_F,B1_R,EA1_F,EA1_R,B2_F,B2_R,EA2_F,EA2_R,B3_F,
       1B3_R,EA3_F,EA3_R,B4_F,B4_R,EA4_F,EA4_R


       COMMON/UCHENNA4/SPACE_STEP,N_NODES

          COMMON /DVOD01/ ACNRM, CCMXJ, CONP, CRATE, DRC, EL(13),
      1                ETT, ETAMAX, H, HMIN, HMXI, HNEW, HSCAL, PRL1,
      2                RC, RL1, TAU(13), TQ(5), TN, UROUND,
      3                ICF, INIT, IPUP, JCUR, JSTART, JSV, KFLAG, KUTH,
      4                L, LMAX, LYH, LEWT, LACOR, LSAVF, LWM, LIWM,
      5                LOCJS, MAXORD, METH, MITER, MSBJ, MXHNIL, MXSTEP,
      6                N, NEWH, NEWQ, NHNIL, NQ, NQNYH, NQWAIT, NSLJ,
      7                NSLP, NYH
       COMMON /DVOD02/ HU, NCFN, NETF, NFE, NJE, NLU, NNI, NQU, NST
       OPEN(UNIT=3,FILE='TPD_MODEL_(2_SITES_PFR)_9_May_2007_5NODES')



C      ENTER THE VALUES OF THE RATE CONSTANTS _ALPHA 1

C      E1_R (J/MOL)
       E1_R  = 0.0D0



C      E4_R (J/MOL)
       E4_R = 0.0D0




C      SET VALUES OF ESTIMATED CONSTANTS TO BE USED IN INTEGRATION OF ODE'S
       A1_F  = BETA(1)
       A1_R  = BETA(2)
```

```
      E1_F  = BETA(3)

      A2_F  = BETA(4)
      A2_R  = BETA(5)
      E2_F  = BETA(6)
      E2_R  = BETA(7)
      A3_F  = BETA(8)
      A3_R =  BETA(9)
      E3_F  = BETA(10)
      E3_R = BETA(11)
      A4_F = BETA(12)
      A4_R = BETA(13)
      E4_F = BETA(14)

      A5_F = BETA(15)
      A5_5 = BETA(16)
      E5_F = BETA(17)
      E5_R = BETA(18)



C     ENTER THE VALUES OF THE RATE CONSTANTS _ALPHA 2

C     E1_R (J/MOL)
      EA1_R  = 0.0D0


C     E4_R (J/MOL)
      EA4_R = 0.0D0


C     ENTER YCO_MAX (USED FOR NORMALIZATION)

      YCO_MAX = 4.20D-03

C     ENTER YCO2_MAX (USED FOR NORMALIZATION)
      YCO2_MAX = 2.19D-03

C     ENTER RESIDENCE TIME (S)
      TAU_T = 0.491D0


C     ENTER TEMPERATURE RAMP RATE
      BETA_T = 3.33D1/6.0D1

C     ENTER CATALYST BED DENSITY IN (KG/M^3)
      RHOB = 1.0D3
C     ENTER BED VOID FRACTION
      EB = 0.45D0

C     ENTER TOTAL REACTOR PRESSURE (Pa)
      PTOT =1.013D5
C     ENTER GAS CONSTANT
      RG = 8.314D0
C     ENTER INITIAL TEMPERATURE
      T_EMP = 296.0D0

C     ENTER CATALYST DISPERSION (IN FRACTION)
      DISP_CAT = BETA(19)

C     ENTER CATALYST METAL LOADING (IN FRACTION)
      CAT_LOADING = 9.9D-01
```

```
C      ENTER MOLECULAR WEIGHT OF ACTIVE CATALYST PHASE (KG/MOL)

       CAT_MW = 55.847D-03

C      ENTER SPACE STEP SIZE
       SPACE_STEP = 0.1D0


       N_NODES = INT(1.0D0/SPACE_STEP)


C      LLL=2
C      ENTER THE NUMBER OF DIFFERENTIAL EQUATIONS
      NEQ = 8*N_NODES
      N_BETA = 28
      TT = 296.0D0
C      DELTAT_STEP=5.0D-01
C      TOUT = TT+DELTAT_STEP

C      DETERMINE INDICES WHERE EACH SPECIES STARTS

       IYCO = 1
       IYCO2 = IYCO + N_NODES
       IYCO_S1 = IYCO2 + N_NODES
       IYC_S1 = IYCO_S1 + N_NODES
       IYO_S1 = IYC_S1 + N_NODES
       IYCO2_S1 = IYO_S1 + N_NODES

       IYC_S2 = IYCO2_S1 + N_NODES
       IYO_S2 = IYC_S2 + N_NODES

C      DETERMINE INDICES WHERE EACH SPECIES ENDS

       IEYCO = IYCO2 - 1
       IEYCO2 = IYCO_S1 - 1
       IEYCO_S1 = IYC_S1 - 1
       IEYC_S1 = IYO_S1 - 1
       IEYO_S1 = IYCO2_S1 - 1
       IEYCO2_S1 = IYC_S2 - 1

       IEYC_S2 = IYO_S2 - 1
       IEYO_S2 = IYO_S2 + N_NODES - 1


C      SET INITIAL CONDITIONS

C      FOR ALL GAS PHASE SPECIES CO(g) AND CO2(g),H2O(g)
       DO I = IYCO,IEYCO2
       YY(I) =      0.0D0
       END DO


C      FOR SURFACE CO-ALPHA 1

       DO I = IYCO_S1,IEYCO_S1
       YY(I) = BETA(20)
       END DO
C      FOR SURFACE C-ALPHA 1
       DO I = IYC_S1,IEYC_S1
       YY(I) = 0.0D0
       END DO

C      FOR SURFACE O-ALPHA 1
```

```
       DO I = IYO_S1,IEYO_S1
       YY(I) = 0.0D0
       END DO
C      FOR SURFACE CO2-ALPHA 1
       DO I = IYCO2_S1,IEYCO2_S1
       YY(I) = 0.0D0
       END DO



C      FOR SURFACE C-ALPHA 2
       DO I = IYC_S2,IEYC_S2
       YY(I) = 0.0D0
       END DO

C      FOR SURFACE O-ALPHA 2
       DO I = IYO_S2,IEYO_S2
       YY(I) = 0.0D0
       END DO



C      SET CONVERGENCE TOLORANCE
      ITOL = 2
      RTOL = 1.0D-04
       DO  I = 1,NEQ

             ATOL(I) = 1.0D-8
       END DO

C RWORK  = Real work array of length at least:
C             20 + 16*NEQ                      for MF = 10,
C             22 +  9*NEQ + 2*NEQ**2           for MF = 21 or 22,
C             22 + 11*NEQ + (3*ML + 2*MU)*NEQ  for MF = 24 or 25.
C LRW    = Declared length of RWORK (in user's DIMENSION statement).
C IWORK  = Integer work array of length at least:
C             30        for MF = 10,
C             30 + NEQ  for MF = 21, 22, 24, or 25.
C          If MF = 24 or 25, input in IWORK(1),IWORK(2) the lower
C          and upper half-bandwidths ML,MU.
C LIW    = Declared length of IWORK (in user's DIMENSION statement).

C      SET DVODE CONSTANTS
      ITASK = 1
      ISTATE = 1
      IOPT = 1
       IIWRK(6) = 900000
      LRW = 59352
      LIW = 200
C      SPECIFY DVODE SOLUTION METHOD
      MF = 22

       DO IOUT = 1,N_DIM
             TOUT = X_TOUT(IOUT)



30        CALL DVODE(FEX,NEQ,YY,TT,TOUT,ITOL,RTOL,ATOL,ITASK,ISTATE,
     1            IOPT,RWORK,LRW,IIWRK,LIW,JEX,MF,RPAR,IPAR)


             FYYCO(IOUT) = YY(IEYCO)
             FYYCO2(IOUT) = YY(IEYCO2)
```

```
C
C      IF (ISTATE .LT. 0)GO TO 80

       END DO


C      WRITE(3,60)IIWRK(11),IIWRK(12),IIWRK(13),IIWRK(19),
C     1           IIWRK(20),IIWRK(21),IIWRK(22)
C  60  FORMAT(/' No. steps =',I4,'   No. f-s =',I4,
C     1       '   No. J-s =',I4,'   No. LU-s =',I4/
C     2       '  No. nonlinear iterations =',I4/
C     3       '  No. nonlinear convergence failures =',I4/
C     4       '  No. error test failures =',I4/)
       RETURN
   80  WRITE(3,90)ISTATE


   90  FORMAT(///1X,I6,1X,' Error halt: ISTATE =',I3)
c      ISTOP = 0
       RETURN
       END




C      FUNCTION SUBROUTINE
       SUBROUTINE FEX (NEQ, TT, YY, YDOT, RPAR, IPAR)
       DOUBLE PRECISION RPAR, TT, YY, YDOT


       DIMENSION YY(NEQ), YDOT(NEQ)
        DIMENSION R1(10),R2(10),R3(10),R4(10),R5(10),
        1R6(10),R7(10),R8(10),THETA_V(10)

        DOUBLE PRECISION R1,R2,R3,R4,R5,R6,R7,R8,THETA_V,T_AU,FACTOR2


        DOUBLE PRECISION DENOM1,FACTOR

        DOUBLE PRECISION A1_F,A1_R,E1_F,E1_R,A2_F,A2_R,E2_F,E2_R,A3_F,
        1A3_R,E3_F,E3_R,A4_F,A4_R,E4_F,E4_R,BETA_T,YCO_MAX,YCO2_MAX

        DOUBLE PRECISION DISP_CAT,CAT_MW,CAT_LOADING,T_EMP,RG,
        1PTOT,EB,TAU_T,RHOB,N_GAS_PHASE_SPECIES,YH2_0

        DOUBLE PRECISION A5_F,A5_R,E5_F,E5_R,B2_F,B2_R,EA2_F,EA2_R,B3_F,
        1B3_R,EA3_F,EA3_R,B4_F,B4_R,EA4_F,EA4_R

        DOUBLE PRECISION SPACE_STEP

        COMMON/UCHENNA/A1_F,A1_R,E1_F,E1_R,A2_F,A2_R,E2_F,E2_R,A3_F,
        1A3_R,E3_F,E3_R,A4_F,A4_R,E4_F,E4_R,BETA_T,YCO_MAX,YCO2_MAX

        COMMON /UCHENNA2/DISP_CAT,CAT_MW,CAT_LOADING,T_EMP,RG,
        1PTOT,EB,TAU_T,RHOB,N_GAS_PHASE_SPECIES,YH2_0

        COMMON/UCHENNA3/A5_F,A5_R,E5_F,E5_R,B2_F,B2_R,EA2_F,EA2_R,B3_F,
        1B3_R,EA3_F,EA3_R,B4_F,B4_R,EA4_F,EA4_R


        COMMON/UCHENNA4/SPACE_STEP,N_NODES

C      ENTER THE CONVERTER FOR RATE IN TOF TO RATE IN (MOL/kg S)
```

```
C
      CONVERTER = DISP_CAT*CAT_LOADING/CAT_MW


      T_AU = TAU_T*(T_EMP/TT)


C     COMPUTER SOME FACTORS AND DENOMINATIOR CONSTANTS

      FACTOR = RG*RHOB*CONVERTER/(EB*PTOT*BETA_T)




      FACTOR2 = T_AU*BETA_T*SPACE_STEP
C     DETERMINE INDICES WHERE EACH SPECIES STARTS

      IYCO = 1
      IYCO2 = IYCO + N_NODES
      IYCO_S1 = IYCO2 + N_NODES
      IYC_S1 = IYCO_S1 + N_NODES
      IYO_S1 = IYC_S1 + N_NODES
      IYCO2_S1 = IYO_S1 + N_NODES

      IYC_S2 = IYCO2_S1 + N_NODES
      IYO_S2 = IYC_S2 + N_NODES


C     DETERMINE INDICES WHERE EACH SPECIES ENDS

      IEYCO = IYCO2 - 1
      IEYCO2 = IYCO_S1 - 1
      IEYCO_S1 = IYC_S1 - 1
      IEYC_S1 = IYO_S1 - 1
      IEYO_S1 = IYCO2_S1 - 1
      IEYCO2_S1 = IYC_S2 - 1

      IEYC_S2 = IYO_S2 - 1
      IEYO_S2 = IYO_S2 + N_NODES - 1



C     SITE BALANCE
      DO J = 1,N_NODES
            DENOM1 = 0.0D0
            DO I= IYCO_S1,NEQ,N_NODES
                  DENOM1=DENOM1+YY(I)
            END DO

            THETA_V(J) = 1.0D0-DENOM1
      END DO


C     COMPUTE REACTION RATES ALPHA 1 SITES:

C     R1: CO* = CO(g) + *

      DO I = 1, N_NODES
            R1(I) = A1_F*EXP(-E1_F/(RG*TT))*YY(IYCO_S1 + I -1)-
     1A1_R*EXP(-E1_R/(RG*TT))*PTOT*YY(IYCO +I -1)*YCO_MAX*THETA_V(I)
      END DO
```

```
C      R2: CO* + * = C* + O*
       DO I = 1,N_NODES

       R2(I) = A2_F*EXP(-E2_F/(RG*TT))*YY(IYCO_S1 + I -1)*THETA_V(I)-
       1A2_R*EXP(-E2_R/(RG*TT))*YY(IYC_S1 +I - 1)*YY(IYO_S1 + I -1)
       END DO


C      R3: CO* + O* = CO2**
       DO I = 1,N_NODES
       R3(I) = A3_F*EXP(-E3_F/(RG*TT))*YY(IYCO_S1 + I-1)*YY(IYO_S1 +I-1)-
       1A3_R*EXP(-E3_R/(RG*TT))*YY(IYCO2_S1+I-1)
       END DO

C      R4: CO2** = CO2(g) + 2*
       DO I =  1, N_NODES

       R4(I) = A4_F*EXP(-E4_F/(RG*TT))*YY(IYCO2_S1 +I-1)-
       1A4_R*EXP(-E4_R/(RG*TT))*
     1PTOT*YY(IYCO2+I-1)*YCO2_MAX*THETA_V(I)**2.0D0
       END DO


C      COMPUTE REACTION RATES ALPHA 2 SITES:

C      R5: CO* = C*_S2 + O*_S2
       DO I = 1,N_NODES

       R5(I) = A5_F*EXP(-E5_F/(RG*TT))*YY(IYCO_S1+I-1)*THETA_V(I)-
       1A5_R*EXP(-E5_R/(RG*TT))*YY(IYC_S2+I-1)*YY(IYO_S2+I-1)
       END DO


C      ENTER DIFFERENTIAL EQUATIONS

C      FOR CO(g)

       YDOT(IYCO) = YY(IYCO)*(1.0D0/TT-1.0D0/FACTOR2)+
       1(TT*FACTOR*(R1(1)))/YCO_MAX


       IF(N_NODES.GT.1)THEN
              K = 1
              DO I = IYCO+1,IEYCO
                           K = K+1
C                          YDOT(I) = YY(I)*(1.0D0/TT-1.0D0/FACTOR2)+
C      1                   YY(I-1)/FACTOR2+(TT*FACTOR*(R1(K)+R5(K)))/YCO_MAX
                           YDOT(I) = (YY(I)/TT)-(YY(I)-YY(I-1))/FACTOR2 +
       1                   (TT*FACTOR*(R1(K)))/YCO_MAX
              END DO
       END IF


C      FOR CO2(g)

       YDOT(IYCO2) = YY(IYCO2)*(1.0D0/TT-1.0D0/FACTOR2)+
       1(TT*FACTOR*(R4(1)))/YCO2_MAX

       IF(N_NODES.GT.1)THEN
              K = 1
              DO I = IYCO2+1,IEYCO2
                           K = K+1
                           YDOT(I) = YY(I)*(1.0D0/TT-1.0D0/FACTOR2)+
```

```
     1                  YY(I-1)/FACTOR2+(TT*FACTOR*(R4(K)))/YCO2_MAX

            END DO
     END IF

C    FOR SURFACE CO (ALPHA 1)
     K = 0
     DO I = IYCO_S1,IEYCO_S1
            K = K+1
            YDOT(I) = (-R1(K)-R2(K)-R3(K)-R5(K))/BETA_T
     END DO

C    FOR SURFACE C (ALPHA 1)
     K = 0
     DO I = IYC_S1,IEYC_S1
            K = K+1
            YDOT(I) = R2(K)/BETA_T
     END DO

C    FOR SURFACE O (ALPHA 1)
     K = 0
     DO I = IYO_S1,IEYO_S1
            K = K+1

     YDOT(I) = (R2(K)-R3(K))/BETA_T
     END DO

C    FOR SURFACE CO2 (ALPHA 1)
     K = 0
     DO I = IYCO2_S1,IEYCO2_S1
            K = K+1
            YDOT(I) = (R3(K)-R4(K))/BETA_T
     END DO



C    FOR SURFACE C (ALPHA 2)
     K=0
     DO I =IYC_S2,IEYC_S2
                  K = K+1
            YDOT(I) = R5(K)/BETA_T
     END DO


C    FOR SURFACE O (ALPHA 2)
     K = 0
     DO I = IYO_S2,IEYO_S2

            K = K+1
            YDOT(I) = (R5(K))/BETA_T
     END DO


    RETURN
    END



C     GENERATE THE JACOBIAN
    SUBROUTINE JEX (NEQ, TT, YY, ML, MU, PD, NRPD, RPAR, IPAR)
    DOUBLE PRECISION PD, RPAR, TT, YY

    DIMENSION YY(NEQ), PD(NRPD,NEQ)
```

```
C
C
      RETURN
      END
```

A.8 Fortran Code for Modeling ITH and Estimating Kinetic Parameters for the Elementary Steps

The sample Fotran code listed below are only driver programs for calling DODRPACK and DVODE. Both DODRPACK and DVODE programs are not included here since they are available online for free at http://www.netlib.org/odrpack/ and https://computation.llnl.gov/casc/software.html respectively.

```
      PROGRAM SAMPLE

C  ODRPACK ARGUMENT DEFINITIONS
C       ==> FCN       NAME OF THE USER SUPPLIED FUNCTION SUBROUTINE
C       ==> N         NUMBER OF OBSERVATIONS
C       ==> M         COLUMNS OF DATA IN THE EXPLANATORY VARIABLE
C       ==> NP        NUMBER OF PARAMETERS
C       ==> NQ        NUMBER OF RESPONSES PER OBSERVATION
C      <==> BETA      FUNCTION PARAMETERS
C       ==> Y         RESPONSE VARIABLE
C       ==> LDY       LEADING DIMENSION OF ARRAY Y
C       ==> X         EXPLANATORY VARIABLE
C       ==> LDX       LEADING DIMENSION OF ARRAY X
C       ==> WE        "EPSILON" WEIGHTS
C       ==> LDWE      LEADING DIMENSION OF ARRAY WE
C       ==> LD2WE     SECOND DIMENSION OF ARRAY WE
C       ==> WD        "DELTA" WEIGHTS
C       ==> LDWD      LEADING DIMENSION OF ARRAY WD
C       ==> LD2WD     SECOND DIMENSION OF ARRAY WD
C       ==> IFIXB     INDICATORS FOR "FIXING" PARAMETERS (BETA)
C       ==> IFIXX     INDICATORS FOR "FIXING" EXPLANATORY VARIABLE (X)
C       ==> LDIFX     LEADING DIMENSION OF ARRAY IFIXX
C       ==> JOB       TASK TO BE PERFORMED
C       ==> NDIGIT    GOOD DIGITS IN SUBROUTINE FCN RESULTS
C       ==> TAUFAC    TRUST REGION INITIALIZATION FACTOR
C       ==> SSTOL     SUM OF SQUARES CONVERGENCE CRITERION
C       ==> PARTOL    PARAMETER CONVERGENCE CRITERION
C       ==> MAXIT     MAXIMUM NUMBER OF ITERATIONS
C       ==> IPRINT    PRINT CONTROL
C       ==> LUNERR    LOGICAL UNIT FOR ERROR REPORTS
C       ==> LUNRPT    LOGICAL UNIT FOR COMPUTATION REPORTS
C       ==> STPB      STEP SIZES FOR FINITE DIFFERENCE DERIVATIVES WRT BETA
```

```
C      ==> STPD     STEP SIZES FOR FINITE DIFFERENCE DERIVATIVES WRT DELTA
C      ==> LDSTPD   LEADING DIMENSION OF ARRAY STPD
C      ==> SCLB     SCALE VALUES FOR PARAMETERS BETA
C      ==> SCLD     SCALE VALUES FOR ERRORS DELTA IN EXPLANATORY VARIABLE
C      ==> LDSCLD   LEADING DIMENSION OF ARRAY SCLD
C     <==> WORK     DOUBLE PRECISION WORK VECTOR
C      ==> LWORK    DIMENSION OF VECTOR WORK
C     <==  IWORK    INTEGER WORK VECTOR
C      ==> LIWORK   DIMENSION OF VECTOR IWORK
C     <==  INFO     STOPPING CONDITION

C  PARAMETERS SPECIFYING MAXIMUM PROBLEM SIZES HANDLED BY THIS DRIVER
C     MAXN          MAXIMUM NUMBER OF OBSERVATIONS
C     MAXM          MAXIMUM NUMBER OF COLUMNS IN EXPLANATORY VARIABLE
C     MAXNP         MAXIMUM NUMBER OF FUNCTION PARAMETERS
C     MAXNQ         MAXIMUM NUMBER OF RESPONSES PER OBSERVATION

C  PARAMETER DECLARATIONS AND SPECIFICATIONS
      INTEGER    LDIFX,LDSCLD,LDSTPD,LDWD,LDWE,LDX,LDY,LD2WD,LD2WE,
     +           LIWORK,LWORK,MAXM,MAXN,MAXNP,MAXNQ
      PARAMETER (MAXM=5,MAXN=25490,MAXNP=100,MAXNQ=5,
     +           LDY=MAXN,LDX=MAXN,
     +           LDWE=MAXN,LD2WE=MAXNQ,LDWD=MAXN,LD2WD=1,
     +           LDIFX=MAXN,LDSCLD=1,LDSTPD=1,
     +           LWORK=18 + 11*MAXNP + MAXNP**2 + MAXM + MAXM**2 +
     +                 4*MAXN*MAXNQ + 6*MAXN*MAXM + 2*MAXN*MAXNQ*MAXNP +
     +                 2*MAXN*MAXNQ*MAXM + MAXNQ**2 +
     +                 5*MAXNQ + MAXNQ*(MAXNP+MAXM) + LDWE*LD2WE*MAXNQ,
     +           LIWORK=20+MAXNP+MAXNQ*(MAXNP+MAXM))

C  VARIABLE DECLARATIONS
      INTEGER          I,INFO,IPRINT,J,JOB,L,LUNERR,LUNRPT,M,MAXIT,N,
     +                 NDIGIT,NP,NQ
      INTEGER          IFIXB(MAXNP),IFIXX(LDIFX,MAXM),IWORK(LIWORK)
      DOUBLE PRECISION PARTOL,SSTOL,TAUFAC
      DOUBLE PRECISION BETA(MAXNP),SCLB(MAXNP),SCLD(LDSCLD,MAXM),
     +                 STPB(MAXNP),STPD(LDSTPD,MAXM),
     +                 WD(LDWD,LD2WD,MAXM),WE(LDWE,LD2WE,MAXNQ),
     +                 WORK(LWORK),X(LDX,MAXM),Y(LDY,MAXNQ)
      EXTERNAL         FCN
       COMMON /DVOD01/ ACNRM, CCMXJ, CONP, CRATE, DRC, EL(13),
     1                ETT, ETAMAX, H, HMIN, HMXI, HNEW, HSCAL, PRL1,
     2                RC, RL1, TAU(13), TQ(5), TN, UROUND,
     3                ICF, INIT, IPUP, JCUR, JSTART, JSV, KFLAG, KUTH,
     4                L, LMAX, LYH, LEWT, LACOR, LSAVF, LWM, LIWM,
     5                LOCJS, MAXORD, METH, MITER, MSBJ, MXHNIL, MXSTEP,
     6                N, NEWH, NEWQ, NHNIL, NQ, NQNYH, NQWAIT, NSLJ,
     7                NSLP, NYH
      COMMON /DVOD02/ HU, NCFN, NETF, NFE, NJE, NLU, NNI, NQU, NST

C  SPECIFY DEFAULT VALUES FOR DODRC ARGUMENTS
      WE(1,1,1)  = -1.0D0
      WD(1,1,1)  = -1.0D0
      IFIXB(1)   = -1




      IFIXX(1,1) = -1
      JOB        = -1
      NDIGIT     = -1
      TAUFAC     = -1.0D0
```

```
c      SSTOL      = -1.0D0
c      PARTOL     = -1.0D0
       SSTOL=1.0D-35
       PARTOL=1.0D-45
C      MAXIT      = -1
       MAXIT      = 1000
      IPRINT     = -1
      LUNERR     = -1
      LUNRPT     = -1
      STPB(1)    = -1.0D0
      STPD(1,1)  = -1.0D0
      SCLB(1)    = -1.0D0
      SCLD(1,1)  = -1.0D0

C  SET UP ODRPACK REPORT FILES
      LUNERR  =   9
      LUNRPT  =   9
c      OPEN (UNIT=9,FILE='REPORT3_12_NOV_2007_LESS_HIGH_TEMP_V2')
      OPEN (UNIT=9,FILE=
       1'HYDROGENATION_FEB_08_UBIQEP_15Feb_438K_20Fe_FIT1')
c      OPEN (UNIT=4,FILE='RESULT_AT_FIRST_POINT')

C  READ PROBLEM DATA
c     OPEN (UNIT=5,FILE='DATA3_LESS_HIGH_TEMPERATURE')
       OPEN (UNIT=5,FILE='DATA_NOT_NORMALIZED_UBIQEP_438K_20Fe_FIT1')

      READ (5,FMT=*) N,M,NP,NQ
      READ (5,FMT=*) (BETA(I),I=1,NP)
      DO 10 I=1,N
         READ (5,FMT=*) (X(I,J),J=1,M),(Y(I,L),L=1,NQ)

   10 CONTINUE

C  SPECIFY TASK AS EXPLICIT ORTHOGONAL DISTANCE REGRESSION
C                  WITH CENTRAL DIFFERENCE DERIVATIVES
C                  COVARIANCE MATRIX CONSTRUCTED WITH RECOMPUTED DERIVATIVES
C                  DELTA INITIALIZED BY USER
C                  NOT A RESTART
C  AND INDICATE LONG INITIAL REPORT
C               NO ITERATION REPORTS
C               LONG FINAL REPORT
C      JOB     = 01010
c      IPRINT  = 2002
       JOB     = 01012
      IPRINT  = 2222

C  INITIALIZE DELTA, AND SPECIFY FIRST DECADE OF FREQUENCIES AS FIXED

       DO IJK = 1,N

             IF(Y(IJK,1).LT.0.0D0 .OR. Y(IJK,2).LT.0.0D0)THEN
           WE(IJK,1,1) = 0.0D0
           WE(IJK,1,2) = 0.0D0
           WE(IJK,2,1) = 0.0D0
           WE(IJK,2,2) = 0.0D0
         ELSE
           WE(IJK,1,1) =   1.0D0
           WE(IJK,1,2) = 1.0D0
           WE(IJK,2,1) = 1.0D0
           WE(IJK,2,2) =  1.0D0
            END IF

       END DO
```

```
C
C
C
C
C  COMPUTE SOLUTION
      CALL DODRC(FCN,
     +           N,M,NP,NQ,
     +           BETA,
     +           Y,LDY,X,LDX,
     +           WE,LDWE,LD2WE,WD,LDWD,LD2WD,
     +           IFIXB,IFIXX,LDIFX,
     +           JOB,NDIGIT,TAUFAC,
     +           SSTOL,PARTOL,MAXIT,
     +           IPRINT,LUNERR,LUNRPT,
     +           STPB,STPD,LDSTPD,
     +           SCLB,SCLD,LDSCLD,
     +           WORK,LWORK,IWORK,LIWORK,
     +           INFO)
      END


      SUBROUTINE FCN(N,M,NP,NQ,
     +               LDN,LDM,LDNP,
     +               BETA,XPLUSD,
     +               IFIXB,IFIXX,LDIFX,
     +               IDEVAL,F,FJACB,FJACD,
     +               ISTOP)

C  SUBROUTINE ARGUMENTS
C      ==> N        NUMBER OF OBSERVATIONS
C      ==> M        NUMBER OF COLUMNS IN EXPLANATORY VARIABLE
C      ==> NP       NUMBER OF PARAMETERS
C      ==> NQ       NUMBER OF RESPONSES PER OBSERVATION
C      ==> LDN      LEADING DIMENSION DECLARATOR EQUAL OR EXCEEDING N
C      ==> LDM      LEADING DIMENSION DECLARATOR EQUAL OR EXCEEDING M
C      ==> LDNP     LEADING DIMENSION DECLARATOR EQUAL OR EXCEEDING NP
C      ==> BETA     CURRENT VALUES OF PARAMETERS
C      ==> XPLUSD   CURRENT VALUE OF EXPLANATORY VARIABLE, I.E., X + DELTA
C      ==> IFIXB    INDICATORS FOR "FIXING" PARAMETERS (BETA)
C      ==> IFIXX    INDICATORS FOR "FIXING" EXPLANATORY VARIABLE (X)
C      ==> LDIFX    LEADING DIMENSION OF ARRAY IFIXX
C      ==> IDEVAL   INDICATOR FOR SELECTING COMPUTATION TO BE PERFORMED
C     <==  F        PREDICTED FUNCTION VALUES
C     <==  FJACB    JACOBIAN WITH RESPECT TO BETA
C     <==  FJACD    JACOBIAN WITH RESPECT TO ERRORS DELTA
C     <==  ISTOP    STOPPING CONDITION, WHERE
C                     0 MEANS CURRENT BETA AND X+DELTA WERE
C                       ACCEPTABLE AND VALUES WERE COMPUTED SUCCESSFULLY
C                     1 MEANS CURRENT BETA AND X+DELTA ARE
C                       NOT ACCEPTABLE;  ODRPACK SHOULD SELECT VALUES
C                       CLOSER TO MOST RECENTLY USED VALUES IF POSSIBLE
C                    -1 MEANS CURRENT BETA AND X+DELTA ARE
C                       NOT ACCEPTABLE;  ODRPACK SHOULD STOP

C  INPUT ARGUMENTS, NOT TO BE CHANGED BY THIS ROUTINE:
      INTEGER          I,IDEVAL,ISTOP,LDIFX,LDM,LDN,LDNP,M,N,NP,NQ
      DOUBLE PRECISION BETA(NP),XPLUSD(LDN,M),FFNEW(LDN,NQ),T
      INTEGER          IFIXB(NP),IFIXX(LDIFX,M),NEWN,LLDN,NNQ
C  OUTPUT ARGUMENTS:
      DOUBLE PRECISION F(LDN,NQ),FJACB(LDN,LDNP,NQ),FJACD(LDN,LDM,NQ)
       DOUBLE PRECISION BETA_THETA1,BETA_THETA2
       DOUBLE PRECISION FYYCH4_1(LDN),FYYCH4_2(LDN),X_TOUT(LDN)
```

```
C
C  CHECK FOR UNACCEPTABLE VALUES FOR THIS PROBLEM
      DO  I=1,N
         IF (XPLUSD(I,1).LT.0.0D0) THEN
            ISTOP = 1
            RETURN
         END IF
       ENDDO

       DO  I=1,NP
         IF (BETA(I).LT.0.0D0) THEN
            ISTOP = 1
            RETURN
         END IF
       ENDDO




       IF (BETA(4)+BETA(5)+BETA(6).GT.1.0D0) THEN
            ISTOP = 1
            RETURN
         END IF


      ISTOP = 0


C  COMPUTE PREDICTED VALUES
      IF (MOD(IDEVAL,10).GE.1) THEN

         KKK = KKK+1



       DO I = 1,LDN
              X_TOUT(I) = XPLUSD(I,1)
       END DO

C      WRITE(4,100)(BETA(I),I = 1,NP)
C
C 100  FORMAT(10(1X,E20.10))
       N_DIM = LDN
       N_NP = NP
       CALL DVODE_DRIVER(BETA,FYYCH4_1,FYYCH4_2,X_TOUT,N_DIM,N_NP)



        DO  I = 1,LDN


                           F(I,1) = FYYCH4_1(I)
C                          F(I,2) = FYYCH4_2(I)
C                          WRITE(4,1000)X_TOUT(I),F(I,1)
                           WRITE(*,*)KKK,I
       END DO

      END IF

1000   FORMAT(2(1X,E20.10))
       ISTOP = 0
      RETURN
      END
```

```
C

      SUBROUTINE DVODE_DRIVER(BETA,FYYCH4_1,FYYCH4_2,X_TOUT,N_DIM,N_NP)
      EXTERNAL FEX, JEX
     DOUBLE PRECISION ATOL, RPAR, RTOL, RWORK, TT, TOUT, YY,BETA


     DIMENSION YY(200), ATOL(200), RWORK(70000), IIWRK(300),BETA(N_NP)
      DOUBLE PRECISION X_TOUT(N_DIM),FYYCH4_1(N_DIM),FYYCH4_2(N_DIM)

      DOUBLE PRECISION R1,R2,R3,R4,R5,R6,R7,R8,R9,R10,R11,R12,R13,
      1R14,R15,R16,R17,R18,THETA_V

      DIMENSION R1(10),R2(10),R3(10),R4(10),R5(10),R6(10),R7(10),R8(10)
      1,R9(10),R10(10),R11(10),R12(10),
     1R13(10),R14(10),R15(10),R16(10),R17(10),R18(10),THETA_V(10)

      DOUBLE PRECISION FK1,RK1,FK2,RK2,FK3,RK3,FK4,RK4,FK5,RK5,FK6,RK6,
      1FK7,RK7,FK8,RK8,FK9,RK9,FK10,RK10,FK11,RK11,FK12,RK12,FK13,RK13,
     1FK14,RK14,FK15,RK15,FK16,RK16,FK17,RK17,FK18,RK18,SPACE_STEP

      DOUBLE PRECISION DISP_CAT,CAT_MW,CAT_LOADING,T_EMP,RG,
      1PTOT,EB,TAU_T,RHOB,N_GAS_PHASE_SPECIES,YH2_0


      DOUBLE PRECISION E1_F,E1_R,E2_F,E2_R,E3_F,E3_R,E4_F,E4_R,
      1                        E5_F,E5_R,E6_F,E6_R,E7_F,E7_R,E8_F,E8_R,
     1                    E9_F,E9_R,E10_F,E10_R,E11_F,E11_R,E12_F,
     1                    E12_R,E13_F,E13_R,E14_F,E14_R,
     1                    E15_F,E15_R,E16_F,E16_R,E17_F,E17_R,
      1                       E18_F,E18_R,E19_F,E19_R


      DOUBLE PRECISION Q0C,Q0H,Q0O,QCO,QCO2,QH2,QCH,QCH2,
      1                        QCH3,QCH4,QOH,QH2O,QCH2O,QCH3O




      DOUBLE PRECISION DCH,DCHO,DH2O,DCH2,DCH3,DCH4,DCO_H,
      1                        DCO_O,DCH_H,DCH2_H,DOH_H,DCH3_H,DCO,
     2                    DH2,DCO2,DXY,QXY,DOH,DH,A,B,DCH2O,DCHO_H,
     3                    DCH3O,DCH3O_1,DCH2O_H,DCH3_O,DC


      DOUBLE PRECISION DELTA_H

      DOUBLE PRECISION A_F(20),A_R(20),TEMP_1
C=====================================================================
=================

      COMMON/UCHENNA/FK1,RK1,FK2,RK2,FK3,RK3,FK4,RK4,FK5,RK5,FK6,RK6,
      1FK7,RK7,FK8,RK8,FK9,RK9,FK10,RK10,FK11,RK11,FK12,RK12,FK13,RK13,
     1FK14,RK14,FK15,RK15,FK16,RK16,FK17,RK17,FK18,RK18,
     1SPACE_STEP,N_GRIDS

      COMMON /UCHENNA2/DISP_CAT,CAT_MW,CAT_LOADING,T_EMP,RG,
      1PTOT,EB,TAU_T,RHOB,N_GAS_PHASE_SPECIES,YH2_0

         COMMON /DVOD01/ ACNRM, CCMXJ, CONP, CRATE, DRC, EL(13),
     1               ETT, ETAMAX, H, HMIN, HMXI, HNEW, HSCAL, PRL1,
     2               RC, RL1, TAU(13), TQ(5), TN, UROUND,
```

```
     3                ICF, INIT, IPUP, JCUR, JSTART, JSV, KFLAG, KUTH,
     4                L, LMAX, LYH, LEWT, LACOR, LSAVF, LWM, LIWM,
     5                LOCJS, MAXORD, METH, MITER, MSBJ, MXHNIL, MXSTEP,
     6                N, NEWH, NEWQ, NHNIL, NQ, NQNYH, NQWAIT, NSLJ,
     7                NSLP, NYH
      COMMON /DVOD02/ HU, NCFN, NETF, NFE, NJE, NLU, NNI, NQU, NST

C=====================================================================
==================================


       QC = BETA(1)
       QO = BETA(2)
       QH = BETA(3)

C      ENTER THE PRE-EXPONTIAL FACTORS FROM TRANSITION STATE THEORY:

       A_F(1) = 2.2D1
       A_R(1) = 1.9D13


       A_F(2) = 1.4D14
       A_R(2) = 1.0D13

       A_F(3) = 2.6D13
       A_R(3) = 1.0D13

       A_F(4) = 2.6D13
       A_R(4) = 4.7D13

       A_F(5) = 1.6D12
       A_R(5) = 9.8D-01

       A_F(6) = 1.7D14
       A_R(6) = 1.0D13

       A_F(7) = 2.7D12
       A_R(7) = 1.0D13

       A_F(8) = 2.1D13
       A_R(8) = 1.0D13

       A_F(9) = 2.6D13
       A_R(9) = 6.8D12

       A_F(10) = 7.7D12
       A_R(10) = 1.0D13

       A_F(11) = 1.1D14
       A_R(11) = 1.0D13

       A_F(12) = 1.1D13
       A_R(12) = 1.0D13

       A_F(13) = 1.1D13
       A_R(13) = 8.2D-1

       A_F(14) = 1.0D13
       A_R(14) = 2.2D-1

       A_F(15) = 1.0D13
       A_R(15) = 6.1D13
```

```
      A_F(16) = 1.7D14
      A_R(16) = 9.6D13

      A_F(17) = 1.0D13
      A_R(17) = 2.8D13

      A_F(18) = 1.0D13
      A_R(18) = 4.2D-1

      A_F(19) = 2.0D13
      A_R(19) = 1.4D12

C     ENTER TEMPERATURE (K) AND GAS CONSTANT

      TEMP_1 = 438
      RG = 8.314


C=====================================================================================
================================
C     COMPUTE ACTIVATION ENERGIES USING UBI-QEP

C     ENTER GAS-PHASE BOND ENERGIES (J/MOL)

      DCO = 1.076D6
      DCO2 = 1.612D6
      DH2 = 4.35D5
      DOH = 4.271D5
      DCH = 3.391D5
      DCHO = 1.147D6
      DCH2O = 1.511D6
      DCH3O = 1.604D6
      DCH3O_1=3.768D5
      DH = 0.0D0
      DC = 0.0D0
      DH2O = 9.211D5
      DCH2 = 7.662D5
      DCH3 = 1.227D6
      DCH4 = 1.662D6
      DCO_H = DCHO-DCO
      DCO_O = DCO2-DCO
      DCH_H = DCH2-DCH
      DCH2_H = DCH3-DCH2
      DOH_H = DH2O-DOH
      DCH3_H = DCH4-DCH3
      DCHO_H = DCH2O-DCHO
      DCH2O_H = DCH3O-DCH2O
      DCH3_O = DCH3O-DCH3

C     COMPUTE THE METAL HEALTS OF ADSORPTION

      Q0C = QC/(2.0D0-(1.0D0/3.0D0))

      Q0H = QH/(2.0D0-(1.0D0/3.0D0))

      Q0O= QO/(2.0D0-(1.0D0/3.0D0))


C     COMPUTE HEAT OF ADSORPTION FOR CO, H2, QOH,CO2, ETC

      QCO = (Q0C**2.0D0)/(Q0C+DCO)

      QH2 = (4.5D0*Q0H**2.0D0)/(3.0D0*Q0H+8.0D0*DH2)
```

```
C
      QOH = (QO**2.0D0)/(QO+DOH)


      QCH = (QC**2.0D0)/(QC+DCH)

      QCO2= (4.5D0*Q0O**2.0D0)/(3.0D0*Q0O+8.0D0*DCO2)

      QCHO = 0.5D0*(((Q0C**2.0D0)/((Q0C/3.0D0)+DCHO))+
     1            (QC**2.0D0)/(QC+DCHO))

      QCH2 = (QC**2.0D0)/(QC+DCH2)

      QCH3 = 0.5D0*(((Q0C**2.0D0)/((Q0C/3.0D0)+DCH3))+
     1            (QC**2.0D0)/(QC+DCH3))


      A = (QOH**2.0D0)*((QOH+2.0D0*Q0H)/(QOH+Q0H)**2.0D0)
      B = (Q0H**2.0D0)*((2.0D0*QOH+Q0H)/(QOH+Q0H)**2.0D0)

      QH2O = (A*B*(A+B)+DH2O*(A-B)**2.0D0)/(A*B+DH2O*(A+B))

      QCH4 = (Q0C**2.0D0)/(Q0C+DCH4)

      QCH2O = (Q0C**2.0D0)/(Q0C+DCH2O)

      QCH3O = (QO**2.0D0)/(QO+DCH3O_1)



C     COMPUTE ACTIVATION ENERGIES FOR R1: H2(g) +2* = 2H*

      E1_F = 0.5D0*(DH2+(QH*QH/(QH+QH))-QH2-QH-QH)

      IF(E1_F.LT.0.0D0)THEN
            E1_F = 0.0D0
      END IF



      E1_R = QH+QH-DH2+E1_F

      IF(E1_R.LT.0.0D0)THEN
            E1_R = 0.0D0
      END IF



C     COMPUTE ACTIVATION ENERIGES FOR R2: C* + H* = CH* + *

      DELTA_H = DCH+QCH-QC-QH

      E2_R = 0.5D0*(DELTA_H+(QC*QH/(QC+QH)))

      IF(E2_R.LT.0.0D0)THEN
            E2_R = 0.0D0
      END IF



      E2_F = E2_R-DELTA_H
```

```
      IF(E2_F.LT.0.0D0)THEN
            E2_F = 0.0D0
      END IF

C     COMPUTE ACTIVATION ENERIGES FOR R3: CH* + H* = CH2* + *

      DELTA_H = DCH_H+QCH2-QCH-QH

      E3_R = 0.5D0*(DELTA_H+(QCH*QH/(QCH+QH)))

      IF(E3_R.LT.0.0D0)THEN
            E3_R = 0.0D0
      END IF
      E3_F = E3_R-DELTA_H


      IF(E3_F.LT.0.0D0)THEN
            E3_F = 0.0D0
      END IF


C     COMPUTE ACTIVATION ENERIGES FOR R4: CH2* + H* = CH3* + *

      DELTA_H = DCH2_H+QCH3-QCH2-QH


      E4_R = 0.5D0*(DELTA_H+(QCH2*QH/(QCH2+QH)))

      IF(E4_R.LT.0.0D0)THEN
            E4_R = 0.0D0
      END IF

      E4_F = E4_R-DELTA_H


      IF(E4_F.LT.0.0D0)THEN
            E4_F = 0.0D0
      END IF



C     COMPUTE ACTIVATION ENERIGES FOR R5: CH3* + H* = CH4(g) + 2*

      E5_R = 0.5D0*(DCH3_H+(QCH3*QH/(QCH3+QH))-QCH4-QCH3-QH)

      IF(E5_R.LT.0.0D0)THEN
            E5_R = 0.0D0
      END IF


      E5_F = QCH3+QH-DCH3_H+E5_R

      IF(E5_F.LT.0.0D0)THEN
            E5_F = 0.0D0
      END IF


C     COMPUTE ACTIVATION ENERIGES FOR R6: CO* + H* = CHO* + *

      DELTA_H = DCO_H+QCHO-QCO-QH

      E6_R = 0.5D0*(DELTA_H+(QCO*QH/(QCO+QH)))
```

```
      IF(E6_R.LT.0.0D0)THEN
            E6_R = 0.0D0
      END IF
      E6_F = E6_R-DELTA_H

      IF(E6_F.LT.0.0D0)THEN
            E6_F = 0.0D0
      END IF



C     COMPUTE ACTIVATION ENERIGES FOR R7: CHO* + H* = CH2O* + *

      DELTA_H = DCHO_H+QCH2O-QCHO-QH

      E7_R = 0.5D0*(DELTA_H+(QCHO*QH/(QCHO+QH)))

      IF(E7_R.LT.0.0D0)THEN
            E7_R = 0.0D0
      END IF
      E7_F = E7_R-DELTA_H

      IF(E7_F.LT.0.0D0)THEN
            E7_F = 0.0D0
      END IF


C     COMPUTE ACTIVATION ENERIGES FOR R8: CH2O* + H* = CH3O* + *

      DELTA_H = DCH2O_H+QCH3O-QCH2O-QH

      E8_R = 0.5D0*(DELTA_H+(QCH2O*QH/(QCH2O+QH)))

      IF(E8_R.LT.0.0D0)THEN
            E8_R = 0.0D0
      END IF
      E8_F = E8_R-DELTA_H

      IF(E8_F.LT.0.0D0)THEN
            E8_F = 0.0D0
      END IF



C     COMPUTE ACTIVATION ENERIGES FOR R9: CH3O* + H* = CH3* + OH*

      DXY = DCH3O+DH-DCH3-DOH
      QXY = QCH3O+QH

      DELTA_H = DXY+QXY-QCH3-QOH

      E9_F = 0.5D0*(DELTA_H+(QCH3*QOH/(QCH3+QOH)))


      IF(E9_F.LT.0.0D0)THEN
            E9_F = 0.0D0
      END IF
      E9_R = E9_F-DELTA_H


      IF(E9_R.LT.0.0D0)THEN
            E9_R = 0.0D0
      END IF
```

```
C
C
C
C      COMPUTE ACTIVATION ENERIGES FOR R10: CO* + O* = CO2* + *

       DELTA_H = DCO_O+QCO2-QCO-QO

       E10_R = 0.5D0*(DELTA_H+(QCO*QO/(QCO+QO)))

       IF(E10_R.LT.0.0D0)THEN
             E10_R = 0.0D0
       END IF
       E10_F = E10_R-DELTA_H

       IF(E10_F.LT.0.0D0)THEN
             E10_F = 0.0D0
       END IF


C      COMPUTE ACTIVATION ENERIGES FOR R11: O* + H* = OH* + *

       DELTA_H = DOH+QOH-QH-QO

       E11_R = 0.5D0*(DELTA_H+(QH*QO/(QH+QO)))

       IF(E11_R.LT.0.0D0)THEN
             E11_R = 0.0D0
       END IF
       E11_F = E11_R-DELTA_H

       IF(E11_F.LT.0.0D0)THEN
             E11_F = 0.0D0
       END IF


C      COMPUTE ACTIVATION ENERIGES FOR R12: OH* + H* = H2O* + *

       DELTA_H = DOH_H+QH2O-QOH-QH

       E12_R = 0.5D0*(DELTA_H+(QOH*QH/(QOH+QH)))

       IF(E12_R.LT.0.0D0)THEN
             E12_R = 0.0D0
       END IF
       E12_F = E12_R-DELTA_H


       IF(E12_F.LT.0.0D0)THEN
             E12_F = 0.0D0
       END IF



C      COMPUTE ACTIVATION ENERIGES FOR R13: H2O* = H2O(g) + *


       E13_R = 0.0D0
       E13_F = QH2O



C      COMPUTE ACTIVATION ENERIGES FOR R14: CO2* = CO2(g) + *
```

```
C
      E14_R = 0.0D0
      E14_F = QCO2


C     COMPUTE ACTIVATION ENERIGES FOR R15: CO* + * = C* + O*

      DELTA_H = DCO+QCO-QC-QO

      E15_F = 0.5D0*(DELTA_H+(QC*QO/(QC+QO)))

      IF(E15_F.LT.0.0D0)THEN
            E15_F = 0.0D0
      END IF
      E15_R = E15_F-DELTA_H

      IF(E15_R.LT.0.0D0)THEN
            E15_R = 0.0D0
      END IF



C     COMPUTE ACTIVATION ENERIGES FOR R16: CO* + H* = C* + OH*

      DXY = DCO+DH-DC-DOH
      QXY = QCO+QH

      DELTA_H = DXY+QXY-QC-QOH

      E16_F = 0.5D0*(DELTA_H+(QC*QOH/(QC+QOH)))


      IF(E16_F.LT.0.0D0)THEN
            E16_F = 0.0D0
      END IF
      E16_R = E16_F-DELTA_H


      IF(E16_R.LT.0.0D0)THEN
            E16_R = 0.0D0
      END IF



C     COMPUTE ACTIVATION ENERIGES FOR R17: CH3O* + * = CH3* + O*

      DELTA_H = DCH3_O+QCH3O-QCH3-QO

      E17_F = 0.5D0*(DELTA_H+(QCH3*QO/(QCH3+QO)))

      IF(E17_F.LT.0.0D0)THEN
            E17_F = 0.0D0
      END IF
      E17_R = E17_F-DELTA_H


      IF(E17_R.LT.0.0D0)THEN
            E17_R = 0.0D0
      END IF



C     COMPUTER ACTIVATION ENERGIES FOR R18: CO* = CO(g) + *
```

```
C
      E18_R = 0.0D0
      E18_F = QCO

C     COMPUTE ACTIVATION ENERIGES FOR R19: CH2O* + H* = CH2* + OH*

      DXY = DCH2O+DH-DCH2-DOH
      QXY = QCH2O+QH

      DELTA_H = DXY+QXY-QCH2-QOH

      E19_F = 0.5D0*(DELTA_H+(QCH2*QOH/(QCH2+QOH)))


      IF(E19_F.LT.0.0D0)THEN
            E19_F = 0.0D0
      END IF
      E19_R = E19_F-DELTA_H

      IF(E19_R.LT.0.0D0)THEN
            E19_R = 0.0D0
      END IF


C     COMPUTE RATE CONSTANTS

      FK1 = A_F(1)*EXP(-E1_F/(RG*TEMP_1))
      RK1 = A_R(1)*EXP(-E1_R/(RG*TEMP_1))

      FK2 = A_F(2)*EXP(-E2_F/(RG*TEMP_1))*BETA(7)
      RK2 = A_R(2)*EXP(-E2_R/(RG*TEMP_1))

      FK3 = A_F(3)*EXP(-E3_F/(RG*TEMP_1))
      RK3 = A_R(3)*EXP(-E3_R/(RG*TEMP_1))

      FK4 = A_F(4)*EXP(-E4_F/(RG*TEMP_1))
      RK4 = A_R(4)*EXP(-E4_R/(RG*TEMP_1))

      FK5 = A_F(5)*EXP(-E5_F/(RG*TEMP_1))
      RK5 = A_R(5)*EXP(-E5_R/(RG*TEMP_1))

      FK6 = A_F(6)*EXP(-E6_F/(RG*TEMP_1))
      RK6 = A_R(6)*EXP(-E6_R/(RG*TEMP_1))

      FK7 = A_F(7)*EXP(-E7_F/(RG*TEMP_1))
      RK7 = A_R(7)*EXP(-E7_R/(RG*TEMP_1))

      FK8 = A_F(8)*EXP(-E8_F/(RG*TEMP_1))
      RK8 = A_R(8)*EXP(-E8_R/(RG*TEMP_1))

      FK9 = A_F(9)*EXP(-E9_F/(RG*TEMP_1))
      RK9 = A_R(9)*EXP(-E9_R/(RG*TEMP_1))

      FK10 = A_F(10)*EXP(-E10_F/(RG*TEMP_1))
      RK10 = A_R(10)*EXP(-E10_R/(RG*TEMP_1))

      FK11 = A_F(11)*EXP(-E11_F/(RG*TEMP_1))
      RK11 = A_R(11)*EXP(-E11_R/(RG*TEMP_1))

      FK12 = A_F(12)*EXP(-E12_F/(RG*TEMP_1))
      RK12 = A_R(12)*EXP(-E12_R/(RG*TEMP_1))

      FK13 = A_F(13)*EXP(-E13_F/(RG*TEMP_1))
```

```
      RK13 = A_R(13)*EXP(-E13_R/(RG*TEMP_1))

      FK14 = A_F(14)*EXP(-E14_F/(RG*TEMP_1))
      RK14 = A_R(14)*EXP(-E14_R/(RG*TEMP_1))

      FK15 = A_F(15)*EXP(-E15_F/(RG*TEMP_1))
      RK15 = A_R(15)*EXP(-E15_R/(RG*TEMP_1))

      FK16 = A_F(16)*EXP(-E16_F/(RG*TEMP_1))
      RK16 = A_R(16)*EXP(-E16_R/(RG*TEMP_1))

      FK17 = A_F(17)*EXP(-E17_F/(RG*TEMP_1))
      RK17 = A_R(17)*EXP(-E17_R/(RG*TEMP_1))

      FK18 = A_F(18)*EXP(-E18_F/(RG*TEMP_1))*BETA(8)
      RK18 = A_R(18)*EXP(-E18_R/(RG*TEMP_1))

      FK19 = A_F(19)*EXP(-E19_F/(RG*TEMP_1))
      RK19 = A_R(19)*EXP(-E19_R/(RG*TEMP_1))

C=============================================================

C     ENTER GAS CONSTANT
      RG = 8.314D0
C     ENTER INLET MOLE FRACTION OF HYDROGEN

      YH2_0 = 0.1D0

C     ENTER REACTOR TEMPERATURE (K)
      T_EMP = 438.0D0

C     ENTER RESIDENCE TIME (S)
      TAU_T = 0.343d0

C     ENTER CATALYST BED DENSITY IN (KG/M^3)
      RHOB = 1.0D3
C     ENTER BED VOID FRACTION
      EB = 4.5D-01

C     ENTER TOTAL REACTOR PRESSURE (Pa)
      PTOT =1.013D5


C     ENTER NUMBER OF GAS PHASE SPECIES:

      N_GAS_PHASE_SPECIES = 5

C     ENTER CATALYST DISPERSION (IN FRACTION)
      DISP_CAT = 2.0D-01*BETA(9)

C     ENTER CATALYST METAL LOADING (IN FRACTION)
      CAT_LOADING = 2.0D-01

C     ENTER MOLECULAR WEIGHT OF ACTIVE CATALYST PHASE (KG/MOL)

      CAT_MW = 55.847D-03


C      N_BETA = 36
      TT = 0.0D0
C      DELTAT_STEP=4.5D0
C      TOUT = DELTAT_STEP
```

```
C
C      ENTER DIMENSIONLESS SPACE STEP SIZE
       SPACE_STEP = 0.2D0

C      COMPUTE NUMBER OF GRID POINTS

       N_GRIDS = INT(1.0/SPACE_STEP)
C      ENTER THE NUMBER OF DIFFERENTIAL EQUATIONS
      NEQ = 18*N_GRIDS


C      DETERMINE THE INDEX WHERE EACH SPECIES START

       IYH2 = 1
       IYCO_G = IYH2 + N_GRIDS
       IYCH4 = IYCO_G + N_GRIDS
       IYCO2 = IYCH4 + N_GRIDS
       IYH2O = IYCO2 + N_GRIDS
       IYH = IYH2O + N_GRIDS
       IYC = IYH + N_GRIDS
       IYCH = IYC + N_GRIDS
       IYCH2 = IYCH + N_GRIDS
       IYCH3 = IYCH2 + N_GRIDS
       IYCO = IYCH3 + N_GRIDS
       IYO = IYCO + N_GRIDS
       IYCHO = IYO + N_GRIDS
       IYCH2O = IYCHO + N_GRIDS
       IYCH3O = IYCH2O + N_GRIDS
       IYOH = IYCH3O + N_GRIDS
       IYYCO2 = IYOH + N_GRIDS
       IYYH2O = IYYCO2 + N_GRIDS

C      DETERMINE THE INDEX WHERE EACH SPECIES END

       IEYH2 = N_GRIDS
       IEYCO_G = IYCH4 - 1
       IEYCH4 = IYCO2 - 1
       IEYCO2 = IYH2O - 1
       IEYH2O = IYH - 1
       IEYH = IYC - 1
       IEYC = IYCH - 1
       IEYCH = IYCH2 - 1
       IEYCH2 = IYCH3 - 1
       IEYCH3 = IYCO - 1
       IEYCO = IYO - 1
       IEYO = IYCHO - 1
       IEYCHO = IYCH2O - 1
       IEYCH2O = IYCH3O - 1
       IEYCH3O = IYOH - 1
       IEYOH = IYYCO2 - 1
       IEYYCO2 = IYYH2O - 1
       IEYYH2O = IYYH2O +N_GRIDS -1


C      SET INITIAL CONDITIONS

C      FOR ALL GAS PHASE SPECIES H2(g),CO(g),CH4(g),CO2(g),H2O(g),ETC
       DO I = IYH2,IEYH2O
       YY(I) =      0.0D0
       END DO


C      FOR SURFACE H
```

```
C
      DO I = IYH,IEYH
             YY(I) = 0.0D0
      END DO

C     FOR SURFACE C
      DO I = IYC,IEYC
             YY(I) = BETA(4)
      END DO
C     FOR SURFACE CH
      DO I = IYCH,IEYCH
      YY(I) = 0.0D0
      END DO
C     FOR SURFACE CH2
      DO I = IYCH2,IEYCH2
      YY(I) = 0.0D0
      END DO

C     SURFACE CH3
      DO I = IYCH3,IEYCH3
      YY(I) = 0.0D0
      END DO

C     SURFACE CO
      DO I = IYCO,IEYCO
      YY(I) = BETA(5)
      END DO

C     SURFACE O
      DO I = IYO,IEYO
      YY(I) = BETA(6)
      END DO

C     SURFACE CHO
      DO I = IYCHO,IEYCHO
      YY(I) = 0.0D0
      END DO

C     SURFACE CH2O
      DO I = IYCH2O,IEYCH2O
      YY(I) = 0.0D0
      END DO

C     SURFACE CH3O
      DO I = IYCH3O,IEYCH3O
      YY(I) = 0.0D0
      END DO

C     SURFACE OH
      DO I = IYOH, IEYOH
      YY(I) = 0.0D0
      END DO

C     SURFACE CO2
      DO I = IYYCO2,IEYYCO2
      YY(I) = 0.0D0
      END DO

C     SURFACE H2O
      DO I = IYYH2O,IEYYH2O
      YY(I) = 0.0D0
      END DO
```

```
C


C      SET CONVERGENCE TOLORANCE
       ITOL = 2
       RTOL = 1.0D-010
        DO  I = 1,NEQ

              ATOL(I) = 1.0D-40
        END DO

C RWORK  = Real work array of length at least:
C             20 + 16*NEQ                      for MF = 10,
C             22 +  9*NEQ + 2*NEQ**2           for MF = 21 or 22,
C             22 + 11*NEQ + (3*ML + 2*MU)*NEQ  for MF = 24 or 25.
C LRW    = Declared length of RWORK (in user's DIMENSION statement).
C IWORK  = Integer work array of length at least:
C             30        for MF = 10,
C             30 + NEQ  for MF = 21, 22, 24, or 25.
C          If MF = 24 or 25, input in IWORK(1),IWORK(2) the lower
C          and upper half-bandwidths ML,MU.
C LIW    = Declared length of IWORK (in user's DIMENSION statement).

C      SET DVODE CONSTANTS
       ITASK = 1
       ISTATE = 1
       IOPT = 1
        IIWRK(6) = 900000
       LRW = 70000
       LIW = 300
C      SPECIFY DVODE SOLUTION METHOD
       MF = 22

        ICOUNT_E2 = 0
        DO IOUT = 1,N_DIM
              TOUT = X_TOUT(IOUT)

              ICOUNT_E2 = ICOUNT_E2+1

30         CALL DVODE(FEX,NEQ,YY,TT,TOUT,ITOL,RTOL,ATOL,ITASK,ISTATE,
     1             IOPT,RWORK,LRW,IIWRK,LIW,JEX,MF,RPAR,IPAR)


              FYYCH4_1(IOUT) = YY(IEYCH4)
C             FYYCH4_2(IOUT) = YY(IEYCH4_2)

C             WRITE(3,70)TOUT,FYYCO(IOUT),FYYCO2(IOUT)

C      IF (ISTATE .LT. 0)GO TO 80

        END DO


C       WRITE(3,60)IIWRK(11),IIWRK(12),IIWRK(13),IIWRK(19),
C      1            IIWRK(20),IIWRK(21),IIWRK(22)
C   60  FORMAT(/' No. steps =',I4,'   No. f-s =',I4,
C      1       '   No. J-s =',I4,'   No. LU-s =',I4/
C      2       '  No. nonlinear iterations =',I4/
C      3       '  No. nonlinear convergence failures =',I4/
C      4       '  No. error test failures =',I4/)

   70  FORMAT(3(1X,D20.10))
       RETURN
```

```
C  80  WRITE(3,90)ISTATE


  90  FORMAT(///1X,I6,1X,' Error halt: ISTATE =',I3)
C     ISTOP = 0
      RETURN
      END


C     FUNCTION SUBROUTINE
      SUBROUTINE FEX (NEQ, TT, YY, YDOT, RPAR, IPAR)
      DOUBLE PRECISION RPAR, TT, YY, YDOT


      DIMENSION YY(NEQ), YDOT(NEQ)

       DOUBLE PRECISION R1,R2,R3,R4,R5,R6,R7,R8,R9,R10,R11,R12,R13,
       1R14,R15,R16,R17,R18,THETA_V

       DIMENSION R1(10),R2(10),R3(10),R4(10),R5(10),R6(10),R7(10),R8(10)
       1,R9(10),R10(10),R11(10),R12(10),
     1R13(10),R14(10),R15(10),R16(10),R17(10),R18(10),THETA_V(10)


       DOUBLE PRECISION DENOM1,DENOM2,DENOM3,FACTOR

       DOUBLE PRECISION FK1,RK1,FK2,RK2,FK3,RK3,FK4,RK4,FK5,RK5,FK6,RK6,
       1FK7,RK7,FK8,RK8,FK9,RK9,FK10,RK10,FK11,RK11,FK12,RK12,FK13,RK13,
     1FK14,RK14,FK15,RK15,FK16,RK16,FK17,RK17,FK18,RK18,
     1SPACE_STEP

       DOUBLE PRECISION DISP_CAT,CAT_MW,CAT_LOADING,T_EMP,RG,
       1PTOT,EB,TAU_T,RHOB,N_GAS_PHASE_SPECIES,YH2_0

       COMMON/UCHENNA/FK1,RK1,FK2,RK2,FK3,RK3,FK4,RK4,FK5,RK5,FK6,RK6,
       1FK7,RK7,FK8,RK8,FK9,RK9,FK10,RK10,FK11,RK11,FK12,RK12,FK13,RK13,
     1FK14,RK14,FK15,RK15,FK16,RK16,FK17,RK17,FK18,RK18,
     1SPACE_STEP,N_GRIDS

       COMMON /UCHENNA2/DISP_CAT,CAT_MW,CAT_LOADING,T_EMP,RG,
       1PTOT,EB,TAU_T,RHOB,N_GAS_PHASE_SPECIES,YH2_0

C      ENTER THE CONVERTER FOR RATE IN TOF TO RATE IN (MOL/kg S)

       CONVERTER = DISP_CAT*CAT_LOADING/CAT_MW

C      COMPUTER SOME FACTORS AND DENOMINATIOR CONSTANTS

       FACTOR = RG*T_EMP*RHOB*CONVERTER/(EB*PTOT)
       DENOM1 = TAU_T*SPACE_STEP
       DENOM2 = 2.0D0*TAU_T*SPACE_STEP

C      COMPUTE NUMBER OF GRID POINTS

       N_GRIDS = INT(1.0/SPACE_STEP)

C      DETERMINE THE INDEX WHERE EACH SPECIES START

       IYH2 = 1
       IYCO_G = IYH2 + N_GRIDS
       IYCH4 = IYCO_G + N_GRIDS
       IYCO2 = IYCH4 + N_GRIDS
       IYH2O = IYCO2 + N_GRIDS
```

```
      IYH = IYH2O + N_GRIDS
      IYC = IYH + N_GRIDS
      IYCH = IYC + N_GRIDS
      IYCH2 = IYCH + N_GRIDS
      IYCH3 = IYCH2 + N_GRIDS
      IYCO = IYCH3 + N_GRIDS
      IYO = IYCO + N_GRIDS
      IYCHO = IYO + N_GRIDS
      IYCH2O = IYCHO + N_GRIDS
      IYCH3O = IYCH2O + N_GRIDS
      IYOH = IYCH3O + N_GRIDS
      IYYCO2 = IYOH + N_GRIDS
      IYYH2O = IYYCO2 + N_GRIDS

C     DETERMINE THE INDEX WHERE EACH SPECIES END

      IEYH2 = N_GRIDS
      IEYCO_G = IYCH4 - 1
      IEYCH4 = IYCO2 - 1
      IEYCO2 = IYH2O - 1
      IEYH2O = IYH - 1
      IEYH = IYC - 1
      IEYC = IYCH - 1
      IEYCH = IYCH2 - 1
      IEYCH2 = IYCH3 - 1
      IEYCH3 = IYCO - 1
      IEYCO = IYO - 1
      IEYO = IYCHO - 1
      IEYCHO = IYCH2O - 1
      IEYCH2O = IYCH3O - 1
      IEYCH3O = IYOH - 1
      IEYOH = IYYCO2 - 1
      IEYYCO2 = IYYH2O - 1
      IEYYH2O = IYYH2O +N_GRIDS -1


C     SITE BALANCE AT ODD NUMBER GRID POINTS


      DO I = 1,N_GRIDS
            DENOM3 = 0.0D0
            DO K= IYH+I-1,IEYYH2O,N_GRIDS
                  DENOM3=DENOM3+YY(K)
            END DO

            THETA_V(I) = 1.0D0-DENOM3
      END DO


C     COMPUTE REACTION RATES:

C     REACTION 1: (H2(g) + 2* = 2H*)
      DO I = 1,N_GRIDS
            R1(I)=(FK1*PTOT*YY(IYH2+I-1)*THETA_V(I)**2.0D0-
     1      RK1*YY(IYH+I-1)**2.0D0)*(4.5d0)
      END DO


C     REACTION 2 : (C* + H* = CH* + *)
      DO I = 1,N_GRIDS

            R2(I)=FK2*YY(IYC+I-1)*YY(IYH+I-1)-RK2*YY(IYCH+I-1)*THETA_V(I)
      END DO
```

```
C
C      REACTION 3 : (CH* + H* = CH2* + *)
       DO I =1,N_GRIDS


         R3(I)=FK3*YY(IYCH+I-1)*YY(IYH+I-1)-RK3*YY(IYCH2+I-1)*THETA_V(I)
       END DO

C      FOR REACTION 4 : (CH2* + H* = CH3* + *)
       DO I = 1,N_GRIDS

         R4(I)=FK4*YY(IYCH2+I-1)*YY(IYH+I-1)-RK4*YY(IYCH3+I-1)*THETA_V(I)
       END DO


C      FOR REACTION 5 : (CH3* + H* = CH4(g) + 2*)
       DO I = 1,N_GRIDS

              R5(I)=FK5*YY(IYCH3+I-1)*YY(IYH+I-1)-
       1      RK5*PTOT*YY(IYCH4+I-1)*THETA_V(I)**2.0D0

       END DO

C      FOR REACTION 6 : (CO* + H* = CHO* + *)
       DO I = 1,N_GRIDS

       R6(I) = FK6*YY(IYCO+I-1)*YY(IYH+I-1)-RK6*YY(IYCHO+I-1)*THETA_V(I)
       END DO

C      FOR REACTION 7 : (CHO* + H* = CH2O* + *)

       DO I = 1,N_GRIDS
       R7(I)=FK7*YY(IYCHO+I-1)*YY(IYH+I-1)-RK7*YY(IYCH2O+I-1)*THETA_V(I)
       END DO

C      FOR REACTION 8 : (CH2O* + H* = CH3O* + *)
       DO I = 1,N_GRIDS

              R8(I) = FK8*YY(IYCH2O+I-1)*YY(IYH+I-1)-
       1      RK8*YY(IYCH3O+I-1)*THETA_V(I)

       END DO

C      FOR REACTION 9 : (CH3O* + H* = CH3* + OH*)
       DO I = 1,N_GRIDS

              R9(I) = (FK9*YY(IYCH3O+I-1)*YY(IYH+I-1)-
       1      RK9*YY(IYCH3+I-1)*YY(IYOH+I-1))

       END DO

C      FOR REACTION 10 : (CO* + O* = CO2**)
       DO I = 1,N_GRIDS
       R10(I)=(FK10*YY(IYCO+I-1)*YY(IYO+I-1)-RK10*YY(IYYCO2+I-1))*0.0d0
       END DO


C      FOR REACTION 11 : (O* + H* = OH* + *)
       DO I = 1,N_GRIDS
       R11(I) = FK11*YY(IYO+I-1)*YY(IYH+I-1)-RK11*YY(IYOH+I-1)*THETA_V(I)
       END DO

C      FOR REACTION 12 : (OH* + H* = H2O* + *)
```

```
      DO I = 1,N_GRIDS

            R12(I)=FK12*YY(IYOH+I-1)*YY(IYH+I-1)-
     1      RK12*YY(IYYH2O+I-1)*THETA_V(I)
      END DO

C     FOR REACTION 13: (H2O* = H2O(g) + *)
      DO I = 1,N_GRIDS

      R13(I)=FK3*YY(IYYH2O+I-1)-RK13*PTOT*YY(IYH2O+I-1)*THETA_V(I)
      END DO
C     FOR REACTION 14 : (CO2** = CO2(g) + 2*)
      DO I = 1,N_GRIDS

            R14(I)=FK14*YY(IYYCO2+I-1)-
     1      RK14*PTOT*YY(IYCO2+I-1)*THETA_V(I)**2.0D0
      END DO

C     FOR REACTION 15 : (CO* + * = C* + O*)
      DO I = 1,N_GRIDS
            R15(I) = FK15*YY(IYCO+I-1)*THETA_V(I)-
     1      RK15*YY(IYC+I-1)*YY(IYO+I-1)
      END DO

C     FOR REACTION 16: (CO* + H* = C* + OH*)
      DO I = 1,N_GRIDS

            R16(I) = (FK16*YY(IYCO+I-1)*YY(IYH+I-1)-
     1      RK16*YY(IYC+I-1)*YY(IYOH+I-1))
      END DO


C     FOR REACTION 17: (CH3O* + * = CH3* + O*)
      DO I = 1,N_GRIDS

            R17(I) = (FK17*YY(IYCH3O+I-1)*THETA_V(I)-
     1      RK17*YY(IYCH3+I-1)*YY(IYO+I-1))
      END DO



C     FOR REACTION 18: (CO* = CO(g) + *)
      DO I = 1,N_GRIDS

      R18(I)=FK18*YY(IYCO+I-1)-RK18*PTOT*YY(IYCO_G+I-1)*THETA_V(I)
      END DO

C     ENTER DIFFERENTIAL EQUATIONS

C     FOR H2(g)


            YDOT(IYH2) = -(YY(IYH2)-YH2_0)/DENOM1 - FACTOR*R1(1)

      IF(N_GRIDS.GT.1)THEN


C     AT ALL OTHER NODES

      KK=1
      DO I = IYH2+1,IEYH2
            KK = KK+1
            YDOT(I) = -(YY(I)-YY(I-1))/DENOM1 -FACTOR*R1(KK)
```

```
      END DO

      END IF

C     FOR CO GAS:


            YDOT(IYCO_G) = -YY(IYCO)/DENOM1 + FACTOR*R18(1)


      IF(N_GRIDS.GT.1)THEN



C     AT ALL OTHER NODES
      KK=1

      DO I = IYCO_G+1,IEYCO_G

            KK=KK+1
            YDOT(I) = -(YY(I)-YY(I-1))/DENOM1 +FACTOR*R18(KK)
      END DO

      END IF

C     FOR METHANE GAS:


            YDOT(IYCH4) = -YY(IYCH4)/DENOM1 + FACTOR*R5(1)


      IF(N_GRIDS.GT.1)THEN



C     AT ALL OTHER NODES
      KK=1

      DO I = IYCH4+1,IEYCH4

            KK=KK+1
            YDOT(I) = -(YY(I)-YY(I-1))/DENOM1 +FACTOR*R5(KK)
      END DO

      END IF
C     FOR CO2 GAS

      YDOT(IYCO2) = -YY(IYCO2)/DENOM1 +FACTOR*R14(1)
      IF(N_GRIDS.GT.1)THEN

C     AT ALL OTHER NODES

      KK =1
      DO I = IYCO2+1,IEYCO2
            KK = KK+1
            YDOT(I) = -(YY(I)-YY(I-1))/DENOM1 + FACTOR *R14(KK)
      END DO

      END IF


C     FOR WATER GAS
```

```
              YDOT(IYH2O) = -YY(IYH2O)/DENOM1 +FACTOR*R13(1)


       IF(N_GRIDS.GT.1)THEN

C      FOR ALL OTHER NODES

       KK = 1
       DO I = IYH2O+1,IEYH2O
              KK = KK+1
              YDOT(I) = -(YY(I)-YY(I-1))/DENOM2 +FACTOR *R13(KK)
       END DO

       END IF

C      FOR SURFACE H
500    K = 0
       DO I = IYH,IEYH
              K = K+1

              YDOT(I) = 2.0D0*R1(K)-R2(K)-R3(K)-R4(K)-R5(K)-R6(K)-R7(K)-
       1      R8(K)-R9(K)-R11(K)-R12(K)-R16(K)
       END DO

C      FOR SURFACE C
       K = 0
       DO I = IYC,IEYC
              K = K+1

              YDOT(I) = -R2(K)+R15(K)+R16(K)
       END DO

C      FOR SURFACE CH
       K=0
       DO I = IYCH,IEYCH
              K = K+1
              YDOT(I) = R2(K)-R3(K)
       END DO

C      FOR SURFACE CH2
       K = 0
       DO I = IYCH2,IEYCH2
              K = K+1

              YDOT(I) = R3(K)-R4(K)
       END DO

C      FOR SURFACE CH3
       K = 0
       DO I = IYCH3,IEYCH3
              K = K+1
              YDOT(I)=R4(K)-R5(K)+R9(K)+R17(K)
       END DO


C      FOR SURFACE CO
       K = 0
       DO I = IYCO,IEYCO
              K = K+1
              YDOT(I) = -R6(K)-R15(K)-R16(K)-R18(K)
       END DO
```

```
C      FOR SURFACE O
       K=0
       DO I = IYO,IEYO
              K = K+1
              YDOT(I) = -R10(K)-R11(K)+R15(K)+R17(K)
       END DO


C      FOR SURFACE CHO
       K = 0
       DO I = IYCHO,IEYCHO
              K = K+1
              YDOT(I) = R6(K)-R7(K)
       END DO

C      FOR SURFACE CH2O
       K = 0
       DO I = IYCH2O,IEYCH2O
              K = K+1
              YDOT(I) = R7(K)-R8(K)
       END DO


C      FOR SURFACE CH3O
       K = 0
       DO I = IYCH3O,IEYCH3O
              K = K+1

              YDOT(I) = R8(K)-R9(K)-R17(K)
       END DO


C      FOR SURFACE OH
       K = 0
       DO I =IYOH,IEYOH
              K=K+1

              YDOT(I)=R9(K)+R11(K)-R12(K)+R16(K)
       END DO


C      FOR SURFACE CO2
       K = 0
       DO I = IYYCO2,IEYYCO2
              K = K+1
              YDOT(I) = R10(K)-R14(K)
       END DO


C      FOR SURFACE H2O
       K=0
       DO I = IYYH2O,IEYYH2O
              K = K+1

              YDOT(I) = R12(K)-R13(K)
       END DO

       K=0
       KK=0

      RETURN
      END
```

```
C
C
C      GENERATE THE JACOBIAN
      SUBROUTINE JEX (NEQ, TT, YY, ML, MU, PD, NRPD, RPAR, IPAR)
      DOUBLE PRECISION PD, RPAR, TT, YY

      DIMENSION YY(NEQ), PD(NRPD,NEQ)


       RETURN
       END
```

A.9 Mathcad Worksheet for Implementing Sequential Design of Experiments

$$T := \begin{pmatrix} 493 \\ 493 \\ 493 \\ 493 \\ 493 \\ 493 \\ 493 \\ 493 \\ 493 \\ 513 \\ 513 \\ 513 \\ 513 \\ 513 \\ 513 \\ 513 \\ 513 \\ 513 \\ 513 \\ 513 \\ 513 \\ 523 \end{pmatrix} \frac{K}{K} \qquad PCO := \begin{pmatrix} 5.125 \\ 4.707 \\ 4.108 \\ 1.347 \\ 3.156 \\ 5.058 \\ 4.419 \\ 4.221 \\ 4.29 \\ 5.105 \\ 4.618 \\ 3.388 \\ 3.303 \\ 2.892 \\ 2.703 \\ 4.645 \\ 1.88 \\ 5.016 \\ 2.524 \\ 3.021 \\ 4.606 \\ 4.103 \end{pmatrix} \frac{atm}{atm} \qquad PH2 := \begin{pmatrix} 10.687 \\ 11.547 \\ 11.114 \\ 3.756 \\ 7.062 \\ 10.554 \\ 11.515 \\ 10.327 \\ 9.2 \\ 10.633 \\ 10.159 \\ 10.55 \\ 10.526 \\ 8.453 \\ 6.643 \\ 10.228 \\ 3.535 \\ 11.901 \\ 5.541 \\ 6.258 \\ 10.186 \\ 9.86 \end{pmatrix} \frac{atm}{atm}$$

$$A_{co} := 9.186 \cdot 10^{5} \frac{\frac{mol}{hr \cdot kg}}{\frac{mol}{hr \cdot kg}} \qquad E_{co} := 6.167 \cdot 10^{4} \frac{\frac{J}{mol}}{\frac{J}{mol}}$$

$$A_{COH2} := \left(4.421 \cdot 10^{-3}\right) \qquad \Delta H_{COH2} := -1.334 \cdot 10^{4} \frac{\frac{J}{mol}}{\frac{J}{mol}}$$

The reaction rate expression is denoted as r_4 and is given below.

$$r4 = \frac{A_{co}\cdot\exp\left(\frac{-E_{co}}{Rg\cdot T}\right)\cdot PCO^{\frac{2}{3}}\cdot PH2^{\frac{5}{6}}}{\left(1 + A_{COH2}\cdot\exp\left(\frac{-\Delta H_{COH2}}{Rg\cdot T}\right)\cdot PCO^{\frac{2}{3}}\cdot PH2^{\frac{1}{3}}\right)^2}$$

$$\frac{d}{dA_{co}}r4 = \exp\left(\frac{-E_{co}}{Rg\cdot T}\right)\cdot PCO^{\frac{2}{3}}\frac{PH2^{\frac{5}{6}}}{\left(1 + A_{COH2}\cdot\exp\left(\frac{-\Delta H_{COH2}}{Rg\cdot T}\right)\cdot PCO^{\frac{2}{3}}\cdot PH2^{\frac{1}{3}}\right)^2}$$

$$dA_{co} := \left[\exp\left(\frac{-E_{co}}{Rg\cdot T}\right)\cdot PCO^{\frac{2}{3}}\frac{PH2^{\frac{5}{6}}}{\left(1 + A_{COH2}\cdot\exp\left(\frac{-\Delta H_{COH2}}{Rg\cdot T}\right)\cdot PCO^{\frac{2}{3}}\cdot PH2^{\frac{1}{3}}\right)^2}\right]\rightarrow$$

$$\frac{d}{dE_{CO}}r4 = \frac{-A_{co}}{Rg\cdot T}\cdot e^{\frac{-E_{co}}{Rg\cdot T}}\cdot PCO^{\frac{2}{3}}\frac{PH2^{\frac{5}{6}}}{\left(1 + A_{COH2}\cdot e^{\frac{-\Delta H_{COH2}}{Rg\cdot T}}\cdot PCO^{\frac{2}{3}}\cdot PH2^{\frac{1}{3}}\right)^2}$$

$$dE_{CO} := \left[\frac{-A_{co}}{Rg\cdot T}\cdot e^{\frac{-E_{co}}{Rg\cdot T}}\cdot PCO^{\frac{2}{3}}\frac{PH2^{\frac{5}{6}}}{\left(1 + A_{COH2}\cdot e^{\frac{-\Delta H_{COH2}}{Rg\cdot T}}\cdot PCO^{\frac{2}{3}}\cdot PH2^{\frac{1}{3}}\right)^2}\right]\rightarrow$$

$$\frac{d}{dA_{COH2}} r4 = -2 \cdot A_{co} \cdot \exp\left(\frac{-E_{co}}{Rg \cdot T}\right) \cdot PCO^{\frac{4}{3}} \cdot \frac{PH2^{\frac{7}{6}}}{\left(1 + A_{COH2} \cdot \exp\left(\frac{-\Delta H_{COH2}}{Rg \cdot T}\right) \cdot PCO^{\frac{2}{3}} \cdot PH2^{\frac{1}{3}}\right)^3} \cdot \exp\left(\frac{-\Delta H_{COH2}}{Rg \cdot T}\right)$$

$$dA_{COH2} := \overrightarrow{\left[-2 \cdot A_{co} \cdot \exp\left(\frac{-E_{co}}{Rg \cdot T}\right) \cdot PCO^{\frac{4}{3}} \cdot \frac{PH2^{\frac{7}{6}}}{\left(1 + A_{COH2} \cdot \exp\left(\frac{-\Delta H_{COH2}}{Rg \cdot T}\right) \cdot PCO^{\frac{2}{3}} \cdot PH2^{\frac{1}{3}}\right)^3} \cdot \exp\left(\frac{-\Delta H_{COH2}}{Rg \cdot T}\right)\right]}$$

$$\frac{d}{d\Delta HCOH2} r4 = 2 \cdot A_{co} \cdot e^{\frac{-E_{co}}{Rg \cdot T}} \cdot PCO^{\frac{4}{3}} \cdot \frac{PH2^{\frac{7}{6}}}{\left(1 + A_{COH2} \cdot e^{\frac{-\Delta H_{COH2}}{Rg \cdot T}} \cdot PCO^{\frac{2}{3}} \cdot PH2^{\frac{1}{3}}\right)^3} \cdot \frac{A_{COH2}}{Rg \cdot T} \cdot e^{\frac{-\Delta H_{COH2}}{Rg \cdot T}}$$

$$d\Delta HCOH2 := \overrightarrow{\left[2 \cdot A_{co} \cdot e^{\frac{-E_{co}}{Rg \cdot T}} \cdot PCO^{\frac{4}{3}} \cdot \frac{PH2^{\frac{7}{6}}}{\left(1 + A_{COH2} \cdot e^{\frac{-\Delta H_{COH2}}{Rg \cdot T}} \cdot PCO^{\frac{2}{3}} \cdot PH2^{\frac{1}{3}}\right)^3} \cdot \frac{A_{COH2}}{Rg \cdot T} \cdot e^{\frac{-\Delta H_{COH2}}{Rg \cdot T}}\right]}$$

$$dAA_{co}(PCOn, PH2n, Tn) := \exp\left(\frac{-E_{co}}{Rg \cdot Tn}\right) \cdot PCOn^{\frac{2}{3}} \cdot \frac{PH2n^{\frac{5}{6}}}{\left(1 + A_{COH2} \cdot \exp\left(\frac{-\Delta H_{COH2}}{Rg \cdot Tn}\right) \cdot PCOn^{\frac{2}{3}} \cdot PH2n^{\frac{1}{3}}\right)^2}$$

$$dEE_{CO}(PCOn, PH2n, Tn) := \frac{-A_{co}}{Rg \cdot Tn} \cdot e^{\frac{-E_{co}}{Rg \cdot Tn}} \cdot PCOn^{\frac{2}{3}} \cdot \frac{PH2n^{\frac{5}{6}}}{\left(1 + A_{COH2} \cdot e^{\frac{-\Delta H_{COH2}}{Rg \cdot Tn}} \cdot PCOn^{\frac{2}{3}} \cdot PH2n^{\frac{1}{3}}\right)^2}$$

Derivatives continued:

$$dAA_{COH2}(PCOn, PH2n, Tn) := -2 \cdot A_{co} \cdot \exp\left(\frac{-E_{co}}{Rg \cdot Tn}\right) \cdot PCOn^{\frac{4}{3}} \cdot \frac{PH2n^{\frac{7}{6}}}{\left(1 + A_{COH2} \cdot \exp\left(\frac{-\Delta H_{COH2}}{Rg \cdot Tn}\right) \cdot PCOn^{\frac{2}{3}} \cdot PH2n^{\frac{1}{3}}\right)^3} \cdot \exp\left(\frac{-\Delta H_{COH2}}{Rg \cdot Tn}\right)$$

$$d\Delta\Delta HCOH2(PCOn, PH2n, Tn) := 2 \cdot A_{co} \cdot e^{\frac{-E_{co}}{Rg \cdot Tn}} \cdot PCOn^{\frac{4}{3}} \cdot \frac{PH2n^{\frac{7}{6}}}{\left(1 + A_{COH2} \cdot e^{\frac{-\Delta H_{COH2}}{Rg \cdot Tn}} \cdot PCOn^{\frac{2}{3}} \cdot PH2n^{\frac{1}{3}}\right)^3} \cdot \frac{A_{COH2}}{Rg \cdot Tn} \cdot e^{\frac{-\Delta H_{COH2}}{Rg \cdot Tn}}$$

$$Jacob(PCOn, PH2n, Tn) := \begin{pmatrix} dA_{co_1} & dE_{CO_1} & dA_{COH2_1} & d\Delta HCOH2_1 \\ dA_{co_2} & dE_{CO_2} & dA_{COH2_2} & d\Delta HCOH2_2 \\ dA_{co_3} & dE_{CO_3} & dA_{COH2_3} & d\Delta HCOH2_3 \\ dA_{co_4} & dE_{CO_4} & dA_{COH2_4} & d\Delta HCOH2_4 \\ dA_{co_5} & dE_{CO_5} & dA_{COH2_5} & d\Delta HCOH2_5 \\ dA_{co_6} & dE_{CO_6} & dA_{COH2_6} & d\Delta HCOH2_6 \\ dA_{co_7} & dE_{CO_7} & dA_{COH2_7} & d\Delta HCOH2_7 \\ dA_{co_8} & dE_{CO_8} & dA_{COH2_8} & d\Delta HCOH2_8 \\ dA_{co_9} & dE_{CO_9} & dA_{COH2_9} & d\Delta HCOH2_9 \\ dA_{co_{10}} & dE_{CO_{10}} & dA_{COH2_{10}} & d\Delta HCOH2_{10} \\ dA_{co_{11}} & dE_{CO_{11}} & dA_{COH2_{11}} & d\Delta HCOH2_{11} \\ dA_{co_{12}} & dE_{CO_{12}} & dA_{COH2_{12}} & d\Delta HCOH2_{12} \\ dA_{co_{13}} & dE_{CO_{13}} & dA_{COH2_{13}} & d\Delta HCOH2_{13} \\ dA_{co_{14}} & dE_{CO_{14}} & dA_{COH2_{14}} & d\Delta HCOH2_{14} \\ dA_{co_{15}} & dE_{CO_{15}} & dA_{COH2_{15}} & d\Delta HCOH2_{15} \\ dA_{co_{16}} & dE_{CO_{16}} & dA_{COH2_{16}} & d\Delta HCOH2_{16} \\ dA_{co_{17}} & dE_{CO_{17}} & dA_{COH2_{17}} & d\Delta HCOH2_{17} \\ dA_{co_{18}} & dE_{CO_{18}} & dA_{COH2_{18}} & d\Delta HCOH2_{18} \\ dA_{co_{19}} & dE_{CO_{19}} & dA_{COH2_{19}} & d\Delta HCOH2_{19} \\ dA_{co_{20}} & dE_{CO_{20}} & dA_{COH2_{20}} & d\Delta HCOH2_{20} \\ dA_{co_{21}} & dE_{CO_{21}} & dA_{COH2_{21}} & d\Delta HCOH2_{21} \\ dA_{co_{22}} & dE_{CO_{22}} & dA_{COH2_{22}} & d\Delta HCOH2_{22} \\ dAA_{co}(PCOn, PH2n, Tn) & dEE_{CO}(PCOn, PH2n, Tn) & dAA_{COH2}(PCOn, PH2n, Tn) & d\Delta\Delta HCOH2(PCOn, PH2n, Tn) \end{pmatrix}$$

Test the Jacobian matrix at P_{CO} = 3 atm, P_{H2} = 10 atm and T = 523 K.

$$AA(PCOn, PH2n, Tn) := Jacob(PCOn, PH2n, Tn)^{T} \cdot Jacob(PCOn, PH2n, Tn)$$

$$AA(3,10,523) = \begin{pmatrix} 2.213 \times 10^{-10} & -4.773 \times 10^{-8} & -0.032 & 3.353 \times 10^{-8} \\ -4.773 \times 10^{-8} & 1.03 \times 10^{-5} & 6.967 & -7.243 \times 10^{-6} \\ -0.032 & 6.967 & 4.799 \times 10^{6} & -4.993 \\ 3.353 \times 10^{-8} & -7.243 \times 10^{-6} & -4.993 & 5.197 \times 10^{-6} \end{pmatrix}$$

$$Det(PCOn, PH2n, Tn) := |AA(PCOn, PH2n, Tn)|$$

$$Det(1,3,523) = 1.213 \times 10^{-24}$$

Generate a matrix of FF(PCOnew,PH2new)

$Tn := 523$

```
PP := | PCOn_1 ← 1
      | PH2n_1 ← 3
      | for i ∈ 1.. 1000
      |     PCOn_{i+1} ← PCOn_i + 0.01
      |     for j ∈ 1.. 1000
      |         PH2n_{j+1} ← PH2n_j + 0.019
      |         Dett_{i,j} ← Det(PCOn_i, PH2n_j, Tn)
      | Dett
```

PP =

	1	2	3	4	5	6	7
1	$1.213 \cdot 10^{-24}$	$1.218 \cdot 10^{-24}$	$1.223 \cdot 10^{-24}$	$1.227 \cdot 10^{-24}$	$1.232 \cdot 10^{-24}$	$1.237 \cdot 10^{-24}$	$1.241 \cdot 10^{-24}$
2	$1.216 \cdot 10^{-24}$	$1.221 \cdot 10^{-24}$	$1.225 \cdot 10^{-24}$	$1.23 \cdot 10^{-24}$	$1.235 \cdot 10^{-24}$	$1.239 \cdot 10^{-24}$	$1.244 \cdot 10^{-24}$
3	$1.218 \cdot 10^{-24}$	$1.223 \cdot 10^{-24}$	$1.228 \cdot 10^{-24}$	$1.232 \cdot 10^{-24}$	$1.237 \cdot 10^{-24}$	$1.242 \cdot 10^{-24}$	$1.247 \cdot 10^{-24}$
4	$1.221 \cdot 10^{-24}$	$1.226 \cdot 10^{-24}$	$1.23 \cdot 10^{-24}$	$1.235 \cdot 10^{-24}$	$1.24 \cdot 10^{-24}$	$1.244 \cdot 10^{-24}$	$1.249 \cdot 10^{-24}$
5	$1.223 \cdot 10^{-24}$	$1.228 \cdot 10^{-24}$	$1.233 \cdot 10^{-24}$	$1.237 \cdot 10^{-24}$	$1.242 \cdot 10^{-24}$	$1.247 \cdot 10^{-24}$	$1.252 \cdot 10^{-24}$
6	$1.226 \cdot 10^{-24}$	$1.23 \cdot 10^{-24}$	$1.235 \cdot 10^{-24}$	$1.24 \cdot 10^{-24}$	$1.245 \cdot 10^{-24}$	$1.249 \cdot 10^{-24}$	$1.254 \cdot 10^{-24}$
7	$1.228 \cdot 10^{-24}$	$1.233 \cdot 10^{-24}$	$1.238 \cdot 10^{-24}$	$1.242 \cdot 10^{-24}$	$1.247 \cdot 10^{-24}$	$1.252 \cdot 10^{-24}$	$1.256 \cdot 10^{-24}$
8	$1.23 \cdot 10^{-24}$	$1.235 \cdot 10^{-24}$	$1.24 \cdot 10^{-24}$	$1.245 \cdot 10^{-24}$	$1.249 \cdot 10^{-24}$	$1.254 \cdot 10^{-24}$	$1.259 \cdot 10^{-24}$
9	$1.233 \cdot 10^{-24}$	$1.237 \cdot 10^{-24}$	$1.242 \cdot 10^{-24}$	$1.247 \cdot 10^{-24}$	$1.252 \cdot 10^{-24}$	$1.256 \cdot 10^{-24}$	$1.261 \cdot 10^{-24}$
10	$1.235 \cdot 10^{-24}$	$1.24 \cdot 10^{-24}$	$1.244 \cdot 10^{-24}$	$1.249 \cdot 10^{-24}$	$1.254 \cdot 10^{-24}$	$1.259 \cdot 10^{-24}$	$1.263 \cdot 10^{-24}$
11	$1.237 \cdot 10^{-24}$	$1.242 \cdot 10^{-24}$	$1.247 \cdot 10^{-24}$	$1.251 \cdot 10^{-24}$	$1.256 \cdot 10^{-24}$	$1.261 \cdot 10^{-24}$	$1.265 \cdot 10^{-24}$
12	$1.239 \cdot 10^{-24}$	$1.244 \cdot 10^{-24}$	$1.249 \cdot 10^{-24}$	$1.253 \cdot 10^{-24}$	$1.258 \cdot 10^{-24}$	$1.263 \cdot 10^{-24}$	$1.268 \cdot 10^{-24}$
13	$1.241 \cdot 10^{-24}$	$1.246 \cdot 10^{-24}$	$1.251 \cdot 10^{-24}$	$1.255 \cdot 10^{-24}$	$1.26 \cdot 10^{-24}$	$1.265 \cdot 10^{-24}$	$1.27 \cdot 10^{-24}$
14	$1.243 \cdot 10^{-24}$	$1.248 \cdot 10^{-24}$	$1.253 \cdot 10^{-24}$	$1.257 \cdot 10^{-24}$	$1.262 \cdot 10^{-24}$	$1.267 \cdot 10^{-24}$	$1.272 \cdot 10^{-24}$
15	$1.245 \cdot 10^{-24}$	$1.25 \cdot 10^{-24}$	$1.255 \cdot 10^{-24}$	$1.259 \cdot 10^{-24}$	$1.264 \cdot 10^{-24}$	$1.269 \cdot 10^{-24}$	$1.274 \cdot 10^{-24}$
16	$1.247 \cdot 10^{-24}$	$1.252 \cdot 10^{-24}$	$1.257 \cdot 10^{-24}$	$1.261 \cdot 10^{-24}$	$1.266 \cdot 10^{-24}$	$1.271 \cdot 10^{-24}$	...

To identify the partial pressures,

List the PCO_{news} and PH_{2news} by index

$$PCOnew := \left| \begin{array}{l} PCOnew_1 \leftarrow 1 \\ \text{for } i \in 1..1000 \\ \quad PCOnew_{i+1} \leftarrow PCOnew_i + 0.01 \\ PCOnew \end{array} \right.$$

$$PH2new := \left| \begin{array}{l} PH2new_1 \leftarrow 3 \\ \text{for } i \in 1..1000 \\ \quad PH2new_{i+1} \leftarrow PH2new_i + 0.019 \\ PH2new \end{array} \right.$$

From a 3D-graph, select the indices of PCO_{new} and PH_{2new} that not only gives the highest value of the determinant but also,
its corresponding PH2/PCO will be within an acceptable range

$$PCOnew_{10} = 1.09$$

$$PH2new_{700} = 16.281$$

$$Det(1.09, 16.281, 523) = 4.003 \times 10^{-24}$$

Now Calculate the inlet values using reactor performance equation

Choose a CO conversion within the new constraints:

$X_{co} := 0.5$ $X_{H2} := 0.5$ $W_{reactor} := 5.69 \cdot gm$ $V_m := 22.4 \frac{L}{mol}$

$PCO := 1.09 \cdot atm$ $PH2 := 16.281 atm$ $Ratio_{out} := \frac{PH2}{PCO}$ $Ratio_{out} = 14.937$

$\Delta H_{COH2} = -1.334 \times 10^{4}$ $Rg := 8.314 \frac{J}{mol \cdot K}$ $T := Tn \cdot K$ $A_{co} = 9.186 \times 10^{5}$

$$r4_{FT} := \frac{A_{co} \frac{mol}{kg \cdot hr \cdot atm^{1.5}} \cdot \exp\left(\frac{-E_{co} \frac{J}{mol}}{Rg \cdot T}\right) \cdot PCO^{\frac{2}{3}} \cdot PH2^{\frac{5}{6}}}{\left(1 + A_{COH2} \cdot atm^{-1} \cdot \exp\left(\frac{-\Delta H_{COH2} \frac{J}{mol}}{Rg \cdot T}\right) \cdot PCO^{\frac{2}{3}} \cdot PH2^{\frac{1}{3}}\right)^2}$$

$r4_{FT} = 1.215 \times 10^{-3} \frac{mol}{kg \cdot s}$

Now Assume that rate of FT is 55% of overall rate of CO

Therefore $r_{CO} := \frac{r4_{FT}}{0.55}$ $r_{CO} = 2.209 \times 10^{-3} \frac{mol}{kg \cdot s}$

$\frac{W_{reactor}}{F_{COo}} = \frac{X_{co}}{r_{CO}}$ Therefore $F_{COo} := \frac{W_{reactor} \cdot r_{CO}}{X_{co}}$ $F_{COo} = 0.091 \frac{mol}{hr}$

Convert to CO and H2 flows rate at STP:

$V_{COo} := F_{COo} \cdot 22.4 \frac{L}{mol}$ $V_{COo} = 33.791 \frac{mL}{min}$

$PCOo := \frac{F_{COo} \cdot Rg \cdot T}{V_{COo}}$ $PCOo = 1.916\,atm$

If Stio ratio of H2: CO = 2.01:1, then

$r_{H2} := 2.01 \cdot r_{CO}$ $r_{H2} = 4.441 \times 10^{-3} \frac{mol}{kg \cdot s}$

$\frac{W_{reactor}}{F_{H2o}} = \frac{X_{H2}}{r_{H2}}$ Therefore $F_{H2o} := \frac{W_{reactor} \cdot r_{H2}}{X_{H2}}$ $F_{H2o} = 0.182 \frac{mol}{hr}$

$V_{H2o} := F_{H2o} \cdot 22.4 \frac{L}{mol}$ $V_{H2o} = 67.92 \frac{mL}{min}$

Specify approximate selectivites for CH4, CO2 and C2+

$Sel_{CH4} := 0.15$ $Sel_{CO2} := 0.3$ $Sel_{C2\_plus} := 1 - Sel_{CH4} - Sel_{CO2}$

$Sel_{C2\_plus} = 0.55$

$F_{CO\_consumed} := X_{co} \cdot F_{COo}$ $F_{CO\_consumed} = 1.257 \times 10^{-5} \frac{mol}{s}$

$F_{H2\_consumed} := X_{H2} \cdot F_{H2o}$ $F_{H2\_consumed} = 2.527 \times 10^{-5} \frac{mol}{s}$

$F_{CH4\_produced} := Sel_{CH4} \cdot F_{CO\_consumed}$ $F_{CH4\_produced} = 1.886 \times 10^{-6} \frac{mol}{s}$

$F_{CO2\_produced} := Sel_{CO2} \cdot F_{CO\_consumed}$ $F_{CO2\_produced} = 3.771 \times 10^{-6} \frac{mol}{s}$

$F_{C2\_plus\_produced} := Sel_{C2\_plus} \cdot F_{CO\_consumed}$ $F_{C2\_plus\_produced} = 6.914 \times 10^{-6} \frac{mol}{s}$

$F_{H2O\_produced\_in\_reaction\_1} := F_{CH4\_produced}$ $F_{H2O\_consumed\_in\_reaction\_3} := F_{CO2\_produced}$

$F_{H2O\_produced\_in\_reaction\_2} := F_{C2\_plus\_produced}$

$F_{H2O\_overall} := F_{H2O\_produced\_in\_reaction\_1} + F_{H2O\_produced\_in\_reaction\_2} - F_{CO2\_produced}$

$F_{H2O\_overall} = 5.028 \times 10^{-6} \frac{mol}{s}$

$$F_{CO\_out} := F_{COo} \cdot (1 - X_{co})$$

$P_{reactor} := 21 \cdot atm$

$$Mole\_fraction\_CO\_in\_reactor := \frac{PCO}{P_{reactor}} \qquad Mole\_fraction\_CO\_in\_reactor = 5.19 \times 10^{-2}$$

$$Mole\_fraction\_H2\_in\_reactor := \frac{PH2}{P_{reactor}} \qquad Mole\_fraction\_H2\_in\_reactor = 0.775$$

$$Moles\_total := \frac{F_{CO\_out}}{Mole\_fraction\_CO\_in\_reactor} \qquad Moles\_total = 0.015 \frac{mol}{min}$$

$$Mole\_fraction\_CH4 := \frac{F_{CH4\_produced}}{Moles\_total} \qquad Mole\_fraction\_CH4 = 7.786 \times 10^{-3}$$

$$Mole\_fraction\_CO2 := \frac{F_{CO2\_produced}}{Moles\_total} \qquad Mole\_fraction\_CO2 = 0.016$$

$$Mole\_fraction\_C2\_plus := \frac{F_{C2\_plus\_produced}}{Moles\_total} \qquad Mole\_fraction\_C2\_plus = 0.029$$

$$Mole\_fraction\_H2O := \frac{F_{H2O\_overall}}{Moles\_total} \qquad Mole\_fraction\_H2O = 0.021$$

$$Mole\_fraction\_inert := 1 - \left(\begin{array}{l} Mole\_fraction\_H2O + Mole\_fraction\_C2\_plus + Mole\_fraction\_CO2 \ldots \\ + Mole\_fraction\_CH4 + Mole\_fraction\_H2\_in\_reactor + Mole\_fraction\_CO\_in\_reactor \end{array} \right)$$

$$Mole\_fraction\_inert = 0.1$$

$$Moles\_inert := Mole\_fraction\_inert \cdot Moles\_total \qquad Moles\_inert = 1.455 \times 10^{-3} \frac{mol}{min}$$

$$V_{inert} := Moles\_inert \cdot 22.4 \cdot \frac{L}{mol} \qquad V_{inert} = 32.597 \frac{mL}{min}$$

Below are the new reactor inlet setpoints

$$\text{COAR\_inlet\_flow} := \frac{V_{COo}}{0.882} \qquad \text{COAR\_inlet\_flow} = 38.312\,\frac{mL}{min}$$

$$\text{Argon\_flow} := \text{COAR\_inlet\_flow} - V_{COo} \qquad \text{Argon\_flow} = 4.521\,\frac{mL}{min}$$

$$V_{Helium} := V_{inert} - \text{Argon\_flow} \qquad V_{Helium} = 28.077\,\frac{mL}{min}$$

$$\text{H2\_inlet\_flow} := V_{H2o} \qquad \text{H2\_inlet\_flow} = 67.92\,\frac{mL}{min}$$

A.10 Developing a Macrokinetic Model That Is Consistent with Theory

Consider the sequence of elementary steps designated as Model 1 in Chapter 5, the LH expression is show below:

$$-r_{CO} = \frac{AP_{CO}^{1/2}P_{H_2}^{3/4}}{\left(1+BP_{CO}^{1/2}P_{H_2}^{1/4}\right)^2} \Rightarrow A = \left(k_4 k_6 K_5 K_1\right)^{1/2} K_2^{3/4} \tag{A-50}$$

$$B = \left(\frac{k_6 K_3 K_5 K_1}{k_4}\right)^{1/2} K_2^{1/4} \tag{A-51}$$

If A, B, and the rate constants for each of the elementary steps are written in Arrhenius form, then

$$A = A_c \exp(Ea_{apparent} / RT)$$
$$B = B_c \exp(\Delta H_b / RT) \quad \text{(A-52)}$$

where

$$Ea_{apparent} = 0.5\left(E_{f4} + E_{f6} + E_{f5} - E_{r5} + E_{f1} - E_{r1}\right) + 0.75\left(E_{f2} - E_{r2}\right) \quad \text{(A-53)}$$

and

$$\Delta H_b = 0.5\left(E_{f6} + E_{f3} - E_{r3} + E_{f5} - E_{r5} + E_{f1} - E_{r1} - E_{f4}\right) + 0.25\left(E_{f2} - E_{r2}\right) \quad \text{(A-54)}$$

The apparent pre-exponential factors Ac and B are given in Appendix A.5. The data fitting procedure is as follows:

1. Make a guess of the binding energies of C, O, and H respectively.
2. Use the UBI-QEP method as demonstrated in Appendix A.4 to calculate the activation energies of the elementary steps in Model 1.
3. Compute the apparent activation energy and heat of adsorption according to Equations A-53 and A-54 respectively.
4. Using the energies calculated in 3 above, the apparent pre-exponential factors, and the partial pressures of CO and H_2, compute CO reaction rate using Equation A-50.
5. Minimize the error between the calculated CO reaction rate and the experimental CO reaction rate by changing the binding energies of C, O, and H respectively.